Cranfield University

School of Mechanical Engineering

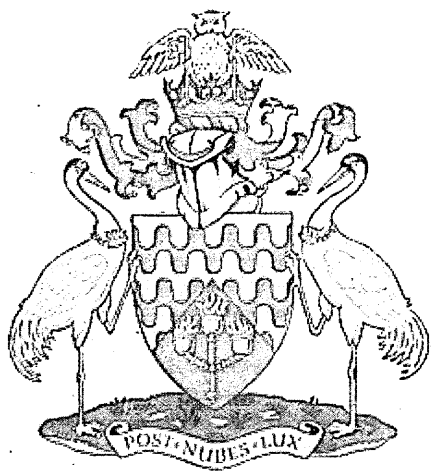

Computational Analysis of High-Speed Axial-Flow Compressors using Two Deterministic Stress Models

PhD Thesis

João Alexandre Amaral Teixeira

Supervisors Dr. Antonios Tourlidakis
Prof. Robin Elder

January 2002

School of Mechanical Engineering

Department of Power, Propulsion and Aerospace Engineering

Ph.D Thesis

Academic Year 2001-2

Computational Analysis of High-Speed Axial-Flow Compressors using Two Deterministic Stress Models

João Alexandre Amaral Teixeira

Supervisor Dr. Antonios Tourlidakis

Prof. Robin Elder

This thesis is submitted in partial fulfilment for the degree of

Doctor of Philosophy

January 2002

Abstract

The employment of CFD methods for the analysis of multistage turbomachinery flows is restricted for the foreseeable future to steady-state methods of which the most widespread one employs the mixing-plane approach. The last method nevertheless is known to introduce jumps in some quantities at the stage interface due to the unphysical pitchwise averaging process it models and when employed in the simulation of multi-stage machines leads to a progressive downstream degradation of the solution accuracy.

Adamczk's average-passage equation system is the steady-state approach which fundamentally overcomes these limitations but the requirement that a set of machine-wide domains be iteratively solved as part of the calculation of each of the rows of interest, entails large computational requirements. A far more economical solution is to combine some of Adamczyk's equation terms accounting for the cyclic components of the unsteady stage effects, the deterministic stress terms, with a mixing-plane steady-state formulation. This is the approach taken by the two semi-empirical models which were employed in this work to study two high-speed axial-flow compressor configurations, the single-stage Rolls-Royce HP9 and the novel three stage Cranfield University High Speed Research Compressor.

The Hall and the Bolger deterministic stress models were combined with the CFD turbomachinery code CFX-TASCflow via a Source Code Interface and results were obtained for the two cases with and without the application of the models. Although the impact of the addition of deterministic stress terms to the solution of HP9 is noticeable but small, these effects are in the Cranfield machine more noticeable and seen to offer some contribution towards the approximation of the computational to the experimental global performance results.

Acknowledgement

The author wishes to express his sincere gratitude to his two academic supervisors, Prof. Robin Elder and Dr. Antonios Tourlidakis who were a source of constant support and unfailing helpfulness.

My thanks are also due to Dr. John J. Bolger who gave me access to his deterministic stress model, used in this work, and Drs. Jason Tan and Ian Bennet who were a regular source of assistance.

I am additionally indebted to all the students of the Turbomachinery Group who were my contemporaries, in particular Clive Lockwood and Antonios Koumoutsos, last heard of sailing to Ithaka.

Finally I am grateful for the support of my family in Portugal and in England, my wife Eleanor and our children Álvaro and Amália, to whom this work is dedicated.

Table of Contents

List of Tables

List of figures

Nomenclature

a	Empirical coefficient
A	Solution coefficients matrix
A^+	Empirical damping factor
b	Empirical coefficient
c	Blade chord, empirical coefficient
C, C_1, C_{cp}	Empirically derived constants
C_ε, C_k , C_μ	Empirical constants of k- ε model
C_D	Drag coefficient
d	Empirical coefficient
D	van Driest's damping length function
E	Total energy per unit volume
f	Conservation equations source terms
F	Body-force vector
F_k	Klebanoff intermittency factor
H	Total enthalpy
k	Coefficient of thermal conductivity, turbulent kinetic energy
l, l_m	Turbulent mixing length
L	Lower solution coefficients matrix
M	Mach number
n	Surface normal
N	Shape functions
p	Static pressure
P	Total pressure
P_r	Prandtl number
$\bar{q}$	Conductive heat transfer vector
r	Time step ratio
R	Universal gas constant

Re	Reynolds number
R_{ij}	Reynolds stress tensor components
s	Streamwise distance
s	Surface tangent
s, t, u	Elemental coordinates
S	Source term, blade-to-blade distance
t	Time
T	Temperature
U	Upper solution coefficients matrix
V	Velocity vector
x, y, z	Cartesian coordinates
X	Bolger model distance function
y	distance from wall along normal
W	Wake parameter

Greek symbols

α	Decay function
α_t	Turbulent coefficient of
β	Empirical constant, decay function
β_M , β_1 , β_2	Air angles
Γ	Diffusion coefficient
δ	Kronecker delta function, semi-wake width
ε	Turbulent dissipation rate
η	Dimensionless axial coordinate, adiabatic efficiency
θ	Heat flux, angular quantity
κ	von Kármán constant
λ	Velocity
μ	Dynamic viscosity
μ_t	Turbulent kinematic viscosity

ν_s	Sub-grid eddy viscosity
ν_t	Turbulent viscosity
ρ	Density
σ	Solidity, deterministic stresses
σ_k , σ_ε	Empirical constants
τ	Viscous stress tensor
ϕ , φ	Generic function
ω	Profile loss coefficient
Ω	Rotational speed
ξ, η, ζ	Computational space coordinates

Subscripts

0	Freestream relative value
dc	Wake centreline deficit
ip	Integration point
IN	Inviscid
nb	Neighbouring node values
o	Previous time-step value
p	Blade profile
S	Quantity/operation applicable to surface
src	Source term quatity
t	Turbulent
u	Evaluated upstream
V	Viscous
V, *Vol*	Quantity/operation applicable to volume
w	Quantity evaluated at wall

Abbeviations

AGARD	Advisory Group for Aerospace Research and Development
BCF	Boundary condition file
CFL	Courant Friedrichs Lewy stability condition number
DFVLR	Deutsche Forschungs-Und Versuchsanstalt Fur Luft-Und Raumfahrt - German Aerospace Research Establishment
HSRC	High Speed Research Compressor
PAC	Physical advection correction
RHS	Right hand side
LPS	Linear Profile Skew
LU	Lower-upper solution method
MLPS	Modified Linear Profile Skew
MWS	Mass Weighted Skew
UDS	Upstream Difference Scheme

Chapter 1

Introduction

1.1 Preamble

The enormous research and development effort that is incorporated in the modern turbofan engines that power the bulk of the civil airline fleet has reached a stage of high refinement in which fractions of a percent of improvement are being sought in all sections of the engine, Wilde, 1994. Due to their relative position in the gas turbine cycle, both absorbing and delivering power, axial-flow compressors are the more critical of the aerodynamic components of these machines.

In functional terms the compression system of most civil aero engines is divided into two separate components, a large inlet fan stage and a multi-staged core compressor. In the former pressure ratios as high as 1.8 are now commonly attainable while passing up to 70% of the total mass flow rate of the machine, whereas in the latter unit pressure ratios reaching 30:1 or more can be achieved.

The discernable trends in the design features of core compressors are firstly the reduction in the number of stages, leading to compressors which are lighter and cheaper to produce but also whose blading is more heavily loaded, secondly the increase in the hub-tip ratio, meaning shorter blades but also ones over which

secondary flow effects are more important, and lastly the reduction of the axial inter-row spacing which in practice is an offshoot of the initial process.

These trends contribute to augment the unsteady blade row interaction effects, higher loading equating with stronger wakes and close aerofoil spacing corresponding to a reduction in wake decay and hence greater potential interaction or in other words they contribute to augment the effects of the unsteady flow features in the machine. In this context the predictive performance of the multistage CFD methods which do not actively incorporate contributions of the large-scale unsteadiness, must be closely questioned. Of the methods that do account for the unsteadiness, one class does so implicitly by computing the time-dependent turbomachine flow field while the other includes these effects explicitly through the extension of Reynolds type averaging to all unsteady fluctuations or nonuniformities.

The contemporaneous design cycle occurs in the presence of very strong commercial pressures and, alongside the essentially technical demands such as higher fuel efficiency and lower manufacturing costs, lead-in times are seen as a major factor in the design space. The incorporation of fast and accurate numerical design tools in the turbomachinery design process is seen as an essential constituent part of the retention of an assertive commercial edge by gas turbine manufacturers.

The integration of CFD within the turbomachinery design space is not complete though as some important conceptual problems remain, turbulence modelling in particular. Although CFD methods are not often able to predict loss with sufficient accuracy for the purposes of design optimization, Giles, 1998, present-day design of aero fans for example relies heavily on the usage of 3D Navier Stokes analysis, Stow, 2000.

These measures of success should not obscure the fact that compressor design remains a non-exact science and many judgments still have to be made based on experience rather than accurate predictions. This lack of predictive capability permeates through the whole design process down to the fine details of three dimensional and unsteady flow behaviour and necessitates the skill and judgment of the engineer at every step, Gallimore, 1998.

Nevertheless as the role of CFD expands from the analysis of isolated blade rows to the computation of whole compressor systems, there is a call for the accounting, from within steady-state multistage calculations, of the unsteady effects of neighbouring blade rows on a row of interest. The present work can be seen, against this background, as a part of the wide collective effort which seeks to identify the models which are better suited to this task and 'bear witness' on their merits when applied to realistic configurations and when employing an established CFD code.

1.2 Literature survey

This section consist of a survey of a number of relevant topics in axial-flow multistage high-speed turbomachinery to include the recognition of the salient aerodynamic features of these machines and their numerical calculation methods. The review of the steady multiblade-row computational studies is limited to 3D methods and consequently leaves out other successful approaches such as the S1-S2 and throughflow methods, the most useful tools in the design of turbomachines, Cumpsty, 1989.

1.2.1 High-speed axial-flow compressor aerodynamics studies

The objective of this section is to explore the most significant features of the flows which are characteristic of high-speed axial-flow compressors and for that purpose the topics of through and secondary flows, tip clearance and wakes, axial spacing, blockage and loss are visited in succession.

In attempting a description of the complex nature of the flowfield environment present in a multi-blade row turbomachine, it is usual to run through a list of the relevant phenomena: the intrinsic flow unsteadiness due to the relative motion of the neighbouring rows, the associated viscous and potential effects, unsteady circulation and vortex shedding, wake chopping and interaction with downstream rows. To these first order effects others such as boundary layer unsteadiness and high intra row

turbulence production ought to be added for completeness. The strongly unsteady nature of the stage flows alluded to above, adds complexity to the experimental evaluation methods which are employed to study these flows.

Although much of the existing knowledge of the specific flow mechanisms predates the use of numerical methods, the availability of ever more sophisticated CFD codes has added to the existing bank of knowledge by providing access to data at a large number of locations of the ducted blading domain, hundreds of thousands in a typical case, including those totally inaccessible to any experimental method. Therefore a study of previous works dealing with the flow physics of axial compressors multistage environment must consequently gather information from both experimental and numerical sources.

As was pointed out in Adamczyk et al., 1994, a compressor is able to impart energy to a flow stream because the flow within is inherently unsteady, a fact overlooked by many researchers because when analyzing the flow through an isolated blade row, the dependence on time may be eliminated by adopting a coordinate system fixed to the blade row. In a multi-blade row machine the interaction phenomena involves periodic events at blading passing frequency and harmonics as well as random occurrences. This interaction can involve blade rows several stages apart as well as those that are adjacent to each other, Schmidt and Okiishi, 1977.

In a typical stage of an axial-flow compressor, wakes from upstream blades are chopped into segments and transported by the next downstream row. The wake segments can somewhat retain their identity as segments throughout and downstream of the chopping row, Tweedt et al., 1985. Works devoted to the characterization of wake behaviour, are also due to Lakshminarayana and Davino, 1979, in an experimental study of the decay behaviour of the IGV and stator wakes in the Pennsylvania University 1.5 stage research compressor, and Suryavamshi and Lakshminarayana, 1991, who used computation and previously reported experimental data to examine the rotor wakes of that same compressor.

Izsak and Chiang, 1993, produced a wakes description work, which includes a review of previous wake modelling attempts, as did Poensgen and Gallus, 1990, in an

experimental study of the flowfield in an annular compressor cascade. In 1970 Kerrbrock and Mikolajczak, in a much quoted paper, showed that the circumferential total temperature nonuniformity of the flow downstream of a stator row of an axial flow compressor is due to the drift of the rotor wake fluid towards the pressure side of that stator. In this same paper the authors developed the so called "negative jet" wake transport model in which wakes are represented as negative jets of the uniform flow.

Kerrbrock and Mikolajczak as well as Tweedt and his co-workers use a kinematic model of wake shearing and transport to describe the unsteady wake/blade row interaction. Kinematic models do not account for the wake recovery effect whereby wakes undergo an increase in length as they convect through a blade passage with the result that some of the secondary kinetic energy is converted into a pressure rise.

Other representative papers to have dealt with the mechanics of wake recovery are those by Adamczyk, 1996, who employed linear flow theory to quantify the wake recovery in a cascade and Van Zante et al., 1997, who compared the wake decay mixing loss of a rotor in isolation, where this decay is solely due to viscous dissipation, with wake decay in a stage environment where it is shown, the dominant decay process is wake stretching, not viscous mixing. These papers present evidence of rotor wake recovery in a high-speed axial compressor stage through experimentation and unsteady numerical simulation.

In 1998, Valkov and Tan in a computational analysis of the effects of unsteadiness on the performance of an embedded stator noted that a beneficial reversible recovery of energy can occur from both wakes and tip leakage vortices, that the impact of these mechanisms can be described on the same physical basis and that the effects of tip vortices and wakes are of comparable importance. A topic closely associated with wake recovery is the influence of the axial gap of adjacent blade rows on the stage performance. Deregel and Tan, 1996, used a 2-D unsteady Navier-Stokes simulation to investigate the magnitude of the time-averaged mixing loss and pressure rise for the cases where the flow mixed predominantly before the blade row or in the intra-blade passage.

Gorrell et al., 1997, studied the interaction between an upstream stator blade row and a downstream rotor blade row in a 1 1/2 stage research compressor. The reported results indicate a reduction in overall performance concurrent with a decrease in axial spacing. This challenged the commonly accepted axial spacing to overall performance relationship suggesting that there may be a flow mechanism overriding any wake recovery process. This mechanism, the paper conjectures, may involve a shock/boundary layer interaction. Another consideration, Gorrell writes, is that most adjacent row interaction studies have historically focused on the rotor/stator case with the stator/rotor case receiving virtually no attention a situation that may have neglected the fact that it is precisely the last of these which is the more important of the two as regards performance.

Authors which have produced representative studies dealing with wake-boundary layer interactions include Walker and Oliver, 1972, who used experimentally obtained results as a vehicle to explain the thickening and thinning of an aerofoil's boundary layers subjected to oscillating stage potential effects and hence circulation bought about by the passing of an adjacent row's blades. Added to these inviscid stage interactions, compressor blades boundary layers are also subject to wake-induced transition and the influence of free stream turbulence.

Studies which address these phenomena are due to Gallus and Hoenen, 1986, and Addison and Hodson, 1991, the latter containing an excellent description of the mechanisms of boundary layer transition as brought about by the passing of wakes from an upstream blade row. Goulas and Stapountzis, 1997, examined experimentally the behaviour of a blade boundary layers in the presence of incoming unsteady wakes modeled as the interaction between a flat plate laminar boundary layer and the wakes generated by the intermittent passing of a cylinder bar. Dorney and Mosebach et al., 1996, produced a parametric numerical simulation study of the effects of the impingement of upstream rotor wakes upon the boundary layers of a compressor exit guide vanes and Cumpsty et al., 1995, reported the role incoming wakes play, in initiating transition.

Halstead et al., 1995, took unsteady boundary layer measurements and presented detailed comparisons of measured data with numerical predictions, the first such study

to have been reported for multistage compressors. Their work demonstrates the existence of large extents of laminar and transitional flow on the suction surface of the embedded stage. Evidence is presented of the periodic washing, over the blade suction surface, of wake-induced transitional strips separated by regions of laminar, calmed or transitional flow according to the chordwise location. This study considered the effect of the Reynolds number, loading, wake frequency, clocking and turbulent intensity variation.

Solomon and Walker, 1995, examined experimentally the extent of the transitional blade region and obtained results, which include a novel presentation of unsteady transitional behaviour in turbomachinery blading, in the form of ensemble average intermittency contour plots, and which included the significant observation that wake induced strips are initially transitional, rather than completely turbulent as previously was widely assumed in the literature.

Wisler et al., 1987, and Leylek and Wisler, 1990, investigated the mixing phenomena in a multistage environment while having as a backdrop what Wennerstrom, 1990, termed, " the great debate ". This debate revolved around the merits of the approach taken by Adkins and Smith, 1982, who claimed that convective secondary flows not dissipative turbulent diffusion was the dominant mechanism of spanwise mixing and Gallimore and Cumpsty, 1986 who took the opposite view.

What Leylek and Wisler found through detailed computational and experimental investigations was that both inviscid secondary flow and turbulent diffusion contribute significantly to both spanwise and cross-passage mixing. The authors went on to describe how convective and diffusive fluxes interact, in some areas augmenting and in others opposing each other. The geometrical configuration and aerodynamic loading control the relative strength of the two mechanisms but secondary flow induced mixing is stronger near the annulus walls, Bolger and Horlock, 1995.

Goto, 1991, reported an experimental investigation of the impact of tip clearance variation upon the mixing coefficient in a stage stator row while the Storer and Cumpsty, 1993, numerical study presents results that show the mixing of flows of

similar speeds but different directions to be the principal mechanism of tip clearance loss.

Dorney et al. and Walker et al., both in 1998, investigated the flow physics of aerofoil clocking in a 1 1/2 stage axial compressor with a inlet guide vanes-rotor-stator arrangement. Dorney's study which used a quasi 3D unsteady numerical simulation, involved obtaining solutions for eight equispaced clocking positions of the second stator with respect to the first. These authors reported efficiency variations of some 0.6-0.7 %, with the maximum gain corresponding to the circumferential positioning of the second stator such that the first stator's wakes impacted the second stator blades immediately below the leading edge. Walker's experimental data showed the freestream periodic unsteadiness field, as distinct from the random turbulence field, to be altered by clocking of the stator.

The combined effects of stator blade clocking and axial row separation variation on a two and half stage low speed compressor were investigated by Gundy-Burlet and Dorney, 1997, who used an unsteady Navier-Stokes two-dimensional approach to obtain machine efficiency and time averaged pressure and pressure amplitude data. This study showed that the relative impact point of the first-stator wake on the second stator passage has a significant effect on the unsteady potential field of the second stator. Their work confirmed the trend identified by Dorney cited before, that to the highest efficiency point corresponds a peak in the unsteadiness amplitude. The authors identified an indexing related efficiency variation of about 0.8 % for the largest axial separation with this value showing a small reduction as the intra-row gap is decreased.

Barankiewicz and Hathway, 1997, used NASA's Lewis four geometrically identical stage Low Speed Axial Compressor to obtain experimental data at the third stage and at two machine operating conditions, peak pressure and efficiency. As a baseline indexing arrangement all stator rows were circumferentially adjusted so that each other's wakes would impinge on the leading edge of the adjacent downstream row.

The overall efficiency gains measured in this much more representative test case are rather modest, 0.2 % for both operating conditions and as is pointed out these are of

the same magnitude as those imputable to blade to blade variation and blade assembly and manufacturing tolerances. The authors calculated that a re-design of the compressor seeking to eliminate the small clocking induced losses might raise the machine efficiency to 0.4 %.

A number of limitations are evident in these studies namely the absence of an analysis of rotor clocking effects in addition to the stator's and about which Gundy-Burlet and Dorney's paper speculates, "may have as much influence on the performance of the compressor as stator clocking". Other factors that limit the generality of these studies are the choice of configurations with equal numbers of stator blades in each stage, either in the choice of experimental subjects or for simulations, through blade scaling and the exclusive reliance on low speed experimental data.

As to the practical outcome of the present research interest in the subject, "since most multistage compressors have in general a different number of stator blades in each stage, the potential for performance gains due to stator indexing is expected to be even less than that measured in the present effort", the Barankiewicz's paper suggests.

1.2.2 Steady multiblade-row numerical studies

In a turbomachine the flow through adjacent blade rows is intrinsically unsteady due to their relative motion. If a prediction of the flow through two or more rows is to be undertaken in a single calculation and computationally expensive time-accurate calculations are to be avoided, some form of averaging of the flow variables is required to remove the effects of inter-row unsteadiness. Essentially two multistage steady-state models are available, those employing a mixing plane and those derived from the Adamczyk's average-passage equation formulation, Adamczyk, 1985.

Computations of turbomachinery including more than a single stage do not abound in the open literature as is shown by Gerolymos and Hanisch, 1999, where a comprehensive listing of published multiblade row CFD work is included. Of the nineteen entries in Gerolymos and Hanisch's list, seven involve turbines and of the balance of compressors only six concern more than single stage machines. The

corollary of this situation is that the bulk of steady state multistage work has therefore been carried out on single stage cases where the accruing effect of the inter-stage averaging processes cannot be adequately evaluated.

1.2.2.1 Mixing-plane method simulations

In the mixing-plane formulation each blade passage is computed in its natural frame of reference and the circumferential averaging and transfer of information between adjacent rows takes place at a plane normal to the axial direction and approximately halfway between the upstream blade trailing edge and the downstream blade leading edge. Since averaging-plane methods often use mixed-out averages, they are commonly referred to as mixing-plane methods. It is worth noting that mixing in this context is that occurring in an axisymmetric frame of reference or streamsheet ignoring spanwise mixing. This pitchwise averaging does not therefore affects the spanwise variation of the flow in exactly the same way as in the throughflow methods. In effect the mixing-plane method can be seen as the three-dimensional equivalent of the throughflow approach.

The pitchwise averaging is not a physically realistic process unless the blade rows are widely spaced and, if performed too close to the leading or trailing edges, can lead to unrealistic predictions of the flow in those regions of the blade, Denton, 1990. Dawes, 1990, listed as minimum required modelling properties for the mixing-plane model, that the averaging ensures conservation of the mass flow and of the values of absolute total pressure and temperature mass averaged over the cross flow plane.

The unknown boundary conditions at the interface between two adjacent blade rows are part of the numerical solution. At every iteration these interface boundary conditions are updated by passing flow variables information from interior cells of the upstream row to the upstream side of the mixing plane, where the set of specified outflow variables is newly averaged, a comparison with the old average performed and a correction issued. The updated information on the flow properties is then transferred across to the upstream side of the downstream row, the inflow boundary conditions established and the process reversed.

Both Ni and Bogoian, 1989 and Huber and Ni, 1989, include examples of the precise mechanics of the exchange of information across the interface planes. Sleiman et al., 1996, contains a representative set of mixing-plane boundary conditions, circumferentially-averaged radial profiles of absolute total temperature, density, radial velocity and absolute tangential velocity specified at the inlet plane of the embedded row and the circumferentially "mixed out" static pressure at the exit.

Depending on the multistage calculation formulation the solution convergence criterion may include besides some specified equation residuals, the matching within a prescribed tolerance of mass flow and circumferential average profiles obtained from upstream and downstream blade rows. The average-plane model suffers from two basic problems. The first is a conceptual one and refers to the fundamentally unphysical assumption that the flow is steady relative to each individual blade row, and hence that flow properties have steady average values at the interfaces between the frames of reference, and the second, a practical one, is due to the closely coupled characteristics of the multistage environment requiring the placement of inlet/outlet boundaries very close to the blade row.

In such closely coupled compressors, these gridded domains offer little downstream extended region for resolving wakes, vorticity, etc., Rhie et al., 1995. Put in other terms, the issue with the assumption of steady flow conditions and circumferential averaging is that it affects the quality of the predictions while the question of the closeness of the boundary conditions to the blade's edges is that it affects the quality of the predictions and the stability of the numerical solution. This is the most serious of the two, Denton, 1990.

The common strategies employed to attack this last problem are, the extension of the grids and therefore the increase of the axial separation of the rows enabling the flow to naturally acquire a pitchwise near uniformity, and the overlapping of adjoining domains so that the boundary conditions are not placed too close to the blade passage.

The disadvantage of the overlapping scheme is that the averaging process takes place over nonunique mixing planes and the conservation of energy, momentum or mass may be poor if the flow exhibits local strong gradients, Arnone and Benvenuti, 1994.

On the other hand the separation of the rows results in a modification of the geometry representing a modification of the flowpath. A grid extension technique was used by Politis et al., 1997, for the computation of a stage of Cranfield's Low Speed Research Compressor.

When the overlapping procedure is utilized two interface planes are required to transmit information between rows. Authors who have used this approach include Yao et al., 1998, where a description of the exchange of information on the overlapped section of the grid can be found and Copenhaver et al., 1992, who in an investigation of a high-throughflow transonic stage used an overlapping grid which occupied the entire blade free region thus extending the computational domain of the rotor to the leading edge of the stator and vice-versa.

An added objection to the circumferential mixing at each spanwise station on either side of the mixing plane is that it leads to a more uniform flow than is realistic for the downstream blade row, Chen and Prueger, 1993, and that all loss implicit in the nonuniform pitchwise flow is mixed out explicitly into loss, Goyal and Dawes, 1992.

As in practice not all of the nonuniformity will actually become a loss, for example through wake recovery or because of convection or insufficiency of space for complete mixing-out to occur, the process introduces an artificial entropy rise and an attendant loss of total pressure and temperature. Moreover in the mixing plane approach the flow variables exhibit jumps across the interface planes due to the upstream wake distortion being removed for the downstream row's axisymmetric upstream boundary condition, Rhie et al., 1995.

Numerical experiments show that the change in entropy is small, even for highly non-uniform flow, Denton, 1985. This is questioned by Fritsch and Giles, 1993, who found that the mixing plane accounted for a surprising twenty percent of the total losses on the stage. The authors comment on this finding by noting that "so far the potentially large magnitude of this loss has found little detailed attention in the CFD community".

Dring and Spear, 1990, showed that mixing averages produce a better equivalent steady inlet condition than any other form of averaging. Dawes, 1991, qualified this assertion by adding that this is the case as long as the flow is not separated, when simpler averaging is required.

In some codes a number of different interface plane treatments are available. Dawes, 1990, presented as the three available options for his code, simple area averaging of the principal flow variables, selective area and mass averaging coupled with the straight transfer of flow angles across the boundaries and a variation of Giles, 1988, non reflecting boundary conditions.

The multiple blade row extension of Denton's code, Denton, 1990, incorporated as an option to the simple averaging of flow properties at the interface plane, a procedure that allowed the circumferential variation of the fluxes up to and on both sides of that plane while preserving the same average value over the whole set of elements. This formulation amounted in practice to the treatment of all the elements on each side of the mixing plane as a single large element over which the fluxes are conserved. This procedure not only contributes to the preservation of the identity of some flow features, e.g. wakes, up to the boundary but more importantly it dispenses with the requirement of uniform circumferential mixing thereby providing a welcome relaxation to the problem of the axial narrowness of the domains.

Comparisons between experimental and numerical single stage studies have been reported by Copenhaver et al., 1992, Chen and Prueger and Dring et al., 1993, Shikano, 1993, Lee et al., 1994, Dorney and Sharma, 1996, Blaha et al., 1997 and Chima, 1998. LeJambre et al., 1995, who employed this method to analyse an eleven stage high-pressure axial compressor, acknowledged the mixing plane technique to be satisfactory at the design point, having been successful in guiding designers in eliminating aerofoil separations when these separations were small but unreliable for determining the cause of a surge margin deficit detected in the machine. The method tended to overestimate the effect of transferring blockage to the downstream blade row, neglected the blockage-producing mechanisms of tip clearance and static cavities and did not match test data at high operating lines. Eventually their code was

modified to operate with an average-passage formulation with which the investigation of the off-design conditions was successfully conducted.

Rhie et al., 1995, showed that this approach tends to overemphasize the effects of upstream blade row separation on the downstream blade row. New averaging plane formulations continue to be proposed, Hall, 1997b, describes an algebraic method for adding some of the average-passage terms to a mixing plane method. Dawes and Denton, 1998, who are often jointly credited with the early development of this multistage technique, remarking on the general accuracy of the average-plane methods state that it cannot be expected that the predictions of boundary layer growth and secondary flows will be very accurate, given the neglect of unsteady interactions and the limitations of the turbulence models. However, the authors point out, the efficiency of many machines is predicted surprisingly well. The implication is that many loss sources in machines are not dependent on small details of the flow but rather on the mixing out of relatively large scale non-uniformities.

The use of a steady-state computational method for the initialization of an unsteady simulation is described in Eulitz and Engel, 1997, who also present a comparison between the two solutions. It was found that a large flow separation seen on the pressure side of the last stator did almost disappear in the time-accurate calculation. This it was felt was due to error accumulation stemming from the non-existing wake-passing effects. The opposite approach has also been reported and unsteady calculations have been used to fine-tune steady multirow pitch-averaging techniques, Arnone and Pacciani, 1995.

1.2.2.2 Average-passage method simulations

The average-passage equation system was formulated by Adamczyk, 1985, to describe the flow in a typical passage of a given blade row when embedded in a multistage environment. Adamczyk's method employs three sequential averaging operations on the Navier-Stokes equation set to filter out the random unsteady effects or turbulence, the deterministic unsteady effects due to stage interaction and the deterministic aperiodic effects that arise when there are in the machine more than two rows and these rows have different blade numbers.

Each filtering operation obtains a time average of some unsteady event with the effects of the filtered out events on the steady flow being accounted for through extra terms added to the steady equations. Numerically the first averaging operation is the ensemble averaging of the Navier-Stokes equation which leads to the classical Reynolds average format. For compressible flows a density-weighed ensemble average is employed. The second operation is the time averaging over a revolution of repeating events whose time scales are those of the shaft rotation or less. Mostly this averaging accounts for the blade passing effects.

The third and last operation is a multistage passage to passage averaging to account for the variation of the steady flow in the passage of a given row. The mathematical formulation of this averaging is derived from Fourier analysis. The last two average operators employ a so-called gate function to disable the algorithm in the portion of space occupied by the blade itself and where the average-passage equation is not instantaneously verified. As noted above each of the operations produces extra terms in the equations and these are from the ensemble average, terms for Reynolds stresses and scalar fluxes, from the time average, body forces, energy sources and energy mixing, and momentum terms and from the passage to passage average further body forces, energy sources and energy spatial mixing and momentum terms.

It is through these terms that the effects of the flow fields of neighbouring blade rows on the flow field of the row of interest are exerted. The resulting set of average-passage flow equations like the Reynolds-averaged Navier-Stokes equations contains more unknowns than equations therefore raising a closure problem. The terms requiring the closure modelling include body forces, energy sources and momentum and energy correlations. Adamczyk's original paper included an outline of a possible strategy for modelling the closure problem and this was pursued further in Adamczyk et al., 1986, with the development of such a closure model for the inviscid form of the average-passage equation system. This model consisted of a set of energy and velocity correlations involving products of variables and subject to the maintenance of consistency between the average-passage equation set and the axisymmetric flow equations and body forces and energy sources. These terms must be modelled from experimental insight or empiricism.

In Mulac et al., 1987, the method was further extended to cover multistage machines and further modifications to the solution algorithm were reported by Adamczyk, 1989, to cover the viscous form of the average-passage equations. In this form the method was employed by Mulac and Adamczyk, 1991, in the investigation of a four stage high speed compressor in order to ascertain the ability of the method in identifying stage mismatch.

Details of a typical solution algorithm of the average-passage equations are reported in Kirtley et al., 1992, who carried out the simulation of a mixed flow turbine in order to compare the performance of a built machine to the design intent. The solution involves two nested loops with the inner loop being occupied with the evaluation of the flow variables for a particular blade row subject to a distribution of body forces, energy sources and energy and velocity correlations that account for the presence of the neighbouring rows and which is repeated for every row and an outer loop that ensures that the axisymmetric averages of each blade row are identical within a set tolerance.

This is the compatibility condition that links the rows. If the axisymmetrical solutions have not converged the values of the body forces, energy sources and energy and velocity correlations are recalculated for each blade row and the inner loop reactivated. The individual blade row flow calculations within the inner loop are completely independent making them very amenable to parallel processing, Mulac et al. 1989.

Kirtley's paper includes a common criticism levelled at the method, namely that this approach is quite expensive computationally when compared with other steady methods. The computational requirements of the method are indeed extensive and were the subject of discussion in Mulac and Adamczyk, 1991. As these authors explain, the average passage code was specifically written for execution on the 8 processors CRAY Y-MP supercomputers. Unlike the steady-state simulations, which simultaneously compute all of the domains that make up the problem, in the average-passage model a separate calculation of that set of domains is required for the computation of each of the rows of interest. An illustration of the computational requirements of this method is given by the recent work of Turner et al., 1999, which

involved the study of 18 blade rows, each gridded with some 0.5 million nodes, required 15 hours of wall clock time while utilizing 121 parallel processors or 1820 CPU hours.

Another shortcoming of the average-passage method concerns the origin and characterization of the source terms included in the equation system. Strictly speaking an accurate computational estimation of these terms would require the evaluation of the unsteady stage interaction of the machine but this approach somewhat defeats the whole point of the technique which is to account for the unsteady stage effects from a steady state formulation.

Representative reports of the predictive performance of the average-passage approach include those of Miller and Podbody, 1990, who employed an Euler version to examine a contrarotating unducted fan to report good agreement with experimental data, despite the neglect of viscosity, Mulac et al., 1989, and Jennions and Adamczyk, 1995, who compared the average-passage and an unsteady simulation of a transonic turbine stage and found a fair agreement between the results of the two. The average-passage solution was then used as the starting solution for the time-dependent computation leading to the latter method achieving convergence "in an incredibly short time due to this use of the average-passage solution which produces such a remarkably good starting solution, that it could be mistaken for a snapshot of the time unsteady solution ". Lately Turner et al., 1999, reported on three multistage turbine simulations and Bardoux et al., 1999, examined a transonic single stage turbine.

An addition to the original formulation was made in Adamczyk, 1992, in a study of the impact of unsteady three-dimensional deterministic flows on blade row performance which concluded that a further term explicitly accounting for the three-dimensional vortices induced by the 3D deterministic flow field was required. This vortex force term was to be added to the radial momentum equation of the average-passage equation system for a downstream stator to insure the proper representation of the incoming vorticity field. Adamczyk's original rigorous approach to the formulation of the average-passage set of equations has enabled a number of authors to employ some of the equation set terms to partially account for the effects of unsteadiness in simpler model formulations.

One such approach is the Lumped Deterministic Stresses (LDS) formulation whereby source terms, which reproduce the effects of the unsteady phenomena, are inserted in the governing time-averaged flow equations. These source terms can be synthesized from either an exact non-linear unsteady computation or from an approximate linear unsteady simulation, that is a steady computation to which a perturbation field has been coupled. Both Busby et al., 1999, and Orkwis et al., 1999, used variations of this approach to study hot streak behaviour in multiblade row turbines.

Another variety of the alternative formulations is the version of Turner, 1986, where instead of the computation of a given blade row requiring, in addition to itself, the solution of all its neighbours, this is limited to just those lying immediately up and downstream. Yet a further reduction in the computational requirements is due to Rhie et al., 1998, who reduced further the primitive computational requirements by including only in the computation of the row of interest, the adjacent downstream row and a fraction of the upstream.

1.2.3 Time-accurate multiblade-row numerical studies

When the time steady numerical simulation of a single turbomachine row is undertaken it invariably involves the computation of a singular blade passage since this is deemed to be representative of all others. The sides of the domain that border on those of its neighbours are accordingly described by spatially periodic boundary conditions. The extension of this method to a multiblade row format is from this point of view quite straightforward given that each of the individual computational domains retains its natural frame of reference and, apart from the interface plane, all the attributes of an equivalent single row computation.

An entirely different situation however arises if we wish to study any stagewise combination of rows and account in the computation, for their aerodynamic interaction. In this class of simulations all rows inherently share the same frame of reference and therefore, if the requirement to solve the smallest pitchwise fraction of the machine possible is to be met, all the blade domains belonging to the simulation

domain must exhibit equal pitchwise periodicity. It is unfortunate therefore that a characteristic feature of axial flow compressor design, arising from well known aeroacoustic and aeroelastic considerations, is that the fitting in adjacent rows of equal or integer multiple numbers of blades is always avoided and as a consequence in real configurations, the pitch ratio in neighbouring blade rows for a small section of the annulus is never unity.

The lack of natural periodicity raises a considerable modelling challenge and throughout the years a number of alternative models have been developed to deal with this issue. It is indeed primarily accordingly to the methodology employed to tackle the unequal pitch modelling problem that unsteady CFD methods are usually categorized.

The natural starting point for a review of unsteady work is the phase-lagged periodic boundary conditions method proposed by Erdos et al., in 1977. Erdos' scheme arose from the consideration that for a given stage, the solution at any particular passage at one instant, can be related to that in another passage at an earlier time.

In this method consequently the requirement of exact spatial periodicity across the stages is dispensed with and instead, the periodic boundary conditions are enforced through the selection of the conditions that pertained to the desired location at an earlier time. It is known that the phase-shifted periodic boundary method of Erdos induces slow convergence rates and generates large storage requirements, Dawes, 1995, which somewhat limits its generality.

An alternative formulation is the scheme first proposed by Giles, 1988, where again only a single passage per blade row is required and where the common periodic boundary condition requirement is instead met through the use of a selective transformation of the time domain termed by its author time-inclination.

As for the limitations of Giles' scheme one can point out to the added post-processing complexity associated with the presence of different time-steps in the different simulation domains and the general increase in the number of terms in the Navier-Stokes equations with a corresponding increase in the computational cost of their

solution. An additional drawback is related to the fact that occasionally, multiple blade passages must be used to overcome the stability limitation of the time-inclination method, for the cases in which the difference in the blade counts of the stage is so large, that in the time-transformed space, the principle of casuality would be violated, Walraevens et al., 1998.

The 2D code UNSFLO reported in Giles, 1990 and employed in the evaluation of a transonic fan stage by Singh and Smith, 1998, employs the time tilting scheme. Other workers that have also employed Giles' formulation include Walraevens et al., 1998.

Although both methods presented above have the attraction of requiring a single passage per blade row, their other limitations led to the emergence of one third model as proposed by Rai, 1987, as that most used in time-accurate studies. In Rai's method the necessary rotor-stator ratios are achieved by scaling one the blade rows while keeping the pitch-to-chord ratio constant in order to keep the blockage effects unaltered.

Authors who have used Rai's approach with 3D Euler formulations include Gerolymos et al., and Liamis et al., both in 1995, both on one-and-a-half stages axial compressors. For 3D unsteady Navier-Stokes simulations a representative work is the single stage analysis of Dawes, 1995. In Dawes' work the loss production directly associated with the unsteady flow was seen to increase, when compared to that of the equivalent steady flow, about 12% in the stator and some 19% at the rotor. The magnitude of these observed losses was such as to prompt the author to call for a reassessment of the mixing-plane style averaging procedures to ensure that multistage not only adequately account for stage losses, but more importantly, are able to replicate the equivalent time-mean operating points.

A synthesis of the two formulations can be found in Yang and Lin, 1994, where the authors employed "O" grids wrapped round the aerofoils and "H" grids which accounted for most of the blade-to-blade as well as inlet and outlet regions. Their numerical procedure involved solving the unsteady forms of the thin layer Navier-Stokes equation in the "O" grid and of the Euler equation elsewhere.

Initially most unsteady work was limited by computational costs to the solution of the 2D Euler equation but the neglect of the viscous effects was seen to miss important features of the flow such as the decay of rotor wakes in stator passages as observed by Ho and Lakshminarayana, 1993.

Having dealt with the first issue that will concern anyone contemplating an unsteady simulation, namely what method to use to describe periodicity over the blade domains, we turn our attention to the ensuing question, that is, how to model their relative motion.

A number of techniques are employed of which the more representative by far is the sliding mesh surface. In a typical implementation of this method the grid or grids corresponding to the moving components will successively rotate through some azimuthal step corresponding to the prescribed time step, pausing while the flow variables are interpolated across the planar internal boundary which separates the adjacent grids. Unlike in the mixing plane methodology presented earlier, the sliding mesh interface plane other than interpolation to cater for different mesh spacings does not interfere with the values of flow variables and has consequently been described as a numerically transparent interface.

The requirement for the global stage grid to accommodate the relative displacement of two of its members can also be met in alternative ways one of which due to Giles, 1988, is the sheared cell technique. The sheared cell formulation was used by Eulitz et al., 1995 for the 2D computation of a transonic compressor.

1.3 Objectives of the present work

As part of the establishment of the Cranfield high speed facility a numerical study of the compressor datum blading was required using the recently acquired commercial code CFX-TASCflow available in the School of Engineering. The initial objective of the research project therefore called for the numerical flow characterization of the

HSRC in order to identify sources of inefficiencies as well as establish the accuracy of the code when employed in multistage simulation work.

Nevertheless given the known limitations subjacent to the basic steady-state approach, the provision of physical insight into the flow phenomena of the machine was seen as being dependent to a considerable extent on the limitations of the method. The inclusion of the cyclic unsteady effects, commonly neglected by conventional steady-state mixing plane approaches, through a deterministic stress source term model is an attempt at recovering some of these neglected multistage flow physics.

Two high speed compressor cases were studied, a single stage and a three and a half stage machine with the aim of accessing the impact of two semi-empirical deterministic stress models under similar but different conditions.

The contributions of the thesis are therefore:

- Development of a TASCflow compatible source code for coupling of the two deterministic stress models to the main code
- Application to the HP9 case of the two models and validation against experimental and numerical data
- Calibration of high-speed model functions from unsteady simulations of HP9
- Evaluation of models in HSRC and development of hybrid version

Although the work was restricted by the perennial problem of insufficient computational resources it is expected to have supplied the groundwork upon which a fuller exploitation of this study can be built upon.

The versions of the TASCflow CFD code employed in this study were 2.7, up to December 1998 and 2.8 onwards.

1.4 Organization of the thesis

This thesis consists of seven chapters with the following arrangement:

Chapter 1 contains an enunciation of the objectives of the research work and a literature survey of numerical and experimental studies covering multistage high-speed axial-flow compressor topics which are pertinent to the understanding of the flow physics of the cases employed in the project. Chapter 2 introduces the mathematical models which describe fluid flow as applied to the turbomachinery problems. Chapter 3 describes the numerical treatments which are employed to convert the equations introduced in the previous chapter to forms amenable to numerical solution. This chapter presents the CFD code employed in the study while seeking to place its salient features within the wider CFD context.

In Chapter 4 the rationale of the deterministic stress models is discussed and the formulation of the two models used for the study of the two test cases is described. Chapter 5 is concerned with the application of the models to test case one, the single stage HP9 high-speed stage compressor. This chapter includes experimental data which enables the validation of the models and a first limited appraisal of their effectiveness.

Chapter 6 covers the application of the deterministic stress models to the Cranfield HSRC where the models are applied to a more appropriate target and the an evaluation of their impact established and discussed. Chapter 7 wraps up the work with the articulation of the conclusions and presents a number of possible avenues for the practical exploitation of the work.

Chapter 2

Turbomachinery flow governing equations

2.1 Introduction

This chapter is concerned with the presentation of the equations on which the mathematical modelling of turbomachinery flows depend and which necessarily constitute the substratum of the corresponding CFD solution. The turbulent character of the flows found in axial flow compressors allied to the practical impossibility of numerically resolving any resident turbulent features down to their natural scale, imposes that a time-mean form of the governing equations be considered and a complementary turbulence model selected. The chapter therefore presents besides the fundamental governing equations a discussion on turbulence modelling issues as well as the casting of the equations in formats which are amenable to their numerical solution.

The type of equations most commonly used to describe physical processes, are partial differential equations. In fluid dynamics as indeed in many other branches of engineering science, the majority of problems involve more than one independent variable and are for that reason governed by this type of equations. For most of the relevant practical situations, the partial differential equations have no analytical solutions or if they do, they are very difficult to find so that numerical methods are the usual means employed in obtaining a solution.

The three varieties in which partial differential equations occur are the elliptic, parabolic and hyperbolic forms, a nomenclature chosen by the analogy between the outcomes the discriminant, $b^2 - 4ac$, takes when employing the "characteristic lines" method of equation classification and when associated with the definition of a conic section.

Elliptical partial differential equations are used to describe steady-state physical processes such as potential fields in electricity or subsonic steady and inviscid flows in fluid dynamics. The common characteristic in these processes is that a full mathematical description in the interior of a given domain may be obtained from the knowledge of the values present at its boundaries. These are equilibrium problems soluble through iterative techniques involving each and every point of the domain.

Parabolic partial differential equations are associated with the description of diffusion or fluid flow problems characteristically with one of the derivatives involving time while the others relate to positional variables. Flows where these conditions are present include in boundary and shear layers, jets and wakes, channel and pipes flows and smoke columns. The computation of parabolic equations will involve the stepwise solution, commonly expressed as "marching", downstream the domain from an initial known set of values

The last type of partial differential equations is used to describe hyperbolic flows two examples of which are unsteady inviscid compressible flows or steady inviscid supersonic flows. These flows share with parabolic flows the trait of only allowing flow information to be conveyed downstream of the point of interest. The solution methods for the equations with hyperbolic characteristics are somewhat more involved and their discussion is postponed until the following chapter.

For the purpose of mathematical classification the Navier-Stokes equations, in their unsteady form, are a system of second order non-linear partial differential equations the character of which is a mixture of hyperbolic and parabolic terms. Although the steady state form of the equations is yet to be presented, once in that formulation the Navier-Stokes equations will take then an elliptic-hyperbolic character. If some of the

terms of the equation were to be dropped, the compressible related terms for example, the character of the equations would then change as well, in this case to a parabolic-elliptic-hyperbolic format. The significance of the particular character of the governing equations will become apparent when in the following chapter we deal with the numerical solution methods the different the types of equations elicit.

2.2 The Navier-Stokes system

The set of partial differential equations which is employed to describe the bulk of fluid flows, and is named in honour of the independent but parallel works of Claude Navier and George Stokes might as well have been called the Newton system of equations since both the motion law upon which it is centrally based as well as the stress/deformation relationship it implies are both due to Newton's ideas.

2.2.1 Instantaneous form of the Navier-Stokes equations

The complete set of Navier-Stokes equations is composed of five conservation equations, a momentum equation in each of the three Cartesian directions, a mass continuity equation and an energy equation. The derivation of the five equations is commonly done by reference to a finite stationary portion of space, the Eulerian notion, over which an evaluation of the laws of mass continuity, momentum conservation as stated in Newton's second law and conservation of energy or the first law of thermodynamics is performed.

For the presentation of the Navier-Stokes equation system we will make use, in the interest of a compact formulation, of the vector differential operator ∇ and of tensor notation, writing the conservation equations in an unsteady forms as:

continuity: $$\frac{\partial \rho}{\partial t} + \nabla \cdot (\rho \vec{V}) = 0 \qquad (2\text{-}1)$$

momentum: $$\frac{\partial (\rho \vec{V})}{\partial t} + \nabla \cdot (\rho \vec{V} \otimes \vec{V}) = -\nabla p + \nabla \tau_{ij} + \rho f \qquad (2\text{-}2)$$

energy: $$\frac{\partial \mathrm{E}}{\partial t}+\nabla\cdot(\mathrm{E}\vec{\mathrm{V}})=\frac{\partial Q}{\partial t}-\nabla\cdot\vec{q}+\nabla\cdot(\tau_{ij}\,\vec{\mathrm{V}})+\rho\,\vec{f}\cdot\vec{\mathrm{V}} \qquad (2\text{-}3)$$

In these equations ρ is the density, $\vec{\mathrm{V}}$ is the fluid velocity vector, τ denotes the separate or overall component of the viscous stress tensor as appropriate, E stands for the total energy per unit volume, Q is the heat addition due to external factors and $\vec{q}$ represents the conductive heat transfer vector. The *f* character represents, in the case of the momentum equations, possible source terms associated with external or body forces acting at a distance, e.g. gravitational, electromagnetic, Coriolis, etc, and for the energy equation, the rate at which work is done when those body forces act on the fluid. In a relative frame of reference rotating with a steady angular speed $\vec{\Omega}$, the absolute and relative velocities, $\vec{\mathrm{V}}$ and $\vec{\mathrm{W}}$, are related through $\vec{\mathrm{V}}=\vec{\mathrm{W}}+\vec{\Omega}\times\vec{r}$.

The viscous stress tensor can be expressed in terms of basic flow variables employing again the tensor notation where $i, j, k = \mathrm{x,y,z}$ as:

$$\tau_{ij}=\mu\left[\left(\frac{\partial u_i}{\partial x_j}+\frac{\partial u_j}{\partial x_i}\right)-\frac{2}{3}\delta_{ij}\frac{\partial u_k}{\partial x_k}\right] \qquad (2\text{-}4)$$

In this equation μ is the dynamic viscosity and δ_{ij} the Kronecker delta function which takes a value of 1 when the subscripts *i* and *j* are equal and 0 otherwise.

In the energy equation the heat transfer vector $\vec{q}$ can also be related to the flow variables through Fourier's law, $\vec{\mathrm{q}}=-\mathrm{k}\nabla\mathrm{T}$, with k representing the coefficient of thermal conductivity and T the temperature. If a solution of these equations is sought in this format a number relationships between thermodynamic and flow variables need to be established to attain closure of the equations and this can be done by invoking the equation of state for perfect gases, p = ρRT, and the Sutherland's viscosity and thermal conductivity formulas, $\mu=\mathrm{C}_1\frac{\mathrm{T}^{\frac{3}{2}}}{\mathrm{T}+\mathrm{C}_2}$ and $\mathrm{k}=\mathrm{C}_3\frac{\mathrm{T}^{\frac{3}{2}}}{\mathrm{T}+\mathrm{C}_4}$. In these formulas R is the universal gas constant, T the temperature and the various 'C's, constants which were empirically derived for various gases.

The form of the Navier-Stokes equations presented above is applicable for a given domain to any scale of space or time. The solution of the instantaneous equations as presented above is the territory of Direct Numerical Simulation (DNS) but this technique has so far only been applied to simplified configurations and low Reynolds number flows due to the prohibitive computational requirements associated with the extremely fine grids, the number of nodes for a 3D simulation is proportional to $Re^{2.25}$, Lacor, 1999, and the very small unsteady solution time-steps.

For most practical flows therefore one must somehow account for the presence of turbulence whose characteristic temporal and spatial scales present a large disparity with respect to those of the main flow. This difficulty is tackled by recourse to a model that will account for the mean effects of turbulence in the flow, in a manner which is compatible with the dominant scale of the problem, thereby dispensing with the requirement of explicitly computing the aerodynamics of the chaotic turbulent structures.

2.2.2 Reynolds-averaged form of the Navier-Stokes equations

The appropriate methods to obtain the average forms of terms containing temporal and spatial derivatives are statistical methods. For a generic function $\phi\,(x,t)$ the form of the statistical average is defined as,

$$\phi(x,t) = \lim_{n\to\infty} \frac{1}{n} \sum_{i=1}^{n} \phi_i(x,t) \qquad (2\text{-}5)$$

where $\phi_i\,(x,t)$ is the value taken by $\phi\,(x,t)$ at the *i th* sampling of the turbulent flow. If the sampling occurs over a dilated period, denoted by T, by comparison with the largest temporal scales of turbulence, one can define a time-averaged form of the generic function, ϕ_T which will tend towards a statistical average of ϕ for a sufficiently large value of T,

$$\overline{\phi}(x,t) = \frac{1}{T} \int_0^T \phi(x,t)\,dt \qquad (2\text{-}6)$$

Having acquired a time-average form of ϕ it is possible to consider that function as being made up of a steady mean and a time-dependent fluctuating component which can be written as, $\phi = \tilde{\phi} + \phi'$. For compressible flows the preferred average form is a mass-weighted Favre average which is assembled as,

$$\tilde{\phi} = \frac{\overline{\rho \phi}}{\overline{\rho}} . \tag{2-7}$$

It is convenient at this point to recall the permutation rules of partial derivatives, $\frac{\partial \overline{\phi(x,t)}}{\partial t} = \overline{\frac{\partial \phi(x,t)}{\partial t}}$ and $\frac{\partial \overline{\phi(x,t)}}{\partial x} = \overline{\frac{\partial \phi(x,t)}{\partial x}}$ which when combined with the decomposed format of ϕ yields the following relationships for some anticipated correlations of ϕ :

$$\begin{aligned}
&\overline{\rho \phi'} = 0 \\
&\overline{\rho \phi_1 \phi_2} = \overline{\rho} \tilde{\phi}_1 \tilde{\phi}_2 + \overline{\rho \phi_1' \phi_2'} \\
&\overline{\rho \phi_1 \phi_2^2} = \overline{\rho} \tilde{\phi}_1 \tilde{\phi}_2^{\,2} + 2\,\overline{\rho \phi_1' \phi_2' \tilde{\phi}_2} + \overline{\rho \phi_2'^2 \tilde{\phi}_1} + \overline{\rho \phi_1' \phi_2'}
\end{aligned} \tag{2-8}$$

The average form of the Navier-Stokes equations can now be recast after some algebra and by taking note of the cancellation of terms which is due both to the decomposition of the instantaneous variables and the removal of terms known to be zero, Tannehill et al, 1997, as:

continuity: $$\frac{\partial \overline{\rho}}{\partial t} + \nabla \cdot (\overline{\rho} \tilde{\vec{V}}) = 0 \tag{2-9}$$

momentum: $$\frac{\partial (\overline{\rho}\, \tilde{\vec{V}})}{\partial t} + \nabla \cdot (\overline{\rho}\, \tilde{\vec{V}} \tilde{\vec{V}}) = -\nabla \overline{p} + \nabla \cdot (\overline{\tau_{ij}} - \overline{\rho \vec{V}' \vec{V}'}) \tag{2-10}$$

energy:

$$\frac{\partial (\overline{\rho} \tilde{H})}{\partial t} + \nabla \cdot (\overline{\rho} \tilde{\vec{V}} \tilde{H} + \overline{\rho \vec{V}' H'} - k \nabla \overline{T}) = \frac{\partial \overline{p}}{\partial t} + \nabla \cdot (\tilde{\vec{V}} \overline{\tau_{ij}} + \overline{\vec{V}' \tau_{ij}}) \tag{2-11}$$

In the energy equation the total energy E, which has been assumed for convenience to comprise only internal and kinetic energy, was replaced by $\rho H - p$.

The terms of the form $\overline{\rho \vec{V}' \vec{V}'}$ and $\overline{\rho \vec{V}' H'}$ that emerged from the time averaging process, describe the transport of momentum and enthalpy due to turbulent action and as such are somewhat analogous to the stress and thermodynamic energetic effects due to the mean motion of the flow. Though these terms are related to the fundamental Navier-Stokes equations variables, their format means that in practice they behave as new variables in the equations thereby raising the number of unknowns and causing a closure problem.

The evaluation of these significant expressions, both in terms of physical meaning and numeric magnitude, in fully developed turbulence the Reynolds stress tensor can easily be as much as 500 times larger than the mean stress tensor, Mathieu and Scott, 2000, is normally achieved through the solution of the additional equations of a turbulence model.

2.3 Turbulence modelling

The need for a mathematical model to describe the Reynolds stress terms and the turbulent heat fluxes has been demonstrated above. In this section we examine some of the alternative approaches which are available to achieve this objective and undertake a nominal appraisal of their relative merits and reported performance.

The averaging process described earlier removes some of the physics which was contained in the original equations especially for mechanisms such as the dissipation of turbulence into heat that is dominated by the smallest scales prevalent in the turbulence. Some of these physics must be recovered through turbulence modelling which relies a great deal on experimental data and thus numerical turbulence

modelling is represented as an interdisciplinary activity involving both numerical analysis and examination and interpretation of experimental data, Rubesin, 1977.

A synthetic first glimpse of the classification of turbulence models can be obtained with reference to the diagram underneath, where it can be seen that the fundamental division is between those models which are based on Boussinesq's assumption and those which aren't.

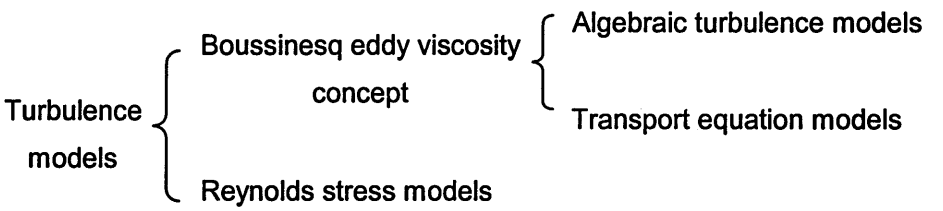

This said, most of the turbulence models employed in engineering CFD work do belong to the first of these categories. In Boussinesq's hypothesis a linear relationship is assumed between the Reynolds turbulent shear stresses represented by the $\rho \overline{u_i' u_j'}$ terms and the mean strain tensor represented by the gradient of the mean flow velocity, the simplified mathematical expression of which is given by,

$$\rho \overline{u_i' u_j'} = \mu_t \frac{\partial \overline{u}}{\partial y} . \qquad (2\text{-}12)$$

In equation 2-12 these two quantities are related through an apparent turbulent viscosity, μ_t, also known as eddy viscosity or eddy diffusivity. When translated in terms of a physical argument, Boussinesq's hypothesis states that the presence of turbulence in a flow can be expressed as an increased viscosity. By analogy with the viscosity attributable to the stress gradients present in the laminar flows and which are represented by the mean flow element of the decomposed unsteady variables, one can make use of similar expressions to correlate the Reynolds stresses to the mean flow variables,

$$-\rho \overline{u_i' u_j'} = \mu_t \left(\frac{\partial u_i}{\partial x_j} + \frac{\partial u_j}{\partial x_i} \right) - \frac{2}{3} \left(\rho k + \frac{\partial u_i}{\partial x_i} \right) \delta_{ij} \qquad (2\text{-}13)$$

and for the heat flux ,

$$-\rho\overline{u_i'\theta} = \alpha_t \left[\frac{\partial T}{\partial x_i}\right] \qquad (2\text{-}14)$$

The central objective of a turbulence model then is to calculate the unknowns of these expressions, the turbulent viscosity μ_t and turbulent kinetic energy, k_t .

2.3.1 Algebraic turbulence models

Many Navier-Stokes simulations of turbomachinery flows have been carried out with algebraic turbulence models the most used of which is the Baldwin-Lomax model. In this class of models only the turbulent viscosity is expressly calculated while the turbulent kinetic energy is assumed to be zero. For the computation of the eddy viscosity these model rely on boundary layer physical properties and have been applied with reasonable success to problems where the turbulence remains in equilibrium with the mean motion or in other words where the turbulent production and dissipation are evenly matched.

The earliest proponent of an algebraic model was Prandtl who in 1925 from dimensional analysis considerations proposed that the turbulent kinematic viscosity, μ_t , could be expressed in terms of some turbulence broad features such as turbulence intensity or velocity scales together with eddy characteristics namely length scale or time scale. Making use of these correlations Prandtl put forward the relationship,

$$\mu_t \cong \text{velocity scale} * \text{length scale} \ .$$

In Prandtl's model the velocity scale was given by, $l_1\left|\frac{\partial \bar{u}}{\partial y}\right|$, where l_1 is a first characteristic length while the length scale is represented by l_2 which is a second characteristic length enabling the writing of the eddy diffusivity as, $\mu_t = \overline{l_1 l_2}\left|\frac{\partial \bar{u}}{\partial y}\right|$ and

by rewriting the term $\overline{l_1 l_2}$ as l_m^2, where l_m is termed the mixing length, the eddy viscosity is finally cast as $\mu_t = l_m^2 \left| \frac{\partial \bar{u}}{\partial y} \right|$.

From experimental work it was concluded that in the near-wall regions the relationship $l_m = \kappa\, y$ applies, κ being the von Kármán constant, $\kappa = 0.41$, and y the distance to the wall. However as one approaches the wall and $\partial l_m / \partial y$ tends to zero, this mixing length relationship is known to cease to be valid and the mixing length experiences a damping action which is attributable to the viscosity of the fluid. A number of modified correlations exist to account for this situation for example van Driest's, $l_m = \kappa\, y \left\{ 1 - \exp\left[-\frac{y\sqrt{(\tau_w / \rho)}}{\nu A^+} \right] \right\}$, where A^+ is an empirically derived damping factor, which can be used in the immediate vicinity of the wall. Conversely in the external regions of the boundary layer an alternative formulation is also required one such being that due to Escudier and Spalding, 1966, which is, $l_m = 0.09\, \delta$, and where δ is boundary layer thickness.

Perhaps the best known of the algebraic models is the Baldwin-Lomax, Baldwin and Lomax, 1978, a two-layer model which employs a Prandtl mixing length model to compute the turbulent viscosity of the near-wall region and a correlation of the mean flow and a length scale for evaluating turbulent viscosity elsewhere.

In the inner region the length scale l is calculated from $l = \kappa\, y$, as seen previously and the viscosity of the near-wall regions is given by,

$$\mu_{t_{inner}} = \rho\, l^2 D^2 |\omega| \qquad (2\text{-}15)$$

where ω is the local vorticity or angular velocity due to the turbulent eddies and D is the van Driest's damping length function given by:

$$D(y) = 1 - e^{\frac{-y^+}{A^+}} \qquad (2\text{-}16)$$

In equation 2.16, y^+ is a law-of-the-wall non-dimensional coordinate and A^+ a damping factor, respectively. The y^+ parameter is calculated from

$$y^+ = \left(\frac{\sqrt{\rho_w \tau_w}}{\mu_w} \right) n, \tag{2-17}$$

the subscripted *w*'s indicating that the terms are evaluated at the wall while *n* denotes the normal distance to the wall. The value of A^+ is usually set as 26.0 irrespective of the fact that this value is strictly appropriate only for simple flat plate cases and that A^+ is known to be sensitive to both pressure gradients and surface mass transfer.

In the outer regions, the turbulent viscosity is given by,

$$\mu_{t_{outer}} = C_1 \, C_{cp} \, \bar{\rho} \, F_{wake} \, F_K(y) \tag{2-18}$$

where $C_1 = 0.0168$ and $C_{cp} = 1.6$ are two empirically derived constants the term F_{wake}, being defined as,

$$F_{wake} = y_{max} \, min \left[F_{max}, \frac{C_{wake} V_m^2}{F_{max}} \right] \tag{2-19}$$

where $C_{wake} = 0.25$ is a further empirical constant, V_m is the difference between the maximum and minimum velocities in a shear layer and y_{max} is the y value at which the maximum of the function $F(y) = y \, D(y) \omega$, denoted by of F_{max}, is reached.

Lastly the Klebanoff intermittency factor F_k accounts for the fact that, what is often designated by the blank label of turbulent flow, contains in effect periods of time during which the flow is genuinely turbulent interspersed by others when the flow acquires laminar features,

$$F_k = \frac{1}{1 + 5.5 \left[\frac{C_k \, y}{y_{max}} \right]^6} \tag{2-20}$$

with yet another empirical constant, $C_k = 0.3$.

The acknowledged central limitation of algebraic models is that these models are by nature boundary layer models, even when employed as part of full Navier-Stokes codes, and not really appropriate for application to free-shear flows where the length scales are problem dependent. Furthermore these models are also known to not take

into account the transport features of the turbulent quantities. In algebraic models the whole boundary layer region is treated as a single tightly coupled module, leading to errors where detachment occurs or multiple shear layers are present.

2.3.2 Transport equation models

Transport equation models make use of turbulence properties rather than mean flow properties and thus rely on the solution of a set of equations that describe the turbulent variables pertaining to the overall flow field. The equations which are employed are partial differential equations, analogous to the Navier-Stokes momentum equations, and therefore since these too describe equivalent diffusive and convective processes they are also termed transport equations.

A simplified description of the modelling approach involving transport equations is performed underneath by means of the familiar quantities, k , the turbulent kinetic energy and ε, the turbulent viscous dissipation rate. If an estimate of the length scale l is obtainable from an experimental or other source, only the equation to compute k is employed.

Once k is known the turbulent viscosity can then be obtained from,

$$\nu_t = C_\mu \sqrt{k}\, l \tag{2-21}$$

and since this method requires only one transport equation for k, it is known as a one-equation turbulence model.

If no estimate of the local length l is available a second partial differential equation for the dissipation rate ε can also be solved and the turbulent viscosity will then be given by,

$$\nu_t = C_\mu \frac{k^2}{\varepsilon} \tag{2-22}$$

hence characterizing the approach as a two-equation turbulence model. If a single length scale is assumed to be representative of the both energy containing and energy dissipating eddies this will then be known from,

$$l = \frac{k^{\frac{3}{2}}}{\varepsilon} \tag{2-23}$$

2.3.2.1 One equation models

The common criticism offered on one-equation models are that they are somehow incomplete, given the requirement that a length scale relating to the particular situation be considered, and that they are also non-local since they make use of length scales which are linked to the boundary layer thickness. Although for many years one-equation models have been seen as the poor relations of the transport equations model family, there has been a reawakening in research interest in this class of models, partly as an alternative to the cruder algebraic models and partly because even the more sophisticated, but also more costly to implement, two-equation models are known to exhibit marked flaws.

One such alternative formulation of one-equation models is the Baldwin and Barth variant, Baldwin and Barth, 1991, which removed the need for an algebraic length scale, and the Spalart-Allmaras, 1992, model which elaborates the concept further. Given the growth in popularity of this particular model over the latter years a description of its general features is undertaken next.

In the Spalart-Allmaras model a single partial differential equation is used to solve directly for ν_t, the turbulent viscosity rather than, as is the conventional approach in one-equation models, computing initially the turbulent kinetic energy, k. As there is no exact transport equation for ν_t the authors adopted an empirical approach and assembled what they call a plausible transport equation for ν_t by collecting terms relating to the physics of turbulent phenomena. Spalart and Allmaras' original paper contains a full stepwise description of the model assembly with the rationale, implementation and validation of the each additional term being discussed and documented.

On the performance side despite the fact that it was been found that the Spalart-Allmaras model sometimes produces premature transitions and has glaring deficiencies in round jets and wakes, Spalart, 2000, a number of authors have reported

added accuracy when compared with established models. Shima and Egami, 1994, found in simulations of a wing with deployed slats and flaps an improved agreement between the Spalart-Allmaras runs and experimental data than when using Baldwin-Lomax and two versions of the q-ω model. Although more readily associated with external flows the model has also been applied to turbomachinery applications, Ning and Xu, 2001, in the form of the two well known NASA cases, Rotor 37 and Rotor 67. In this instance the authors found that the model produced generally good results in spite of the underprediction of the turbulence mixing.

2.3.2.2 Two Equation models

Two-equation turbulence models solve two transport equations the first being usually for turbulent kinetic energy while the second will be for a variable related to the time or length scales of turbulence. Even though the k and ε properties are frequently employed to illustrate the general modelling philosophy behind the two-equation turbulence approach, a number of other turbulence property combinations have also been successfully applied to turbomachinery computations. These include the k-ω, Wilcox, 1984, k-ω^2, Wilcox and Rubesin, 1980 and q-ω, Coakley, 1983, to say nothing of the plethora of variants of the original k-ε model, Jones-Launder, Chien, Lam-Bremhorst, Speziale, So, Chen and Patel, Rodi and Huang-Coakley, to mention but a few.

The k-ε model, Launder and Spalding, 1972, has become the industry standard two-equation turbulence model, a status which is due to the successful compromise between computational cost and performance, the capability of predicting a wide range of flows with minimal adjustment of the coefficients and the fact that the model does not expressly requires a near-wall correction term.

As its name indicates the k-ε model employs two transport equations to compute k the turbulent kinetic energy defined as, $k = \frac{1}{2}\overline{u_i' u_i'}$, and ε the turbulent energy viscous dissipation rate, $\varepsilon = \frac{\mu}{\rho}\overline{\frac{\partial u_i'}{\partial x_j}\frac{\partial u_i'}{\partial x_j}}$.

In this model the kinematic turbulent viscosity ν_t is given by $\nu_t = C_\mu \frac{k^2}{\varepsilon}$. Making use of the substantive derivative $\frac{D}{Dt}$ notation, the partial differential equations for turbulent kinetic energy production and turbulence dissipation rate can be written as:

$$\frac{Dk}{Dt} = \nabla \cdot \left[\nu + \frac{\nu_t}{\sigma_k} \right] \nabla k + P_k - \varepsilon \tag{2-24}$$

and

$$\frac{D\varepsilon}{Dt} = \nabla \cdot \left[\nu + \frac{\nu_t}{\sigma_\varepsilon} \right] \nabla \varepsilon + C_{\varepsilon_1} \frac{\varepsilon}{k} P_k - C_{\varepsilon_2} \frac{\varepsilon^2}{k} \tag{2-25}$$

The empirically derived constants C_μ, C_{ε_1}, C_{ε_2}, σ_k and σ_ε generally take the values of 0.09, 1.44, 1.92, 1.0 and 1.3 respectively. The constants were adjusted to match the effects of three well documented cases, turbulence behind a grid, over a flat plate and shear flow turbulence, on the decay of homogeneous turbulence.

From the computed values of k and ε the turbulence length scale is simply calculated from,

$$l = C_\mu^{\frac{3}{4}} \frac{k^{\frac{3}{2}}}{\varepsilon} \tag{2-26}$$

Although the k-ε model has been applied with success in a large number of flow conditions, some of its limitations are also well known:

- failure to account for rotational strain or shear
- under adverse pressure gradients the model significantly overpredicts the shear stress levels and delays, or even completely prevents, separation
- simplistic modelling of the creation and destruction of turbulent energy

- eddy-viscosity approach entailing eddy isotropy with the same values being taken for the different Reynolds stresses
- excessively dissipative nature of the model with overprediction of the turbulent viscosity in recirculating flows leading to undue damping out of vortices
- underprediction of flow separation past steps and obstacles
- standard model applicable only for high turbulent Reynolds numbers
- inability to account for the amplification or relaxation of the components of the Reynolds stress tensor

The appreciation of the weakness intrinsic to the primitive k-ε formulation helps to explain the appearance of such a high number of variations of the original Launder and Spalding version which seeks to improve the physical base of the model and hence its predictive capabilities. Two of these variants were available in TASCflow the commercial code employed in the present study, a renormalization group, RNG, based approach and the Kato-Launder formulation.

The RNG k-ε model which is due to Yakhot and Orszag, 1986, employs the renormalization group theory to systematically eliminate the small scales of turbulence up to a resolvable scale and includes the effects of the removed scales through an effective or renormalized viscosity, Kirtley, 1991. In practice the RNG theory enables the removal of the experimentally adjustable parameters from the model, the coefficients for the various terms in the equations being obtained from the RNG theory.

One of the coefficients in the dissipation equation is expressed as a function of the ratio between the time scales of the turbulence parameters and the mean flow thus making it possible to have a spatially as well as a temporally varying balance between the production and destruction terms of the k-ε equation. This dynamic balance feature which is based on group theory and is unique to the k-ε RNG model, Choi et al, 1994, is responsible for the general reduction in the predicted eddy viscosity of the model by comparison with the baseline k-ε. The RNG model is allegedly quite capable in the calculation of separation and reattachment situations but its

performance in other conditions, jets and plumes for example, is judged inferior to that of the standard k-ε model.

The k-ε model, as all other two-equation turbulence models, overestimates the turbulent kinetic energy in stagnation points, with this overproduction of k being caused by the presence of normal stresses in the production expression, Michelassi et al, 1998. To avoid this Kato and Lauder, 1993, introduced a modification to the standard k-ε model as a reformulation of the turbulence production rate, Niestroj and Came, 1998, as the product of rotational and irrotational contributions and its practical benefits include the prediction of boundary layer separation in adverse pressure gradients, Biesinger et al., 1998.

The experience of the writer with either version of the k-ε model when applied to the computation of an established transonic single rotor test case, NASA's Rotor 37, by comparison with the base version is nevertheless somewhat unconvincing with the results obtained with both formulations exhibiting hardly any impact on the overall computed flow fields.

Another well established two-equation formulation is the k-ω model which in addition to solving an equation for the turbulent kinetic energy k, employs the second transport equation to evaluate ω, the specific turbulent dissipation rate or turbulent frequency. Unlike the k-ε model, which is very inaccurate for boundary layers subject to adverse pressure gradients, even when the gradients are mild, the k-ω model suffers no deterioration in accuracy as the pressure gradient increases all the way up to incipient separation, Wilcox, 1993, but in free-shear flows the k-ω model is much less satisfactory.

A further attraction of the k-ω formulation when used in the near-wall viscous sub-layer is that unlike the low Reynolds numbers k-ε models, all of which employ damping functions in some form or another, Menter, 1993, the k-ω model does not make use of damping functions and utilizes instead plain Dirichlet boundary conditions leading to a significant benefit in terms of numerical stability.

2.3.3 Near-wall approaches

Although turbomachinery CFD grids are invariably clustered around annulus and blade walls in order to resolve to some extent the local gradients, the option exists of either extending the clustering process right up to the walls or effectively removing the near-wall boundary layers from the active domain and thus removing the need to solve locally the Navier-Stokes and turbulence model equations.

If the first approach is taken, a highly refined grid in the regions immediately adjacent to these surfaces is required due to the very high gradients found locally, particularly in the viscous sub-layer, together with an appropriate turbulence model capable of handling the enhanced near-wall damping effects. If the second choice is favoured, the approach employed to remove the fine grid constraint is to make use of semi-empirical formulae which supply, in that region, boundary conditions both for the mean flow and turbulence transport equations. An extensive source of information on dedicated turbulence models designed for low-Reynolds number near-wall flows is found in Patel et al, 1984.

2.3.3.1 Low Reynolds numbers methods

If law of the wall models are not employed in the solid boundary regions, the turbulence model utilized in the throughflow areas can be coupled with a low Reynolds number variant, either one or two equations or an algebraic model.

Low Reynolds number k-ε models are generally based on quasi-homogeneous approximations and require empirical damping functions in order to prevent the model failure near the walls where turbulence is strongly non-homogeneous and turbulence mixing is suppressed due to wall blocking. These damping functions, often involving exponential functions, are rather arbitrary having been derived to be consistent with experimental or numerical data for constant pressure boundary layers, and are consequently often blamed for the inaccurate solutions of complex problems, Kwon and Ames, 1995.

The conversion of a standard k-ε model into a Low Reynolds formulation entails the multiplication of the C_μ, C_{ε_1} and C_{ε_2} coefficients of the original k-ε model by functions, f_μ, f_{ε_1} and f_{ε_2}.

These functions are computed for example in the Low Reynolds k-ε version due to Lam and Bremhorst, 1981, as:

$$f_\mu = [1 - exp(-0.0165\, Re_y)]^2 \left[1 + \frac{20.5}{Re_t}\right]$$

$$f_{\varepsilon_1} = 1 + \left(\frac{0.05}{f_\mu}\right)^3$$

$$f_{\varepsilon_2} = 1 - exp(-Re_t^2) \qquad (2\text{-}27)$$

where Re_y and Re_t are two local Reynolds numbers calculated as, $Re_y = \frac{k^2}{\nu\,\varepsilon}$ and $Re_t = \sqrt{k}\,\frac{y}{\nu}$.

There are known difficulties in the implementation of these model namely the stiff nature of the constituent equations of low-Re versions and some complexity in the boundary conditions for ε as this requires the knowledge of the second derivative of k in a direction normal to the wall, $\left(\partial^2 k / \partial^2 y\right)$.

Lastly an alternative approach, when two-equation models are used, is to employ a two-layer variant of the code whereby a division of the computational domain into high and low Reynolds numbers takes place and two dedicated forms of the transport equations are applied in turn to the separate sectors.

2.3.3.2 Wall Function methods

Turbulent boundary layers are known to present common characteristics in terms of the representation of the near-wall velocities.

If we define the variables y^* and u^* as,

$$y^* = \frac{\nu}{u^*} \tag{2-28}$$

and

$$u^* = \sqrt{\nu \frac{\partial \bar{u}}{\partial y}}\Big|_{y=0} \tag{2-29}$$

we can further designate,

$$y^+ = \frac{y}{y^*} \quad \text{and} \quad u^+ = \frac{\bar{u}}{u^*}$$

where $\bar{u}$ is the time averaged velocity parallel to the wall.

It is known from experimental work that immediately near the wall, in the region known as the viscous sub-layer whose limits are, 0 y^+ 20 , the mean flow is almost linear in y^+ ,

$$u^+ = y^+.$$

For a y^+ value of between 20 and 100 the experiments show that the u^+-y^+ relationship is instead given by

$$u^+ = \frac{1}{\kappa} \log y^+ + 5.5$$

where κ is the von Kármán constant and this region is known by reference to this correlation as the logarithmic layer.

These empirical formulae are used to establish a law of the wall which will act as near-wall boundary conditions to the mean flow Navier-Stokes equations and turbulence transport equations.

It is through these formulae that the wall values of the relevant quantities, i.e. wall shear stress, are related to the corresponding quantities at the near-wall node which is deemed to be positioned within the fully turbulent fluid. The serious limitation of this approach arises though when separation and recirculation occur, entailing with them a change of sign in $\frac{\partial \bar{u}}{\partial y}$ and occasioning the failure of the method.

2.3.4 Reynolds stress models

In these models a new differential transport equation is introduced for each Reynolds tensor component but while more complex than two equation models by an order of magnitude it is not clear that they perform an order of magnitude better, Mohammadi and Pironneau, 1994, besides which closure models are still required and the physical and mathematical significance of these new terms is often uncertain. Further the implementation of these models is perceived as difficult as well as being prone to be numerically unstable. Nevertheless the main attraction of the Reynolds stress models is that they can automatically capture the anisotropic features of the flow given that they depend on the solution of the individual stresses transport equations rather than on simplifying modelling as done in the eddy viscosity approaches.

The generic form of the Reynolds stress transport equations can be cast as,

$$\partial_t R_{ij} + U_k \frac{\partial R_{ij}}{\partial x_k} - \frac{\partial R_{ijl}}{\partial x_l} = -P_{ij} + \phi_{ij} + \phi_{ji} + \varepsilon_{ij} \qquad (2\text{-}30)$$

with R_{ij} representing the components of the Reynolds stress tensor, $R_{ij} = -\overline{u_i' u_j'}$, with the terms of the equation representing convection, diffusion, production, pressure redistribution and viscous dissipation effects. Most of the terms of the equation require closure models including the turbulent dissipation rate, ε, which is computed from the solution of a dedicated transport equation.

Reynolds stress models are one of the approaches of what are collectively known as second-order closure methods while another is the algebraic stress model. The rationale behind this method lies in the desirability of reducing the number of the Reynolds stress equations to be solved and Rodi, 1980, proposed one such model. In Rodi's stress model, algebraic expressions for R_{ij} are assembled by assuming that the transport part of the equations for R_{ij} is proportional to the transport part of the equation for k. The combined expressions contain both k and ε and while they are solved for those variables as in the $k-\varepsilon$ model there is a significant difference in that unlike this latter model no assumption of isotropy is proposed.

Although algebraic stress models enjoy the universality of Reynolds stress models at a cost similar to a two equation models and provide a prediction performance similar to the former they are known to encounter problems in flows where significant transport of R_{ij} occurs.

2.3.5 DNS and LES

No account even brief of the methods of turbulence evaluation ought to omit a reference to the Direct Numerical Simulation (DNS) and Large Eddy Simulation (LES) methods even though these methods are due to their direct nature often left out of the turbulence modelling categorization.

The underlying principle of the DNS approach was mentioned above in the context of the presentation of the instantaneous form of the Navier-Stokes equation. Unlike all other turbulence calculation processes Direct Numerical Simulation solves all scales of motion down to the Kolmogorov length scale, $l=(\nu^3/\varepsilon)^{1/4}$, at which turbulent kinetic energy is finally dissipated as heat. The colossal computational requirements of the method nevertheless are likely to ensure that DNS, as a turbulence computation method, will for a long time remain confined to the research status thus inhibiting its emergence as a practical proposition.

In the approach known as Large Eddy Simulation a compromise method is adopted whereby the large scale turbulent flow features, where most of the turbulent energy resides, are directly computed whereas the small dissipative scales are accounted for through a subgrid model. In this approach a subgrid eddy viscosity, ν_s, analogous to the turbulent eddy viscosity met above, is defined and it is the calculation of this variable that occupies the model division of the method. The assumption of isotropy which as before is implicit in the model is in LES less inaccurate as it is known that the small scale eddies are fundamentally isotropic.

2.4 Closure

The subject of the relative merits of turbulence models is a vexed question which in the CFD broad community is capable of stirring up emotions as probably no other. Nevertheless if a clear-cut and detached perspective of the matter is sought one should not so much depend on individual turbulence model author claims but preferably consider comparative studies such as those produced as a result of the 1968 Stanford conference on turbulence modelling, Kline et al, 1969, and the AGARD work reported by Dunham and Meauzé, 1998. The latter study represents the outcome of an invitation, which the AGARD Working Group on turbomachinery flow prediction methods extended to interested CFD practitioners, to submit calculations of two well documented test cases, the much reported transonic fan, NASA Rotor 37, and an annular turbine cascade tested by the German Research Establishment, DLR.

Although there is a natural desire to cross-compare the performance of the different turbulence models, the task is largely thwarted by the disparity in grid and flow solver features, that can by themselves obscure the genuine model differences. As a result the comparison was restricted to only those cases where the contributing authors had submitted solutions which employed the same code and grid but alternative turbulence models.

The broad conclusion of the comparison was that models of the algebraic mixing length type, such as the Baldwin-Lomax model described above, produced solutions that were generally inferior to the predictions obtained using transport equation models in those regions where the flow was separated or highly three-dimensional. This, it is pointed out, is the obvious limitation of any turbulence model requiring a "distance to the nearest wall" as a way of defining the shape of the whole boundary layer and tuned to predict two-dimensional turbulent boundary layers.

This marginal superiority of the transport equation models had also been identified in the Stanford conference on turbulence alluded to before where it was seen that the models that solved partial differential equations yielded better results than those which didn't, Birch, 1993. At the time of the Stanford conference, most of the

transport equation models did in fact only solve one partial differential equation for turbulent kinetic energy, but at a later conference held in 1972 at NASA Langley, two-equation models were judged to offer improved performance for complex turbulent flows over one-equation and algebraic turbulence models.

For the concluding word on the subject of turbulence modelling we will again borrow from Dunham and Meauzé's report of the AGARD Working Group on turbomachinery flow prediction methods mentioned before: " The Working Group was unable to identify any one turbulence model which always gave good loss predictions. It is well known that this is an area of continuing vigorous research and it needs to be."

Chapter 3

Computational methods

3.1 Introduction

The conservation equations which underpin the Computational Fluid Dynamics solution of turbomachinery flows have been presented in the previous chapter and in the present one we detail the steps required to numerically obtain their solutions. The chapter seeks to lead the reader through the logical simulation path from the assembly of a grid through the choice of discretization methods and towards the issues concerning the solution methods.

3.2 Grid generation

3.2.1 Initial remarks

It is a central tenet of discrete numerical methods that a distribution of points within the computational domain to be studied needs to be supplied in order to define the elemental sub-regions of the domain. If meshless methods are ignored, a justifiable choice in view of their level of application in practical CFD work, it is safe to define grid generation as a procedure to distribute an array of points in an orderly fashion over the domain of interest. More often than not these points will be assigned to a fixed location in the physical space for the duration of the simulation, which in turn reinforces the requirement for a judicious initial distribution, or they can, as is the

case of adaptive meshes, dynamically congregate where the ongoing solution has identified the flow variable gradients to be located.

The building of the grid corresponds to the discretization of the physical space, but the specific manner of that discretization is dependent on the particular method employed in the conversion of the continuous forms of the governing equations, as described in the previous chapter, and their discrete corresponding forms, to be developed below.

All of the three common discretization schemes make use of meshes in order to assemble the discrete analogue of the continuous equations. In the finite volume method, a number of nodes will be associated with a portion of the volume of the domain over which the conservation equations are applied. In the finite difference method it is the values of a node and its neighbours which are used to assemble the conservation equations. Lastly in the finite element approach the nodes are assembled into elements over which the variation of flow properties can be functionally described.

A summary description of the classification of grids according to their type is usually done along the lines of the diagram underneath.

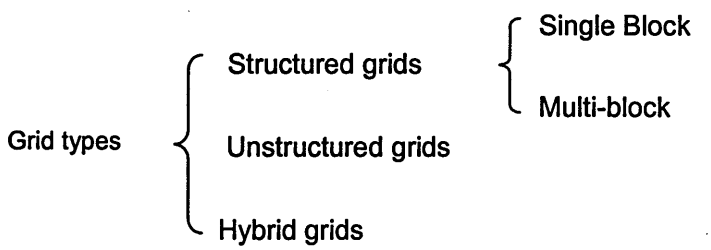

The grids employed in TASCflow belong to the first type and to either of its two sub-types and there is no provision for automatic solution adaption or refinement. We will in the next sections address the issues related to the theoretical background and practical implementation of structured mesh construction, as well as describe the strengths and limitations of the gridding method employed in the code.

3.2.2 Structured meshes characterization

In structured grids the nodes are distributed along grid lines which are related to a grid coordinate system where lines belonging to the same coordinate do not cross each other. The advantage of this sort of ordered arrangement in CFD is that the relationship of any node with its neighbours is very easy to establish by recourse to an i-j-k index formulation. The fundamental benefit of such an ordered nodal arrangement is that it enables the mapping of the physical grid onto a corresponding regular computational domain with an associated simplification of the solution algorithms including parallel computations.

For turbomachinery applications a number of possible grid arrangements exist and these are likely to fall into one of the three formats depicted in Figure 3-1. The element of choice between the three configurations is dictated primarily by the whereabouts of the most highly skewed region of the grid as well as ease of assembly of the mesh.

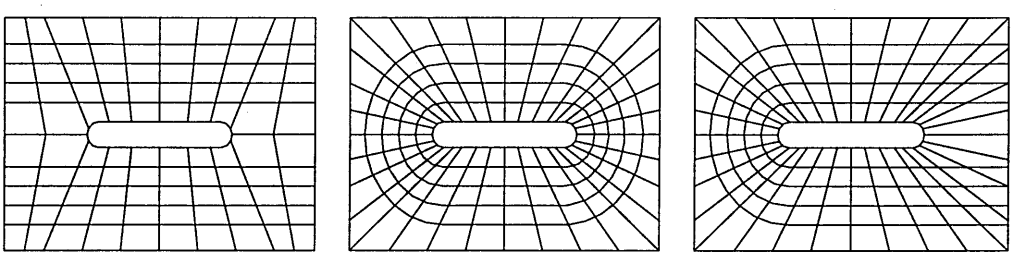

H grid **O grid** **C grid**

Figure 3-1 Structured grid types

H grids are the easiest to set-up and have the advantage of presenting the boundary and periodic regions of the domain, with well behaved patches of grid which offer a benefit in terms of local accuracy, but in the zones of the blade leading and trailing edges these grids are prone to high skew. This situation can be further complicated by any additional refinement of the grid which will invariably lead to an increase in the local grid shearing.

O grids employ sets of conformal grid lines expanding from the blade surface outwards and are therefore very good near the blade edges although in turn likely to experience skew difficulties in the domain boundaries. Computationally O grids can be thought of as being a length of half-width passage grid which is wrapped in a full loop around a centrally placed blade.

C type grids are somewhat similar to O grids in that they too are wrapped around the blades but in this case over just half a loop, with the ends of the initial length of grid becoming placed side by side rather than end-to-end as in the O grid format. In C grids the regions of skewedness are concentrated in one of the blade edges and at the inlet and periodic boundaries. When employed as a single block, O grids become quite coarse as the distance from the blade leading edge to the inlet is increased which limits the practical upstream dimensions of domains that can best make use of this type of meshes.

Although some codes are more tolerant of skewedness than others, in general very skewed grids can significantly retard a solver convergence towards a steady-state solution or even inhibit convergence altogether. The reason for this will be made clear underneath but at this point it suffices to say that skewedness is related to the introduction of numerical errors which will either hinder convergence as suggested or present a simulation of degraded quality.

It is possible to identify a number of benefits associated with use of structured grids:

- high degree of user node control
- hexahedral and quadrilateral elements typical of structured grids are quite tolerant of skew and stretching
- flow solvers which employ structured grids use less memory than unstructured solvers for an identical grid size
- ease of post processing tasks through the availability of arrays of ordered grid planes

However a number of disadvantages can also be pointed out:

- the generation of structured grids is frequently a lengthy process and one which calls for considerable user experience
- on some geometries structured grids are not the best solution, as is the case in sharp edges for example
- grid adaption involves a large number of nodes remote from the place of interest

An alternative to the single block grids is to make use of a number of different meshes of a given type in the discretization of the domain and selecting a particular type to occupy the locations where it is best suited. When several grids are simultaneously employed, these can either have a contiguous interface where the exchange of information between the grids takes place or present regions where the grids physically overlap. The question of the nature of the information exchange across these interfaces is quite important as these can and often do impact negatively on the robustness of the computation and degrade the accuracy of the prediction.

The fundamental grid generation techniques commonly used in structured grids are presented in a diagrammatic format below.

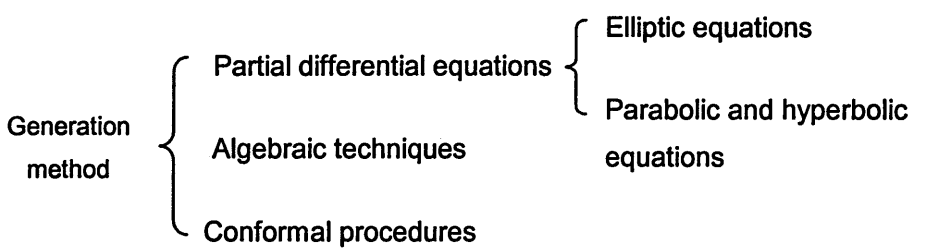

The type of partial differential equations which are used to describe steady-state physical processes such as potential fields is, as it will be recalled from the previous chapter, the elliptic format associated with equilibrium problems.
One important characteristic of the equations of this type, is their smoothing effect on the boundary data and this property is exploited in elliptic grid generators to distribute nodes on surfaces once the distribution on the boundaries has been set.

Besides the elliptical equations both parabolic and hyperbolic grid generation equations have also been tried but despite some attractive features, namely the increase in computational efficiency of the two systems, their use has been confined

to simple geometries. The drawbacks of both of these methods are related to the difficulty with the smoothing of discontinuities introduced by the boundary conditions.

Algebraic grid generation is based essentially on the interpolation between the boundaries and/or the intermediate surfaces of the physical domain. Transfinite interpolation consists of the interpolation between the functions which are defined along curves and surfaces rather than, as is done in the algebraic method, between point values.

Conformal mapping as a grid generation technique is based on the principle that an intricate geometry can be mapped onto a simple domain where a grid can then be assembled in a straightforward manner perhaps through a basic interpolation routine. The process is complete with the mapping of the intermediate grid from the basic shape back to the original domain.

3.2.3 TASCflow grid generation approach

The code can make use of grids which are either assembled by an external grid generation package or constructed through a dedicated suit of mesh building programs contained within the overall TASCflow package.

The basic steps of the grid assembly process occur within the TASCflow mesh generator, TASCgrid, where four programs are run sequentially to, construct the domain geometry, TASCgridg, distribute nodes on the lines of the domain, TASCgridc, distribute nodes over the domain surfaces, TASCgrids, and finally distribute the nodes within the interior volumes, TASCgridi. The last operation also includes the writing of GRD, the complete grid file which can then be imported into TASCbob3D, the pre-processor program of TASCflow.

The grids generated through this method are structured body-fitting single-block sheared meshes. All the TASCgrid programs require some form of user input coding although the running of each of the first three modules produces a basic template of the piece of code which is to be used in the next program. We will next address some

of the theoretical aspects of the methods employed in the generation of grids through the TASCgrid set of programs.

3.2.3.1 TASCgrid interpolation schemes

We can obtain at a glance an idea of the grid generation algorithms employed by the code by reference to the diagram underneath.

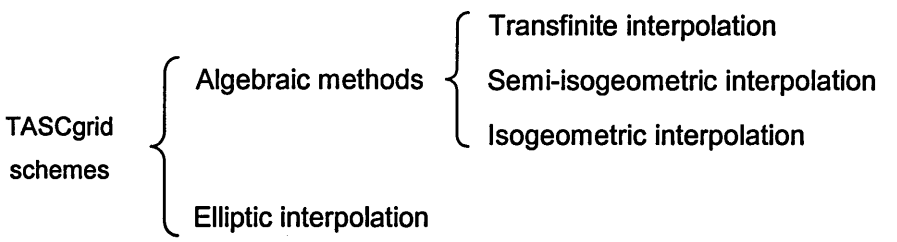

As has been noted above, algebraic methods employ simple interpolation schemes between boundaries to locate the interior grid nodes. All of the sub-variants of the algebraic method employed in TASCflow make use of the same equations to map points between the physical (x,y,z) space and the regular (ξ,η,ζ) computational space. The equations contain two weighting functions and it is according to the particular method which is used to calculate these that the sub-division of the algebraic schemes is carried out.

In the transfinite method, the simplest of the implementation versions of the algebraic schemes, the weighting functions are simply defined as uniform in the computational domain. The drawback of this approach lies in the implicit neglect of the boundary distributions and consequently in regions where uneven node spacings are prescribed the use of this scheme leads to possible wiggling in the grid.

In semi-isogeometric interpolation the effects of the boundary distributions are accounted for through the parametrization, in terms of local parameters s,t,u, of the region of interest. This step is, for 3D cases, equivalent to the interspersing of a mapping to a unit cube, in between the physical-to-computational transformation. This is the most general of the algebraic schemes implemented in TASCgrid.

The isogeometric interpolation approach is virtually identical to that of the semi-isogeometric interpolation except for a minor variation in the way of the definition of the boundary points whereby these are related to the interior nodes.

Elliptic interpolation schemes on the other hand involve a much more sophisticated approach and require the solution of a coupled system of Poisson partial differential equations in order to supply the nodal coordinates of the region. The reasoning behind the employment of elliptic equations as grid generators was established above but the idea can be developed further if source terms are attached to the elliptic equations. It is easy to imagine that through these source terms, the position of isopotential lines can to some extent be controlled.

In practice the physical domains require in TASCgrid a volumetric sub-division and it is over these component surfaces and volumes that individual interpolation schemes are applied. It is therefore possible that for the assembly a given grid, diverse algebraic formulations as well as an elliptic scheme, may have been employed simultaneously.

Part way through the duration of the present research project, the code developers released Turbogrid, a dedicated turbomachinery semi-automatic grid generation package which combines the four component codes of TASCgrid described above with an extensive library of macros and a GUI interface. Although subsequent versions of the Turbogrid code have largely removed some of the limitations of the early editions, namely the absence of operator control over blade-to-blade clustering ratios, the assembly of good quality meshes on other than 'easy' configurations is often quite time consuming and not always very successful.

For this reason the assembly of all the grids used in the test cases of the present study was carried out through the TASCgrid approach.

3.2.3.2 Grid quality assessment

There are a number of widely accepted measures of grid quality or in other words of the fitness of the grid to make the best possible use of CFD code that exploits it

without, by itself, being the cause of the introduction of errors in the computation. These measures, which are largely universal throughout CFD, are expressed in TASCflow as follows:

Smoothness – any sharp discontinuities in the grid spacing are a source of imprecision in the evaluation of the nodal averaged quantities, due to the uneven biasing of the contributions of the cell boundaries, and must for that reason be avoided.

Skewness – the degree of skewness of an element, which is a measure of the departure from orthogonality in any given adjacent flux element surfaces, is set by TASCflow at a lower bound of 20 degrees as the maximum value of skew which entails no accuracy penalty. Between this angle and 10 degrees the code will exhibit some deterioration in terms of solution accuracy as well as convergence performance degradation. Below 10 degrees the operator is expected to regenerate the mesh since the code treats these skew values as error conditions.

Aspect ratio – many codes enforce strict limits on cell aspect ratio, 10 is a common value, but in TASCflow, essentially due to the ancestry of the code being rooted in river flows calculations, these limits are quite relaxed being set at 100.

Alignment of flow streamlines and grid lines – the alignment of grid lines with the local flow streamlines has a beneficial effect in helping to reduce numerical diffusion and the code recommends that wherever possible this should be pursued.

3.2.4 Effect of the grid on the simulation

It is known that a number of grid features can have an identifiable impact on the quality of a simulation namely the grid size and type, the near-wall clustering and smoothness of the mesh, the aspect ratio of elements and their measures of distortion, skewedness and stretching, and for turbomachinery applications the type of tip clearance gap treatment. In addition to these sources of uncertainty in the

computation, others of grid origin will be further added for compound meshes, due to the complications introduced by the inter-block data exchange.

To isolate these sources of error, it is an accepted good practice in CFD that whenever possible a grid dependency study ought to be carried out so that a measure of the impact of the grid features alluded to above, particularly local and overall densities, can be ascertained and some measure of grid dependence or independence of the solution be established.

One detailed grid dependency study was that reported by Arnone et al, 1997, on the subject of the well known NASA Rotor 37 single blade row transonic compressor case. In their systematic analysis Arnone and his co-workers divided the computational domain into several regions comprising the leading and trailing edges, inlet, passage and boundary layer regions, and at each of these the grid density was changed in order to investigate the impact on the solution. Their conclusion was that for all the grid independent regions to be considered, the overall grid needed to come close to one million points even though a point distribution optimisation procedure was employed.

The issues of grid density as well as type were considered in Dunham and Meauzé, 1998, who reported on behalf of the AGARD working group set up to promote further study of the Rotor 37 test case in view of the scatter of results observed in the original ASME test. In this work it is pointed out that a moderate grid of about 200,000 nodes is required to capture the overall performance characteristics and that much finer grids with as many as 1,000,000 nodes are needed to isolate the detailed flow features such as endwall secondary flows and tip clearance flows. This number however is suggested for the cases where no wall functions were employed and where they were the authors found evidence that for the prediction of losses some "well chosen" 300,000 nodes per blade passage were needed and that if fuller details of the three-dimensional flow pattern were needed a grid of 500,000 or more points were required.

The theme of the provision of the amount of grid points required to capture fine flow details and the relative impact of these on the overall flow, is further pursued by Gerolymos and Vallet, 1998, in the context of the study of tip-clearance flows. The

authors employed grids of one, two and three million nodes, of which some 140,000 were used within the gap region alone. This unparalleled level of discretization enabled them to obtain ever more detailed velocity profiles inside the tip clearance gap although elsewhere the results were seen to be grid independent at the 2,000,000 nodes level.

3.3 Discretization of the flow governing equations

Having defined an array of points distributed throughout the physical region of interest where the variables of the modelled flow can be evaluated, the task of obtaining a form of the governing flow equations which is appropriate for a numerical solution method, can then be undertaken.

The three essential discretization approaches are the finite element, finite difference and finite volume methods but in most turbomachinery CFD applications the latter two are preferred. The finite element method is based on a division of the physical domain into a number of finite elements over which the variables field is interpolated using linear shape functions. As the TASCflow code employed in the present study utilizes a finite volume formulation, we shall devote the following section to a description of this method.

3.3.1 Finite volume method

In the finite volume method the physical domain is subdivided into a set of very small sub-domains or elemental control volumes by making use of the grid of nodes which was defined through one of the methods outlined above. Although the finite volume model is equally valid for unstructured grids we will confine the presentation to the structured grids case.

There are a number of advantages associated with the use of the finite volume method namely the fact that the integral formulation ensures the conservation of the

fundamental flow properties of mass, momentum and energy. One other benefit is that this approach is recognized as being intuitively clear to grasp, given that it has as its starting point, the discrete partition of the flow domain.

The definition of a finite volume from a structured grid distribution can be made either in terms of the volume surrounding individual nodes, the node centred or cell-vertex approach, Figure 3-2, or in terms of the intra-nodal volumes of the cell centred concept, Figure 3-3, where it is the adjacent nodes which are employed to define the finite volume.

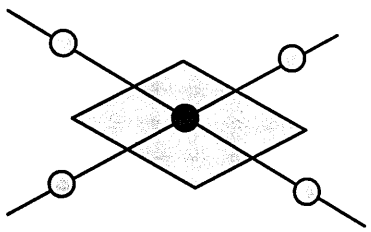

Figure 3-2 Node centred approach

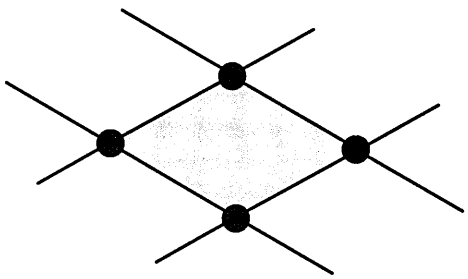

Figure 3-3 Cell centred approach

The fundamental difference between the two methods refers to where the location of the unknowns is placed, the cell centred approach making use of the centroid of the cell to store variables while for node centred schemes this storing occurs in nodes at the cell vertices.

3.3.1.1 TASCflow implementation of the finite volume method

The TASCflow code employs a technique borrowed from the finite element method to discretize the domain into flux elements by linking neighbouring nodes into hexahedral tri-linear configurations characteristic of node centered or cell vertex schemes. The finite element connection is introduced through the use of shape functions which the code employs to define coordinates of the sub-elemental geometry connected with the assembly of the control volumes.

We shall for simplicity confine the description of the volumetric discretization method employed by the code to planar grid set-ups. The elements are subdivided into four parts and when this process is performed over the elements that share a common node, a node centred control volume can be assembled as seen in Figure 3.4.

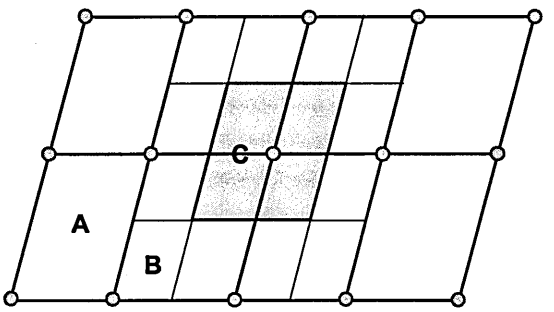

Figure 3-4 Control volume formulation

In this figure **A** designates the element and **B** the quadrant, in 3D grids the nodes are instead surrounded by octants, while **C** indicates the assembled control volume which for interior nodes is composed of four quadrants or octants as the case may be.

The discretization of the governing equations proceeds with their integration over the separate finite control volumes by means of Gauss' theorem which states that a volume integral is expressible as the sum of the appropriate surface integrals.

We shall for convenience make use of the continuity equation to illustrate the process starting with the conversion of the divergence form of the equation,

$$\frac{\partial \rho}{\partial t}+\frac{\partial(\rho u_i)}{\partial x_i}=0 \tag{3-1}$$

into its integral analogue as applicable to a discrete control volume,

$$\frac{\partial}{\partial t}\left(\int_V \rho \, dV\right)+\int_S \rho u_i \, d n_i = 0 \tag{3-2}$$

In equation 3.4 the subscripts V and S denote whether the integration takes place over the volume or the surfaces of the control volume, respectively, while n_i represents the

Cartesian components of the outward normal surface vector. The surface integrals correspond to the physical fluxes whereas the accumulation of variables is accounted for through the volume integrals.

The next step in the finite volume procedure consists in the transformation of the integral transport equations through the replacement of the continuous functions with their discrete algebraic counterparts. The continuity equation will by this process be then cast as,

$$\rho \, \mathrm{Vol}\left(\frac{\rho - \rho^{0}}{\Delta t}\right) + \sum_{ip} (\rho \, u_j \, \Delta n_j)_{ip} = 0 \; . \tag{3-3}$$

The subscript *ip* of equation 3.5, indicates that the evaluation of the expression is to be carried out at the different integration points, which are disposed along the surfaces of the control volume as shown in Figure 3.5 below, where for convenience, use is made again of a 2D example.

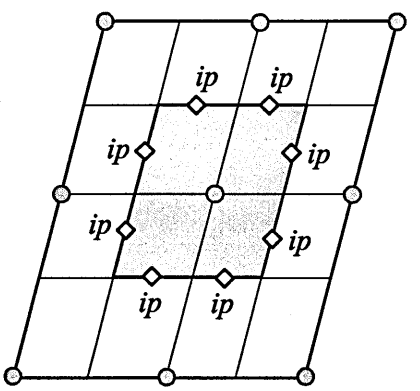

Figure 3-5 Location of integration points in a 2D grid layout

The discrete momentum equations are cast in TASCflow as,

$$\rho \, \mathrm{Vol}\left(\frac{u_i - u_i^{0}}{\Delta t}\right) + \sum_{ip} \dot{m}_{ip} \, (u_i)_{ip} = \sum_{ip} (P \Delta n_i)_{ip} + \sum_{ip} \left(\mu_{\mathrm{eff}} \left(\frac{\partial u_i}{\partial x_j} + \frac{\partial u_j}{\partial x_i} \right) \Delta n_j \right)_{ip} + \mathrm{S}_{u_i} \, Vol \tag{3-4}$$

where the first term corresponds to the time step, the *o* superscript indicating that the value refers to the previous iteration or time step. The second term describes the convective effects of the flow while the first term of the RHS of the equation is the pressure gradient term followed by the diffusive and volumetric source terms respectively.

3.3.1.2 Treatment of the convective transport terms

In TASCflow the convective transport terms are normally modeled through a physically corrected skew upwind scheme whereby one of the variants of a skew upwind scheme is combined with a Physical Advection Correction (PAC) term. Skew schemes tend to influence the accuracy in the transverse direction of the flow, such as false diffusion levels, whereas the PAC term tends to influence the accuracy in the streamwise direction, such as the conservation of total pressure or shock sharpness, Lesage and Raw, 1992.

The placement of the integration points was described in Figure 3.5 and in order to obtain algebraic closure, the term corresponding to each of the integration points needs to be related to the neighbouring nodal variables and that relationship is established through the particular advection discretization scheme which is employed.

The general form of the advection scheme for any given conserved quantity, ϕ, can be written as,

$$\phi_{ip} = \phi_{upstream} + \Delta\phi \tag{3-5}$$

where $\phi_{upstream}$ is the upstream term, supplied by the upwind scheme, and $\Delta\phi$ is a possible streamwise correction term. The operator of the code is faced with a choice of four advection schemes designed as Upstream Difference Scheme (UDS), Mass Weighted Skew (MWS), Modified Linear Profile Skew (MLPS) and Linear Profile Skew (LPS).

The essentials of the different procedures named above can be described with reference to Figure 3.6 below, where $\mathbf{V}_{ip}$ symbolizes the velocity vector of the streamline denoted by the dashed line.

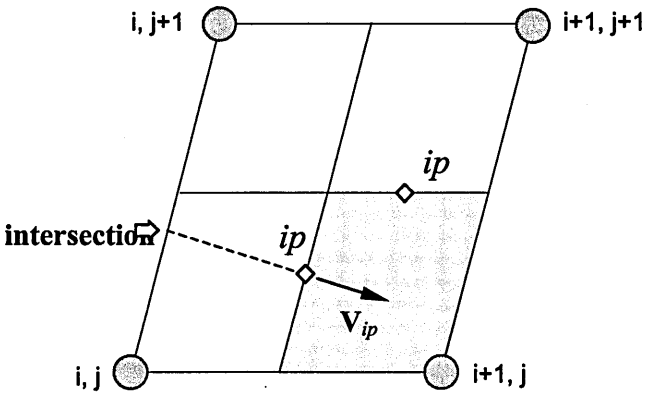

Figure 3-6 Flux element outline

In the basic UDS formulation the conserved quantity, ϕ, is simply,

$$\phi_{ip} = \phi_{i,j} \tag{3-6}$$

where $\phi_{i,j}$ corresponds to the value ϕ takes at the i, j node. Though this scheme is very robust it is also fairly inaccurate as it suffers from excessive numerical dissipation and hence from a tendency to overpredict the total pressure losses. The code manual cautions the operators against its use in other than a starting role for the simulation of difficult problems, where more accurate but less robust schemes, may well encounter initial convergence difficulties.

The second of the alternative schemes available, the Mass Weighted Skew formulation, represents an attempt at reducing the levels of false diffusion present in the basic UDS, through the inclusion of the effects of neighbouring nodes. Specifically in MWS the value of $\phi_{upstream}$, which is the value of ϕ taken on the streamline upstream of the point of interest, is based on an average of the surrounding nodal values of ϕ, weighted according to the mass flows which pass through the control volume faces that are adjacent to $\phi_{upstream}$. This scheme is as robust as the UDS and has a lower level of false diffusion, but although it shows a reduction in smearing, it still has high artificial total pressure losses when used in the momentum equation, Thomas et al, 1989.

Both UDS and MWS are first-order accurate schemes while the second set based on the linear profile skew approach, MLPS and LPS, are second-order even though under some conditions the former of these schemes does revert to first-order accuracy. The LPS approach, which represents an enhancement of Raithby's Skew Upwind Difference Scheme, Raithby, 1976, is based on the idea of the inclusion of information concerning the local flow vector in the formulation of the upwind term.

The directional effect is accounted by reference once again to Figure 3.6, where the location of a possible intersection of the streamline with the edge of the flux element is represented. Assuming a linear variation between the nodes which define the edge, the conserved quantity, ϕ, can be expressed as,

$$\phi_{ip} = a\,\phi_{i,j} + (1-a)\,\phi_{i,j+1} \tag{3-7}$$

a being a function of the intersection point location.

The benefits of the linear profile skew methodology include a significant reduction in smearing, by comparison to first-order schemes, and the inexistence of longitudinal solution wiggles as can occur in second-order central difference schemes. In practice some wiggles do crop up but these happen only in a transverse direction, are on a small scale and are known to dampen out quite quickly. Although the scheme is nominally second-order accurate, this condition is only verified for the primitive form of the convection term,

$$\frac{\partial(\rho\, u_i \phi)}{\partial x_i} \,. \tag{3-8}$$

When source terms are included however, the scheme is then just first-order although it is possible to reinstate its second-order status through the inclusion of a supplemental term modelling the physics of the streamwise convection of ϕ .

A pure version of LPS is implemented in TASCflow, corresponding to the most accurate but also least robust of the code discretization schemes, but the operator retains control over the blending of this scheme with a more robust variant of the linear profile skew formulation. In the Modified LPS the value of $\phi_{upstream}$ is initially calculated as for the basic LPS but this is followed by an adjustment of the

interpolation coefficients so that $\phi_{upstream}$ is more evenly dependent on the nodal values upstream and downstream of the integration point. In the interests of solution stability this scheme is by default blended with 5% UDS.

The idea of the coupling of a Physical Advection Correction (PAC) term with a variant of a Skew Upwind scheme was introduced in the preamble of this section but we are now in a position to expand on the subject further. The argument for a need of a PAC term can be established with reference to a 1D simplification of the situation described by Figure 3.6. Written in terms of a node *i* and employing a second-order Taylor series, the expansion of ϕ_{ip} is expressed as,

$$\phi_{ip} = \phi_i + \frac{\Delta x}{2}\frac{d\phi}{dx} + O(\Delta x^2). \qquad (3\text{-}9)$$

This expression can be compared with the UDS analogue of Equation 3.4, which for 1D is simply, $\phi_{ip} = \phi_i$, while noting at the same time that this is also the form which all skew schemes assume in one dimension. The comparison of the two forms provides evidence that unless the term $\frac{d\phi}{dx}$ is also represented the scheme is first order only.

The conventional approach to the representation of the derivative term would be to employ one of the schemes which are based on the generic formulation,

$$\frac{d\phi}{dx} = a\frac{(\phi_i - \phi_{i-1})}{\Delta x} + b\frac{(\phi_{i+1} - \phi_i)}{\Delta x} + (1 - a - b)\frac{(\phi_{i+2} - \phi_{i+1})}{\Delta x} \qquad (3\text{-}10)$$

and selecting different combinations of a and b. In this way a number of well known schemes can be assembled, Central Difference, Second Order Upwind, Leonard's QUICK, Leonard, 1979. These schemes however are all known to suffer from one or more limitations associated with poor physical influence, unphysical solution wiggles, solution smearing and poor convergence characteristics for iterative solvers, TASCflow Theory Manual, 1997.

The method employed by the code to represent the derivative is termed Physical Advection Correction and is based on the principle that the correction term must be

representative of all the modelled physical processes. Considering the finite volume general form of a transport equation,

$$\int_V \left[\frac{\partial(\rho u_i \phi)}{\partial x_i} + \frac{\partial}{\partial x_i}\left(\Gamma \frac{\partial \phi}{\partial x_i} \right) \right] dV = \int_V S_\phi \, dV \qquad (3\text{-}11)$$

where the first, second and third terms represent the convective and diffusive and source processes respectively, and making use of the continuity equation, a PAC evaluation term can be assembled which will, in one-dimensional form, be expressed as,

$$\frac{d\phi}{dx} = \frac{1}{\rho u}\left[-\frac{d}{dx}\left(\Gamma \frac{d\phi}{dx} \right) + S_\phi \right] \qquad (3\text{-}12)$$

Although there are alternative implementations of the PAC method, in TASCflow this evaluation is always combined with one of the three Skew Upstream Differencing Scheme (SUDS) variants, and this association determines the PAC evaluation procedure. The code evaluates the PAC term explicitly as a lagged expression in the flow equations and this value is recalculated at each iteration.

3.3.1.3 Treatment of the diffusion terms

Unlike the convective terms there is no physical directional influence in the propagation of information associated with the diffusive terms and therefore these lend themselves to discretization by a central scheme. However the characterization of the diffusive fluxes is dependent not only on the knowledge of the unknowns but also the gradients of these unknowns.

The code makes use of the shape functions, equation 3.2, to evaluate these unknowns' gradients with the derivative, in the x direction, of the generic variable ϕ taken at an integration point being calculated from,

$$\left. \frac{\partial \phi}{\partial x} \right|_{ip} = \sum_n \left. \frac{\partial N_n}{\partial x} \right|_{ip} \phi_n \qquad (3\text{-}13)$$

where the summation occurs over the n shape function of the element. The Cartesian derivatives of the shape functions are expressed in terms of the local derivatives through the use of the Jacobian transformation matrix,

$$\begin{bmatrix} \frac{\partial N}{\partial x} \\ \frac{\partial N}{\partial y} \\ \frac{\partial N}{\partial z} \end{bmatrix} = \begin{bmatrix} \frac{\partial x}{\partial s} & \frac{\partial y}{\partial s} & \frac{\partial z}{\partial s} \\ \frac{\partial x}{\partial t} & \frac{\partial x}{\partial t} & \frac{\partial x}{\partial t} \\ \frac{\partial x}{\partial u} & \frac{\partial x}{\partial u} & \frac{\partial x}{\partial u} \end{bmatrix}^{-1} \begin{bmatrix} \frac{\partial N}{\partial s} \\ \frac{\partial N}{\partial t} \\ \frac{\partial N}{\partial u} \end{bmatrix} \tag{3-14}$$

In practice the calculation of the derivatives of the shape functions does not take place at the precise *ip* position, since it has been found that for highly skewed elements, as well as those with large aspect ratios, this often leads to problematic solutions and poor convergences. In order to improve the robustness of the solution TASCflow evaluates the shape function gradients at the locations where the *ip* surface intersects the element boundary, denoted by **x** in figure 3.6.

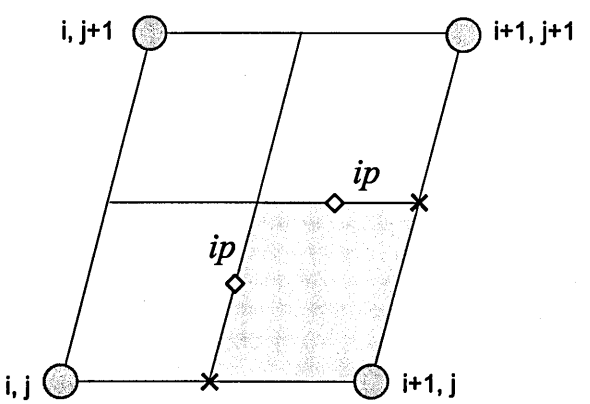

Figure 3-7 Location of the shape function gradient evaluation points

The disadvantage of the shift in the location of the estimation points from their formal *ip* position is that the former method, the tri-linear evaluation, is second-order accurate in orthogonal meshes and first-order accurate in non orthogonal ones while the latter approach, the linear-linear evaluation, is first-order always.

3.3.1.4 Treatment of time terms

The code which formerly employed a strictly steady-state formulation acquired during the early stages of the current project an unsteady computation capability and therefore the treatment of the transient term is dependent on the mode in which it is employed.

Steady-state – TASCflow uses a first-order backward Euler approximation to represent the time term. The code employs for steady-state computations a transient formulation as a convenient means of introducing relaxation into the iterative non-linear solution, Galpin and Raithby, 1986. If only the steady-state solution is of interest the time step Δt is used as a free parameter through which the convergence rate is optimized. Relaxation introduced via a time step is preferable to other relaxation schemes, such as E factor[1] or steady formulations with explicit under-relaxation, because it ensures that the linear momentum and energy equation solutions advance the dependent variables by a consistent amount in each update cycle. This corresponds to the use of a pseudo-time which is employed solely to advance the solution in an iterative manner

Transient solution – The first-order Euler representation of the time term which is employed in the steady state analysis is also the default implementation used for the code unsteady simulation formulation. In this approximation,

$$\frac{\partial \phi}{\partial t} \approx \frac{1}{\Delta t}(\phi - \phi^{o}) \tag{3-15}$$

the error in the transient representation reduces linearly as the time step is refined. In later versions of TASCflow the code incorporated an alternative formulation of the transient term in the form of a second order accurate backward Euler scheme,

$$\frac{\partial \phi}{\partial t} \approx \frac{1}{\Delta t}\left(\frac{1}{r(r+1)}\right)\left[(2+r)r\phi - (1+r)^{2}\phi^{o} + \phi^{o-1}\right] \tag{3-16}$$

---

[1] TASCflow enables the user to substitute the time step for an E factor formulation. It is the ETFACT local time step factor parameter the theory of which is presented in van Doormaal and Raithby, 1984.

where r, which is the new and old implicit time steps ratio is given by,

$$r = \frac{\Delta t^{o}}{\Delta t} . \tag{3-17}$$

For the constant time step case, r will of course take the value of 1 and in this situation Equation 3.18 can be rewritten as

$$\frac{\partial \phi}{\partial t} \approx \frac{1}{\Delta t}\left(\frac{1}{2}\right)\left[3\phi - 4\phi^{o} + \phi^{o-1}\right] \tag{3-18}$$

When expressed as above the error in the transient representation reduces quadratically as the time step is refined linearly.

3.3.1.5 Colocation and compressibility treatment

The method used in TASCflow to prevent the occurrence, in incompressible flow solutions, of the familiar pressure field checkerboard problem found in collocated grids, is to set up in the continuity equation a pressure-velocity coupling which produces a diagonally dominant equation for pressure.

Recalling the discrete algebraic formulation of the continuity equation which we can write for the steady-state as,

$$\int_{Surf} \rho\, u_i\, dn_i = \sum_{ip} \rho_{ip} (u_i\, dn_i)_{ip} , \tag{3-19}$$

one can relate the integration point values of the velocity variable, u_{ip}, to the nodal variables, in one-dimension and for the incompressible case, and making use of linear interpolation as,

$$u_{ip} = \frac{1}{2}(u_i + u_{i+1}) . \tag{3-20}$$

This process which does not involve the pressure in the continuity equation leads to the decoupled pressure fields alluded to above. A pressure-velocity coupling is set up if the integration point velocity variable, u_{ip}, is obtained from,

$$u_{ip} = \frac{1}{2}(u_i + u_{i+1}) + D\left(\frac{p_{i+1} - p_i}{\Delta x}\right) - \frac{1}{2} D\left(\left.\frac{dp}{dx}\right|_i + \left.\frac{dp}{dx}\right|_{i+1}\right) \tag{3-21}$$

where D is a parameter derived from the consideration of the velocity-pressure coupling in the momentum equations.

Pressure correction methods are usually associated with incompressible flow computations given that the solution of continuity equation tends to be related to the calculation of the pressure rather than, as is done in time marching schemes, associated to the computation of the density.

It can be seen from an examination of equation 3.21 that when considering compressible flows the status of density within the equation follows the pattern set for the other transported variables, the velocity for example. The corollary of this observation is therefore that the density is amenable to be the subject of the same treatment, skew schemes and PAC, as other variables. In TASCflow the density is therefore calculated from

$$\rho_{ip} = \rho_{upstream} + \mathrm{PAC}_{\rho} \tag{3-22}$$

where the PAC term is given by $\mathrm{PAC}_{\rho} = -\frac{l\rho}{V}\frac{\partial u_i}{d x_i}$, in which l and V are the distance from the integration point to $\rho_{upstream}$ and the local velocity magnitude respectively.

Once the density is computed the pressure is introduced via the equation of state for perfect gases, $P^n \approx \rho^n R T^o$, where the n and o superscripts are used to denote in turn the updated and old values of the variable and which establishes the required pressure-density coupling. In this way the continuity equation incorporates pressure from both the pressure-velocity coupling associated with the calculation of the velocity terms u_i and from the pressure-density coupling introduced by the evaluation of the density ρ_i.

In flow regimes containing strong and in particular moving shocks, the solution of the continuity equation can encounter difficulties which arise from the updating of the linearization coefficients from a combination of old and new values. The code includes therefore an optional continuity loop, which can be inserted between the

sequential solver inner sweeps and the outer coefficient updating loop or time-step, in which an extra iteration on the mass flow is carried out in order to resolve the non-linearities present at the given time-step.

Through this approach the code is able to evaluate a wide variety of flow problems ranging from low speed incompressible to high Mach numbers.

3.4 Turbomachinery Boundary conditions

One of the accepted advantages of the employment of a collocated method lies in the relative ease with which turbomachinery boundary conditions can be applied. Several of the boundary conditions types implemented in TASCflow have a direct bearing on the simulation of these machines, inlet types include the specification mass flow, of velocity components, total pressure and temperature, with either a Cartesian or cylindrical direction system and radial distributions of variables. At the outlet the code static pressure average values can be selected with the particular form of the radial gradient being solution dependent.

The code makes use of three grid attachment methods which are classed according to the particular node matching process they employ, exact or one-to-one, approximate or many-to-one and arbitrary, this one utilizing the General Grid Interface (GGI) formulation.

In the first of these methods there is a one-to-one correspondence of faces and nodes between the contacting regions while in the second there is no requirement for the nodes each of the sides of the grid interface to match. Often the attachment between the two grids regions requires that adjustments are made in order to assemble the connection. Since these adjustments are made directly to the grid file the original node locations are not recoverable.

The General Grid Interface of the latter method the can be used to connect grids whose topology is different on either side of the interface and is the interface model

employed by the code in the simulation of turbomachinery problems. The three dedicated blade row attaching models are Stage, used in steady state with averaging in the direction of relative motion, Frozen Rotor also steady state, with a fixed relative position across the interface and Rotor/Stator employed in transient computations.

The central feature of the GGI is the use of a control surface which are two dimensional surfaces over which the conservation of variables is enforced via flux balances. The analysis of this method is examined in greater detail when considering the rotor/stator unsteady approach.

3.4.1 Mixing-plane steady-state approach

When two or more relatively rotating components occupying different frames of reference are the object of a combined simulation and only the steady state is of interest, an averaging plane can be employed to process the inter-boundary exchange of information. In TASCflow this approach is known as the 'Stage' model where the GGI interface is combined with a circumferential averaging algorithm, whose specific implementation details have not been disclosed, to condition the flows which traverse the inter blade row boundaries.

The Stage interface model assumes a complete mixing of the upstream velocity profile, thereby eliminating the circumferential influence of one component on another, while maintaining the meridional plane interaction between components including the provision of recirculation. The scheme is conservative of fluxes.

3.4.2 Transient rotor/stator approach

From Version 2.8 onwards, released in 1998, the code acquired a transient rotor/stator capability thereby enabling the computation of two or more relatively rotating components to be simultaneously carried out in a single frame of reference. The enabling of the time-accurate turbomachinery method required, besides the solution of the transient terms of the transport equations, some means of accounting for the angular displacement between the neighbouring blade domains and this problem is

tackled in the code via a dedicated boundary condition which is termed in TASCflow, sliding interface.

Before proceeding to describe the implementation features of the sliding interface it is useful to introduce a further form of turbomachinery specific boundary condition available in the code, the Frozen Rotor interface boundary condition. Where the ratio of the pitches of a stage configuration approaches unity, or alternatively where a multiple of the blades in one of the blade rows can be combined with its neighbours in order to allow that ratio to occur, it may be of interest to study the flow in that configuration at a given point in time.

The flow field obtained from such a simulation would correspond to obtaining a snapshot of the dynamic interaction process and hence be roughly equivalent to the situation where the rotor angular motion is frozen. Although the interface accounts internally for pitch change, scaling the flows as they cross the boundary and stretching or contracting the pitchwise profiles of the variables, the Frozen Rotor condition is strictly applicable only to the components of stages whose pitch ratios are very close to unity as accuracy is quickly degraded with pitch variation.

In TASCflow the transient rotor/stator method is an extension of the Frozen Rotor model with the two approaches differing primarily in whether or not the relative grid positions are updated with the sequence of time steps. The implementation procedure of the transient sliding interface condition proceeds as follows:

1. At the start of a particular time step the new relative position of each side of the interface is recalculated.
2. Assembly of a zero thickness sliding interface grid which is distinct from either of the grids on either side of itself. The elemental components of the interface grid are control surfaces and with these are associated control surface nodes, variables and control surface equations.
3. Evaluate the fluxes in and out of the surface by accounting for all control volumes in contact with the particular control surface. The flux discretizations are done through the schemes employed in the other internal flux evaluations

except that at the interface a combination of nodal dependent variables and interface variables are used.

4. Assemble the local equations, one for the control volumes adjoining the interface, where the coefficients are a mixture of control volume and control surface variables, and a second for the control surface with control surface variables.
5. Solve the linear equations to calculate the fluxes.

An application of the unsteady capability of the code is presented in Chapter 5 when the single stage case Rolls-Royce HP9 is studied.

3.5 Solution procedures

3.5.1 The TASCflow solver

The approach employed by the TASCflow code to solve the set of linear and coupled, algebraic equations is based on the combination of two techniques, an iterative relaxation solver and a multigrid accelerator.

The solution approach taken by the code to the coupling of the mass and momentum equations, which occurs in the former though a velocity gradient and in the latter through the gradient of the pressure, is to carry out the solution of these equations simultaneously. The scalar equations, such as those of k and ε, are in turn solved in a segregated way.

The solution progresses through a sequence of time steps or outer loop iterations where after the linear solution, the non-linear problem is advanced, the equations re-discretized and the linear system solved again. It is worth noting here that the term 'time step' is somewhat misleading when applied to a steady-state pressure correction code.

The main computed variables are the Cartesian components of the velocity vector, the pressure and the temperature, and it is from these that the other main solution variables, such as density, are in addition calculated.

3.5.1.1 Relaxation solver set-up

The relaxation scheme employed in the code belongs for purposes of classification to the Lower-Upper factorization family which is itself a part of the implicit schemes division. In the classic LU methods the solution of a linear system,

$$A\,\boldsymbol{x} = \boldsymbol{b} \tag{3-23}$$

is readily solved once A is factored into a product of lower and upper triangular matrices,

$$A = L\,U \tag{3-24}$$

where L is lower triangular and U upper triangular. Combining these two equations one gets,

$$L\,U\,\boldsymbol{x} = \boldsymbol{b} \tag{3-25}$$

and by defining $\boldsymbol{y}$, a new n by 1 matrix, we can write,

$$U\,\boldsymbol{x} = \boldsymbol{y} \tag{3-26}$$

and therefore recast 3.25 as,

$$L\,\boldsymbol{y} = \boldsymbol{b} \tag{3-27}$$

which is then solved for $\boldsymbol{y}$. From this point on we simply have to insert the values of $\boldsymbol{y}$ in equation 3.26.

Although the LU process entails the solution of two systems rather than the original one, the fact that both coefficient matrices L and U are triangular and hence much easier to solve, more than makes up for the apparent additional work. In practice the inversion of triangular matrices is a straightforward procedure and the systems are easily solved by forward and backward sweeping over the integration domain. However for the LU method to work strong diagonal-dominance is required and

therefore schemes which promote such dominance are an essential requisite of the method.

Within an iterative solution method the solution vector x is updated at every recalculation of the system and is thus expressible as,

$$x = x^n + x' \tag{3-28}$$

where x^n is the last approximate result that has been obtained and x' is the correction to be supplied by the current iteration. Replacing 3.30 into 3.25 leads to the form,

$$A\,x' = b - A\,x^n \tag{3-29}$$

where the RHS term represents the residual of the present solution and which we will henceforth denote as R. Making use of this notation and employing the method described above we can arrive at the equivalent form of equation 3-29,

$$L\,y = R \tag{3-30}$$

whose solution,

$$y = L^{-1}\,R \tag{3-31}$$

leads to the correction calculation,

$$x' = U^{-1}\,y \tag{3-32}$$

from where an updating of the solution can be assembled and the process advanced towards convergence or not in function of the magnitude of the calculated residual.

It is worth at this point to qualify further the approach employed by TASCflow within the wide LU methods. The code does not make use of the exact form of the A matrix, if that was to be the case the solution would be achieved after just one iteration, but rather of an approximate form which we will denote as Ã. The assembly of the preconditioning matrix Ã, is done in TASCflow through the incomplete lower-upper (ILU) method, the 'incomplete' part of the name implying the neglect of the fill-in of all the off-diagonal entries within the band.

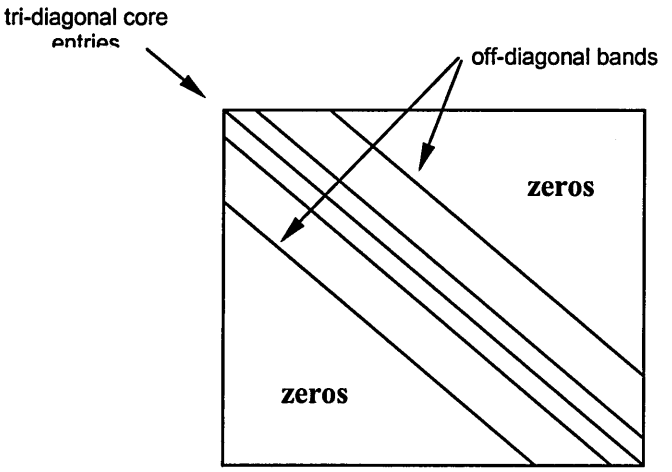

Figure 3-8 Solution matrix arrangement

Given the approximation noted above the decomposition of the matrix $\tilde{A}$ is more exactly expressed as,

$$\tilde{A} = \tilde{L}\,\tilde{U} \tag{3-33}$$

with the observation that when A is tri-diagonal, $\tilde{A}$ reverts to A.

It is well known that the likeness of $\tilde{A}$ and A is strongly dependent on the bandwidth with the narrower bandwidths corresponding to the greater closeness between the two matrices. The issue of the bandwidth management can be illustrated through an example employing a 2D grid elemental molecule and where the subscripts define the neighbouring nodes through the usual cardinal points.

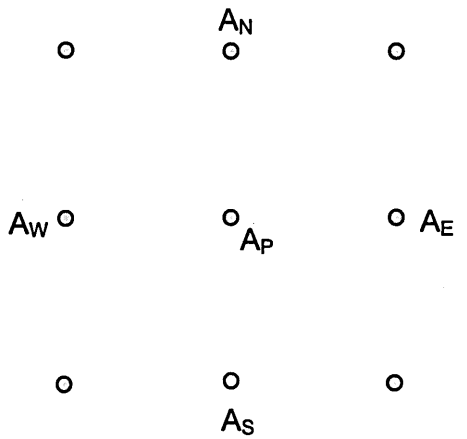

Figure 3-9 Two dimensional grid elemental molecule

The relationship between the inter-nodal connectivity of the molecule and the bandwidth is graphically demonstrated in figure 3.8 from where it will be apparent that limitation of storage requirements act as the main motivation behind bandwidth control. However as is also clear in that figure, bandwidth reduction comes at a price in the form of reduced connectivity and hence the neglect of some of the information contained in the original matrix.

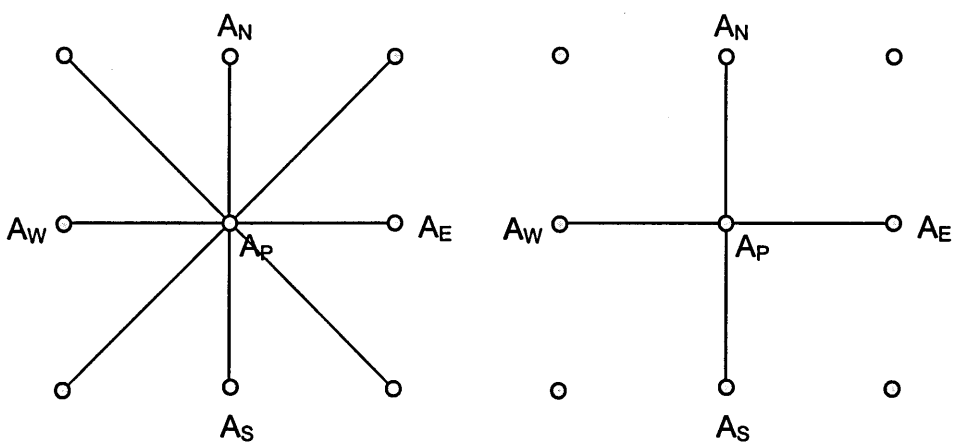

complete bandwidth and connectivity **reduced bandwidth and connectivity**

Figure 3-10 Bandwidth and connectivity relationship in a 2D grid

The information lost in the bandwidth reduction process is mostly in the form of long-wave eigenmodes and to recover this, many iterative solvers employ globalization or acceleration techniques. The main available methods are divisible into three major groups following the methodology adopted previously,

acceleration techniques
- operator based – Tshebishev
- grid based – projection (+1) and multigrid (+n)
- matrix based – algebraic multigrid (AGM)

The approach employed by the code is the matrix based algebraic multigrid method.

3.5.1.2 Multigrid acceleration

The code makes use of a solution acceleration technique denoted as multigrid solution which is an approach designed to reduce the global linear residuals by some factor in between the solution of the non-linear terms.

The rationale underpinning multigrid acceleration is rooted in the observation that iterative solvers tend to reduce errors which are correlated with short grid spacings much faster than they do to those correlated with longer lengths. Typical multigrid processes do therefore employ a succession of ever coarsening grids such that the reduction of errors of all wavelengths can be performed in the grid with the most appropriate spacing.

Unlike in many conventional multigrid techniques, in the TASCflow implementation of the method, which utilizes an algebraic rather than geometric multigrid methodology, no discretization on coarser grids is required and only the initial mesh is employed. The code does assemble coarser grid equations but these are based on the relative values of the equations which are being solved and therefore the coarsening has an anisotropic character. An excellent graphic representation of this concept can be found in Raw, 1996 from where Figure 3-11 has been sourced.

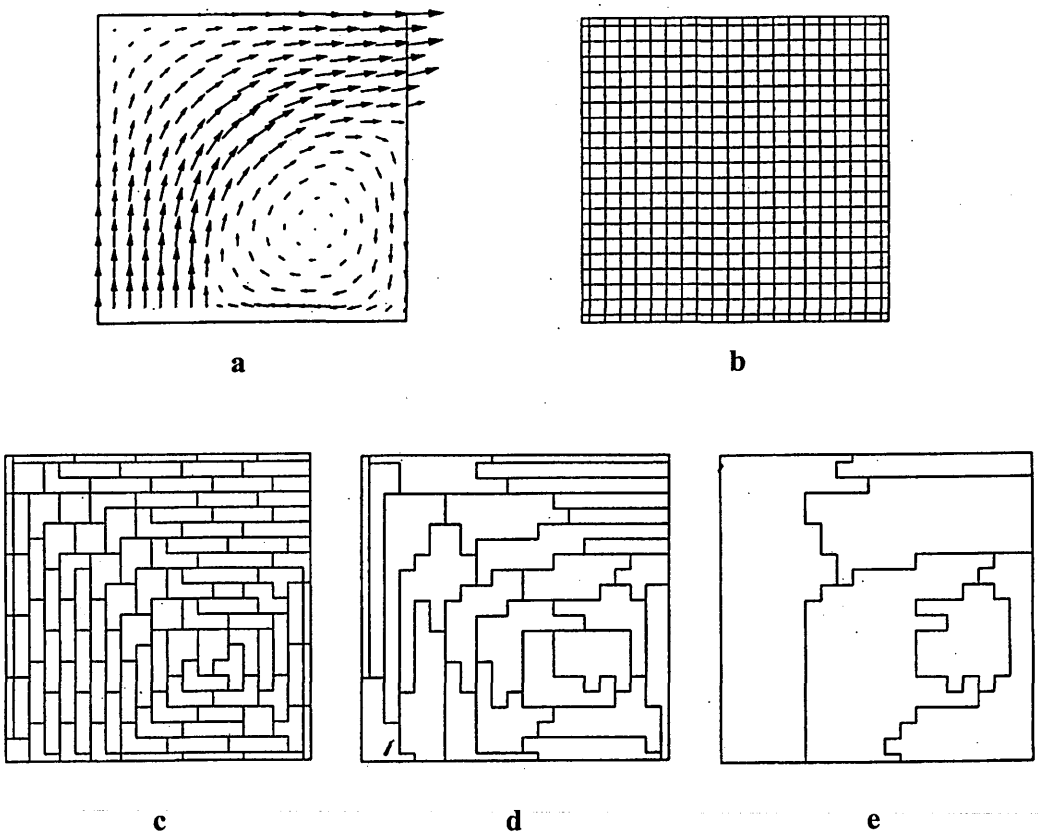

Figure 3-11 Coarsening steps for a fine grid in a recirculating flow, Raw, 1996

Once the coarse grid is assembled the relaxation scheme is applied to it in order to reduce the grid-relative short wavelength errors. The sequential solution of the ever coarsening grids followed by the reversal of that procedure is the simplest form of multigrid cycling, the 'V' cycle, but around this process a number of combinations are possible. Equally a cycle may be fixed, where the coarsening and refining follow a prescribed sequence, or be related to some solution dependent parameters in which case the exact path of the cycling process is not defined a priori.

TASCflow employs by default a 'W' fixed cycle, Figure 3-12, whereby after the initial full coarsening, the refining is done in such a way that any time a new refined level is reached, this is followed by a new complete re-coarsening.

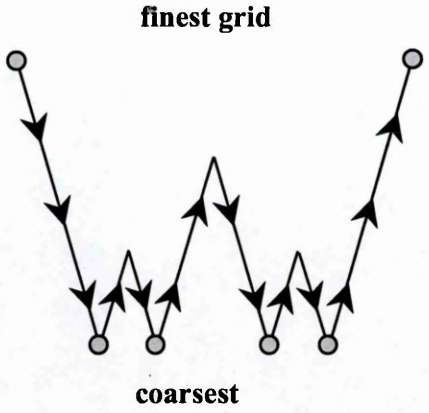

Figure 3-12 Multigrid W fixed cycle

The incentive to employ this particular fixed cycle in the code is associated with the fact that in the 'W' cycle, the exchange of information between finer and coarser grids within a cycle happens twice and this has been proven to lead to a speeding up of the convergence rates. For a source on the algebraic multigrid method employed in TASCflow see Raw, 1996.

Chapter 4

Accounting for unsteady effects in a steady state simulation

4.1 Introduction

The conventional multiblade row simulation approach involves the simultaneous solution of each blade passage in its own frame of reference. This technique assumes that the flow in each of the blade passage is steady and that the flow field unsteadiness which is due to stage aerodynamic interaction effects can be meaningfully represented by the circumferential averaging of the flow variables at the interface planes which separate the different frames of reference.

A number of drawbacks can be ascribed to this method:

- Offers no account of the transient effects and hence of nonlinear aerodynamic phenomena such as vortex shedding and shock-boundary layer interaction and separation.

- Presents the downstream row with inlet conditions that are more uniform both temporally and spatially than those which would be supplied by the locally equivalent time average of the actual flow.

- Introduces an entropy step due to the sudden mixing out of upstream wakes at the interface planes.

These factors contribute to the often-observed discrepancy between averaging-plane steady-state analyses and the time-averaged form of the unsteady simulations. Nonetheless steady multiple frame of reference simulations are an attractive proposition not only on account of the very modest time and computational resources they require, when compared to other competing multistage techniques, but also because conceptually this approach is the easiest to understand and employ.

Furthermore it is not immediately apparent how the results of an unsteady calculation can be exploited in the design process, other than through an averaging manner, given that the turbomachinery conventional development is invariably sourced in a steady state conceptual model. These reasons have prompted the efforts seen in recent years to develop techniques which can combine typical averaging-plane type calculations, with some account of stage interaction unsteady effects.

It is worth noting at this juncture that although as is noted above some differences between steady-state analyses and the time-average of time-dependent simulations are often evident these can in many cases be quite small provided regions of flow separation are small or nonexistent.

The foremost contribution in this field of CFD is indisputably that due to the work of John Adamczyk from NASA Lewis who in a series of papers from 1985 onwards laid out the physical rationale as well as the mathematical formulation of a machine wide averaging procedure which is termed the average passage equation.

The chapter begins with the presentation of the features of the TASCflow 'software port', the source code interface (SCI), which enables the integration of the two deterministic stress models with the TASCflow mixing plane formulation. The chapter then goes on to describe the derivation of Adamczyk's method and introduce some of the derivative formulations which are closely related to it. Next the two semi-empirical models, which have been selected to be evaluated in the present study, are introduced and finally the implementation strategies developed to incorporate them within the code are discussed.

4.2 TASCflow source code interface

The solver part of TASCflow, labeled TASCflow3D, consists of a set of Fortran and C routines most of which are not included in the program as source code pieces but rather as compiled executable components. In order to enable the user to incorporate into the standard executable, modifications that allow for a dedicated application of the code on the solution of specific problems, TASCflow contains a software port designated as the Source Code Interface (SCI).

The SCI is composed of a set of Fortran 'stub' routines which are available for modification by the user in order to either generate source terms for the transport equations, create boundary conditions, define fluid properties or create further specialized post-processing fields. The stub routines provide the framework for the development of custom coding and eventually for the assembly of associated executables which will be appended to the main code executable options.

The two deterministic stress models presented above are incorporated in the CFD solution as source terms of the momentum and energy equations and therefore this section starts with a glance at the theoretical foundation of generation of these terms within the TASCflow approach.

4.2.1 Theoretical background

The stereotypical conservation equation for a generic variable ϕ can be written as,

$$\frac{\partial(\rho\phi)}{\partial t} + \frac{\partial(\rho u_j\phi)}{\partial x_j} = \frac{\partial}{\partial x_j}\left(\Gamma\frac{\partial\phi}{\partial x_j}\right) + S \qquad (4\text{-}1)$$

where Γ is the diffusion coefficient and S is a volumetric source term, all other symbols taken their accepted significance. The discrete form of this equation is in turn,

$$A_P \phi_P + \sum A_{nb} \phi_{nb} + S \delta V = 0 \tag{4-2}$$

and here the subscript P denotes that the value of the generic variable is that of a given node P while nb designates the corresponding values at the neighbouring nodes. The finite volume coefficients A contain the contributions of the temporal, convective and diffusive terms of equation 4.1, with the central coefficient A_P being given by,

$$A_P = -\sum A_{nb} . \tag{4-3}$$

The source term S quite likely will characterize some function of the dependent variable at point P which is then designated as ϕ_P . Often when operating the code with added source terms it is a requirement in order to secure a well-behaved convergence to perform a linearization of the source term along the lines of,

$$S = B_{src} + A_{src} \phi_P \tag{4-4}$$

the symbols B_{src} and A_{src} representing respectively the constant component of the source and the coefficient of the linearly varying element of the source. One can now rewrite equation 4.2 in terms of ϕ_P while making use of the relationships established in 4.3 and 4.4 as,

$$\phi_P = \frac{\sum A_{nb} \phi_{nb} + B_{src} \delta V}{\sum A_{nb} - A_{src} \delta V} . \tag{4-5}$$

This equation is nearly identical to the one employed in the code to compute the dependent variables, the missing feature being the decomposition of the current value of the generic variable ϕ in terms of the value which was calculated at the previous iteration, ϕ^o, and amount of the correction of the present, ϕ',

$$\phi = \phi^o + \phi' . \tag{4-6}$$

When such decomposition is applied to equation 4.2 this can be written as,

$$A_P (\phi_P^o + \phi_P') + \sum_{nb} A_{nb} (\phi_P^o + \phi_P') = - A_{src} (\phi_P^o + \phi_P') \delta V - B_{src} \delta V \tag{4-7}$$

from whence one obtains,

$$(A_P + A_{src} \delta V) \phi_P' + \sum_{nb} A_{nb} \phi_{nb}' = - A_P \phi_P^o - \sum_{nb} A_{nb} \phi_{nb}^o - A_{src} \delta V \phi_P^o - B_{src} \delta V \tag{4-8}$$

the RHS of which is the residual we will call R. As the iterative solution progresses the value of R will tend towards zero.

The rearrangement of 4.8 leads to the form which is similar to equation 4.5 albeit expressed in a residual manner,

$$\phi_P = \frac{\sum A_{nb}\phi'_{nb} - R}{\sum A_{nb} - A_{src}\,\delta V} \tag{4-9}$$

this being the equation employed by TASCflow to solve for every dependent variables.

4.2.2 General source term implementation

The computation and application of user defined source terms make use of the Fortran USRSRC routine from the TASCflow SCI library of stub routines.

As the solver loops over the complete set of equations that it will solve for a given iteration it will come across each one of the three momentum equations, U, V and W, the energy equation or even user defined transport equations. When an USRSRC based executable is in existence and the main code initiates the solution of any of the transport equations alluded to above, the call statement

```
CALL USRSRC (LABEL , ...
```

is performed and the character string LABEL, which contains the name of the equation variable to which the individual source terms are to be added, is tested against the identity of the equation being solved.

Within the USRSRC routine a number of utility sub-routines are available to perform particular functions such as defining parameters and adding sources and active coefficients to the transport equations. A description of the function of the utility sub-routines which were employed in the present work is presented in Table 4-1, underneath.

name	function
GETPNT	sets a pointer within temporary workspace
GETRAR	gets a real array
PUTSRC	puts an array into a source term

Table 4-1 USRSRC sub-routine functions

The source terms are applied in TASCflow to volumetric computational regions and these are accessible to the SCI through a problem global indexing which is relevant to the solution matrix block rather than the computational domains that stemmed form the grid generation process. It is therefore crucial that the user be aware of the transformations operated on the original grids by the assembly procedure of the solution matrix block with information on those transformations being available either within the boundary conditions file or through the use of one of the SCI specialist sub-routines, GETGBL.

We shall make use of one of the test cases employed in this study, the single stage Rolls-Royce HP9 high-speed compressor, to illustrate the grid transformation procedure as well as the problems this raises for the transfer of information to and from the USRSRC routine.

One of the grids employed in the HP9 study was composed of three blocks, a larger one accounting for the rotor blade passage and two equal sized smaller ones corresponding to two of the stator blades. The stator grids were scaled to present, when assembled together side-by-side, the same pitch displacement as that of the rotor blade. A general layout of the grid domains is shown in Figure 4-1.

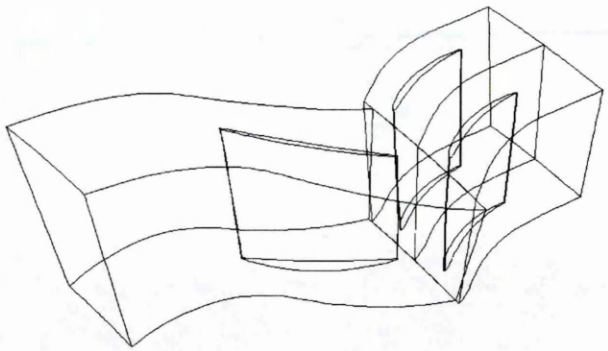

Figure 4-1 HP9 grid domain with a rotor and two stators

The individual grid dimensions in nodal units along the *i*, *j*, *k* coordinate system were, rotor, 26 x 33 x 62 and 26 x 21 x 57 for each of the two identical stator grids. For the purpose of solution the three grids were combined in a single matrix block of dimensions, 42 x 105 x 91.

Figure 4-2 provides a graphic representation of the individual grid blocks prior to their assembly into a solution block while in Figure 4-3 the grids are shown when as part of that overall block.

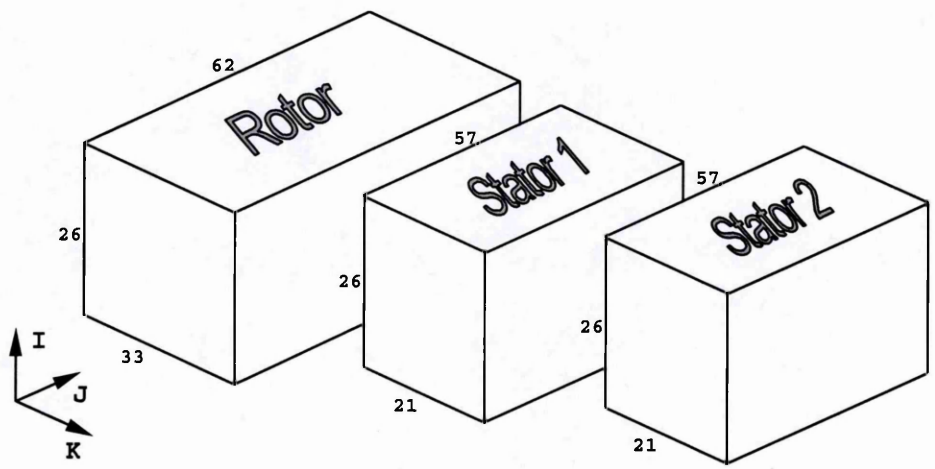

Figure 4-2 HP9 Individual grid blocks prior to the assembly of the solution matrix

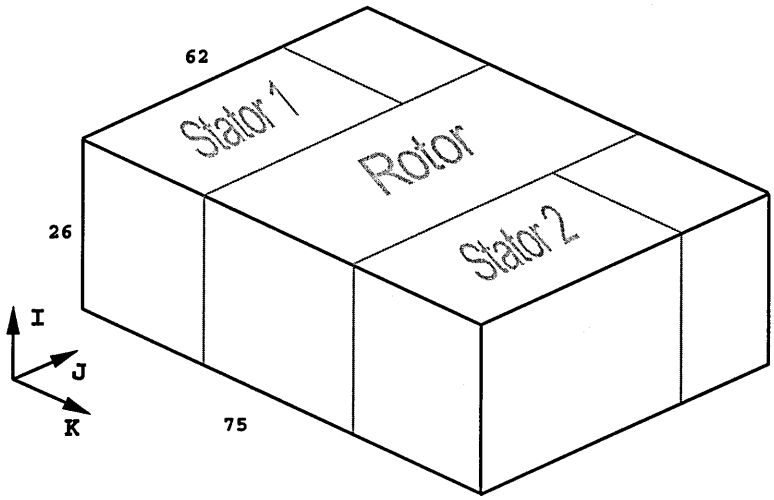

Figure 4-3 Global solution matrix block for HP9 case

The function of the two extra blocks of nodes which are placed behind the two stators and are visible in the figure above is simply to help complete the master block

An excerpt of the section of the boundary conditions file (BCF) which contains the information relating to transformations operated on the local grids is presented underneath. By default TASCflow will denote the initial grid to be loaded into the TASCbob3D pre-processor program as MAIN with for the present case that denomination will correspond to the STATOR1 grid defined previously.

In each of three records the first of the columns defines the local coordinates of the particular grid while the entries for the second column must be added to the those of the first to locate the limits of the local grid within the global coordinates and therefore account for any translations. Finally the information on any rotation action is presented in the form of a transformation matrix for each of the grids.

```
1 MAIN
26      0      1      0      0
21      0      0      1      0
57      0      0      0      1

2 STAT2
26      0      1      0      0
21     54      0      1      0
57      0      0      0      1

3 ROTOR
26      0      1      0      0
33     21      0      1      0
62      0      0      0      1
```

4.3 Adamczyk's average-passage equation system

A rigorous mathematical description of the steady-state flowfield of multistage turbomachinery has been provided by Average-Passage system of equations devised by J. Adamczyk in 1985. Adamczyk's approach is founded on the systematic filtering of the sources of unsteadiness which are known to occur in the flows through multiblade row turbomachines. The three sources of unsteadiness which are formally addressed by the Average-Passage averaging procedures are turbulence in the flow, correlated in the model with ensemble-averaging, the unsteady deterministic or recurring events due to blade interaction, which are correlated with time-averaging and the random unsteady effects due to multiblade row blade count dissimilarity, accounted for through a passage-averaging formulation. Whilst a condensed derivation of the Average Passage equation system is presented underneath the reader is guided to the work of Lockwood, 1999, for a fuller account of the process.

4.3.1 Average Passage equation derivation

We shall, in the interest of practicality, make use in the derivation of the Average Passage model, of the continuity equation and follow in Adamczyk's steps by employing throughout a cylindrical coordinates formulation.

The continuity equation when cast in a cylindrical coordinate frame is written as,

$$\frac{\partial \rho}{\partial t}+\frac{\partial (\rho V_r)}{\partial r}+\frac{1}{r}\frac{\partial (\rho V_\theta)}{\partial \theta}+\frac{\partial (\rho V_z)}{\partial z}=0. \tag{4-10}$$

Ensemble-averaging: the first step in this approach requires the decomposition of the instantaneous flow field variables, here exemplified by the velocity vector V, into a deterministic component $\widetilde{V}$ and a stochastic turbulent variation V',

$$V=\widetilde{V}+V' \tag{4-11}$$

This decomposition of the velocity can be schematically represented thus,

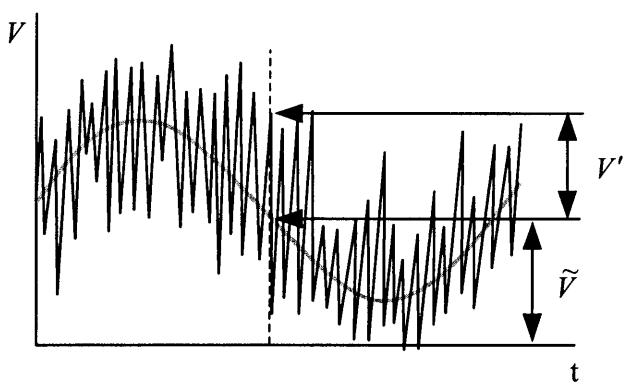

Figure 4-4 Instantaneous turbulent velocity decomposition

Mathematically the deterministic component, $\widetilde{V}$, is obtained through the application of a density-weighted ensemble (Favre) averaging procedure,

$$\widetilde{V}=\lim_{N\to\infty}\frac{1}{\overline{\rho}\,N}\sum_{n=1}^{N}\rho_n V_n. \tag{4-12}$$

Replacing the decomposed form of Equation (4-2) into (4-1) yields,

$$\frac{\partial \rho}{\partial t}+\frac{\partial\left(\rho \tilde{V}_r+\rho V_r'\right)}{\partial r}+\frac{1}{r}\frac{\partial\left(\rho \tilde{V}_\theta+\rho V_\theta'\right)}{\partial \theta}+\frac{\partial\left(\rho \tilde{V}_z+\rho V_z'\right)}{\partial z}=0 \quad (4\text{-}13)$$

which is subsequently ensemble averaged as a whole and from which, by making use of equivalences such as $\overline{(V_i+V_j)}=\overline{V}_i+\overline{V}_j$, $\overline{\frac{\partial V}{\partial x}}=\frac{\partial \overline{V}}{\partial x}$, $\overline{\rho V}=\overline{\rho}\,\tilde{V}$, $\overline{\rho V}=\overline{\rho \tilde{V}}+\overline{\rho V'}$ and $\overline{\rho V'}=0$, will lead to the Reynolds averaged form of the continuity equation,

$$\frac{\partial \overline{\rho}}{\partial t}+\frac{\partial\left(\overline{\rho}\tilde{V}_r\right)}{\partial r}+\frac{1}{r}\frac{\partial\left(\overline{\rho}\tilde{V}_\theta\right)}{\partial \theta}+\frac{\partial\left(\overline{\rho}\tilde{V}_z\right)}{\partial z}=0\,. \quad (4\text{-}14)$$

The effects of the filtered-out random unsteadiness are accounted for in the resulting equations by the Reynolds stress terms which, for the momentum equations, have the form $\overline{\rho\, V_i'\, V_j'}$.

Time-averaging: in order to sift the unsteady component, one further averaging procedure is required and to this end $\tilde{V}_i$ the unsteady deterministic velocity is in turn decomposed as,

$$\tilde{V}_i=\tilde{\overline{V}}_i+\hat{\tilde{V}}_i \quad (4\text{-}15)$$

where $\tilde{\overline{V}}_i$ is the constant mean value calculated from,

$$\tilde{\overline{V}}=\frac{1}{T\,\tilde{\overline{\rho}}}\int^{+T}\overline{\rho}\,\tilde{V}\,dt \quad (4\text{-}16)$$

and $\hat{\tilde{V}}_i$, the unsteady deterministic fluctuation, T being the time interval of a shaft rotation. This decomposition can in turn be expressed in a graphic form thus,

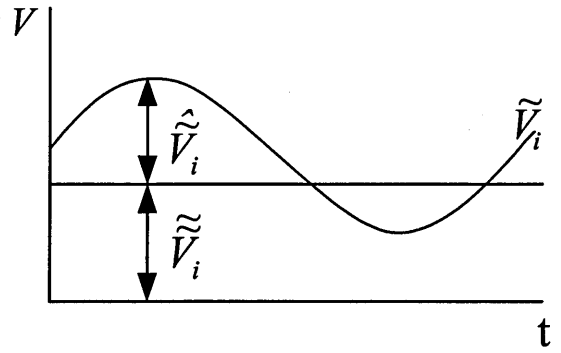

Figure 4-5 Instantaneous unsteady velocity decomposition

and by substituting the decomposed expression of Equation 4.6 into 4.5 one obtains,

$$\frac{\partial \bar{\rho}}{\partial t}+\frac{\partial\left(\bar{\rho}\tilde{\tilde{V}}_r+\bar{\rho}\hat{\tilde{V}}_r\right)}{\partial r}+\frac{1}{r}\frac{\partial\left(\bar{\rho}\tilde{\tilde{V}}_\theta+\bar{\rho}\hat{\tilde{V}}_\theta\right)}{\partial \theta}+\frac{\partial\left(\bar{\rho}\tilde{\tilde{V}}_z+\bar{\rho}\hat{\tilde{V}}_z\right)}{\partial z}=0 \qquad (4\text{-}17)$$

The time-averaging operation is now carried out by employing the operator,

$$\bar{\bar{V}}=\frac{1}{T\lambda}\int_t^{t+T} H\,\bar{V}\,dt \qquad (4\text{-}18)$$

where λ, the blockage factor which accounts for the effects due to the presence of the blade is calculated as,

$$\lambda=1-\frac{(\theta_x-\theta_n)N}{2\pi}, \qquad (4\text{-}19)$$

and H stands for a gate function taking 1 or 0 values, depending on whether the variable location is situated within the fluid flow region or the metal blade volume respectively.

The outcome of the time-averaging operation on equation 4.8, taking into account the cross correlations mentioned previously in connection with the ensemble averaging process, can be presented as,

$$\frac{\partial \bar{\bar{\lambda\rho}}}{\partial t}+\frac{\partial\left(\bar{\bar{\lambda\rho}}\tilde{\tilde{V}}_r\right)}{\partial r}+\frac{1}{r}\frac{\partial\left(\bar{\bar{\lambda\rho}}\tilde{\tilde{V}}_\theta\right)}{\partial \theta}+\frac{\partial\left(\bar{\bar{\lambda\rho}}\tilde{\tilde{V}}_z\right)}{\partial z}=0 \qquad (4\text{-}20)$$

Passage-averaging: the flow field described by the application of the two averaging processes described above is only truly steady-state if applied to a single stage machine or else to a multistage machine whose blade counts are identical across the blade rows. However a situation where the blade counts are identical is never countenanced in turbomachinery design, due to the obvious propensity for harmonic excitation of such an arrangement. For that reason one further form of aperiodic unsteadiness, arising from the complex machine-wide blade row interactions, needs to be taken into account before an accurate steady-state flow description of the flow, valid for each and every blade passage of the turbomachine is reached.

The form of the variable decomposition which underpins this final averaging procedure is,

$$\tilde{\tilde{V}} = \tilde{\tilde{\bar{V}}} + \hat{\tilde{V}} \tag{4-21}$$

which once replaced in equation 4-11, and by including the effects of a further number of operators, leads to the assembly of the average passage form of the continuity equation,

$$\frac{\partial \bar{\bar{\lambda}}\bar{\bar{\rho}}}{\partial t} + \frac{\partial\left(\bar{\bar{\lambda}}\bar{\bar{\rho}}\tilde{\tilde{V}}_r\right)}{\partial r} + \frac{1}{r}\frac{\partial\left(\bar{\bar{\lambda}}\bar{\bar{\rho}}\tilde{\tilde{V}}_\theta\right)}{\partial \theta} + \frac{\partial\left(\bar{\bar{\lambda}}\bar{\bar{\rho}}\tilde{\tilde{V}}_z\right)}{\partial z} = 0 \tag{4-22}$$

4.3.1.1 Average-passage equation closure issues

Having made use of the continuity equation to highlight the generic average-passage derivation process we shall hereafter make use of one of the momentum equations to consider some of the closure issues raised by the introduction of terms brought about by the three sequential averaging operations.

The average passage form of the tangential momentum equation is written as,

$$\frac{\partial\left(\lambda_i \rho \overline{\overline{\tilde{V}}}_\theta\right)}{\partial t_1}+\frac{\partial\left(\lambda_i \rho \overline{\overline{\tilde{V}}}_r \overline{\overline{\tilde{V}}}_\theta\right)}{\partial r}+\frac{1}{r}\frac{\partial\left(\lambda_i \rho \overline{\overline{\tilde{V}}}_\theta \overline{\overline{\tilde{V}}}_\theta\right)}{\partial \theta}+\frac{\partial\left(\lambda_i \rho \overline{\overline{\tilde{V}}}_z \overline{\overline{\tilde{V}}}_\theta\right)}{\partial z}+\frac{1}{r}\left(\lambda_i \rho \overline{\overline{\tilde{V}}}_r \overline{\overline{\tilde{V}}}_\theta\right)=$$

$$\frac{\partial \lambda_i\left(\overline{\overline{\tau}}_{r\theta}-\overline{\overline{\rho V_r' V_\theta'}}-\overline{\overline{\rho \hat{\tilde{V}}_r \hat{\tilde{V}}_\theta}}-\overline{\overline{\rho \tilde{\tilde{V}}_r \tilde{\tilde{V}}_\theta}}\right)}{\partial r}+\frac{1}{r}\frac{\partial \lambda_i\left(\overline{\overline{\tau}}_{\theta\theta}-\overline{\overline{\rho V_\theta' V_\theta'}}-\overline{\overline{\rho \hat{\tilde{V}}_\theta \hat{\tilde{V}}_\theta}}-\overline{\overline{\rho \tilde{\tilde{V}}_\theta \tilde{\tilde{V}}_\theta}}\right)}{\partial \theta}$$

$$+\frac{\partial \lambda_i\left(\overline{\overline{\tau}}_{z\theta}-\overline{\overline{\rho V_z' V_\theta'}}-\overline{\overline{\rho \hat{\tilde{V}}_z \hat{\tilde{V}}_\theta}}-\overline{\overline{\rho \tilde{\tilde{V}}_z \tilde{\tilde{V}}_\theta}}\right)}{\partial z}+\frac{\lambda_i}{r}\left(\overline{\overline{\tau}}_{r\theta}-\overline{\overline{\rho V_r' V_\theta'}}-\overline{\overline{\rho \hat{\tilde{V}}_r \hat{\tilde{V}}_\theta}}-\overline{\overline{\rho \tilde{\tilde{V}}_r \tilde{\tilde{V}}_\theta}}\right)$$

$$-\frac{1}{r}\frac{\partial \lambda_j \overline{\overline{p}}}{\partial \theta}+F_{IN}^{(\theta R)}+F_V^{(\theta R)}+F_{IN}^{(\theta S)}+F_V^{(\theta S)}$$

(4-23)

and it can be seen that the terms which correspond to each of the averaging procedure are not only clearly identifiable but are also essentially analogous to the Reynolds stresses which, as was seen in Chapter 2, represented in the steady-state form of the Navier-Stokes equations the effects of the filtered-out turbulent action.

Specifically in equation 4-23 one can identify the Reynolds stresses terms, of the form $\overline{\overline{\rho V_i' V_j'}}$, albeit cast in an uncharacteristic form due to the two further time-averaging operations, and two average-passage characteristic terms, deterministic stresses corresponding to the form, $\overline{\overline{\rho \hat{\tilde{V}}_i \hat{\tilde{V}}_j}}$ and passage-average aperiodic correlations, $\overline{\overline{\rho \tilde{\tilde{V}}_i \tilde{\tilde{V}}_j}}$.

The methods to achieve closure of the average-passage equations such as 4-23 are outside the scope of this work but it will suffice to say that this closure can either involve the modelling of all the terms in the equations, though perhaps neglecting those terms whose influence is judged to be secondary, or to group together the effects of all the individual terms and only assess their lumped equivalent effect.

In this work were we focus on obtaining an account of first-order unsteady cyclic effects from within a steady-state formulation, no further consideration will be given

to either the Reynolds stresses, already accounted for through the turbulence models available in the code, or the passage-average aperiodic correlations whose calculations depend on overlapped grid models incompatible with the mixing-plane blade row interface found in TASCflow.

The object of our interest are therefore the terms in these equations which account for the effects of the deterministic unsteadiness on the averaged flowfield and which are, discounting the final average-passage averaging procedure, $\overline{\overline{\rho}\hat{\tilde{V}}_i\hat{\tilde{V}}_j}$ for the momentum equations and $\overline{\overline{\rho}\hat{\tilde{H}}\hat{\tilde{V}}_j}$ for the energy equation.

Physically these terms result from the transport of momentum by the periodic deterministic features of the flow field such as blade wakes, leakage and shed vortices and secondary flows. Insofar as deterministic stresses represent fluctuating flow quantities they are analogous to the turbulent stresses but the time scale of the deterministic motion is of course much larger than that of the random turbulent motion correlating as it does with blade passing and shaft rotation speeds.

For closely coupled compressor configurations the deterministic stress terms contribute as much to the flow physics of the machine as do the effects of turbulence in viscous layers as well as in the free stream, Adamczyk, 1992. A number of researchers have produced numerical and experimental studies which seek to assess the magnitude and location and hence and more importantly, given the form of the Navier-Stokes equations, of the gradients of the deterministic stresses correlations through multiblade row configurations.

Suryavamshi *et al*, 1998, obtained experimental data of the unsteady velocity and total temperature downstream of an embedded stator which showed that the deterministic periodic normal and shear stresses were most significant in the stator wakes away from the endwall regions. Of the stress correlations the dominant terms were found to be those due to the tangential gradients with a prominence to the shear stress correlation between the axial and tangential velocity components. For rotor flows the experimental results of Adamczyk, 1992, suggested that all six components of stress

were largest near the end walls, those at the hub proceeding from a corner stall while at the casing the source was the tip clearance flow. Moreover away from walls the stress components were seen to be almost independent of span.

4.3.2 Simplified modelling of the deterministic stress terms

The rationale that underpins the use of deterministic stress models within mixing-plane type steady-state computations is described by Dawes and Denton, 1998, with reference to an imaginary situation involving a two-dimensional idealized description of the flow across the mixing-plane of a multiblade row turbomachine.

In the blade-to-blade 2D situation of Figure 4-6, an upstream wake is subject to a uniformly mixing operation at it crosses the dashed line which denotes the location of a mixing-plane.

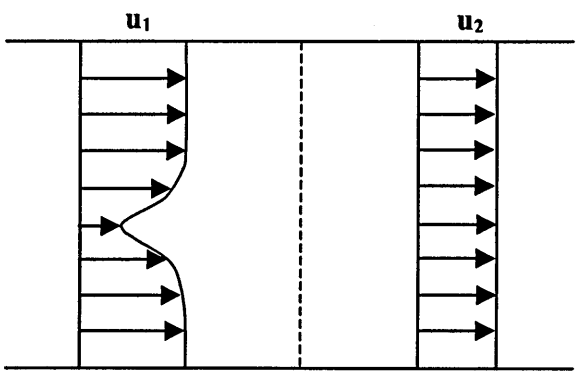

Figure 4-6 Two-dimensional mixing problem

This procedure corresponds to performing a conventional mixing approach for a constant area which for incompressible flow can be written for continuity as,

$$\int \rho u_1 \, d\theta = \rho \tilde{u}_2 \tag{4-24}$$

and for momentum as

$$\int \left(\rho u_1^2 + p_1\right) d\theta = \rho \tilde{u}_2^2 + \tilde{p}_2 \tag{4-25}$$

based on the simplifying assumption that pitch is unity and where the tilde denotes a mixed-out average.

If one now defines for example an area-averaged upstream pressure,

$$\overline{p}_1 = \int p_1 \, d\theta \tag{4-26}$$

the pressure at station 2 can be calculated from reference to equations 4-24 and 4-25 as,

$$\widetilde{p}_2 = \overline{p}_1 + \int \rho u_1^2 \, d\theta - \rho \left(\int u_1 \, d\theta \right)^2, \tag{4-27}$$

and it follows that if there is a sizable difference between the second term of the RHS of 4-27, the 'square mean' of the velocity and the third term, the 'mean square', there will be a jump in static pressure across the mixing-plane and to this jump will therefore be associated with a certain degree of false blockage introduced by the averaging process as well as some variation in the flow direction.

When a method which employs deterministic stresses is used, the continuity and momentum equations are rewritten respectively as,

$$\int \rho u_1 \, d\theta = \rho \overline{u}_2 \tag{4-28}$$

and

$$\int \left(\rho u_1^2 + p_1 \right) d\theta = \rho \overline{u}_2^2 + \overline{p}_2 + S \tag{4-29}$$

so that unlike previously, where only the velocities were area averaged, $\overline{u}_2 = \overline{u}_1$, now the pressure too is also area-averaged or $\overline{p}_2 = \overline{p}_1$.

The S term which is responsible for the non-introduction of false blockage by the method is the deterministic stress term is given by,

$$S = \int \rho u_1^2 \, d\theta - \rho \left(\int u_1 \, d\theta \right)^2 \tag{4-30}$$

For a CFD practitioner the question raised by the identification of the deterministic stress terms, as holders of blockage information, is the determination of the appropriate level of complexity which is required for the evaluation of their decay. Whether this evaluation justifies the added complexity of the implementation of a full

average-passage formulation, dependant on the solution of multiple grids with their added computational costs, which is not the approach favoured by these two authors, or whether a cruder model suffices as they suggest.

In the present work, the latter of these approaches is adopted and the remainder of the present chapter is occupied with the description of two such models as well as the facilities present in the TASCflow code for their implementation.

4.4 Hall's deterministic stress model

The deterministic stress model developed by Hall, 1997, employs an algebraic method to add some of the terms of Adamczy's Average-Passage equation method to a standard mixing-plane formulation in order to offer, within steady-state multi blade row simulations, some account of the unsteady stage interaction effects. The model combines some elements of the theoretical framework of Adamczyk's method with the analysis of a multistage compressor flow physics, obtained from data acquired from steady state and time dependent numerical simulations as well as from experimental work.

4.4.1 Physical background

The key machine which is used to provide the physical insight on which Hall's model is based is the much reported Pennsylvania State University Research Compressor. The key aerodynamic characteristics of this compressor are:

- 3 ½ stages
- Hub-tip ratio (average) – 0.843
- Blade loading (average) – 0.438
- Flow coefficient (average) – 0.509
- Mach number at the tip - about 0.5
- Pressure ratio - 1.35
- Peak efficiency – 90.7 %
- Mass flow - 8.61 kg/s at 5400 rpm

The Penn State research compressor is in terms of both blade loading and rotational speed, roughly similar to the equivalent embedded portion of contemporaneous high-speed gas turbine compressors. The experimental data was obtained from area traverses of 1 ½ passages downstream of stator 2, rotor 3 and stator 3 through the use of five-hole and aspirating probes, slanted single sensor slanted hot wires and thermocouple probes.

The numerical simulations made use of the time-marching finite-volume APDAC code, Hall and Delaney, 1995, which can be used for either steady-state or time-accurate calculations. The code employs a Baldwin-Lomax turbulence model with wall functions and a mixing-plane approach for solving multi blade row turbomachinery cases.

The mixing plane formulation which was employed in Hall's work is based on the simple averaging of the conserved variables, ρ, ρu ,ρv ,ρw and ρE, a method which that author found to be numerically robust, to conserve mass and momentum and to help preserve velocity triangle information across the interface more accurately than other approaches. The downside of the scheme nevertheless was that both total pressure and temperature were found not to be conserved but since the discrepancies were very small this was thought acceptable in view of the other features of this particular implementation.

The computational research schedule involved the investigation of three levels of grid density, about 500 000, 2 000 000 and 3 500 000 nodes over the seven blade domains, in connection with the steady-state simulations. The time-accurate computations were carried out on the Stator2/Rotor3/Stator3 combination and for simplicity the blade count was made uniform so as to enforce pitchwise similarity. The grid used for the unsteady work contained 1 500 000 nodes and the solution involved 100 time steps per blade passing period and the calculation of some 20 blade cycles.

The analysis of the experimental and computational data enabled Hall to advance the following main propositions:

1. In the inter-blade row region the stator-relative fluctuating velocity field, as obtained from the axial and circumferential time-histories, is closely approximated by the time-average of the rotor wake profile.

2. The cyclic potential stage interactions of adjacent blade rows induce the periodic displacement of structured flow features such as boundary layers and more particularly wakes. This is the mechanism that leads to the thickening of wakes on the time-average depiction of unsteady stage flows both experimental and numerical. These periodic velocity fluctuations are responsible for the deterministic stresses encountered in the immediate wake region.

3. The time-average of experimentally acquired measurements of total pressure and hence of velocity, obtained in a common frame of reference immediately upstream and downstream of a relatively rotating blade row, show that the some of the circumferential non-uniformity of the wake is present across the relatively rotating row.

This model's central premise is therefore that the upstream row wake provides an approximation to the characterization of the time histories of the unsteady flow accountable for the deterministic stresses, and that this wake somehow survives the relatively rotating row to display a steady axial decay between the two experimental stations. This Hall termed an 'apparent wake'.

The experimental investigation of the phenomenon of stator wake decay in the presence of a rotor interaction was reported by Poensgen and Gallus, 1990, in a study in which two rows of cascades were employed between which a rotor could be made to spin, Figure 4-7.

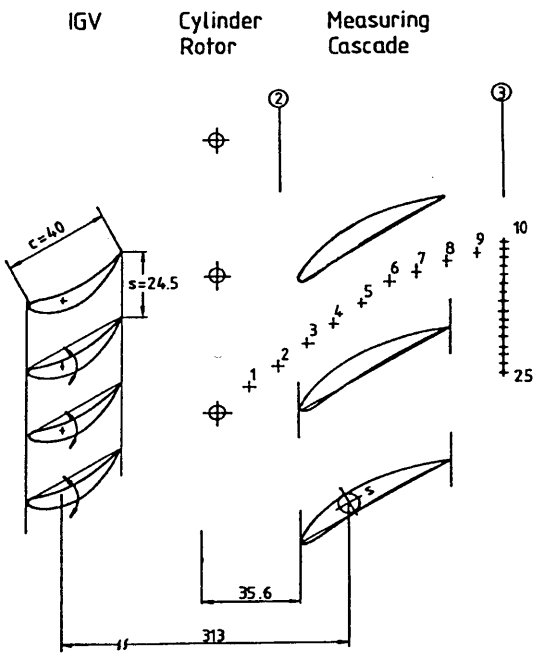

Figure 4-7 Cascade geometry at mid-span and locations of measurement points

These authors presented results where the effects of the presence of the rotor were compared to the situation where no rotor was employed and their conclusions pointed to a significant increase in the rate of decay of the upstream cascade wake for the case when the rotor was present and moreover that this decay was seen to be essentially unaltered by the variation of the blade loading characteristics. The data acquired in this work enabled Hall to modify an existing algebraic wake decay model to account for the increased decay characteristics brought about by the presence of a downstream relatively rotating row.

4.4.2 Theoretical background

The rationale behind the employment of wake models to obtain the deterministic fluctuating quantities that make up the stress correlations described above in sections 4.3.1 and 4.3.2, can be illustrated by recalling the schematic form of the decomposition of the coherent unsteady velocity presented before, Figure 4-5.

When one considers $\hat{\tilde{V}}_i$, the instantaneous deviation of the deterministic fluctuating quantity $\tilde{V}_i$ from the corresponding time-average $\tilde{\bar{V}}_i$, it can be seen that to the spatial

average of $\tilde{V}_i$ in a given frame of reference corresponds a similar value of a temporal average in a neighbouring relatively rotating frame of reference.

As an alternative way to look at this transformation, one can imagine that to an observer fixed to the relatively rotating blade row, the time-averaged wake profile due to an upstream aerofoil will appear as a time-dependent perturbation caused by the relative motion of that same upstream aerofoil. This approach is equivalent to applying the transformation $t = \frac{\theta}{\Omega}$ where t represents the temporal, θ the angular variations and Ω the machine rotational velocity. The schematic representation of this transformation when applied to a rotor/stator combination can be presented as follows:

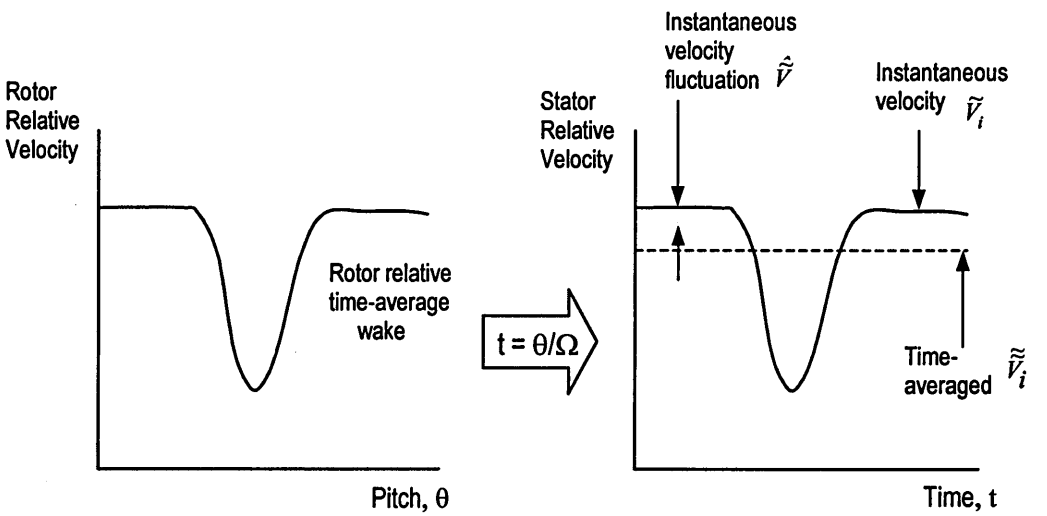

Figure 4-8 Space-relative to time-relative frame transformation

It should be noted however that the area average of the wake profile is not equal to the time average of the actual temporal disturbance experienced by the neighbouring relatively rotating blade row. It is a well known fact that the wake profiles computed by steady simulations are somewhat narrower than the corresponding time average of both experimental and unsteady wake data. This difference stems from the lack of account of the unsteady phenomena caused by the stage interaction, namely the cyclic potential interaction effect on the flow field of an upstream blade inducing a varying,

circulation, boundary layers growth transition location and intensity, and location of vortex shedding.

In this environment it is not difficult to see why the wake defining parameters will experience a periodic displacement whose temporal average will differ from the static situation experienced by a blade row for which the boundary conditions are time-steady. A corollary of this situation in terms of the deterministic stresses is that when analyzing time-accurate data, the smearing of the wakes or other distinct flow structures due to transient effects denote the location of these stresses. It naturally follows that the larger this spread, the more intense the stage interaction and consequently the magnitude of the deterministic stresses.

There has been over a large number of years a steady production of empirical models characterizing the viscous wakes shed by compressor blading in terms of wake width and velocity defect as a function of downstream distance, these models falling largely into either algebraic or exponential formats. Representative of the former type is the linear rational model of Majjigi and Gliebe, 1984, whose general form is given by,

$$y = \frac{a\,x + b}{c\,x + d}. \tag{4-31}$$

Unlike the wake models presented by previous authors, namely those of Reynolds and Lakshminarayana, 1979, and Ravindranath and Lakshminarayana, 1980, which differentiate between the near and far wake regions, in Majjigi's formulation only one expression is needed to correlate over the entire region of interest.

Majjigi and Gliebe's model which assumes the wake to be symmetric, defines the semiwake width in terms of the parameter δ which corresponds to the width of the wake at the location where the velocity defect is equal to one-half of the wake centerline velocity defect, Figure 4-9. For high solidity blading this correlation is written as,

$$\frac{\delta}{S} = \frac{a\left(\frac{s}{c}\right)C_D^{\frac{1}{8}} + b}{c\left(\frac{s}{c}\right)C_D^{\frac{1}{8}} + d} \tag{4-32}$$

where $\frac{s}{c}$ and C_D represent respectively, the streamwise distance downstream of the blade trailing edge normalized by the rotor chord and the drag coefficient respectively and S is the blade to blade spacing. The constants a through d are experimentally determined.

The second model is based on the observed fact that wake decay experimental data is best fitted by some form of exponential function. Exemplar of this sort of correlation is that found in Stauter *et al.*, 1991, which takes the form,

$$\delta^*(\eta) = e^{-2.295\eta} \tag{4-33}$$

where η denotes a dimensionless axial coordinate obtained by the ratio of the axial distance from the blade leading edge to the blade aerofoil chord. The normalized wake parameter is $\delta^* = \frac{\delta}{\delta_0}$, δ being the difference between the free-stream velocity and the minimum wake velocity and δ_0 the corresponding extrapolated value at $\eta = 0$.

A number of manifest limitations intrinsic to both models can be pointed out namely:

- The decay of rotor and stator wakes is substantially different.
- The sides of wakes are asymmetric, steeper behind the pressure side and an increase in blade loading causes a further decrease in the suction side's gradient.
- The wake decay characteristics are somewhat distinct in the near and far regions of the wake.

4.4.3 Model formulation

Hall's model is a simplistic deterministic stresses models based on the wake decay patterns introduced above and which is suitable for implementation within the framework of the mixing-plane steady flow multistage approach. The departing wake

decay correlation used by Hall is that of Philbrick and Topol (1993), which gives the wake width and the centreline velocity deficit as a function of the aerofoil drag coefficient and the non-dimensional streamwise distance from the blade trailing edge. This correlation is itself a modification of an earlier wake model due to Majjigi and Gliebe, 1984, derived from data acquired from lightly loaded low tip-speed fan experiments.

Philbrick and Topol employed data sets collected from both NASA's transonic Rotor 67 and the subsonic Rotor 55 to produce an improved speed decay correlation which could be representative of the conditions found in an actual modern gas turbine. Their two-part correlation has the form:

$$\frac{\delta}{S} = \frac{1.63632\left(\frac{s}{c}\right)C_D^{\frac{1}{8}} - 0.01944}{5.5755\left(\frac{s}{c}\right)C_D^{\frac{1}{8}} + 1.0} \tag{4-34}$$

where again, δ is the semi-wake width, S the blade-to-blade distance, c the rotor aerodynamic chord, s the streamwise distance from rotor trailing edge and C_D the section drag coefficient, and

$$\left(\frac{W_{DC}}{W_0}\right)\left(\frac{1}{C_D^{\frac{1}{4}}}\right) = \frac{1.17543\left(\frac{s}{c}\right) + 1.28626}{10.79857\left(\frac{s}{c}\right) + 1} \tag{4-35}$$

where W_{DC} is the wake centreline total relative velocity deficit and W_0 is the total relative velocity in the freestream.

The geometric definition of the δ and W_{DC} terms are presented graphically in Figure 4-9.

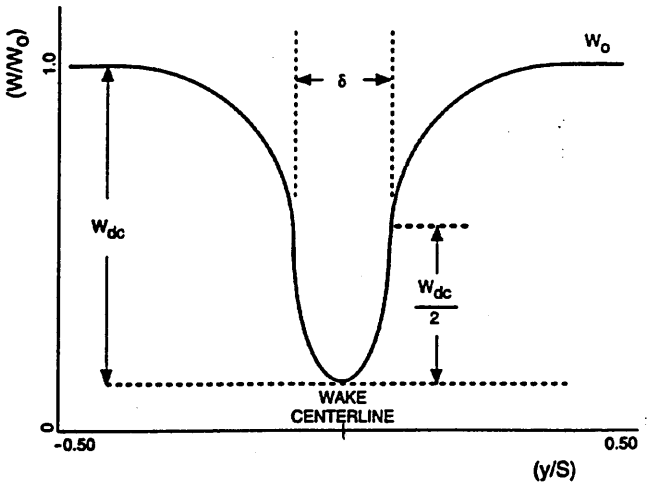

Figure 4-9 Definition of semi-wake width and velocity deficit used in wake decay model

The drag coefficient can be calculated using Lieblein's[2] equation

$$C_D = \frac{\varpi_p \cos^3 \beta_M}{\sigma \cos^2 \beta_1} \tag{4-36}$$

where $\beta_M = \tan^{-1} \frac{\tan \beta_1 + \tan \beta_2}{2}$, β_1 and β_2 are the relative air angles at inlet and outlet respectively, ϖ is the profile loss coefficient and σ is the solidity or chord to pitch ratio.

The profile loss coefficient is in turn obtained from the expression,

$$\varpi = \frac{P_{2ideal} - P_2}{P_1 - p_1}, \tag{4-37}$$

[2] Lieblein *et al.*, 1953

where P_{2ideal} is the ideal total pressure at the trailing edge, P_2 the actual total pressure at the trailing edge, P_1 the total pressure at the leading edge and p_1 the static pressure at the leading edge.

Figures 4-10 and 4-11 present a comparison between the decay behaviour of wake width and velocity deficit, predicted by the original (Majjigi) and high speed (Philbrick) versions of the model, as functions of the normalized streamwise distance downstream of a rotor trailing edge when applied to the NASA's Rotors 67 and 55 test cases.

In the semiwake width plot the ordinate value of s/c is normalized by $C_D^{1/8}$ while in the velocity deficit plot it is the y-coordinate W_{dc}/W_0 that is normalized by $C_D^{1/4}$.

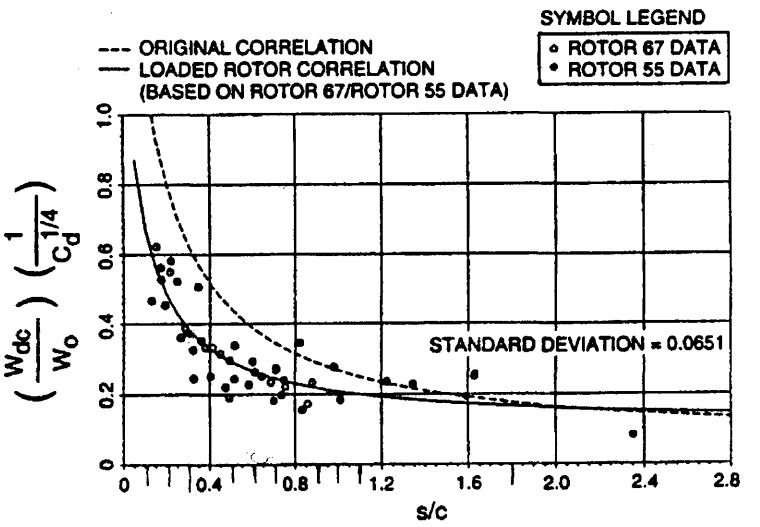

Figure 4-10 Decay of W_{dc} wake correlation parameter with streamwise distance, Philbrick and Topol, 1993

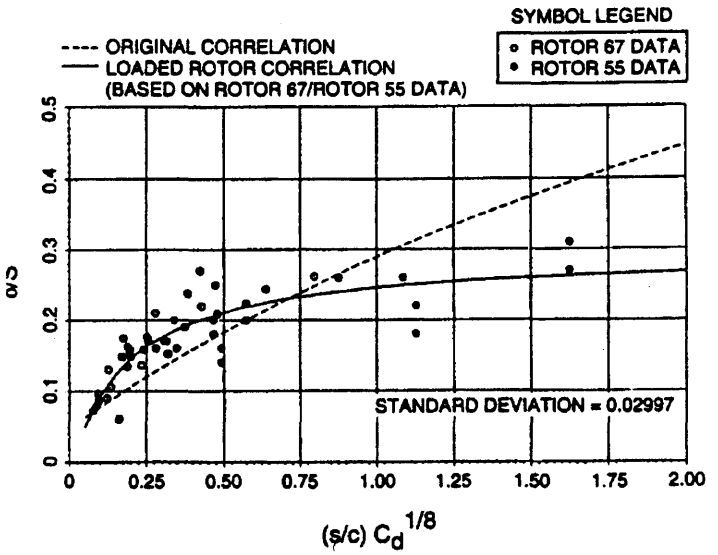

Figure 4-11 Decay of δ wake correlation parameter with streamwise distance, Philbrick and Topol, 1993

The decays which are illustrated in Figures 4-10 and 4-11 apply solely to single rotor configurations but benefiting from the Poensgen and Gallus experimental work detailed above, Hall was able to modify Philbrick's correlation in order to account for the presence of adjacent blade rows and thus assemble an improved version of the wake decay model.

The enhanced form of the correlations is written as,

$$\frac{\delta}{S}=\frac{1.63632\left(\frac{s}{c}\right)C_D^{\frac{1}{8}}-0.01944}{2.5\left(\frac{s}{c}\right)C_D^{\frac{1}{8}}+1.0} \tag{4-38}$$

and

$$\left(\frac{W_{DC}}{W_0}\right)\left(\frac{1}{C_D^{\frac{1}{4}}}\right)=\frac{1.17543\left(\frac{s}{c}\right)+1.28626}{21.0\left(\frac{s}{c}\right)+1.0} \tag{4-39}$$

The scheme employed by Hall for the inclusion of the deterministic stress terms in the equations of motion, as assembled from data contributed by the modified wake

correlations was detailed in the original paper which provided a description of the model. The steps detailed in Hall's work were discriminated as follows:

1. At fixed spans circumferential variations in flow properties define the upstream blade row wake at the interface between two blade rows.
2. The term W_{DC}/W_0 is approximated by the difference between the wake minimum relative velocity and the circumferentially averaged relative velocity.
3. The interface value of s/c is extracted from the modified wake correlation based on the known W_{DC}/W_0.
4. The enhanced wake decay correlation is then employed to define the time-averaged characteristics of the wake for positions through the next downstream blade row. The length scale s/c is computed as the arc length along an ideal flow streamline represented by the camberline (extended upstream and downstream) of the downstream blade row.
5. A spatial/temporal transformation is applied ($t = \theta / \Omega$) which equates the relative rotation of the time averaged wake description to define the fluctuating velocity field at each point in the downstream blade row.
6. The wake-defined velocity fluctuations are integrated in time to construct each of the deterministic stress correlation terms (i.e. $\overline{\bar{\rho}\,\hat{\tilde{v}}_r\,\hat{\tilde{v}}_\theta}$, $\bar{\rho}\,\hat{\tilde{v}}_\theta\,\hat{\tilde{v}}_\theta$, etc) at each cell center. The resulting deterministic stress field is axisymmetric, since all points at a given axial station and span employ the same time averaged upstream wake description.

The deterministic stress correlation terms are directly inserted into the finite volume differencing scheme and are handled in a similar manner to the viscous stress terms (e.g. τ_θ) based on the average passage equation system.

Although the original paper omits to mention this the deterministic stress correlations assembled though Hall's model include only the correlations not containing radial velocity contributions. Furthermore the calculations presented in that paper assumed a constant value of C_d of 0.01.

4.4.4 Implementation of Hall's model in TASCflow

The model implementation strategy which was followed in the present study was loosely based on the steps outlined in Hall's paper and reproduced above but where it was found expedient to employ alternative approaches consistent with the philosophy of the model these were often employed.

Specifically it was thought that in the absence of precise information about the particular velocity which might have been used by the author of the model to possibly non-dimensionalise the W_{dc} and W_0 terms is was advisable to explicitly compute the s/c values at the stage interfaces.

The structure of the source code for the Hall's model is as follows:

- Convert the velocities from a Cartesian to a cylindrical coordinate basis and compute their pitchwise average and minimum at the upstream side of the interface plane to approximate W_{DC}, the wake velocity defect.
- Explicitly calculate the interface value of the $\frac{s}{c}$ term.
- The evaluation of the $\frac{s}{c}$ values throughout the downstream row is done by calculating the streamwise lengths both upstream and downstream of the blades from the computed blade air angles. Between the leading and trailing edges of the blade the mid-camber is employed.
- Compute the Cd from equation 4-36 and the profile loss coefficient from 4-37.
- The values of the total velocity defect, W_{dc}, applicable over the downstream row are computed from Equation 4-39 while the wake semi-width, δ, is extracted from Equation 4-38.
- Employing the relationships $\frac{W_d}{W_{dc}} = \frac{W_0 - W}{W_0 - W_{min}}$ and $\eta = \frac{y}{\delta/2}$ where y is the tangential distance from the wake centreline and W_d the local velocity defect, one of the two common wake similarity profile functions, $\frac{W_d}{W_{dc}} = e^{-0.693\,\eta^2}$ or

$\frac{W_d}{W_{dc}} = sech(1.317\eta)$, can be used to compute the decayed velocity profiles relevant to the axial/radial axisymmetric grid lines of the stator domain.

This last operation supplies an array of decaying wakes from which the deterministic stresses are assembled.

4.5 Bolger's deterministic stress model

4.5.1 Bolger's model theoretical background

As starting point to modelling the deterministic stresses in a steady-state calculation the method devised by Bolger requires the evaluation of these terms at calculation stations immediately before and after the inter blade row mixing-plane.

This procedure, illustrated in Figure 4-12, seeks to preserve the tangential distributions of the wake variables up and downstream of the interface plane, from 'contamination' by the mixing-plane averaging process.

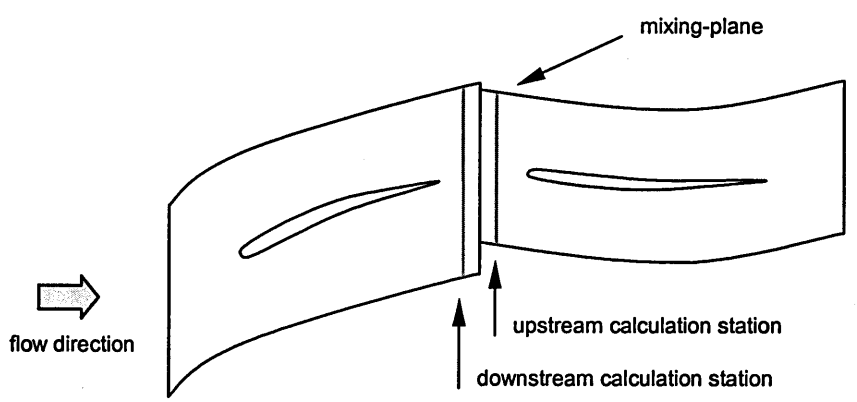

Figure 4-12 Placement of the deterministic stress calculation stations

In the Bolger model the separate direction of the stresses generated by stage interaction, viscous and potential, is explicitly accounted for, through the inclusion of distinct upstream and downstream stress decay rates. Consequently for the computation of the downstream row inviscid potential effects upon the upstream blading flow field, the calculation station downstream of the mixing-plane is used to provide the initial values and a suitable upstream decay rate of the relevant stresses employed. Conversely the computation of the deterministic stresses associated with the viscous effects has as starting point the calculation station upstream of the mixing-plane with the stress values migrating downstream and being subject to its separate decay model.

The method adopted by Bolger to couple the deterministic stresses to the steady analysis, is similar to that described in Denton, 1986, whereby distributed body forces obtained from an empirical model, were used to simulate the action of viscosity in 3D flow calculations, as part of an effort to append to an inviscid code some account of the viscous effects. For the practical implementation of Bolger's model in a finite volume scheme, the deterministic stresses are associated with the elemental areas over which they are exerted, in order to obtain forces which once integrated over the control volume yield the elemental body forces. This approach instead of the more conventional addition of the deterministic stresses to the total stress tensor, is adopted in view of the observed large savings in computational storage and speed.

To assess the stresses decay rate, Bolger conducted steady and unsteady simulations, later validated against experimental data, from which correlations defining that decay as function of the axial chord of the blade row responsible for their generation, were derived. The form of these correlations is, for the downstream acting stresses,

$$\sigma_{wake}(x) = \sigma_{mix(u)}\, e^{-\beta\, X_u} \tag{4-40}$$

with the different symbols taking the following significance:

- $\sigma_{wake}(x)$ - decaying wake stress component as function of axial distance
- $\sigma_{mix}(u)$ - mixing stress evaluated at the upstream calculation station
- β - empirically derived deterministic stresses axial decay rate exponent

X_u - distance function relative to the upstream calculation station and which has the form:

$$x_u = \left\{ \frac{x - x_{min}}{x_{\text{trailing edge}(up.row)} - x_{leading\ edge(up.row)}} \right\} \tag{4-41}$$

For the upstream acting stresses the correlation is in turn,

$$\sigma_{\text{potential}}(x) = \sigma_{mix(d)}\ e^{-\alpha X_d} \tag{4-42}$$

in which symbols take the following denotation:

$\sigma_{potential}(x)$ - decaying potential field stress as function of axial distance

$\sigma_{mix(d)}$ - mixing stress evaluated at the downstream calculation station

α - empirically derived deterministic stresses axial decay rate exponent

x_d - distance function relative to the downstream calculation station with the form:

$$x_d = \left\{ \frac{x_{mix} - x}{x_{trailing\ edge(d.row)} - x_{leading\ edge(d.row)}} \right\}$$

To derive values for the rate of decay α and β functions, data acquired during the unsteady simulation of a single stage of Cambridge's Deverson Rig, Liu et al., 1998, was employed allowing the individual velocity and energy deviations from the local time average to be directly computed and eventually assembled into a domain-wide stress correlations field from which the decay rates could be estimated. This exercise showed the decay rates to be substantially independent of operating point, a fact which is reflected in the choice of a single value for the decay functions for any given stress correlations. Moreover these results showed that the stresses of potential origin are about one order of magnitude smaller than those whose source is viscous in nature.

Given the aerodynamic characteristics of the Deverson machine, low speed (500 rpm) and a rotor midspan $R_e \approx 3.1 \times 10^5$, the generality of the values obtained for the

deterministic stresses decay rates shown in tabular form underneath is clearly questionable.

Deterministic Stress Component	Upstream Decay, α	Downstream Decay, β
$\overline{\rho v'_x v'_x}$	14.0	3.7
$\overline{\rho v'_x v'_r}$	15.0	3.1
$\overline{\rho v'_x v'_\theta}$	15.0	5.0
$\overline{\rho v'_r v'_r}$	0.0	0.7
$\overline{\rho v'_r v'_\theta}$	15.0	2.5
$\overline{\rho v'_\theta v'_\theta}$	13.0	4.1
$\overline{\rho v'_x H'_0}$	15.0	4.5
$\overline{\rho v'_r H'_0}$	15.0	2.5

Table 4-2 Bolger model deterministic stresses axial decay rate

The practical implementation of this model is detailed in the following section.

4.5.2 Bolger's model implementation scheme

The point of departure for the computation of the downstream deterministic stresses is the characterization of the upstream blade row wakes at the upstream side of the stage interface plane subject to a one node displacement. As a note on this last point, two locations, at the interface plane and displaced by one node, were tried in the HP9 case and it was found that in TASCflow as well, values obtained using both locations, i.e. radial distributions of deterministic stresses etc, differed by amounts that were not explainable by the axial separation of the two planes alone.

As Adamczyk's Average Passage Equation system is invariably cast in a cylindrical form, which for rotating machinery provides direct calculation of curvature related terms, yields more accurate numerical results and is intuitively more comprehensible, the code Cartesian velocity components are as a perquisite transformed into their cylindrical equivalents.

The calculation of the deterministic stresses at the displaced interface planes follows the sequence:

- At each radial nodal position integrate the velocity fluctuations, with respect to θ and divide the integral by $\Delta\theta$. This operation yields the averaged form of the velocity, $\tilde{\tilde{V}}_i$ as "seen" from the adjoining relatively rotating blade row and is equivalent to applying the spatial/temporal transformation, $t = \theta / \Omega$.
- At each nodal position of each radial station of the displaced interface plane the three $\hat{\tilde{V}}_i$ values are computed as the fluctuations from the average value $\tilde{\tilde{V}}_i$.
- The radial values of the axisymmetric deterministic stress correlations $\overline{\rho \hat{\tilde{V}}_i \hat{\tilde{V}}_j}$ at the displaced interface plane are calculated as $\dfrac{\sum \left[\rho_{nodal} \left(\hat{\tilde{V}}_{i(nodal)} \hat{\tilde{V}}_{j(nodal)} \right) \right] \Delta t}{\Delta T}$

  It will be recalled that the primitive flow variables accessible in the code for the assembly of the deterministic stresses correlations, have by definition already been separated from their random unsteady counterparts as part of the time-averaging of the conservation equations for turbulent flows.

- Calculate Xu, the length function of Bolger's stress decay model throughout the downstream row, and the downstream decay of the deterministic stresses according to the type decay rate β function supplied in Table 4-2 or from other source. A symmetrical step can be carried out for the upstream decay based on the corresponding functions if the second order potential effects are to be included.
- Compute the axial and radial differentials of the nodal deterministic stresses for inclusion in the motion equations, $\dfrac{\partial}{\partial r}\left(\overline{\rho \hat{\tilde{V}}_r \hat{\tilde{V}}_r} \right)$, $\dfrac{\partial}{\partial r}\left(\overline{\rho \hat{\tilde{V}}_\theta \hat{\tilde{V}}_r} \right)$, $\dfrac{\partial}{\partial r}\left(\overline{\rho \hat{\tilde{V}}_z \hat{\tilde{V}}_r} \right)$, $\dfrac{\partial}{\partial z}\left(\overline{\rho \hat{\tilde{V}}_z \hat{\tilde{V}}_z} \right)$, $\dfrac{\partial}{\partial z}\left(\overline{\rho \hat{\tilde{V}}_z \hat{\tilde{V}}_r} \right)$ and $\dfrac{\partial}{\partial z}\left(\overline{\rho \hat{\tilde{V}}_z \hat{\tilde{V}}_\theta} \right)$ which for convenience will be expressed here as A, B, C, D, E and F.

- Assemble the three momentum equations contributions as:

tangential = –B –F –DetS_tr/radius

radial = –A –E –DetS_tt/radius

axial = –C –D .

The dimensions of these terms, of both types, are quotients of stress and length the same is to say volumetric or body forces and once these forces are converted to a Cartesian format, their inclusion in the motion equations is done via the TASCflow source code interface stub routine.

Although it is mentioned in the code manual that the use of a source code is likely to involve the need to linearize the source term this requirement applies strictly only where its absence would lead to the performance of the convergence process being compromised. Given the fact that the deterministic stresses are ultimately fairly weak functions of the primitive variables this requirement in TASCflow can be relaxed. In practice the convergence rates for the cases where source terms were applied showed a detectable but small difference with the performance of the comparable 'plain' runs.

4.6 Chapter closure

Two models designed to account for the deterministic stresses from a steady-state simulation have been described and details of their implementation strategies discussed.

The fundamental difference between Hall's and Bolger's models lies in that the former uses the wake characteristics of the near-interface to yield deterministic stresses that are then decayed, while the latter applies a decay model to the wakes themselves and only then extracts from these the stresses. Consequently for their implementation both models share the requirement of extracting deterministic stresses from pitchwise wake profiles and a section of the respective codes is therefore common.

Chapter 5

Computational investigation of the Rolls-Royce HP9 single compressor stage

5.1 Introduction

This chapter provides a detailed evaluation of the effects of the employment of the two deterministic stress models previously described on a high-speed single stage compressor case. Section 5.2 introduces the salient aerodynamic design features of the Rolls-Royce HP9 single stage axial-flow compressor and compares these with those of the three-and-half stage Cranfield High Speed Research Compressor. The two following sections, 5.3 and 5.4, present the results of the steady and unsteady simulations of this case as well as their validation against published experimental data. In 5.5 a critical assessment of the effect of the use of the two deterministic stress models is undertaken.

Once the decision was taken to include in the study of the HSRC a form of semi-empirical deterministic stresses model, a suitable test case preferably consisting of a single stage with characteristics similar to those of the Cranfield machine was sought from the open literature. As the objective of the exercise was to conduct an evaluation of the effect of adding one or other such models, it was hoped that any existing data for this test case would comprise unsteady experimentally or numerically acquired measurements presenting the most approximate possible picture of the true flow

conditions. Only in the possession of such data can the question of knowing whether any of the semi-empirical models offer some contribution towards closing the gap found between the steady-state simulations and the time-average of either unsteady simulations or time-accurate experiments, be conclusively answered.

A summary list of the assembled potential candidates is displayed in Table 5-1.

CASE	ROWS	TYPE	GEOMETRY	INSTRUMENTATION TYPE	EXPERIMENTAL DATA	REPORTS	REMARKS
DFVLR	SINGLE STAGE	TRANS SONIC	YES	CONVENTIONAL PROBES L2F	PERFORMANCE MAP 5 SPEEDS RADIAL DISTR. P RATIO & MACH M. REL. PLOTS 4	AGARD TEST CASE	LITTLE BLD-TO-BLD DATA ON ROTOR & NONE ON STATOR
R-R HP9	SINGLE STAGE	SUB SONIC	YES	PNEUMATIC PROBES	RADIAL VAR. P & T RATIO & MACH NUMBER + YAW ANGLE CIRCMF. VAR P & T RATIO	AGARD TEST CASE	NO BLADE-TO BLADE DATA
U2	2 1/2	LOW SPEED	POSSIBLE	N/A	N/A	ERCOFTAC TEST CASE	Gerolymos, 1995
ECL3	IGV & STAGE	SUB SONIC	N/A	N/A	STEADY/UNSTEADY EULER SIMULATION	ÉCOLE CENTRALE LYON	ERCOFTAC TEST CASE IN 1997
NASA STAGE 67	1 & 2 STAGES	SUB SONIC	ROTOR	CONVENTIONAL PROBES & LASER ANEMOMETRY	RADIAL PROFILES OF PERFORMANCE PARAMETERS (1978)	NASA ROTOR 67 IN ISOLATION MUCH REPORTED	Shang et al.,1991. Ng and Eps., 1984, Fritsch, 1992, Hathaway, 1986
DERA C148	SINGLE STAGE	TRAN SONIC	N/A	3 D PROBES & YAWMETER 2D CFD SIMULATION	N/A	-	Bryce et al.,1995. Cherrett et al., 1995
DUT	SINGLE STAGE	SUB SONIC	N/A	3 D L2F FIVE HOLE PROBES	80 & 90 % SPEED DATA	DARMSTAT UNIVERSITY OF TECHNOLOGY	LOW BLADE COUNT (16 / 29) - VERY DIFFERENT FROM CRANFIELD HSRC
ECL4	IGV & STAGE	SUB SONIC	N/A	CFD SIMULATIONS	N/A	SNECMA	Burgaud, 1995 AGARD CP 571
NASA STAGE 37	SINGLE STAGE	80 % SPEED STAGE 37	R35+ S37 PROBABLE	CONVENTIONAL PROBES LASER FRINGE ANEMOMETRY 3 D UNSTEADY	N/A	NASA LEWIS RESEARCH CENTRE	-

Table 5-1 Selection table of high-speed single stage axial-flow compressors

The chosen case, Rolls Royce's HP9, is in practice the *only* single stage subsonic compressor to feature in the open literature, with all the other considered alternatives being either substantially different aerodynamically, mostly being transonic machines, or insufficiently reported and likely to remain so due to industrial or academic proprietary restrictions.

In the event it is fortunate that the selected machine shares some relevant design parameters with the HSRC, as is apparent from the analysis of Table 5-2, the aerodynamic variables being referred to each machine's design point.

	HP9	HSRC stage 1 stage 2 stage 3
Pressure ratio	1.24	2.4 (overall)
Mass flow	9.1 Kg/s	10.6 Kg/s
Speed (rpm)	9262.5	9300
s/c (mid-span)	0.9 rotor 0.7 stator	0.60 0.55 0.70 rotor 0.57 0.59 0.57 stator
Hub/tip ratio	0.84	0.85 0.88 0.91
Aspect ratio	0.9	1.1/1.1 0.9/1.0 0.9/0.9
No blades	41/73	71/91 89/109 85/116

Table 5-2 Comparison of design parameters of R-R HP9 and Cranfield HSRC

Details of the geometry and experimental results of Rolls-Royce's HP9 single stage axial flow compressor were publicly circulated as one of the twelve turbomachinery test cases selected by the AGARD Working Group 18 in 1990 as representative of the then state-of-the-art design practices. The assembled WG18 collection of cases comprised a number of high-speed compressor configurations, namely the single rotor NASA Rotor67 and the DFVLR single stage, both operating in transonic regimes besides the subsonic single stage Roll-Royce HP9.

5.2 Test case description

The single-stage HP9 test compressor was designed to model the aerodynamic flow features characteristic of the embedded later stages found in the high-pressure compression system of contemporary civil gas turbine engines and predictably this compressor is characterized by annular dimensions entailing high hub-tip ratio blading. Figure 5-1 depicts the general layout of the rig and the location of the data gathering planes with respect to the rotors and stators.

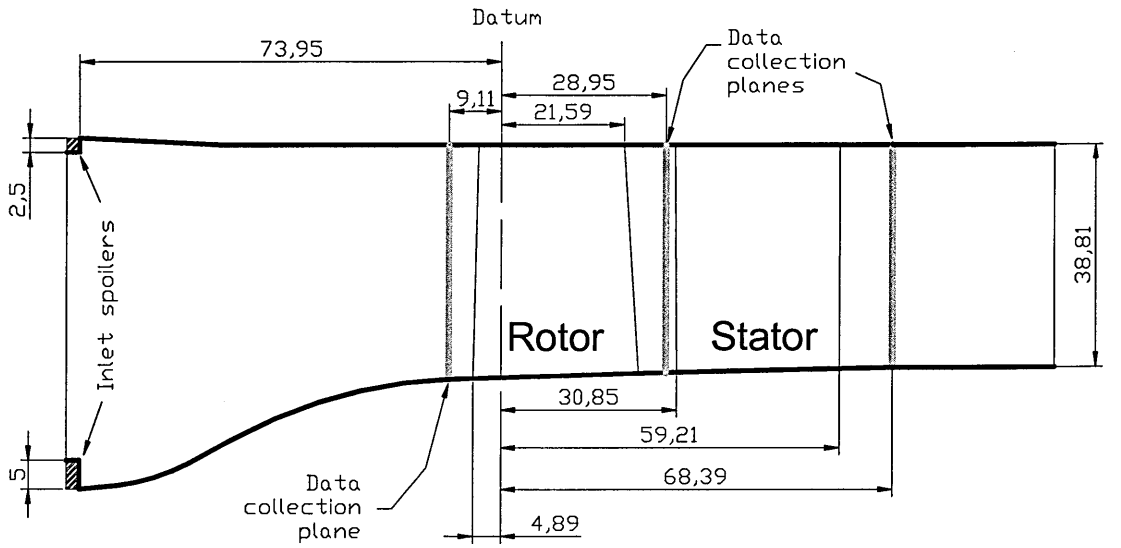

Figure 5-1 HP9 test rig shematic layout

5.2.1 Blade design features

The reported build, the 'RD' case, is a close-coupled stage of conventional design, 41 Double Circular Arc blades being fitted in the rotor and 73 C4 mod 2 in the stator. It is instructive at this point to consider in some detail the choice of blade profiling employed in this test case.

The stator's C4 profile is a design deeply rooted in early British compressor work, i.e. Howell,1942, and was originally developed for use in the cascade method of design for axial flow compressors, Ruglen, 1966. C4 blades were extensively used in the systematic work carried out in the immediate post-war period by Howell and his contemporaries and accordingly the cascade aerodynamic behaviour of these aerofoils has been widely documented.

C4 profiles are constructed from a given thickness form bent around either a parabolic or circular arc camber line about which the aerofoils are symmetrical. Within the

constraints of the profile's basic design philosophy considerable latitude exists for substantial fine-tuning of particular versions.

When evaluating the high speed aerodynamic performance of the C4 family of profiles, the objections usually lined up against it include the inherent leading edge bluntness, a consequence of the location of the maximum thickness towards the leading edge by comparison with contemporaneous designs, the rapid rise in pressure loss at Mach numbers beyond about 0.7, McKenzie, 1997, and the corresponding narrowing of the loss coefficient envelope, Cumpsty, 1989.

As a consequence of the C4 leading edge relative dimensions, low pressure regions can be found in this area, on both suction and pressure surfaces, which in turn bring about a speeding up followed by a brisk deceleration of the local boundary layers. Such pressure distribution can only promote the innate appetence of the compressor boundary layers for instability, given the unfavourable pressure gradients in which these machines necessarily operate. With increasing Mach numbers, patches where sonic conditions pertain develop, but the occurrence of local detachment inducing shocks, never a recipe for stability, is in the C4 blades associated to the particular design features mentioned above, that make after-shock boundary layer re-attachment rather less likely.

Keeping in mind the limitations listed above it would therefore appear sensible in this case to restrict the employment of C4 blading to the machine's stators whose location is made more compatible with those aerofoils by the lowering of the blade relative Mach number which is induced by the rotor turning action .

The Double Circular Arc rotor profile, which as its name indicates, is assembled from two sets of arcs, has demonstrated despite its formally simplistic design to offer for flows either side of transonic regimes better performance than the C series blades. This advantage arises not only from the lower leading edges radius, typically about half that of a C4, but also from the smoother distribution of thickness along the blade chord. Although DCA blades are known to generally operate with separated suction surface boundary layers some distance ahead of the trailing edge, the contribution of this to the blade loss is mostly small, Cumpsty, 1989. The benefits of the DCA

geometry, when compared to C4 or equivalent profiles, are apparent in the form of smoother pressure distribution on both blade surfaces, a wider operating range at high Mach numbers and a raising of the choking threshold.

To conclude the appraisal of the HP9 blading approach, one ought to say that the choice of profiles employed in the case was decidedly conservative by the standards current at the time of the release of the test case and would therefore not be representative of forward looking design practice of that period. By then high-pressure/speed blade aerofoils would normally have benefited from the application of reasonably capable computers on which, benefiting from the experience acquired elsewhere with supercritical wing design, blade aerofoils would have been assembled to meet a prescribed surface velocity or pressure distribution, McKenzie, 1997.

In Chapter 6 a return to the topic of controlled diffusion blade design will be made when a description of the aerodynamic characteristics of the datum build of the Cranfield HSRC is carried out.

The rotor of HP9 is unshrouded unlike the stator which is fitted with a fixed inner shroud ring. The nominal rotor tip clearance is about 0.25% of the span corresponding to a theoretical gap of some 0.15 mm. Given the known presence of an abradable lining in the tip clearance region, guidance on the effective extent of the clearance gap was sought from Mr Don Harris of Rolls-Royce, Derby, who supervised the HP9 experimental work and who advised that this clearance is in practice of the order of a tenth of a millimetre.

5.2.2 Test case general flow features

It is well known that in the high-pressure section of an axial compressor the radial profiles of velocity and temperature will eventually develop into a virtually unchanging configuration, as one travels downstream through the machine, and that about three or four stages are required for this repeating pattern to become established.

In Figure 5-2, extracted from Broichhausen, 1994, the development of a repeating pattern is clearly observable for a three-and-half stage machine while in Fig. 3.15, Page 122 of Cumpsty's *Compressor Aerodynamics*, 1989, which depicts total temperature and axial velocity profiles for stages 4-11 of a 12 stage compressor, there is very little evidence of profile variation with increasing stage numbers.

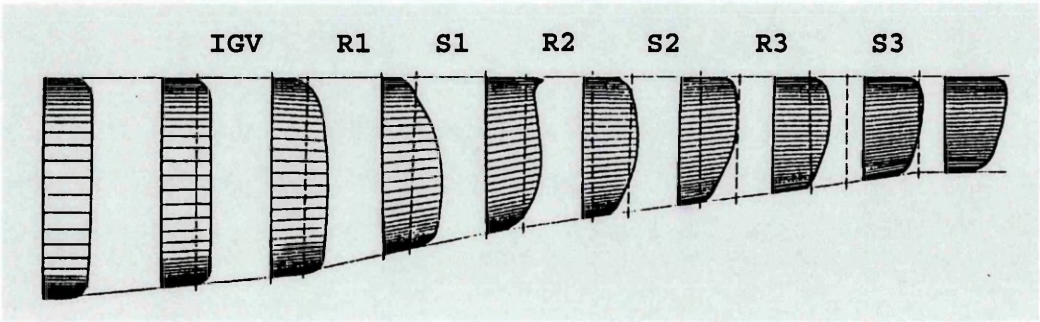

Figure 5-2 Repeating radial pattern development, Broichhausen, 1994

Although some evidence of this phenomenon was documented as early as 1945 by Howell, later experimental work, ie Smith, 1969, enabled a greater clarification of the number of stages involved in the process. Nonetheless it was the contributions of Adkins and Smith, 1982, and Gallimore and Cumpsty, 1986, alluded to in Chapter 1, which drew attention to the radial mixing and diffusing mechanisms that underpin the physics of the repeating stage process.

A consequence of what is noted above is that in order to replicate the inlet velocity profile appropriate to the flow regime typical of latter high pressure stages, the HP9 testing rig is fitted with spoiler rings on the hub and shroud. The inlet spoiler rings, which are positioned about three axial chords upstream of the rotor and comprise both perforations and lacing with wire, are responsible for the generation of fairly thick rotor inlet endwall boundary layers, amounting to some 10-20 % of local annulus height. These inlet boundary layers are of dissimilar sizes with the hub spoiler ring dimensions being twice those of the matching shroud ring. This amount of annulus wall blockage was modelled in the only paper which has to date dealt with the numerical simulation of this case, specifically employing an axisymmetric quasi-3D S1-S2 formulation, Calvert, 1999, as a 2.5% flow blockage.

In the S1-S2 method a solution is obtained from the synchronized iteration between what are fundamentally two 2D approaches, one corresponding to a blade-to-blade plane and the other to a meridional throughflow plane. The version employed by Calvert comprises the S1BYL2 inviscid-viscous time-marching solver, which is used to obtain the solution of the blade-to-blade flow field and the SC90 streamline-curvature code which computes the throughflow. For a succinct introduction to the S1-S2 method see Page 95 of Cumpsty's *'Compressor Aerodynamics'*, Cumpsty, 1989.

Experimental data for three operating conditions at 100% speed, 9262.5 rpm, were documented in the test case and these are designated as max-flow, mid-chic and near surge respectively. The mass flows corresponding to these three points were supplied in terms of the mass function $M\sqrt{T_{ref}}/P_{ref}$ with T_{ref} and P_{ref} taking the values of 294 K and 13.84 Psi or 95426.8 Pa, respectively. Values of the compressor three experimental mass flows are tabulated below.

Flow regime	Mass function	Mass flow rate (Kg/s)
Max Flow	26.5	9.70
Mid-Chic	23.9	8.82
Near Surge	21.1	7.23

Table 5-3 Experimental operating point mass flow rates

5.2.3 Experimental methods – overview

Three main types of data sensing device were employed in the rig testing of the HP9 case, steady-state pneumatic pressure transducers, temperature thermocouple sensors and an input power torquemeter.

The calibrated pressure transducers are employed in the following fixed locations:

- inlet airmeter
- inlet total pressure measurement upstream of spoiler rings - 4 probes
- outlet total pressure 5.5 axial chords downstream of stator – 7 8-point rakes
- wall static tappings distributed throughout the compressor

and also as part of the traverse mechanisms:

- rotor inlet, rotor outlet and stator outlet – radial traverses by 3-hole cobra probes
- stator outlet – area traverses with 3-hole cobra probes

For temperature data collection shielded thermocouples are employed which are also either fixed:

- outlet total temperature downstream of the stator – 3 8-point thermocouple rakes

or fitted to the radial and area traverse mechanisms:

- as for the pressure measurements – shielded thermocouples fitted to the 3-hole cobra probes

The probes which are used in the radial traverses are of the self-aligning type with the local flow angle being obtained from the probe direction. For the area traverses the probes were set at an appropriate yaw angle at each of the radial locations and kept at that setting for the corresponding pitchwise sweep. This approach ensures the angular stability of the probe in the areas of high sheared flow present in the upstream blade wakes over which the probe calibration curves are known not to apply, Robinson, 1991. The calculation of the local flow angle from the experimental values is done by reference to a set of tunnel-defined calibration curves defined beforehand.

When the probe is fixed the angle which is worked out from the differential readings of the side pressure tappings can be said to be qualitative at best in real turbomachinery applications. Research has shown that significant errors can result as a function of freestream turbulence intensity and vorticity, Japiske, 1986. A mass flow balance calculation may be carried out to check on the validity of the flow survey and some angle adjustments may be necessary in order to satisfy the mass conservation law. However this should only be done if the corresponding static and total pressures

are known to be accurate. A torquemeter is used for the calculation of the input shaft power. An outline of the features and limitations of the experimental set-up employed in the aerodynamic survey of the HP9 compressor is undertaken in the following subsections.

5.2.4 Experimental methods – pressure sensing devices

Two types of pressure measurements were carried out in the experimental survey of the HP9 rig, total pressure employing probes and static pressure based on wall tappings.

All pressure measurements were made using a conventional steady-state pneumatic system with the expression conventional indicating that the technique incorporates some form of time-averaging and is subject to a number of errors when applied to unsteady flows. The basic frequency of the pressure fluctuations in turbomachinery is derived from the rotating speed and the blade numbers and values of 10KHz or more are commonly encountered.

The components of the measurement system are a sensor, either as a probe head or pressure tap, the connecting tubes and a remote low frequency pressure to voltage signal transducer. At its simplest form this last component will be some form of manometer but ordinary transducers are based on a pressure bearing diaphragm displacement being related either directly to a capacitance variation or indirectly to a strain gauge measured beam deflection. Heidrick, 1986, lists details of around 100 pressure transducers of both types with typical accuracies of 0.5% full scale for the capacitance type and 0.35% for strain gauge and a corresponding level of repeatability of about 0.1% for both types.

When the pressure time-variation is small, conventional pneumatic systems can deliver time-averaged values which are fairly accurate but in strongly fluctuating flows such as those found directly downstream of a rotor blade row, noticeable errors do occur. Figure 5-3 shows the size of the relative pressure error $\left(\overline{P}_p - \overline{P}\right)/\overline{P}$, where $\overline{P}_p$ is the indicated pneumatic average and $\overline{P}$ the actual time average of the local

pressure, against the ratio of maximum to minimum fluctuating pressures, P_{max} / P_{min} for two stereotypical forms of pulsation, sine and square waves.

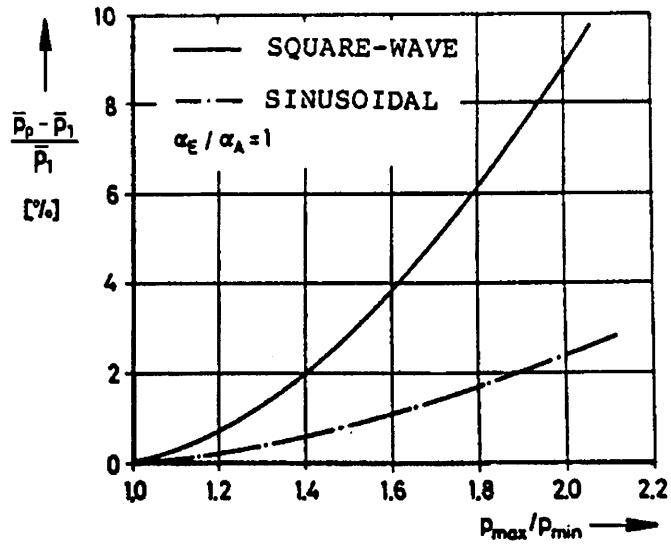

Figure 5-3 Pneumatic measuring system error, Eckardt, 1986.

The discrepancy between the indicated and the true time-weighted pressures present in conventional pneumatic systems arises mostly from the compressibility of the medium in the connecting air line but is also a function of the dynamic characteristics or frequency response of the transducer.

The effects of the pneumatic system errors outlined above spill in turn into the global performance calculations as is graphically demonstrated below. In Figure 5-4 the error in efficiency is plotted against pressure ratio for two given pressure ratio errors, 1 and 3 percent, respectively. What this picture makes clear is that in the pressure ratio range of the HP9 compressor, about 1.2 to 1.3, a 2% error in the evaluation of the pressure ratio will in turn engender an error of similar magnitude in the computation of the efficiency.

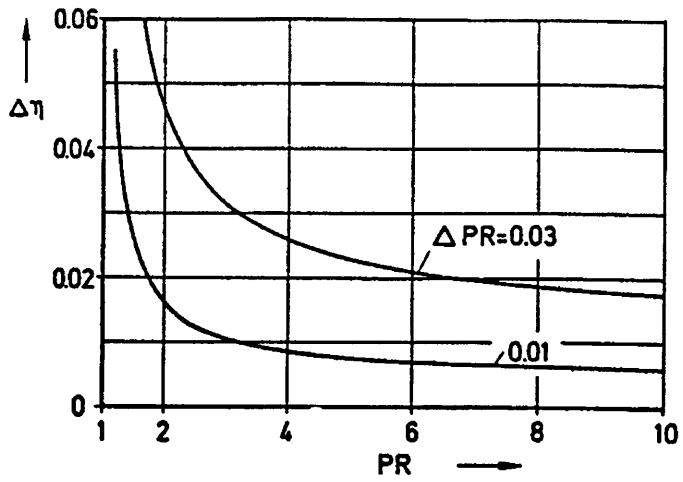

Figure 5-4 Compressor efficiency error variation

A recognition of the limitations implicit in the use of the pneumatic probes is clearly expressed in the HP9 report, Ginder and Harris, 1990. The main weakness of the test case is the uncertainty surrounding rotor exit conditions which arises from the limitations of conventional steady-state instrumentation. Measurements with high-response pressure transducers would considerably enhance the value of the test case as without such data checking the rotor exit conditions from a calculation involving the rotor or the complete stage cannot be done to a high degree of accuracy.

5.2.4.1 Total pressure measurements

The quantification of this form of pressure is inextricably linked to the evaluation of the local flow direction and therefore the probe design should incorporate features that make it less sensitive to flow misalignment. When flow direction is also an outcome of the measurement, a self-balancing actuator can be fitted to a three-hole probe so that a pressure differential in between the outer holes is nulled out and the probe is made to constantly face the flow so that besides the yaw angle, the probe measures total pressure directly from the central tapping.

Nevertheless when the measurement station is subject to unsteady effects in wake regions, i.e. von Karman vortex streets, these are not appropriately resolved by this method and as a result the statistical average is somewhat different from the

equivalent average of the actual fluctuating flow condition. In the experimental investigation of the single-stage Pennsylvania University low-speed axial flow compressor, Prato and Lakshminarayana, 1993, found the five-hole probe yaw accuracy to be ± 2 degrees.

Sitaram and Lakshminarayana, 1983, listed a number of errors to which five-hole probes are subject but this is equally valid for the three-hole probes used in the HP9 analysis: probe misalignment, wall and blade vicinity effects, finite dimension of the probe tip in a velocity and/or pressure gradient, effects of probe blockage, Reynolds and Mach number effects. The approach employed to account for the Reynolds number effects is to calibrate the probes in the same range of Reynolds numbers encountered in the flow field of the compressor during measurements. The Mach number can be varied during calibration so as to appear as one parameter in the calibration functions, Heneka and Bubeck, 1939, a procedure carried out in the HP9 runs. Blockage errors can be minimized by the calibration of the probes in the support structures used for the experimental run.

The wall proximity effects, fundamentally translated as a local static pressure increase but also as a possible yaw angle sensitivity, are documented as acting well outside the boundary layers and being related to probe geometry, Smout and Ivey, 1997, or in other words, related to the probe-surrounding airflow distribution a given configuration will instigate. This problem can be lessened through the choice of probe configuration and cobra probes, as employed in the HP9 survey, have the advantage over other types of being able to approach walls with comparative accuracy.

One added advantage of cobra probes is that they allow rotation about the stem axis without altering the measuring position, a feature which is of considerable advantage during calibration because it allows the selection of the most suitable region of the calibration function during measurement, Shepherd, 1979.

In HP9, radial traverse data were collected near the shroud to within 1% of the annulus height but due to physical constraints, near the inner wall, that distance was somewhat larger. The total pressure at the endwalls was estimated by assuming the

local absolute Mach number to be zero and hence that the total pressure values are those of the measured local static pressures.

It is in practice impossible to work out the cumulative effects of the errors outlined above from first principles and probes are generally calibrated in dedicated wind tunnels, typically a 100mm diameter free jet exhausting to atmosphere.

5.2.4.2 Static pressure measurements

Static pressure is very difficult to measure accurately because its indicated value is strongly affected by hole size, compressibility effects, orifice edge form and surface irregularities, Fleeger and Seyb, 1975. Furthermore in the presence of turbulence, static pressure is not only a difficult quantity to measure but even to define and absolute accuracy in interstage measurements cannot be expected when the degree of turbulence, the swirl angle, the effective flow area and the radial and peripheral pressure gradients are not known with precision, Dimmock, 1963.

The measurement of static pressure in routine compressor testing is seldom performed by any means other than by tappings fitted to annular walls of the compressor, often only to the outer casing depending on the design features of the hub, the radial distribution of the variable being calculated from the measured end values. This dependence on wall information alone is somewhat unfortunate for although it is recognized that the static pressure variation is much greater axially and in pitch than in the spanwise direction, a variation across the flow field is quite possible due to the streamline curvature or the presence of swirl and static pressure is known to change when strong total pressure gradients occur.

5.2.5 Experimental methods – temperature sensing devices

Unlike the static pressure case seen in the pressure measurement section above, there is no practical means of measuring the freestream or static temperature in a non-intrusive manner. The action of bringing the flow to a rest by the introduction of a probe in a gas stream does in practice lead to an entropy increase in the probe boundary layer or in other words, there is a localized temperature rise above that of

the neighbouring freestream. This heating effect due to friction and the presence of local shearing flows is however offset by the added probe heat removal action of the surrounding airstream.

The ratio of shearing effects to heat transfer effects is represented by the Prandtl number, $P_r = \frac{c_p \mu}{k}$, C_p being the specific heat at constant pressure and μ and k the viscosity and thermal conductivity coefficients respectively. These coefficients are also related to thermodynamic variables using kinetic theory and can be presented as the viscosity and thermal conductivity Sutherland formulas, $\mu = C_1 \frac{T^{\frac{3}{2}}}{T + C_2}$ and $k = C_3 \frac{T^{\frac{3}{2}}}{T + C_4}$, where T is the gas temperature and the various 'C's, empirically derived constants for different gases.

In real gases at gas turbine conditions the Prandtl number is invariably less than one, Pr = 0.72 for air at standard conditions, and thus heat transfer dominates over viscous effects meaning that when at equilibrium conditions, the probe temperature will be below that of the local stagnation temperature.

The capability of the probe to account for the dynamic temperature component of the flow without a contribution of conduction or radiation errors is commonly denoted as the recovery of the probe with a recovery factor being defined as,

$$R = \frac{T_{ind} - T_{static}}{T_{total} - T_{static}} \qquad (5\text{-}1)$$

In equation 5.1 T_{ind} is the indicated temperature given by the thermocouple with the other terms taking their normally accepted significance.

Essentially the recovery factor encompasses all energy transfer mechanisms and since it is impossible to calculate analytically the heat transfer properties of the complete thermocouple probe system accurately, the evaluation of the recovery factor is experimentally determined in a small calibrated wind tunnel over a representative

range of flow conditions. Details of one such experimental set up can be found in Fleeger and Seyb, 1975, while Haig, 1960 and Smout and Cook, 1991 contain examples of the equations used to model the velocity, conduction and radiation errors. The calibration method is in itself a source of errors as the tunnel settled flow conditions are atypical of the turbulent and heavily unsteady environment which is characteristic of turbomachines.

Besides the error related to the inability to bring the flow to rest isentropically, the velocity error, one must add those due to the probe stem conduction and radiation effects and to these a use dependent error is further added when the probe is operated in close proximity to the heated surfaces of a turbomachine.

This situation can be minimised though by fitting shields or Kiel-shrouds to the probes and for the HP9 temperature survey the thermocouple probes sport this form of protection. Further benefits associated with the use of these shrouds are the increase in the global level of temperature recovery, a reduction in flow incidence angle sensitivity and a general increase in environmental protection.

Thermocouples are based on the general principle that when two different metals are joined together an electrical potential difference is established. The magnitude of the potential difference is dependent on the temperature of the junction of the two metals and this is the feature that makes thermocouple junctions applicable in thermometry. Amongst the number of metal combinations which are used in thermocouple wire applications a well known one is chromel/alumel due to its high contact potential, about 4mV for every 100 °C difference between the hot and cold junction elements of the thermocouple, high temperature capability, up to 1100 °C, and an absence of catalytic effects. The accuracy of thermocouples based on this alloy combination is not particularly good at about 3% but this figure is halved if for example, different combinations of platinum and platinum rhodium are employed.

As in the case of pressure probes, temperature measurements in regions of periodic high flow unsteadiness levels are subject to errors that are additional to those which are identifiable when the probe is tested in a wind tunnel. Moffat and Dean, 1967 and Eckardt, 1986, have both contributed theoretical models to account for these effects

but the preferred approach is to calibrate the probes in situ so as to implicitly incorporate in the recovery factor the impact of the turbomachine working environment.

Although no indication is given in the publicly released HP9 experimental data about the accuracy of the temperature probes, these instruments carry typically a 2-3% measuring error corresponding in this case to some 5-7 K.

5.2.6 Experimental methods – torquemeter and airmeter description

Conventional torquemeters are made by employing a length of a calibrated shaft to which a strain-gauge is fitted in order to quantity the torsional deflection of the shaft under a twisting load. This technique provides the means to evaluate the mechanical input power and in the HP9 case corrections were applied to account for torquemeter heating effects and losses due to bearing friction and blade disk windage.

Lastly, a 0.305 m diameter airmeter layout, consisting of a carefully shaped bellmouth leading to a section of constant radius ducting which is fitted with an array of static taps, is employed to measure the mass flow. The reader is directed to McKenzie, 1997, for a specific geometrical arrangement of an airmeter together with added design information for these devices.

The efficient operation of the airmeter is dependent on the success of the flared bellmouth in minimizing the growth of the boundary layers that reach the plane containing the static pressure tappings. The measure of success in achieving this objective is expressed as the discharge coefficient C_d, the actual flow area divided by the geometric inlet area, the value of which is for a well designed system of the order of 0.99. The mass flow across the shaded plane ① of Figure 5-5 is computed from,

$$\dot{m} = Q\left(AP/T^{\frac{1}{2}}\right) \tag{5-2}$$

where A is the cross sectional flow area and P and T the local total pressure and temperature. Q which is obtained from

$$Q = (1/R)(V/T^{\frac{1}{2}})(T/t)(p/P) \qquad (5\text{-}3)$$

where the symbols R, V,t and p are the air gas constant, velocity, static temperature and pressure.

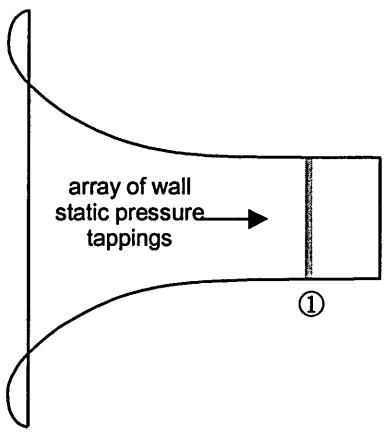

Figure 5-5 Generic arrangement of an airmeter

5.2.7 Experimental results considerations

The following section includes an abridged version of the considerations contained in the published version of the experimental report of the HP9 compressor stage.

5.2.7.1 Overall performance

The inlet pressure value assumed in calculating the overall performance is an area-weighted radially-averaged rotor inlet value which is derived from the total pressure measured upstream of the spoiler ring by means of a correction curve. The correction curve is based on radial traverses carried out at rotor inlet over a range of mass flows. The exit total pressure is derived from the delivery rakes but the exit total temperature is derived from the torquemeter reading since the thermocouples were not considered to be accurate enough to enable reliable values of efficiency to be calculated at low values of temperature rise.

5.2.7.2 Traverse results

The traverse results are generally measured values, the data being subject to the following qualification:

a) During the radial traverses data were taken to within 1% of annulus height of the outer wall but due to physical constraints it could not be taken as close in the inner wall. Total pressure values at both walls is inferred by assuming that the absolute Mach number is zero, and hence that the total pressure equals the measured or inferred wall static pressure.

b) The total temperature at the walls is obtained by extrapolation of the measurements with the values at the inner wall thought to be suspect.

c) The values of Mach number are derived from the ratio of local total to static pressures, $\frac{P}{p}=\left(1+\frac{\gamma-1}{2}M^2\right)^{\frac{\gamma}{\gamma-1}}$. The required values of local static pressure are obtained by extrapolating the measured outer wall value across the annulus using a static pressure gradient estimated using throughflow analysis.

The presentation of experimentally collected data is deferred to the sub-section which contains the results of the CFD simulations where these values are then employed in a comparative manner.

5.3 Numerical simulation programme

The CFD investigation plan for the HP9 case is described below by reference to the following tasks:

1) Obtain a computational aerodynamic survey of the machine for comparison with published experimental data – steady-state simulation employing a grid of about 250,000 nodes.
2) Apply two deterministic stress models to case 1) and evaluate model effects.
3) Conduct unsteady simulation with reduced grid size– about 115,000 nodes - to calibrate Bolger's model for use with high-speed axial-flow compressor simulations.
4) Run a steady-state version of the reduced size grid in order to compare with unsteady results obtained in 3).
5) Extract deterministic stress terms from unsteady simulation and compare with the values of stresses yielded by the two semi-empirical models.
6) Apply the two deterministic stress models to the reduced size grid as well as the unsteady simulation sourced deterministic stress and carry out a triangular comparison.

5.4 Steady-state simulation I - large grid

5.4.1 Grid generation issues

The grid used in the present study is of H-type on both the rotor and stator domains and was built using the programmable TASCgrid set of grid generating codes. The rotor grid has 40 nodes spanwise, 43 pitchwise and 91 axially, 156,520 nodes in all, while the stator has 40, 35 and 79 nodes in the same corresponding directions, or 110,600 nodes. 94% of the total count are active nodes. Given the practical size of the tip clearance noted above the numerical model does not include a tip clearance. The general grid layout at mid-span is depicted in Figure 5-6 below.

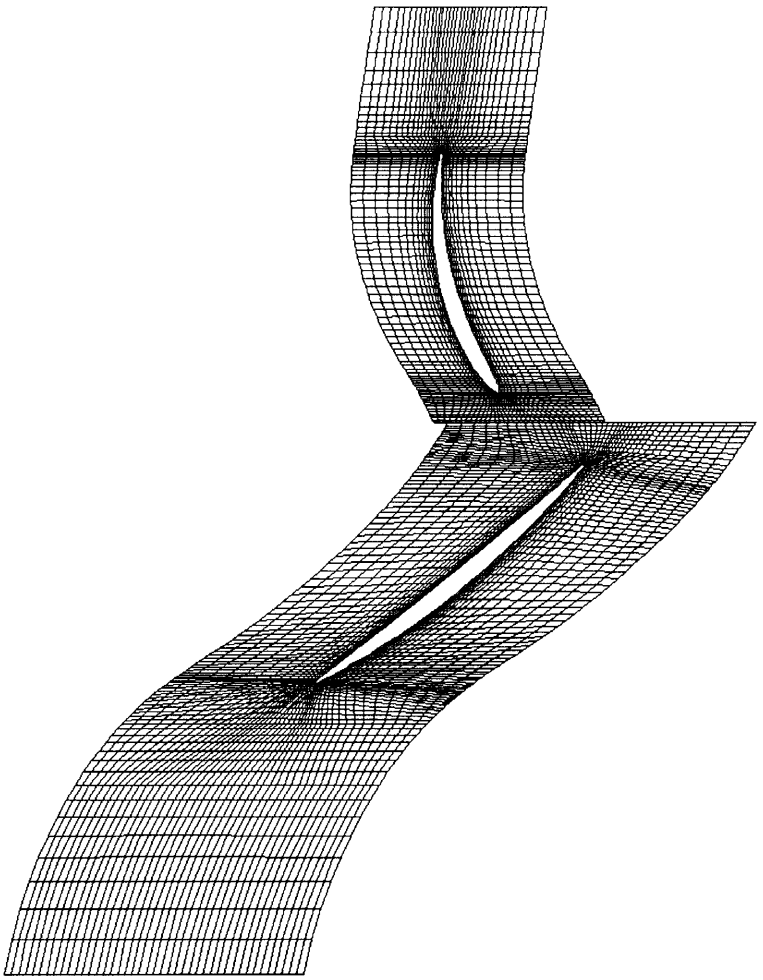

Figure 5-6 HP9 compressor stage grid layout at mid-span

The placement of the global inlet and outlet planes, although arbitrary in relation to the known geometry of the test rig, was dictated by good practice in CFD which consists of placing inflow and outflow boundaries no closer than about a blade chord to the blade relevant edges.

This procedure and the fact that the interface plane was placed, as is usual practice, mid-way between the rotor trailing edge and the stator leading edge, meant that no natural boundary of the computational domain coincides with the experimental data collection planes.

The location of these three planes is depicted in the ringed indices of Figure 5-7.

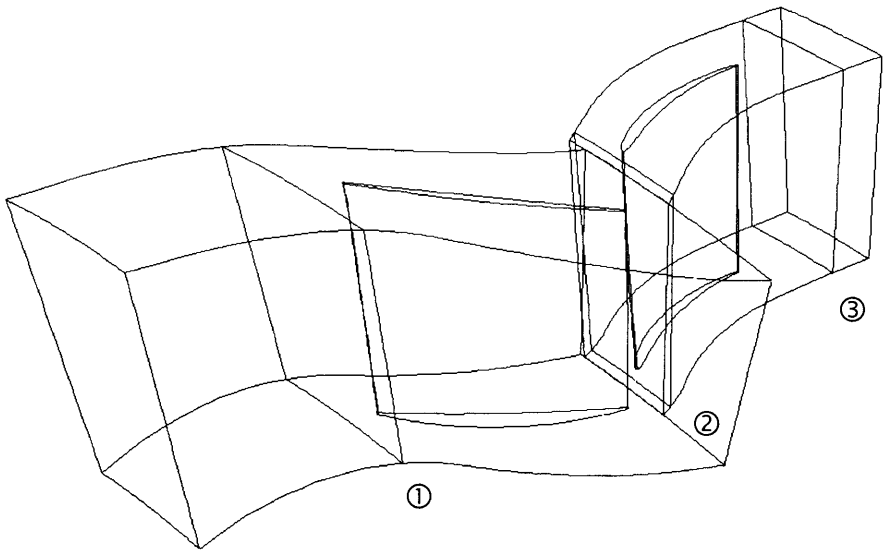

Figure 5-7 Location of the HP9 experimental data collection planes

As the model is primarily used for the purpose of applying deterministic stresses source terms over the stator domain and these have by the nature of their mathematical, though not physical, formulation an axisymmetric distribution, the stator domain grid has itself an equally axisymmetric structure, Figure 5-8.

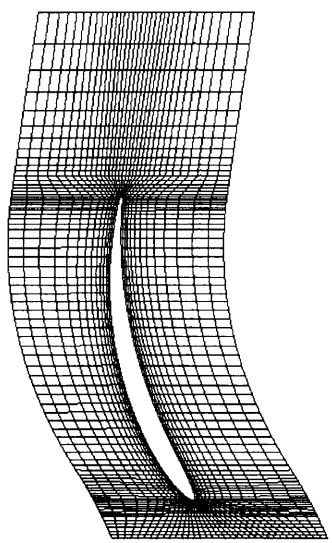

Figure 5-8 HP9 stator grid at mid-span

A closer look at this figure will however reveal that over a section of the leading and trailing edges,

Figure 5-9 and 5-10, the pitchwise lines are in fact not axisymmetric as was stated above. This arrangement was thought to provide the best possible compromise between the code grid requirements in terms of minimum angles and the needs of the deterministic stresses model.

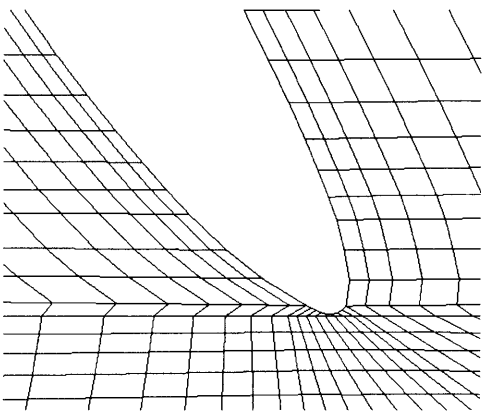

Figure 5-9 HP9 leading edge grid detail

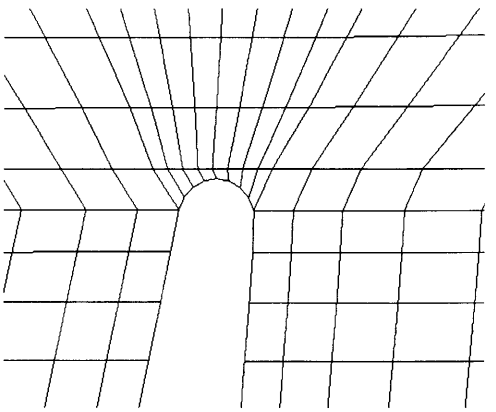

Figure 5-10 HP9 trailing edge grid detail

Nonetheless in order to completely establish whether this departure from axisymmetry did by itself introduce any or some modifications to the flow, a test run of the stator grid in isolation was conducted.

For the purpose of this run the blade domain was not blocked-off, Figure 5-11, a uniform axially-aligned inlet total pressure and outlet average static pressure was specified and a linearly decaying source term applied to the axial component of the momentum equations.

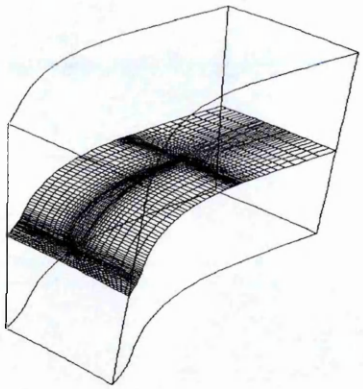

Figure 5-11 HP9 stator domain without blade block-off

As Figure 5-12, a plot of the axially aligned velocity component W clearly shows, the velocity field does not exhibit any deviations in the blade region thereby confirming that the local lack of asymmetry does not engender any flow turning when body forces are applied.

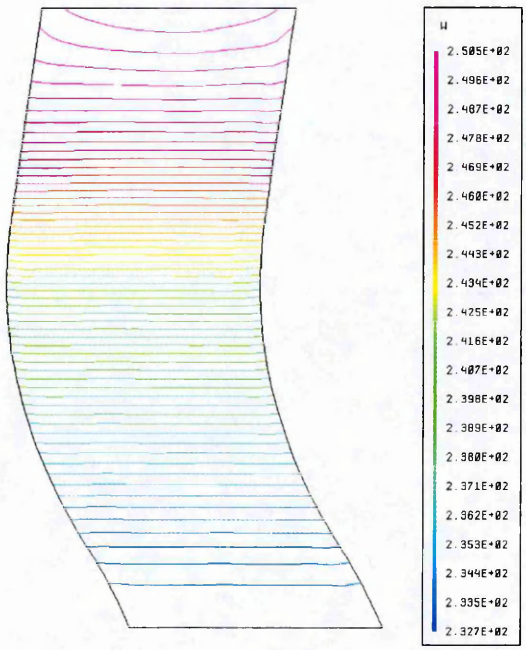

Figure 5-12 HP9 stator domain plot of W component of velocity at mid-span

5.4.2 Solution parameters and boundary conditions

The available set of experimental data comprises three flow conditions, maximum-flow, mid-chic and near-surge corresponding to the mass flows of 9.70, 8.75 and 7.23 Kg/s as outlined in Table 5-3. For each of these operating points, area-averaged radial profiles of total pressure at the rotor inlet experimental data collection plane, and of static pressure at the stator exit plane, marked ① and ③ respectively in Figure 5-7, are available for use as inflow and outflow boundary conditions.

However the requisite to preserve the shape of the inlet pressure profile and hence the description of the thick endwall boundary layers which are a feature of this case, was thought to be problematic given the axial distance between the experimental inlet plane and the computational domain inlet and the considerable tapering of the hub between the two.

To ascertain whether a noticeable departure from the experimental inlet profile caused by the boundary displacement did indeed take place, a simple grid of the inlet region between the two planes was assembled, Figure 5-13, and a number of runs carried out at the max-flow condition. These runs highlighted the need to align the inlet local velocity vector with the hub taper in order to produce the closest possible agreement between the experimental plane pressure profile and its local numerical equivalent.

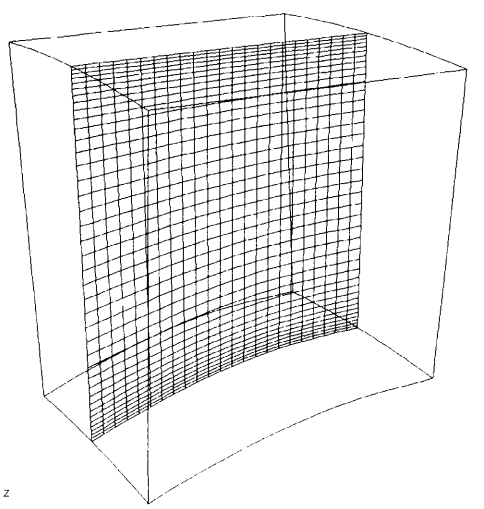

Figure 5-13 Reduced rotor inlet domain

Figure 5-14 presents a comparison between four radial profiles of total pressures for the same operating point, max-flow. The first profile was acquired experimentally at the rotor inlet plane, the second and third set as inlet boundary condition for the reduced domain and the calculated profile at outlet respectively, and the final is the profile calculated by the full stage grid at the same axial station.

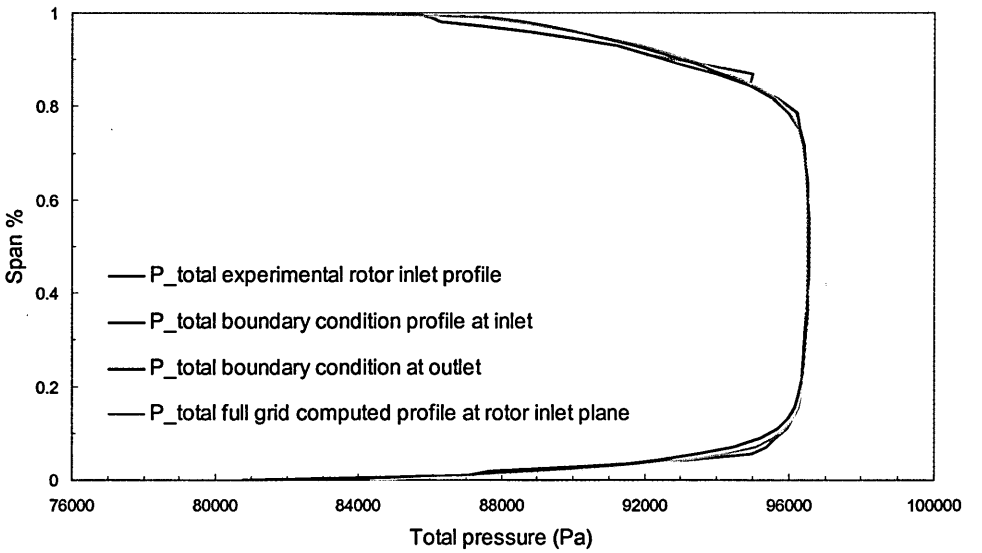

Figure 5-14 Comparative plot of radial rotor inlet total pressure distributions

At the outflow of the stage domain the use of the experimental static pressure radial distributions, Fig. 14, was found to yield mass flow values which were slightly different from the target for the particular operating point i.e. –2.5 % for max-flow and +3.3 % at mid-chic.

This discrepancy is supposedly attributable to the use, for the establishment of the static pressure radial profiles, of the extrapolation of the measured outer wall value across the annulus using a static pressure gradient estimated using throughflow analysis. As a result the outlet boundary condition is set as an average value of static pressure whose radial distribution is determined by local radial equilibrium.

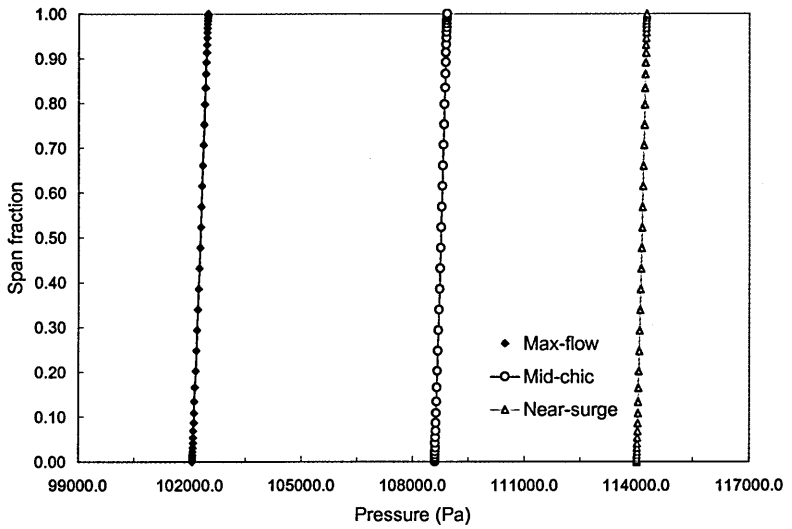

Figure 5-15 Radial profiles of static pressure at stator outlet

As the three flow conditions are stated in terms of mass flow values, it would be reasonable to prescribe this as one of the boundary condition and given the noted requirement of the supply of an inlet total pressure and hence velocity profile, it would then be natural to specify mass flow as the outlet boundary condition. However some attempts to run the code with this combination of boundary conditions met with failure as shown in Figure 5-16, the convergence history plot of mass flow exit boundary condition, making the use of a static pressure boundary condition over this region inevitable.

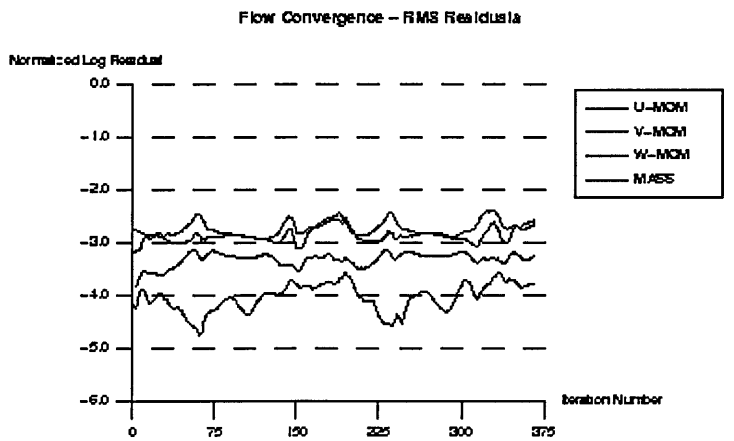

Figure 5-16 Convergence plot of mass flow exit boundary condition

The consequence of this selection is however, that to achieve a 'hit' on the target mass flow through back pressure variation, becomes a very time consuming process and the results presented herein are in fact based on approximate values with reference to those of the experimental dataset rather than those exact figures themselves.

The simulation was carried out with the VISCOUS_WORK_MODEL parameter enabled. The fluctuating viscous work terms arise from the time-averaging of the energy equation and are analogous to the Reynolds stresses in that they also cannot be expressed as functions of the mean flow variables and are therefore dependent on a turbulence model for the supply of a closure form. These terms are cast as $\overline{\rho\, u_i'' \tau_{ij}''}$ and for inclusion in the energy equation they are approximated as $\frac{\partial(\overline{\rho\, u_i'' \tau_{ij}''})}{\partial x_j} \approx \overline{\frac{\partial}{\partial x_j}\left(\mu \frac{\partial \tilde{k}}{\partial x_j}\right)}$ subject to the assumptions that the turbulence is isotropic and homogeneous and that the density fluctuations can be ignored for the purpose of turbulence modelling and hence that $\tilde{k}$, the mass weighted form of the turbulent kinetic energy, can be represented by k, its steady-state equivalent.

The default form of the energy equation implemented in TASCflow neglects the viscous stress work terms and indeed the equivalent modelled Reynolds terms but in version 2.7.3 the parameter VISCOUS_WORK_MODEL was introduced as an option of the high-speed model whose features were deemed by the code's manual not to impact significantly on the simulation of flows whose Mach numbers are below three. In the latter versions of the code, 2.8 onwards, it is recommended that this parameter be used in all high speed flows as a default in order to obtain the most accurate prediction.

The time-step is specified via the parameter ETFACT, the distorted time step factor, this being set at a value of 5. In TASCflow the ETFACT parameter can be set between 3 and 20 with the first of these values corresponding to maximum solution robustness although at a minimum convergence speed and vice-versa for the upper bound. The selection of a very low local time step factor proved to be robust enough to provide a shallow convergence rate. The Modified Linear Profile Scheme advection scheme, corresponding to setting the ISKEW parameter as 3, was employed together

with the PAC term. The inlet turbulence boundary conditions were set as 3% turbulence intensity and 10 mm eddy length scale.

The convergence criterion was set as an rms residual target of 5.000E-07 but this was matched with a maximum ceiling of 1000 iterations, the simulation being interrupted as soon as the first of these conditions was met. An additional measure of convergence was provided by the examination of the difference between the inlet and outlet mass flows, with net flow values of the order of 10^{-5} and below corresponding to well converged solutions. The typical CPU runtime on a EV5 processor was about 130000 seconds or one-and-half days for around 600 iterations with the solution occupying some 120MB of RAM or about 1000 bytes per node when employing the default single precision setting.

5.4.3 HP9 large grid baseline results

Of the three flow regimes for which experimental data is available only the two highest one have been successfully simulated with the present grid. Compressor rotors operating at low mass flows where large tracts of blade separated flow are known to occur are beset, even when seen from a steady-state relative frame, by temporal and spatially unsteady flows. The presence of such varying conditions, is by definition incompatible with a steady-state approach, where the convergence process is dependent on the subsequent solution iterations solving a flow field, where the succeeding changes are those introduced by the computation process alone.

Furthermore it is worth recalling that for closely coupled stages the intra-blade spacing is often so small that the placement of mixing-planes in the middle of these regions constrains the individual row domain to contain too small a space over which the code can resolve the large gradients often found in these regions, a situation leading to well known convergence difficulties.

5.4.3.1 Overall performance calculations

The integrated global performance results of the baseline simulations, where no source terms are added to the basic code formulation, are presented in a tabular configuration below as well as in the form of plots. The calculation of the pressure ratio was done in accordance with the method mentioned in 5.2.7.

Performance parameter	Operating point	Numerical	Experimental
Pressure ratio	max-flow	1.189	1.196
	mid-chic	1.251	1.236
Temperature ratio	max-flow	1.062	1.061
	mid-chic	1.076	1.080
Adiabatic efficiency %	max-flow	82.3	85.7
	mid-chic	86.7	88.3

Table 5-4 Comparison between the experimental results and large grid numerical predictions for the HP9 test case

An examination of the overall performance parameters of Table 5-4 will predictably single out adiabatic efficiency as a quantity whose numerical estimate is significantly flawed. Recalling the expression for adiabatic efficiency,

$$\eta_{isen} = \frac{PR^{\frac{\gamma-1}{\gamma}} - 1}{TR - 1} \tag{5-4}$$

where PR and TR are the pressure and temperature ratios respectively, it is apparent that η is far more strongly affected by any given variation in TR than an equivalent variation in the PR term. This effect is graphically illustrated in Figure 5-17 below, were both pressure and temperature ratios are independently varied by between plus and minus 1% while keeping the value of the other parameter constant.

What this figure shows is that the efficiency shortfall, measured between the horizontal blue and red lines, can either be made up by some 0.3% *decrease* in temperature ratio or about a 0.9 % *increase* in the pressure ratio.

Put in other terms, one can attribute the efficiency miscalculation to either an underestimate by the code of the pressure rise or an overestimate of the temperature or indeed a combination of both but in all cases it translates into an overestimate of losses.

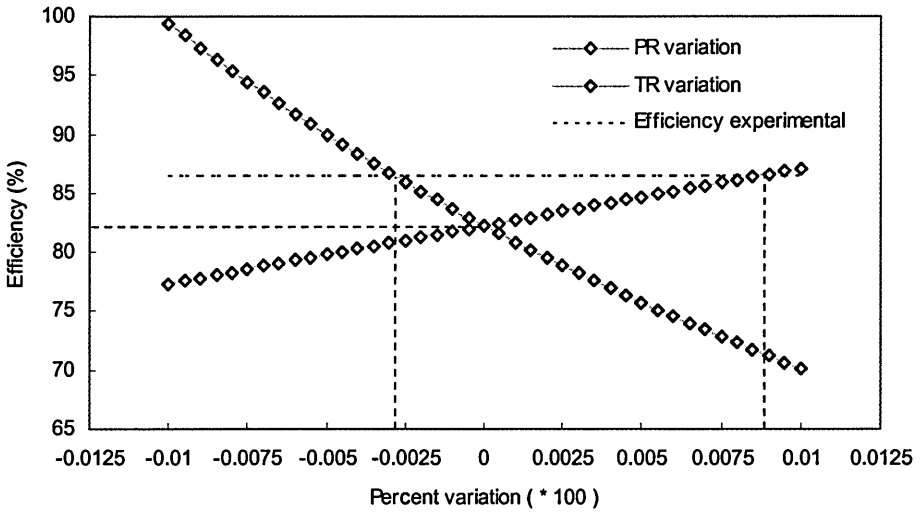

Figure 5-17 Efficiency variation with change in *PR* and *TR* terms

There is little and conflicting evidence in the wide turbomachinery CFD literature about the ability of codes to accurately compute global values of efficiency. One can examine many dozens of papers covering numerical predictions and find precious little in terms of reported efficiency results which include either single global values or even radial profiles.

A part explanation for this scarcity of information can be found in a paper by Chima, 1998: There are many reasons for the scarcity of turbomachinery performance calculations in the early literature. One reason is that pressure field calculations are relatively independent of viscous effects and can be calculated with simple models. Conversely, efficiency and loss calculations are highly dependent on viscous effects

and require careful attention to the viscous terms, turbulence modelling, artificial viscosity and grid resolution for successful calculation.

A useful overall view of performance parameter calculations is contained in a 1999 paper by Hah and Loellbach of NASA Lewis: As is widely recognized in the turbomachinery aerodynamics CFD community, the current generation of CFD codes provides very useful numerical solutions for design purposes. The most useful information from CFD solutions is obtained by calculating variations between different designs. Because current turbulence models do not accurately represent the complexity of real flows, and numerical procedures need further refinements, CFD calculations do not always predict absolute values of aerodynamic properties accurately. Accurate prediction of changes in aerodynamic parameters due to changes in the design can be more important than the prediction of absolute values. Accurate prediction of the shapes of spanwise property distributions can also be more useful than the absolute values of integrated properties.

The AGARD report of the Propulsion and Energetics Panel Working Group which examined some eighteen simulations of the NASA Rotor 37 case, Dunham and Meauzé, 1998, noted that most codes predicted too high a pressure ratio and too low an efficiency. Interestingly of the two TASCflow entrants, 250000 and 72000 nodes grids, the coarsest one showed the closest agreement. The efficiency underprediction was on average some 3% between 10 and 80% of the blade span but near the tip the efficiency deficit was much larger suggesting that the final figure could have been one or more points greater.

What then is the reason for the CFD underestimation of efficiency? Of the many possible contributing factors of either aerodynamic, geometric or CFD modelling origin, the most applicable to multi-stage simulations may well be that advanced by Bolger and Horlock, 1995: " This effect [the impact of a particular mixing plane treatment] can be minimised by a reduction in grid spacing between blade rows although the calculated stage efficiency is compromised to a much greater extent by the assumption of fully turbulent boundary layers throughout the calculation domain. In reality, significant portions of laminar flow do exist on the blade surfaces. "

5.4.3.2 Radial distributions

The predicted radial distributions of pressure ratio, temperature ratio and adiabatic efficiency are presented in Figures 5-18 through to 5-20 for the max flow condition and Figure 5-21 through 5-23 for the mid-chic point.

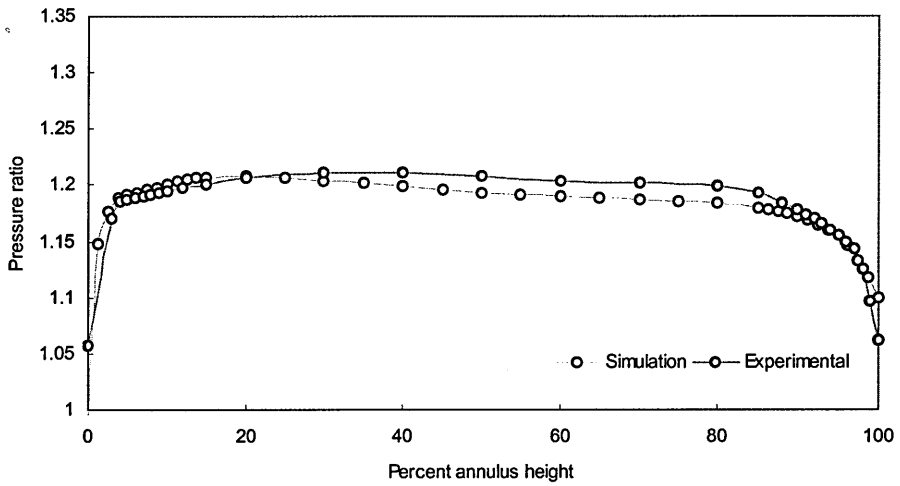

Figure 5-18 Radial distribution of total pressure ratio at max-flow

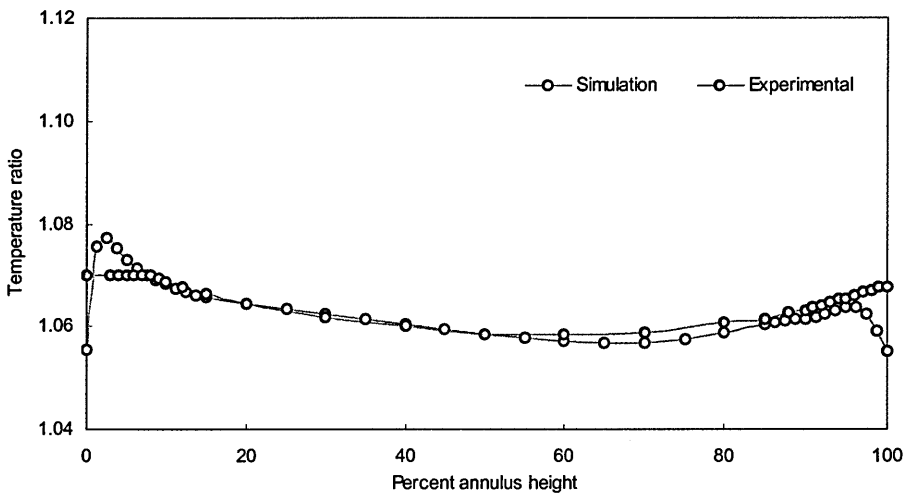

Figure 5-19 Radial distribution of total temperature ratio at max-flow

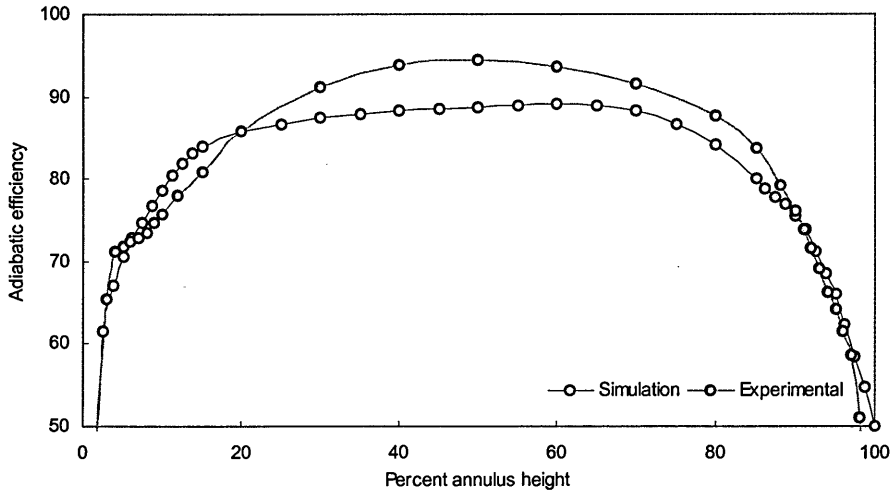

Figure 5-20 Radial profiles of adiabatic efficiency at max-flow

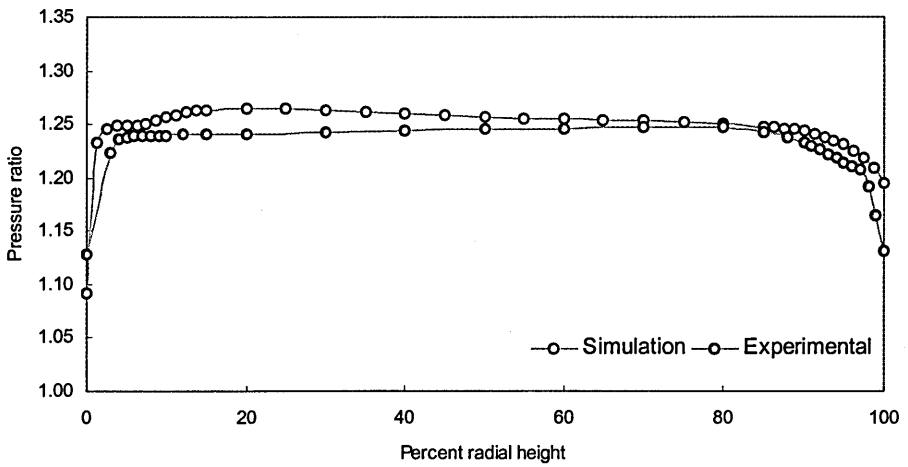

Figure 5-21 Radial distribution of total pressure ratio at mid-chic

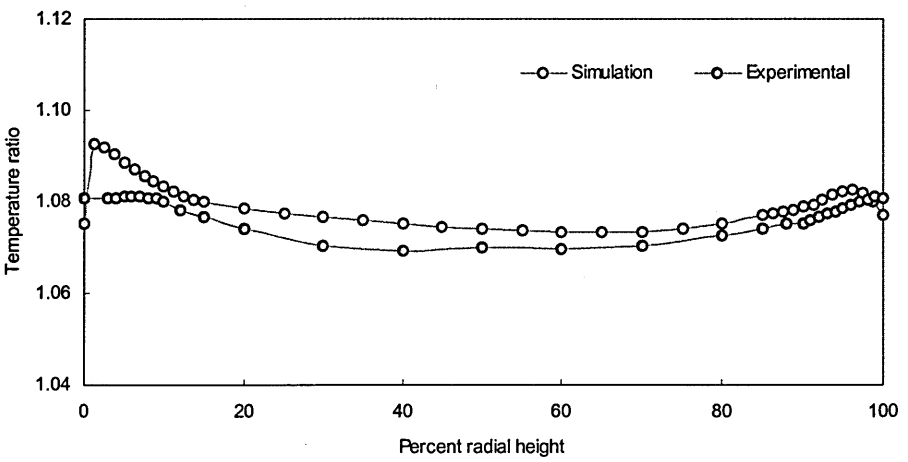

Figure 5-22 Radial distribution of total temperature ratio at mid-chic

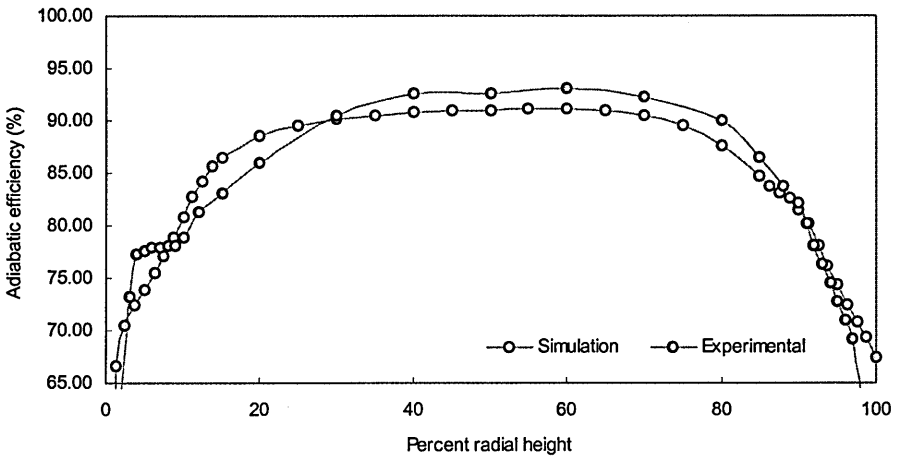

Figure 5-23 Radial profiles of adiabatic efficiency at mid-chic

The method employed to compute the radial plots of pressure ratio is based, as for the global values, on the use of a single inlet pressure value as seen before. All the radial plots show that for the performance parameters there is generally good agreement between the computed and measured quantities in terms of the broad shape of the radial distributions. Locally there are some discrepancies namely near the endwalls, particularly for the temperature ratio, and in the mid-span region in the case of the adiabatic efficiency.

It is worth noting that although the numerical model does not represent the tip clearance, no appreciable difference between the two sets of results in the near shroud seems to result. This is probably due to the fact that the rotor blade geometry is known to present an uncommonly tight fit near the shroud and therefore the predictable occurrence of sizable losses in that region is not seen to occur.

The computed and experimentally obtained yaw angle values for rotor inlet, rotor outlet and stator outlet are displayed in Figure 5-24 through 5-26 for the max flow condition.

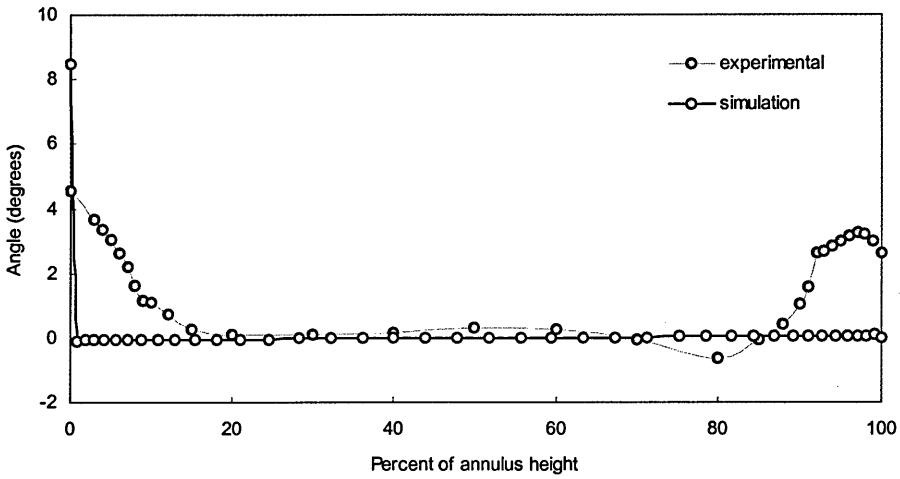

Figure 5-24 Rotor inlet yaw angle radial traverse at max flow

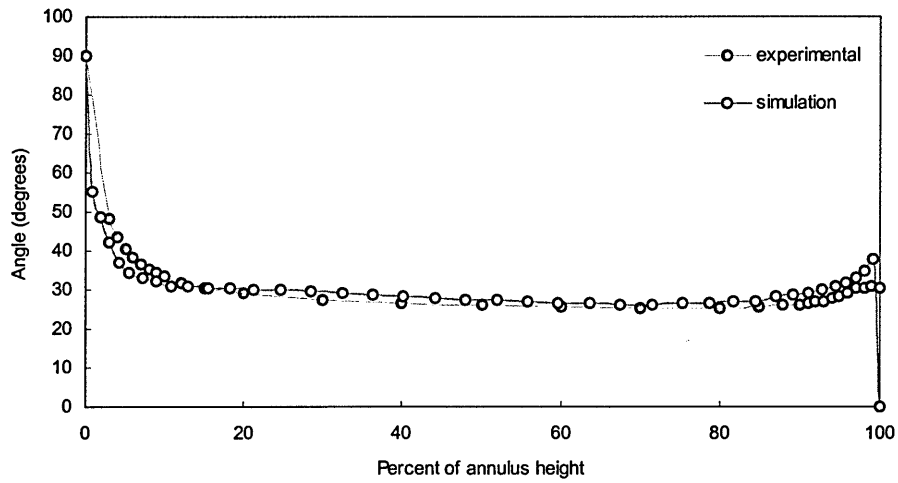

Figure 5-25 Rotor outlet yaw angle radial traverse at max flow

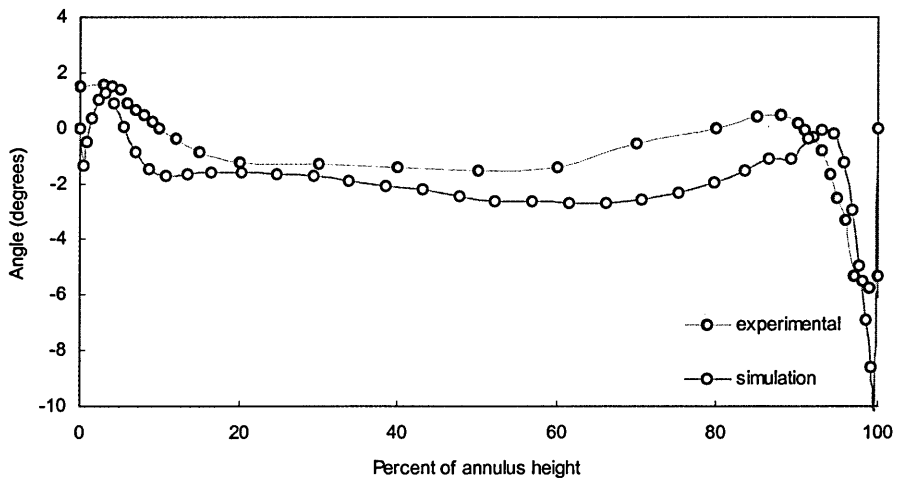

Figure 5-26 Stator outlet yaw angle radial traverse at max flow

The level of agreement is again quite reasonable when the different scales used in the plots are considered.

Another source of comparison data is the work carried out as a S1-S2 simulation, Calvert, 1992, in what is the only known numerical study of this build of the HP9 compressor stage to have been published to date in the open literature. For this purpose the TASCflow numerical results are superimposed over scanned plots from Calvert's paper where the S1-S2 results are themselves validated against the experimental results. Given the approximate nature of the purely graphic overlay this comparison provides at best a rough estimate of the relative performance of the two numerical methods.

The experimental quantities employed in the assembly of the following plots are the stator outlet area traverse rather than the radial traverses as used above. The experimental data originating from the stator exit area traverses is subject to an arithmetic circumferential averaging process but where needed overall mean values were derived from radial distributions by area-weighted averaging.

Although the level of agreement of the TASCflow simulations is generally better, particularly for the max flow condition, it is remarkable by how much the predictions of a supposedly less sophisticated method can approach the experimental values and 3D RANS results.

The S1-S2 method used by Calvert is an inviscid code which is connected to a viscous calculation part, consisting of three parts to estimate the corresponding phases of boundary layer development, and which can be employed to calculate blade section overall performance such as exit flow angle and losses. When used in the prediction of complete blade rows, a throughflow calculation is coupled to the code in order to provide an evaluation of the spanwise variations of the flow and ensure that radial equilibrium is satisfied.

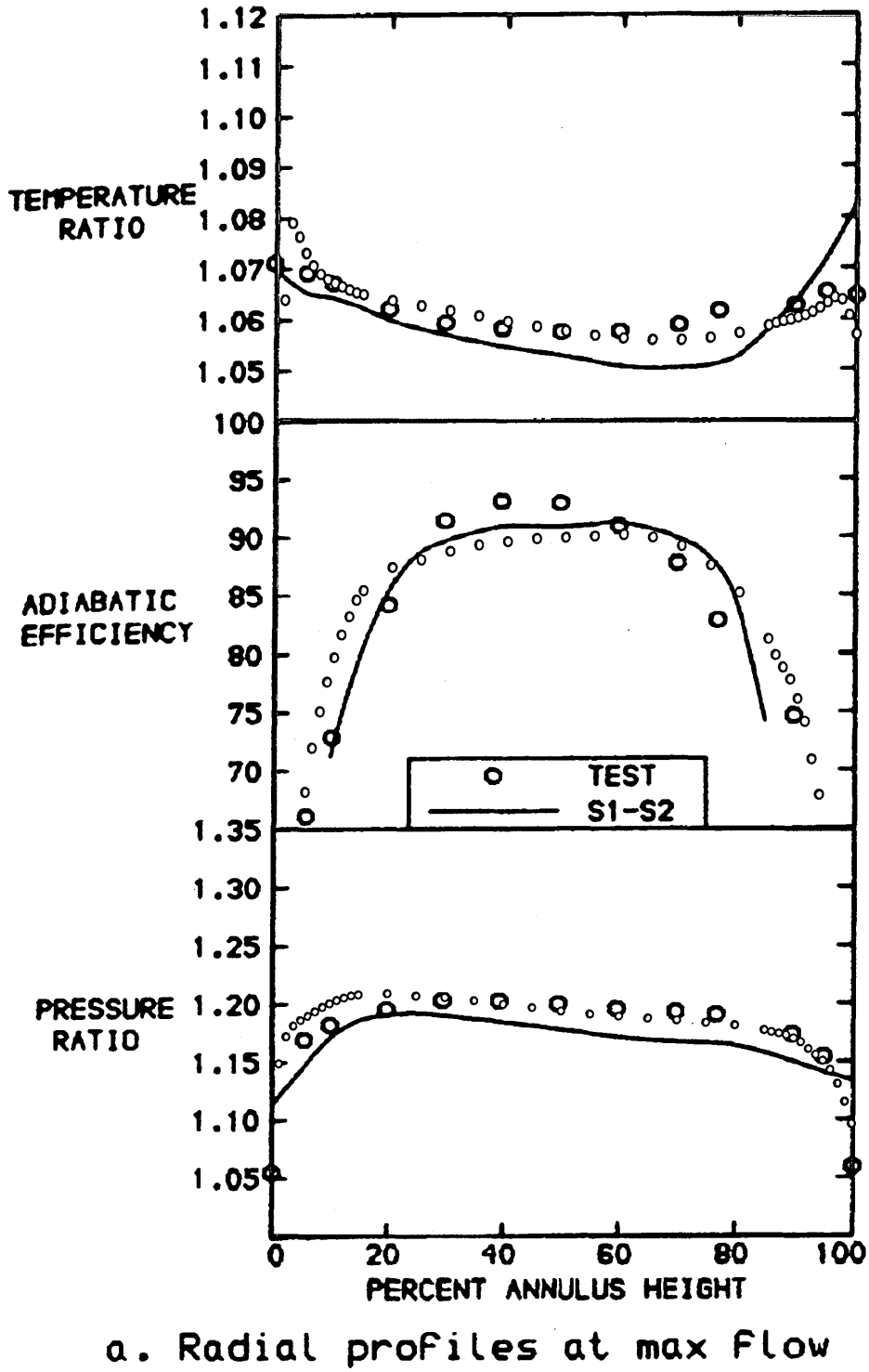

Figure 5-27 S1-S2, experimental and TASCflow results comparison at max flow

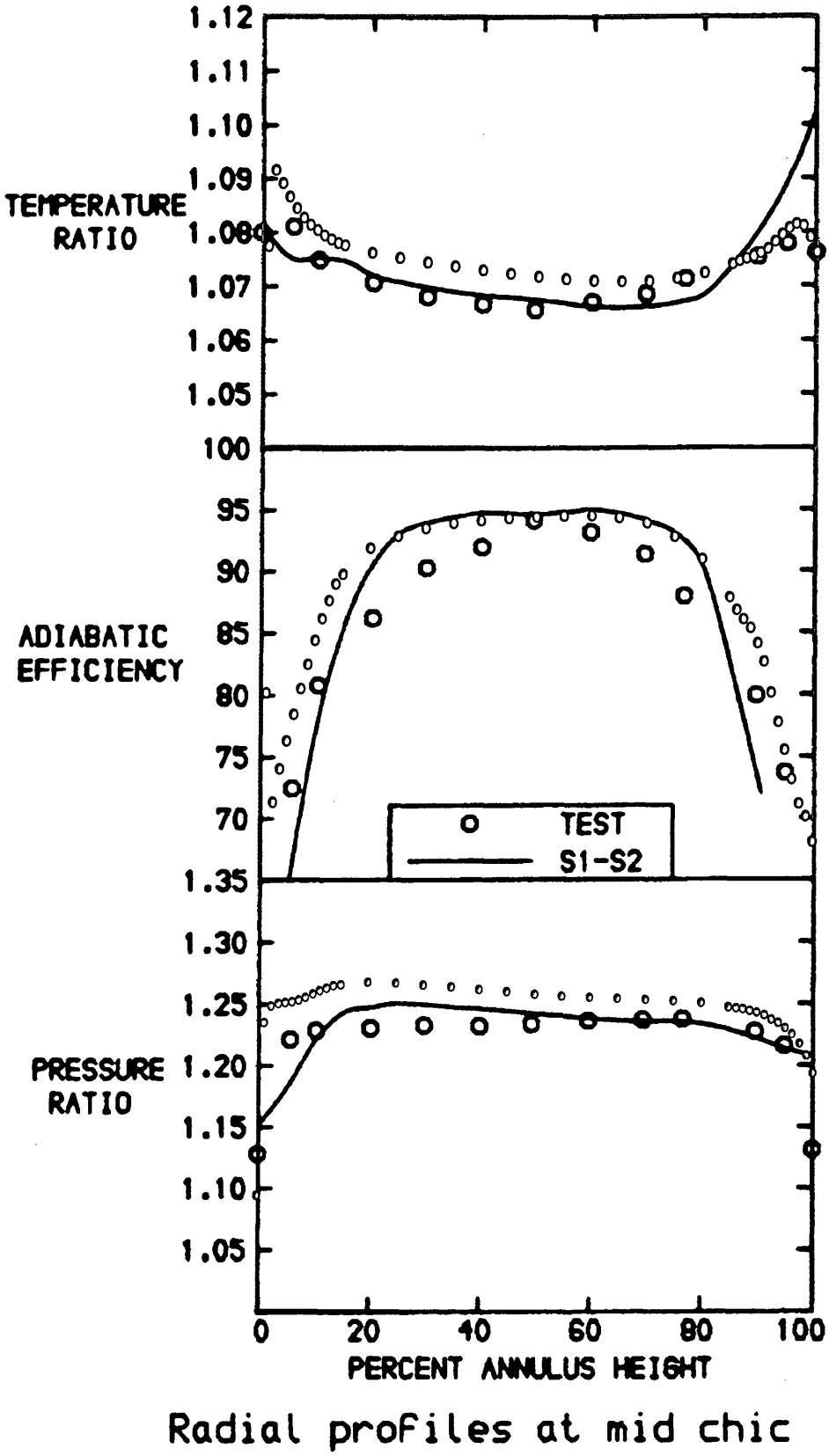

Figure 5-28 S1-S2, experimental and TASCflow results comparison at mid chic

In practice the S1-S2 method is dependent on the empirical supply of extra loss information near the blade ends and though this dependence acts as a limitation on the generality and automation of the method it also enables the tuning of the model for a given compressor and the achievement of a correspondingly high degree of accuracy as is seen in the present case.

Further comparisons with the results presented in Calvert's paper are the mid-span Mach number contour plots, Figure 5-29 through to Figure 5-36.

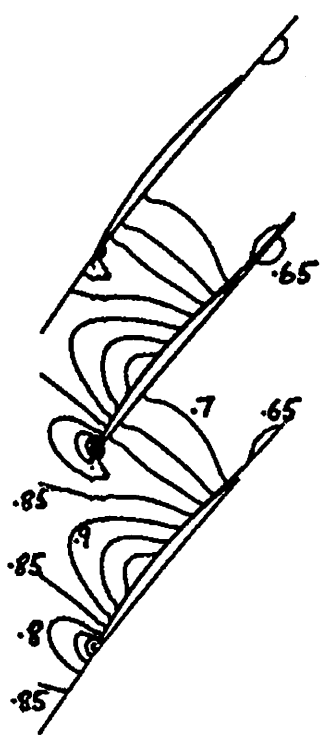

Figure 5-29 S1-S2 rotor Mach number contour predictions at max flow

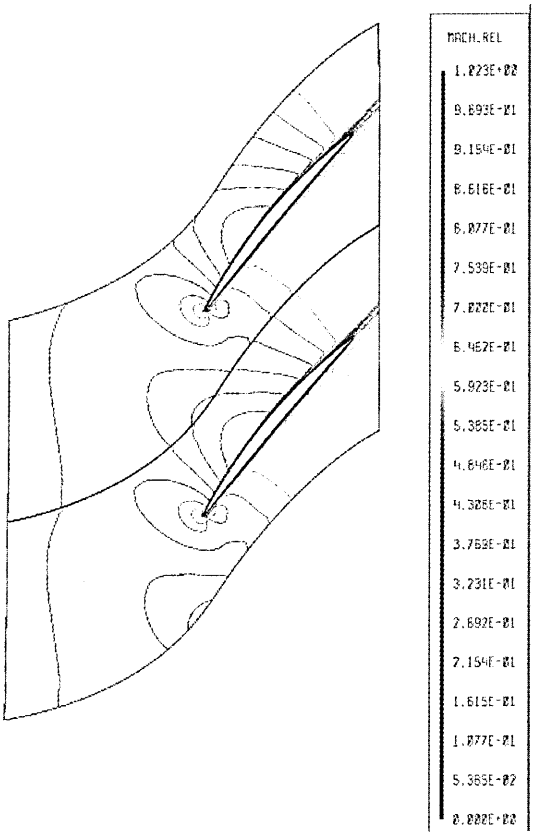

Figure 5-30 TASCflow rotor Mach number contour predictions at max flow

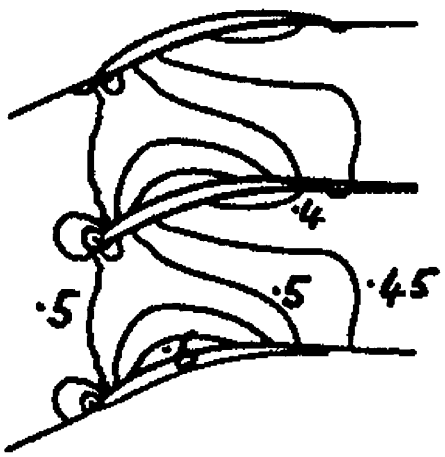

Figure 5-31 S1-S2 stator Mach number contour predictions at max flow

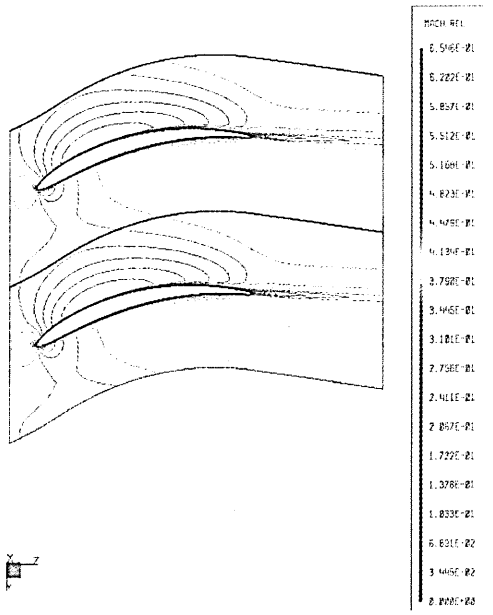

Figure 5-32 TASCflow stator Mach number contour predictions at max flow

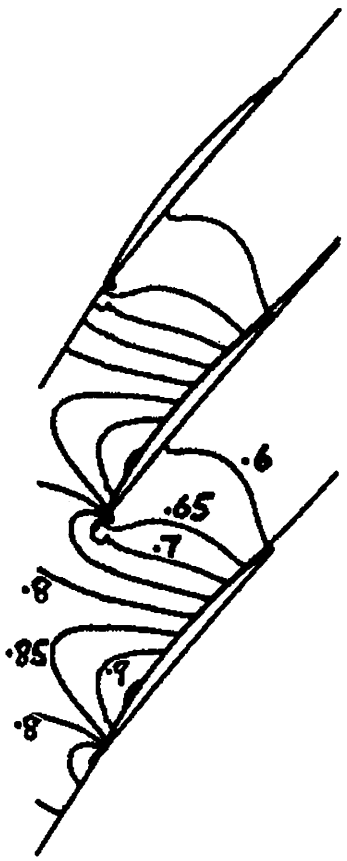

Figure 5-33 S1-S2 rotor Mach number contour predictions at mid-chic

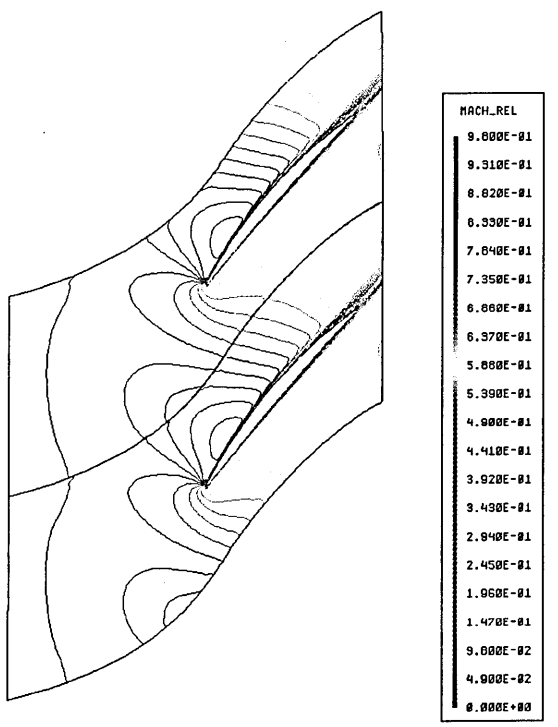

Figure 5-34 TASCflow rotor Mach number contour predictions at mid-chic

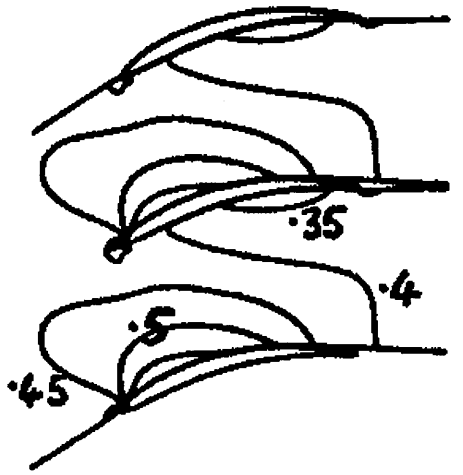

Figure 5-35 S1-S2 stator Mach number contour predictions at mid-chic

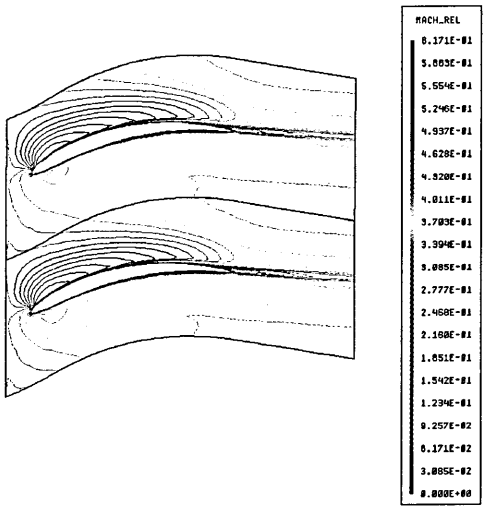

Figure 5-36 TASCflow stator Mach number contour predictions at mid-chic

Generally there is good agreement between the results of the two methods, S1-S2 and TASCflow, but in specific regions the output of the two codes shows Mach number patterns having dissimilar distributions. A further source of comparison between experimental and numerical results are the waterfall plots of total pressure and total temperature obtained from stator area traverses.

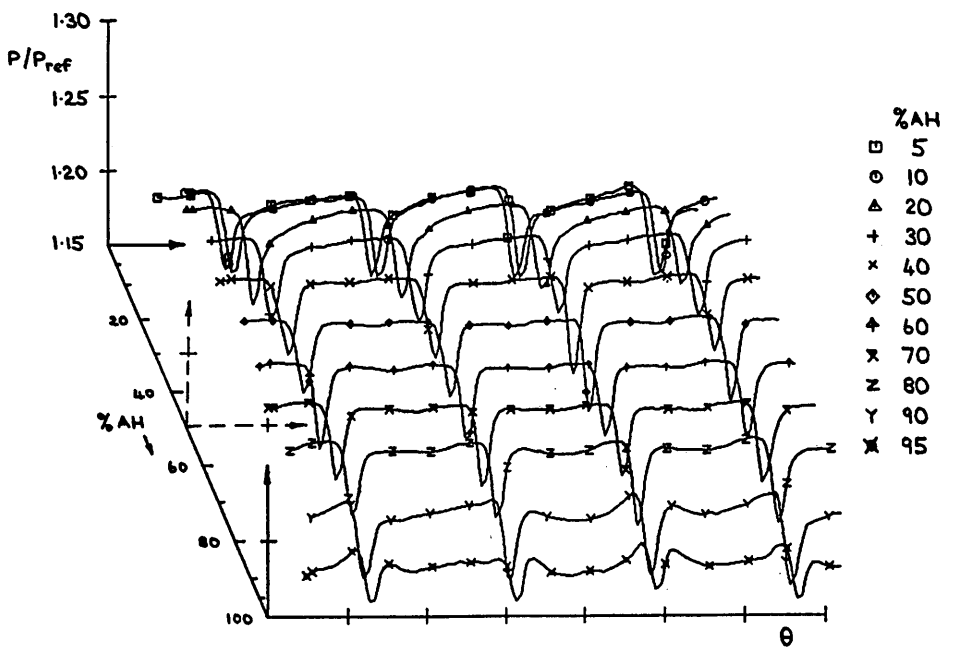

Figure 5-37 Total pressure area traverse at max flow – experimental results

The comparison is restricted to the max flow condition and three radial locations for the total pressure and a single point for the total temperature.

The wake profiles such as that of Figure 5-38 have been isolated from the particular waterfall plots for evaluation purposes.

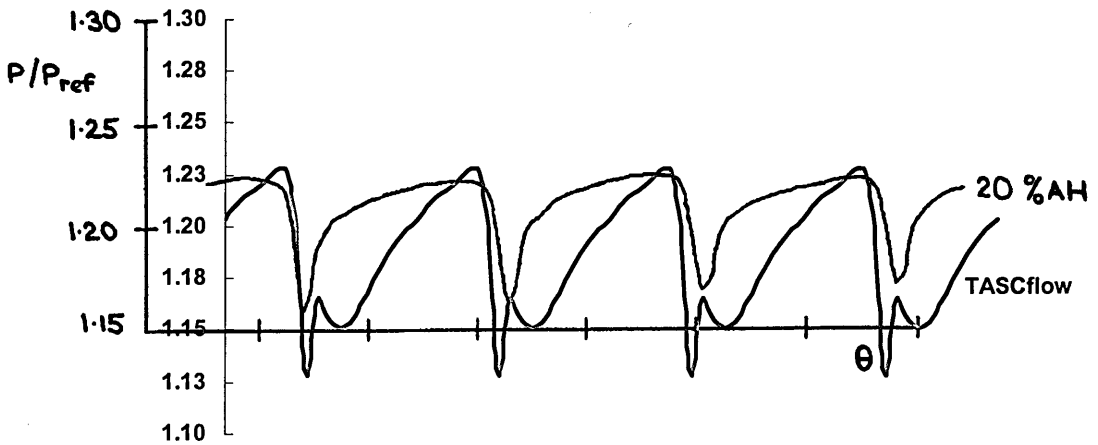

Figure 5-38 Stator outlet total pressure comparison at 20% span

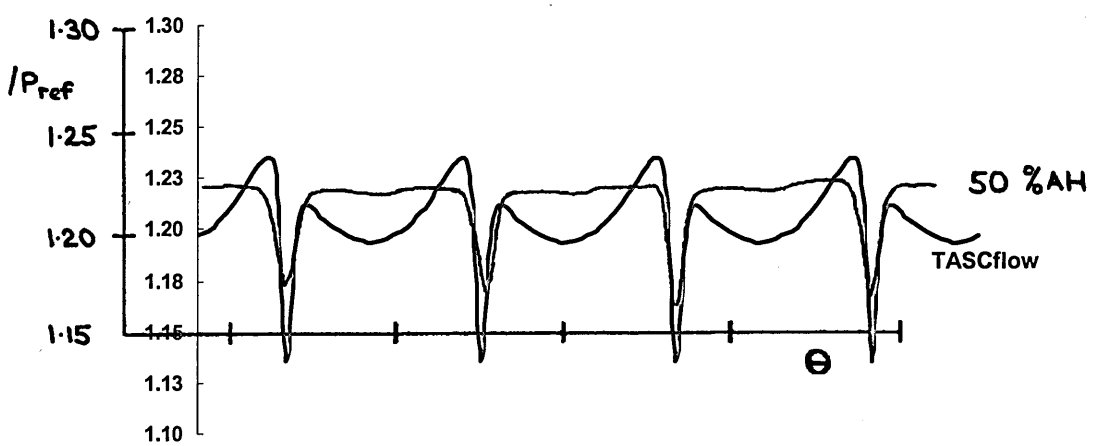

Figure 5-39 Stator outlet total pressure comparison at mid-span

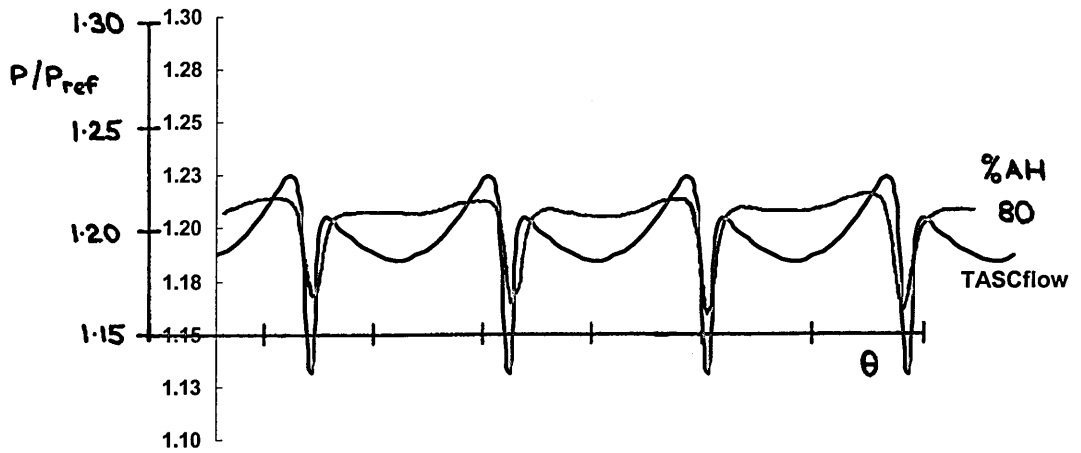

Figure 5-40 Stator outlet total pressure comparison at 80% span

The level of agreement between the pitchwise distributions of total pressure of experimental and numerical origin is, for the max flow regime, patently poor. The wakes calculated by the CFD code are invariably deeper, narrower and much less regular than that which is presented by the experimental data. Despite the approximate nature of the comparison, due once again to the simple superposition of graphs, the differences are unmistakable and consistent.

The narrowness of the wakes predicted by steady-state simulation when compared to the equivalent experimental results is due, as was pointed out in the previous chapter, 4.4.1.2, to the fact that conventional steady-state computations lack information on the random and deterministic stage interaction effects and hence of the spatial perturbations of the viscous wakes. When presented in an averaged form these perturbations will define the mean location of the wake as occupying a wider area than what was suggested by the steady-state simulation.

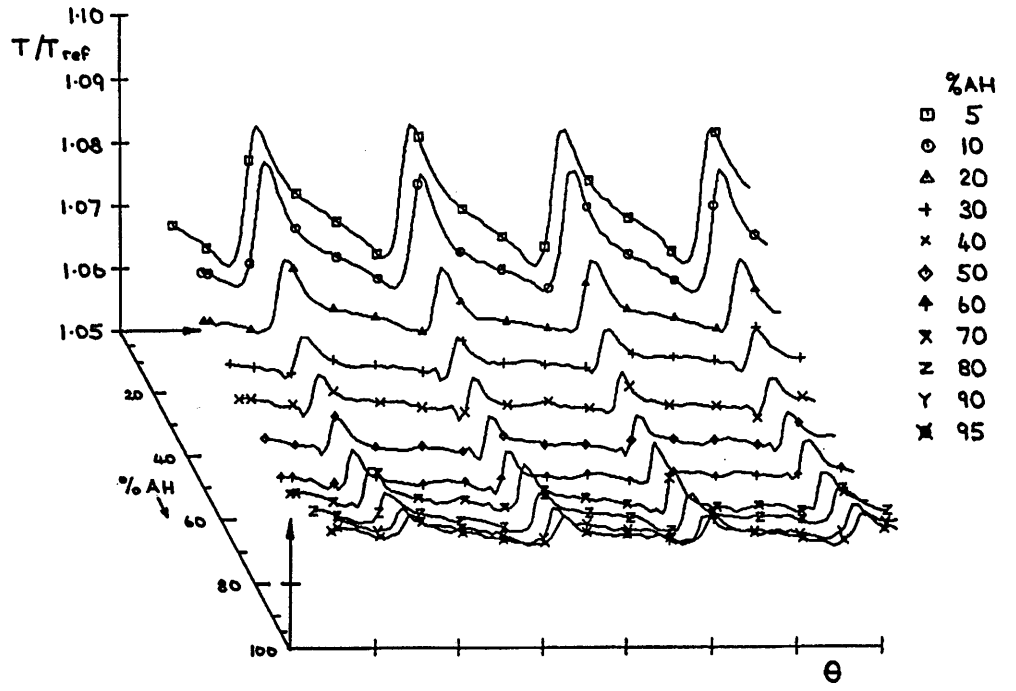

Figure 5-41 Total temperature area traverse at max flow – experimental results

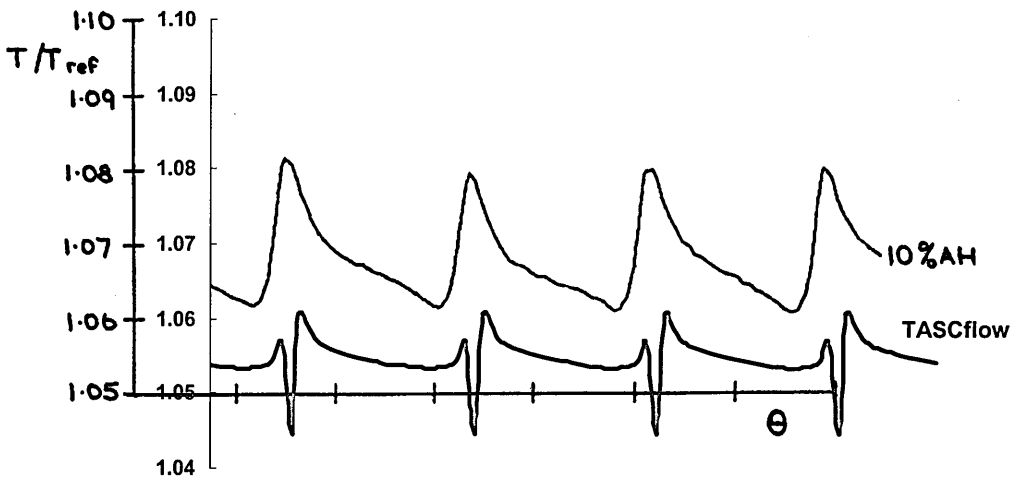

Figure 5-42 Stator outlet total temperature comparison at 10% span

In terms of total temperature the agreement is even more tenuous with the two methods showing significant differences in both values and distribution

configurations. Nevertheless when the amplitude of the fluctuation is considered then the agreement between the two sets of data is actually much more acceptable.

It is worth remembering when analysing in a comparative manner the two sets of plots that the CFD simulation assumes a steady distribution of variables, in both time and space, while the experimental method depends on the measurement of dynamic quantities which, even when the measuring technique can only supply mean quantities, aren't necessarily accurately characterized by a pre-emptive steady-state mean representation.

5.5 Unsteady simulation

As has been stated in Chapter 3 the code gained an unsteady capability throughout the duration of the research programme and it was therefore decided to make use of this feature to conduct a set of unsteady runs of the HP9 case. The objective of these simulations was to calibrate the decay parameters contained in Bolger's model as well as to acquire a feeling for the magnitude of values that are known to separate the flow fields computed through a steady-state method and by time-averaging an unsteady calculation. Additionally the deterministic stresses which correspond to a given operating point can be directly calculated from these simulations, their magnitudes compared with the values obtained from the two semi-empirical models and further the effects of their injection back into a steady-state analysis evaluated.

5.5.1 Background comments

Before the introduction of a TASCflow unsteady computation facility it had been the intention to make use of the work of a contemporary student of the Cranfield turbomachinery CFD group, to perform the unsteady simulation runs on the HP9 case. This work consisted of the coupling to a steady-state simulation of the 'external' solution of the unsteady term, $\frac{\partial(\rho\phi)}{\partial t}$ and the inclusion of its effects as source terms of the conservation equations, Koumoutsos, 1999. Instead the timely release of a TASCflow proprietary version enabled this be the approach taken in order to benefit

from the ancillary post-processing features inbuilt in the unsteady version code. Use has nevertheless been made of the experience acquired by A. Koumoutsos in the running of TASCflow in an unsteady mode in the selection of run parameters, etc.

The central issue concerning an unsteady multi-blade row simulation, is that of the treatment of the periodicity of the pitch of the adjacent components, the three established ways to tackle the problem having been introduced in Chapter 1, together with the mention of the earlier proponents of the distinct approaches. The method adopted by the code which is employed in this work, corresponds to that described in Rai, 1987, which consists of enforcing, through a scaling operation, the pitchwise geometric periodicity.

Recalling that the blade count for the HP9 stage is 73 blades for the rotor and 41 for the stator, it can be seen that no exact periodic combination exists other than when the whole two blade rows are considered. In three instances a number of blade count combinations present a quasi exact angular displacement on both stage components, Table 5-5, but even the most favourable of these, 9 rotor blades and 16 stator blades would present, for the computational assets available at the time of the present study, an untenably large demand on resources and time.

Rotor blade number	**Rotor angular displacement (deg)**	**Stator blade number**	**Stator angular displacement (deg)**
9	79.02	16	78.90
23	201.95	41	202.19
32	280.98	57	281.10

Table 5-5 Pitch angular displacements for HP9 blade geometry

It follows from the argument above that the only practicable option consists of modifying the geometry according to the approach developed by Rai and to this end the stator blade count was assumed to be 82, rather than 73, corresponding to a 73/82 or 0.890 factor reduction in the blade passage pitch. In this way one rotor and two

stator blades can be joined together for simulation purposes, while ensuring that the pitch ratio of the combination is set to one. The scaling operation performed on the blade pitch requires in turn that the stator blading axial chord be accordingly scaled down by the same factor so that the pitch-to-chord stator ratio remains unaltered. The importance of retaining this ratio lies in its direct effect on the generation of blade borne blockage, Yang and Lin, 1994, and the need to maintain that quantity constant following the scaling process.

The choice of grid size was primarily determined by the storage requirements of the code when operating in a time-dependent mode, as well as by the size of the forecasted simulation clock time, both of which had been the subject of investigation during the research work of A. Koumoutsos alluded to above. For that reason a broad limit of about 100,000 nodes was adopted with the gridding of the domains being performed in TASCgrid. The rotor grid contains 26 nodes in the radial, 33 in the pitchwise and 62 in the axial directions and each of the two identical stator grids 26, 21 and 57 in those same directions, the total figures being 53,196 nodes on the rotor domain and 31,122 nodes on each of the stators amounting to a grand total of some 115,440 nodes.

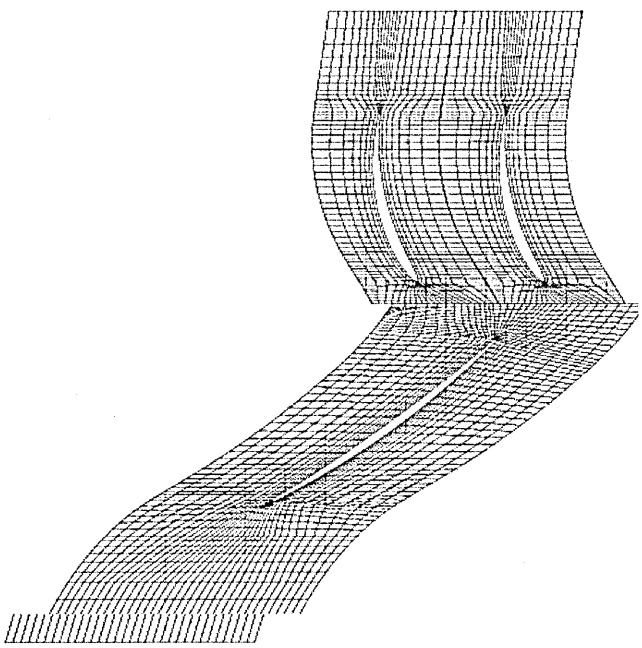

Figure 5-43 Blade-to-blade perspective of unsteady-simulation grid at mid-span

In the stator grids the lines which are broadly orthogonal to the machine axis are set in an axisymmetric manner whereby all the nodes at a given axial and radial station share the same relevant coordinate values. This configuration is a requirement brought about by the constraints of Adamczyk's deterministic stress model.

The grids are quite coarse in terms of what is the standard of the late nineties Navier-Stokes simulations, even when considering a time-accurate calculation. Nevertheless it was felt that the exercise could provide worthwhile information despite its evident limitations. Solutions obtained in the past with about 40,000 nodes per blade element, for example Krain et al., 1989, have been able to capture sufficient flow physics and be in sufficiently good agreement with data to make the exercise worthwhile, Dawes, 1995.

5.5.2 Unsteady simulation parameters and boundary conditions

The solution procedure consists usually of the calculation of a large number of time steps, each of which corresponding to a relative angular displacement of the rotating component, and the computation, within the individual time steps, of a number of iterations in order to resolve the new flow field that is consistent with the updating of the transient geometry of the machine.

Although it is possible to start an unsteady rotor/stator computation from a simple initial guess, it is far more economic in time and resources to employ a 'Frozen Rotor' converged solution as a starting point for the unsteady simulation. It will be recalled that in a Frozen Rotor type of connection of two adjacent rows, the relative motion between the components is suspended and the numerical interface plane, through which the two grids are connected, acts purely as a 'transparent' connection, through which the flow of information in both directions is freely exchanged.

This situation portrayed by a Frozen Rotor solution is equivalent to obtaining a snapshot in time of the unsteady flow field and is readily employable as the distribution relating to the time nought of the unsteady simulation.

The selection of the size of time step is not subject to any specific limitation other than the need to resolve the flow fields associated with the relative change in position of the components. Given the implicit nature of the solution scheme the employment of the Courant number as the time step selection criterion lacks justification. Nevertheless the code manual suggests the selection of a time step in the range of $0.01/\omega$ to $0.05/\omega$, where ω is the angular velocity.

The setting of the time step was done by considering the time lapse occupied by one whole revolution of the machine and from here the part corresponding to a single rotor blade. This value which in HP9 is 0.0001579 seconds is then divided by the discrete number of time steps selected for the completion of a single blade sweep. As part of the present work an investigation was conducted into the effects of the time step variation on the robustness of the solution given the severe initial convergence difficulties frequently experienced. As a rule it was seen that an increase in the size of the time step was accompanied by a strengthening of the overall convergence behaviour. Initial runs making use of 30 time steps per pitch sweep, corresponding to an individual time step of 5.2662 E-06, were consistently leading to the crashing of the code. The variation of the number of iterations per time step, from a minimum of 15 up to 30 showed no impact on the overall robustness of separate solutions.

It is now thought that the origin of these failures is attributable to problems associated with the numerics of the early unsteady capability implementation within the code which are known to have been addressed in latter versions. Nevertheless at the time the transient simulations were performed, the way around the time step limitation involved obtaining a repeating time history pattern while employing about 12 time steps per blade sweep, δt =1.316567 E-06, and then doubling this number for a small number, 3 or 4, of additional sweeps.

One of the attractive features of the unsteady implementation of the code is the availability of dedicated files in which the time histories of the primary calculated quantities can be recorded dispensing with the need to interrogate the overall flow domain of each of the fractional solutions. In order for a time history file to be written

the operator needs to nominate a corresponding node which the code designates as a monitor point. It is possible to select up to 100 such points. Figure 5-44 below shows the location of five of the monitor points located in the mid-span region of the grid.

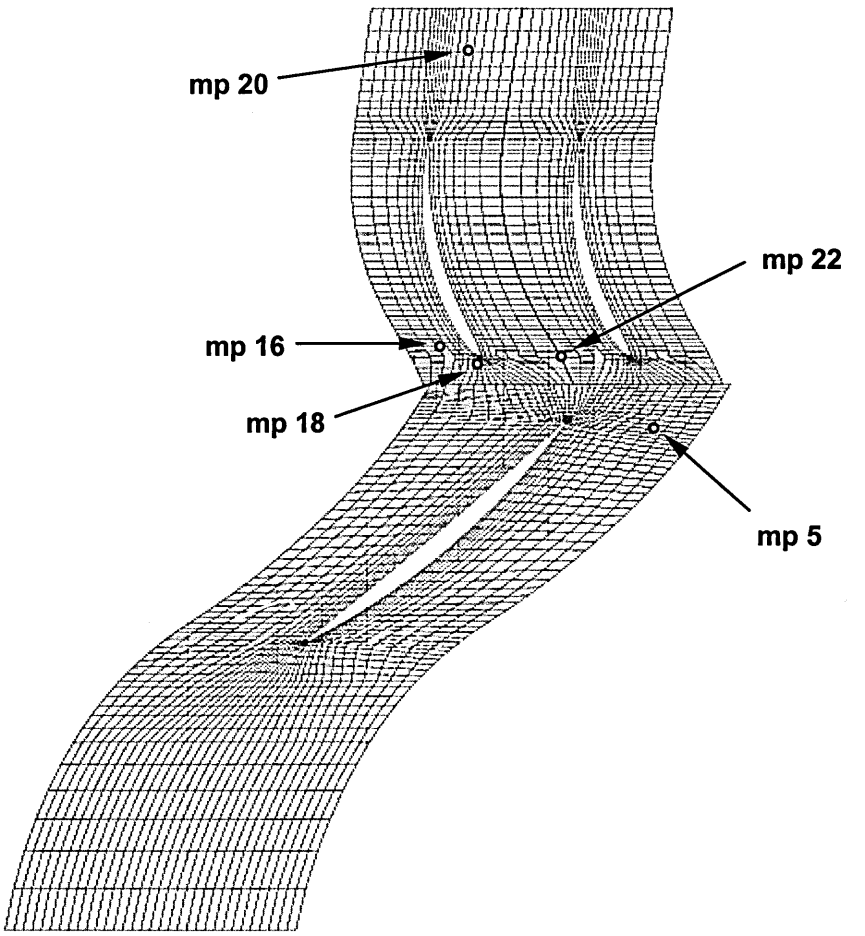

Figure 5-44 HP9 grid at mid-span - location of time history monitor points

The plot of Figure 5-45 displays the time history of the axial velocity at monitor point five (mp5) from the initiation of the simulation to its interruption. This chart clearly illustrates the existence of a strong transient period at the specified location and the eventual settling of the flow into a deterministic cyclic pattern. Given that the location of the monitor point of this plot is set within the rotor domain, the perturbations depicted in the figure are caused by the relative motion of the stator blades. Since the monitor point 'sees' two perturbations per rotor pitch sweep, the 58 peaks visible in

Figure 5-45 correspond to 29 sweeps of the rotor computational domain.

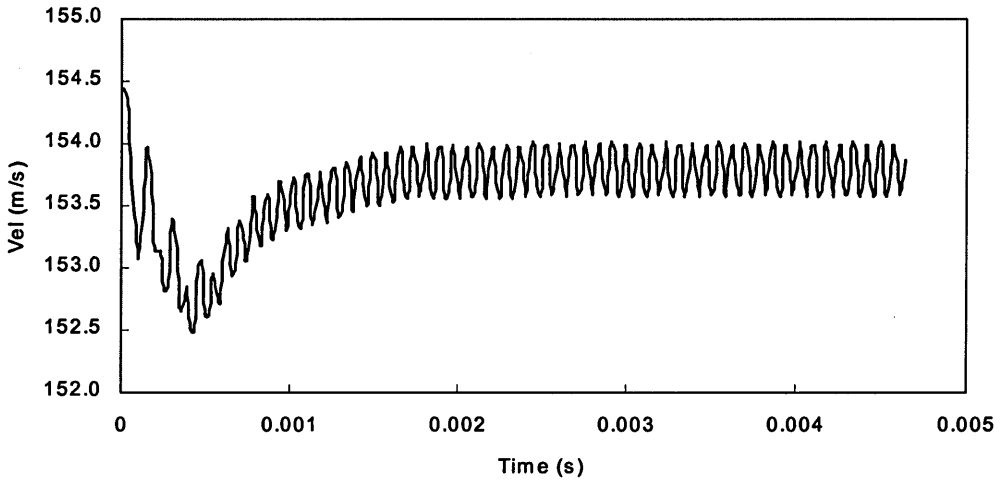

Figure 5-45 Axial velocity time history at max flow – monitor point 5

To give a measure of the computational cost involved in the production of a simulation capable of producing a flow time history, such as shown above, it must be borne in mind that even when employing a coarse time step, such as 12 per sweep, 348 whole flow field solutions must be resolved.

The size of the individual time step calculation files, denoted in the code as say trn.20 for the twentieth time step, was for this case 5.81 Mb corresponding thus to 2.02 Gb if the whole simulation is to be stored. It is to dispense with the need to retain this mass of information for the purposes of assembling time histories that the code employs the monitor point scheme.

Figure 5-46 which shows a plot of the fractional time histories of monitor point 18, located ahead of the stator blade leading edge, and monitor point 20, placed downstream of those blades, illustrates the discrete makeup of the simulation fluctuating quantities. This plot provides also evidence of the significant effect that the proximity of the passing rotor blade exerts on the axial velocity of point 18 by contrast with the monitor point 20. Furthermore it can be seen that the phase of the two signals are staggered by around half a cycle due to the transversal washing of the rotor wakes over the downstream domains.

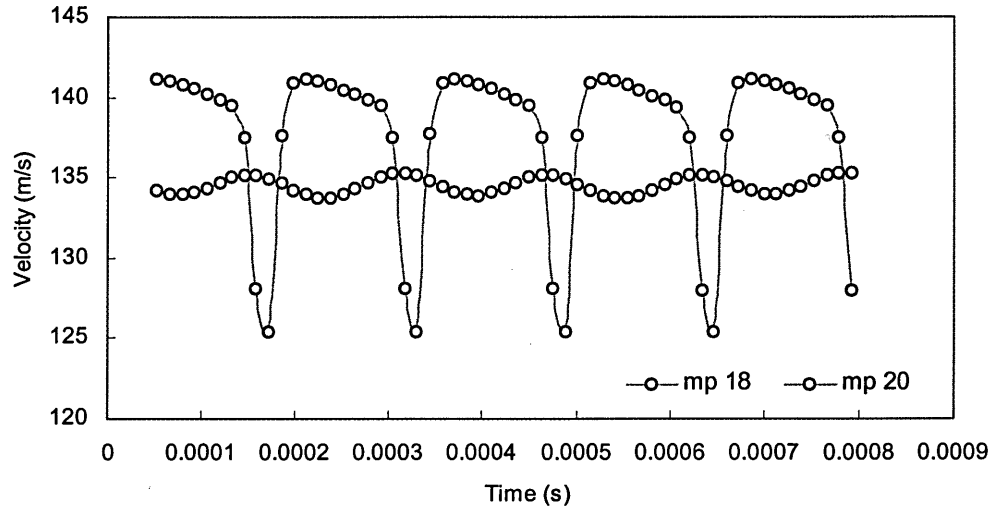

Figure 5-46 Axial velocity time history at max flow – monitor points 18 and 20

The disparity of pressure variation between the two points is however even more marked than before with Figure 5-47 providing evidence of the presence of strong potential effects in the neighbourhood of the rotor.

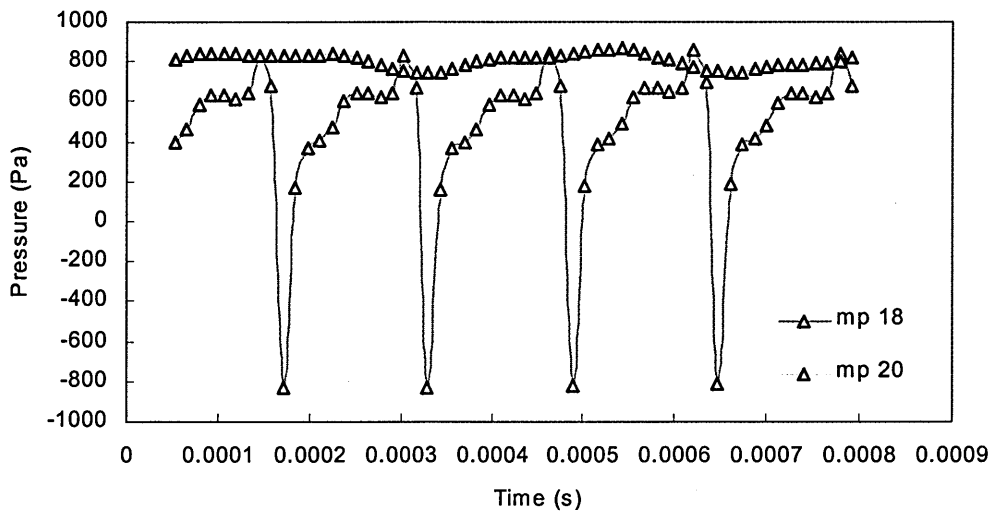

Figure 5-47 Static pressure time history at max flow – monitor points 18 and 20

The pressure values of the abscissa are expressed as a gauge pressure whose datum is the reference pressure value which was input as part of the code solution parameters. The reference pressure value for all simulations run for the present work was set at 101325 Pa.

It is clear in addition that the time history pressure trace of monitor point 20, Figure 5-47, is not entirely cyclical unlike the velocity variables, including those of the exact same location. It has been observed that particularly near the outlet boundary condition, the employment of a time-invariant boundary condition pressure value, is linked to the local lack of inclination of the pressure values to adopt an orderly rhythmic pattern, irrespective of the extent of the run and number of sweeps.

Nevertheless given both the locality of the phenomenon and the fact that the fluctuating velocity quantities, which are to be employed in the assembly of the deterministic stress terms, are well behaved, it is thought that the absence of an absolute cyclical pattern everywhere in the domain is unlikely to undermine the general accuracy of the calculation.

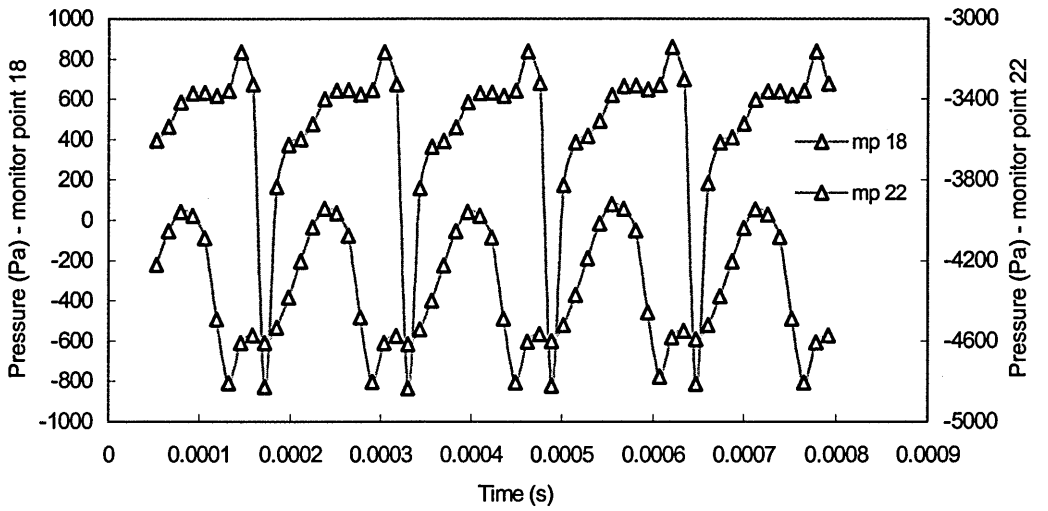

Figure 5-48 Static pressure time history at max flow – monitor points 18 and 22

Besides the potential effects observed in point 18 by comparison with point 20 there is also an interesting variation between the pressure histories of monitor points 18 and

22 which can be seen to share, by reference to Figure 5-44, virtually the same axial position.

The effect of the placement of point 18 within the stator blade potential field is denoted by its average higher pressure by comparison with point 22. This staggering of pressure values is accounted for in
Figure 5-48 by the provision of equally spaced but separate pressure scales.

5.5.3 Unsteady computational aerodynamic results

The unsteady simulation programme is limited to the highest of the two points employed in the large grid steady-state computations. The averaging process performed on the unsteady aerodynamic data was carried out as the simple average of the unsteady fluctuations which occur within a window containing the most satisfactory cyclical patterns.

The global performance calculated from unsteady simulations is shown in the table underneath together with the results obtained from the steady simulation described in 5.4.3.

Performance parameter	Operating point	Steady-state simulation (large grid)	Unsteady simulation	Experimental
Pressure ratio	max-flow	1.189	1.190	1.196
Temperature ratio	max-flow	1.062	1.062	1.061
Adiabatic efficiency %	max-flow	82.3	82.6	85.7

Table 5-6 HP9 test case - experimental results, unsteady and steady-state large grid prediction comparison

The presentation of qualitative results and radial distributions is deferred to a later section where these results are shown in a comparative way against others obtained from a steady-state calculation.

5.5.4 Deterministic stress computation results

The knowledge of the spatio-temporal fluctuations of the flow field enables the direct assembly of the nodal values of the deterministic stress from the variation of the relevant primitive variables. At a given point the stresses $\overline{\rho \tilde{\hat{V}}_i \tilde{\hat{V}}_j}$ are given by the form,

$$\frac{\sum \left[\rho_{nodal} \left(\tilde{\hat{V}}_{i(nodal)} \tilde{\hat{V}}_{j(nodal)} \right) \right] \Delta t}{\Delta T} \qquad (5\text{-}5)$$

As will be readily apparent the stress field obtained by the operation of Equation (5.3) does not have an axisymmetric distribution, in effect, no more than any of its components.

Recalling the physical character of these stresses, their location is likely to coincide with the regions where the distinctive resident flow features, particularly wakes, permanent vortices and secondary flows, are the subject of a vibrating motion through the interaction effects of the relatively rotating blading.

The presentation of the deterministic stress fields is limited to the maximum flow condition. For expediency the velocity correlation stress terms $\overline{\rho \tilde{\hat{V}}_r \tilde{\hat{V}}_r}$, $\overline{\rho \tilde{\hat{V}}_\theta \tilde{\hat{V}}_\theta}$, $\overline{\rho \tilde{\hat{V}}_z \tilde{\hat{V}}_z}$, $\overline{\rho \tilde{\hat{V}}_\theta \tilde{\hat{V}}_r}$, $\overline{\rho \tilde{\hat{V}}_z \tilde{\hat{V}}_r}$ and $\overline{\rho \tilde{\hat{V}}_z \tilde{\hat{V}}_\theta}$ are denoted in the plots by the short form DETS_RR, DETS_TT, DETS_AA, DETS_TR, DETS_AR, and DETS_AT respectively.

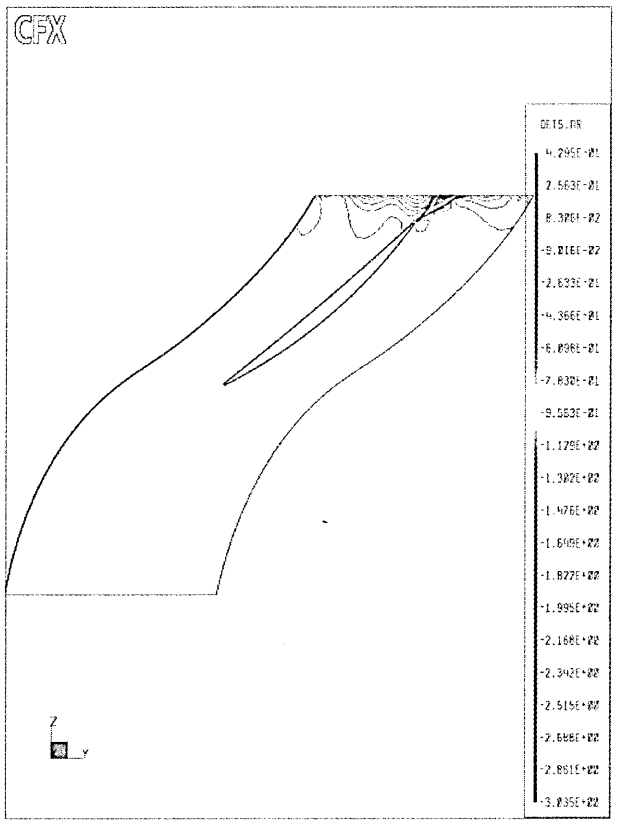

Figure 5-49 Blade-to-blade distribution of DETS_AR at mid-span and max flow

5.5.4.1 Rotor domain

The blade-to-blade contour at mid-span of the $\overline{\rho \tilde{\tilde{V}}_z \tilde{\tilde{V}}_r}$ term is shown in Figure 5-49. The rotor domain field of this quantity is fairly typical of the distribution of the stresses which are induced by the relative motion of the stator blades on the rotor region. The presence in the neighbourhood of the stage interface plane of regions of visible presence of deterministic stresses seems to be related to the occurrence of local secondary flows induced by the passage of the stator.

Elsewhere in the rotor domain the correlations are virtually imperceptible when the natural scale of the plot is employed. This does not necessarily mean that no such values occur there but that the scale of whatever does occur is simply swamped by the

magnitude of the events occurring near the interface boundary. In practice the generation of the upstream acting deterministic stresses is overwhelmingly due to the stator blade potential effects and since these do not extend very far it is quite plausible to encounter the distribution described in Figure 5-49 and those of its siblings.

Given that in Hall's model these upstream acting deterministic stresses are not modelled and that in Bolger's model their magnitude is calculated as a tenth of their viscous downstream acting equivalent stresses, no further consideration is given in this work to these terms. There was in the case of HP9 a further incentive to dispense with the rotor acting stresses. As has been seen grids in which these stresses are applied require an axisymmetric disposition of the pitchwise lines and these configurations are often a source of problems in terms of cell skew in the vicinity of blade leading edges. For the HP9 geometry the dispensation of the enforcement of axisymmetry on the rotor domain provided therefore some desirable relaxation to the grid assembly process.

5.5.4.2 Stator domains

The situation in the stator domains where the primarily viscous perturbations are subject to a convection process is much less uniform with a significant variation between the different correlations being evident. In Figure 5-50 where the $\overline{\rho \hat{\tilde{V}}_z \hat{\tilde{V}}_z}$ deterministic stress field at mid-span is portrayed, there is evidence of how the interface region stresses dominate and of the quasi-axisymmetric nature of their local distribution. The extent of this region is nevertheless quite limited with the axial decay taking place along a nearly uniform front. Around the blade boundary there is evidence of a dissimilar distribution of stress with the suction surface registering the presence of a gradient whose direction is broadly orthogonal to the blade surface.

This arrangement is consistent with the occurrence of unsteady blade loading translated in a thinning and thickening of the suction surface boundary layers together with a variation of the incidence. This latter feature might, when associated with the presence of negative incidence which is a characteristic of high mass flow regimes, be responsible for

the existence of a small region of accelerating flow near the pressure side of the leading edge. It is quite possible therefore that when subjected to a periodic pulsation the varying boundary extent of that low pressure area would induce the sort of quantities variation associated with the production of deterministic stresses.

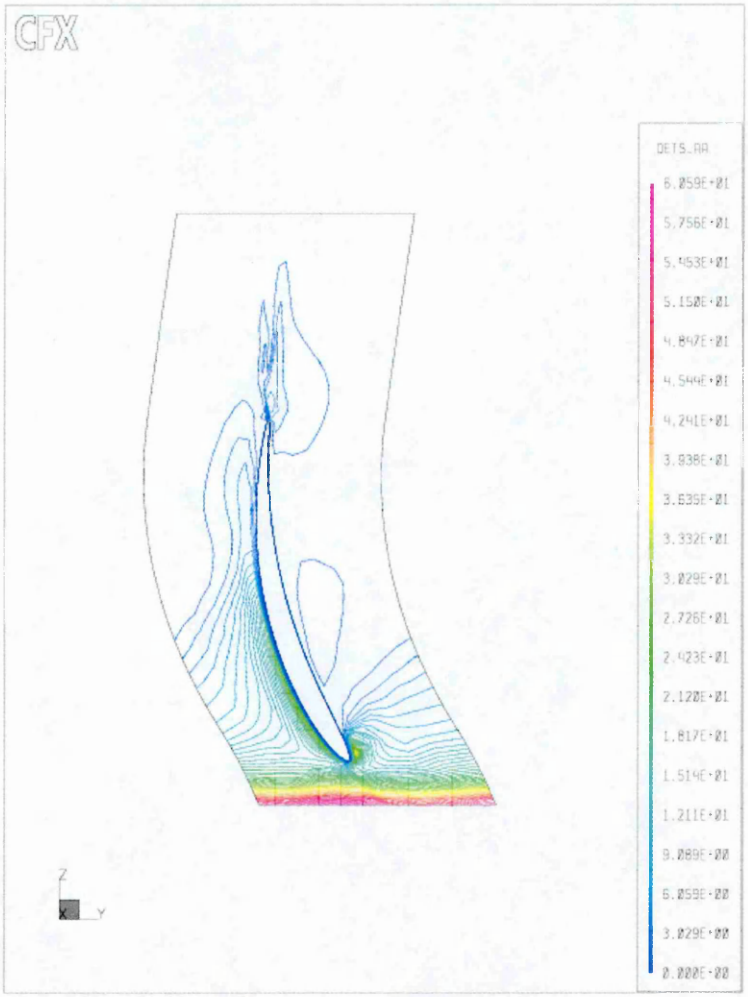

Figure 5-50 Blade-to-blade distribution of DETS_AA at mid-span and max flow

Downstream of the blade there is also some indication of the presence of deterministic stresses associated with stator wake but these are substantially decayed in intensity and present some imprecise spatial distribution characteristics. It must be noted that where the value of a variable is very shallow by comparison to those of its neighbours the definition

of its precise configuration is brought somewhat into doubt by the interpolation method employed by the graphics routine of the code.

This is clearly shown in Figure 5-51 below, portraying the stator blade passage distribution of the average form of the radial velocity, $\tilde{\tilde{V}}_r$ where a vestige of the underlying grid is evidently affecting the definition of the isocontours. The variable depicted in this plot is associated with a very weak spatial variation and in coarse grids, such as the one employed in the unsteady simulations, the inter-nodal visualisation interpolations are compromised by the sparseness of the mesh and the attendant lack of diffusion of the contour gradients.

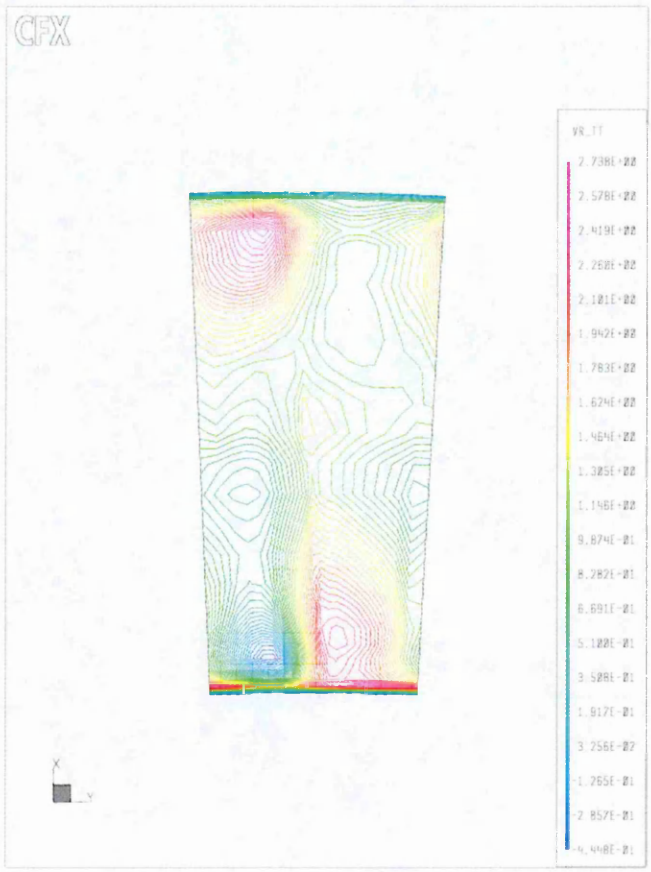

Figure 5-51 HP9 stator passage (experimental station 2) $\tilde{\tilde{V}}_r$ distribution at max flow

The presentation of the passage distributions of deterministic stresses is made in terms of the two experimental data collection planes, number two placed upstream of the stator blade leading edge,

Figure 5-52, and number three which is located downstream of the blade, Figure 5-53.

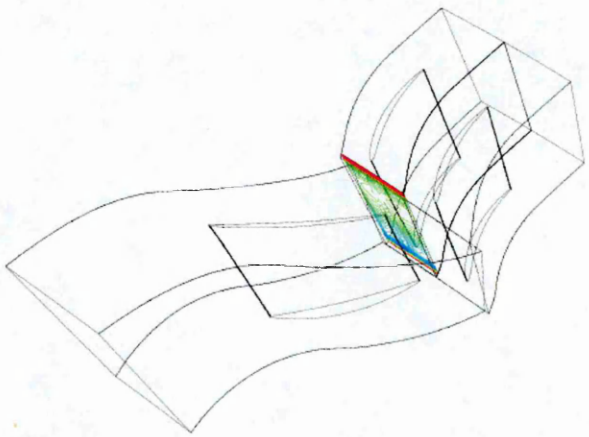

Figure 5-52 Experimental data collection plane number two

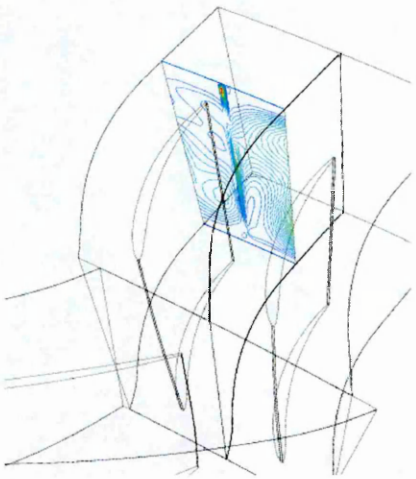

Figure 5-53 Experimental data collection plane number three

The passage distribution of the $\overline{\rho \hat{\tilde{V}}_z \hat{\tilde{V}}_z}$ deterministic stress taken at the experimental plane two is shown in Figure 5-54. The salient feature in this plot is the presence of a strong band of stresses near the hub.

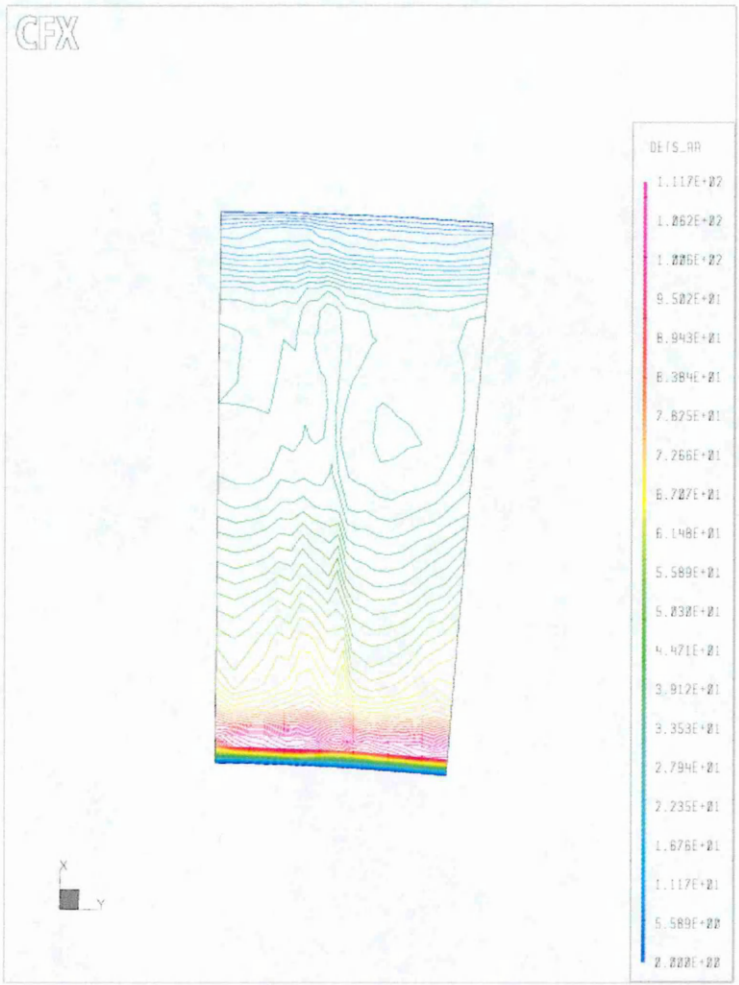

Figure 5-54 HP9 stator passage distribution of DETS_AA at max flow – experimental station two

The source of this feature is best understood through the examination of the plot of $\tilde{\tilde{V}}_z$, Figure 5-55, taken at the same location. As this plot shows, the boundary layer is considerably thick in both endwalls but more particularly so near the hub of the machine. This region is supposedly subject to the influence of the broadest of the rotor wakes which are associated with the additional thickness of the rotor blade root as well as low momentum flows or even corner stalls. Another interesting feature of the plot of Figure 5-54 is the presence of a narrow near vertical region of stresses whose origin is related to

the potential bow wake due to the stator blade. This characteristic is observable in all the plots taken in this region.

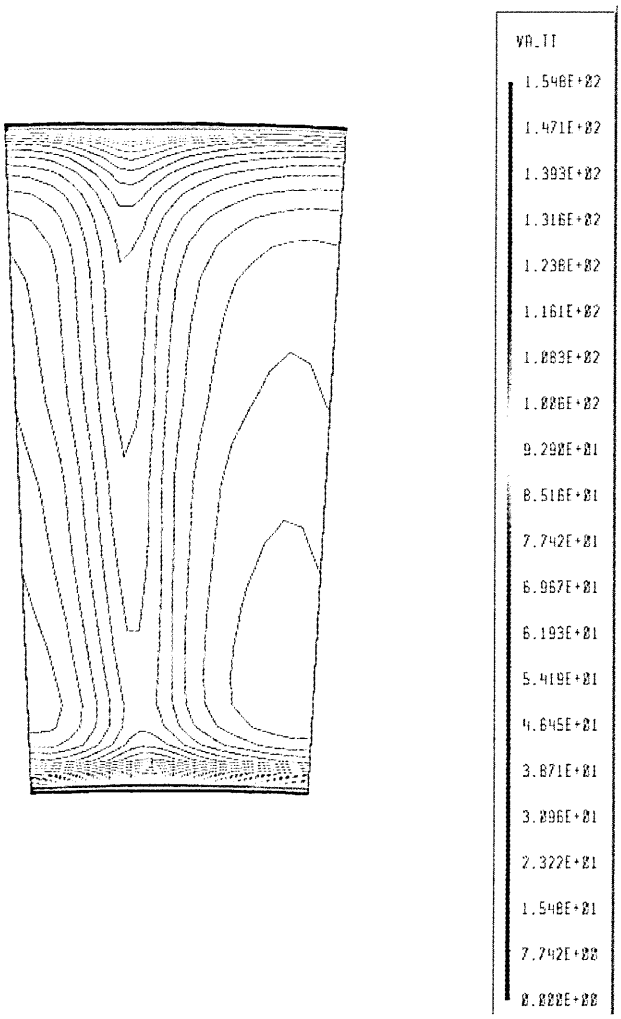

Figure 5-55 HP9 stator passage distribution of $\widetilde{\widetilde{V}}_z$ at max flow – experimental station two

The inherent three-dimensionality of the deterministic stress distributions is further demonstrated though the distributions visible in Figure 5-56 taken from a near meridional plane whose disposition is roughly parallel to the stator blade chord.

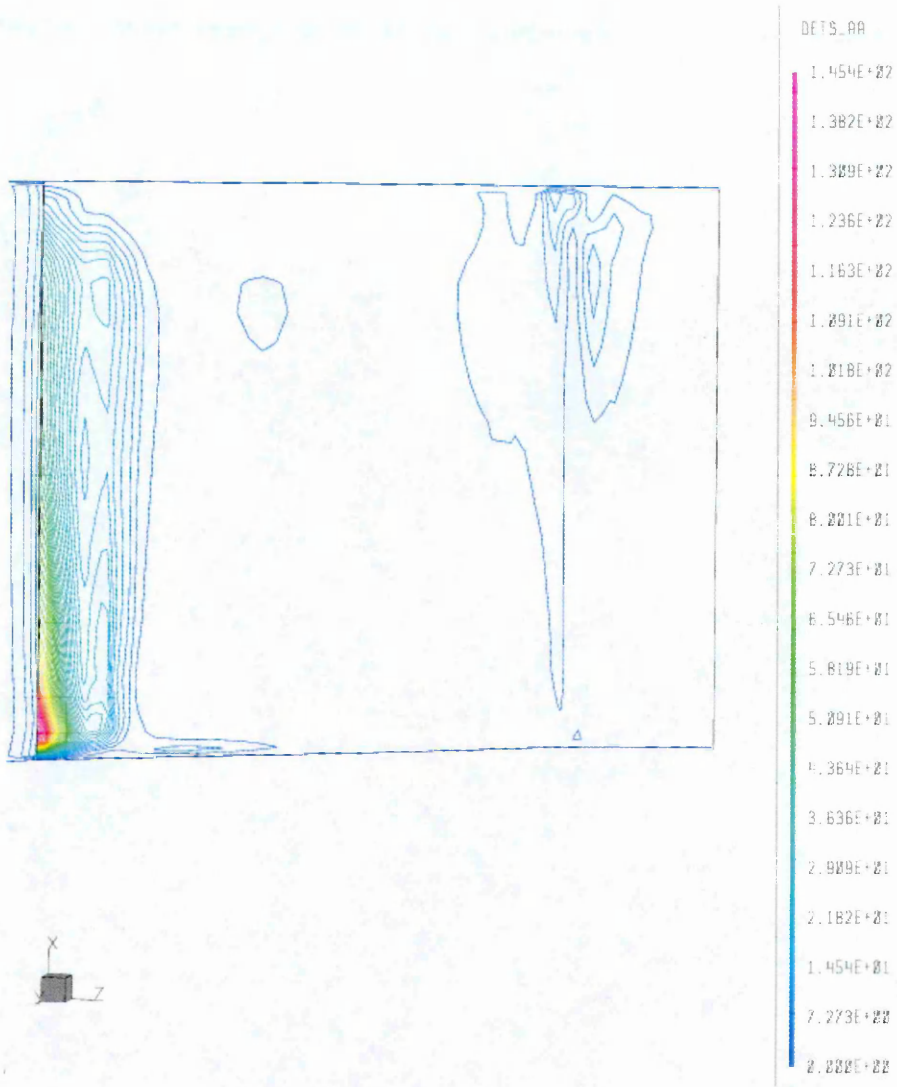

Figure 5-56 HP9 stator passage DETS_AA deterministic stress distribution at max flow

Lastly the stress field associated with the experimental plane three is presented for completeness. As will be seen the stress structure at this plane is associated almost exclusively with wake borne instability with a preponderance of the blade root originating flows being again in evidence.

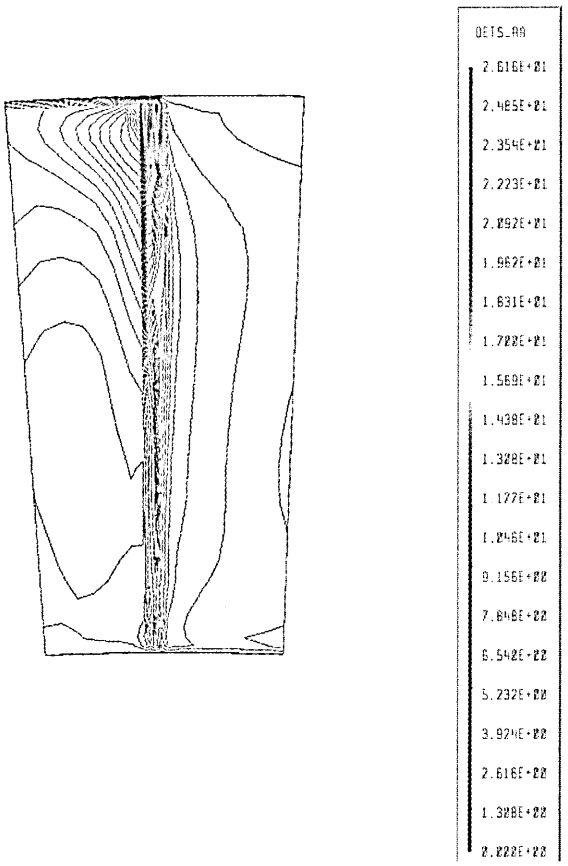

Figure 5-57 HP9 stator passage distribution of DETS_AA at max flow – experimental station three

The three-dimensional deterministic stress field obtained from the unsteady simulations was employed to carry out the following tasks:

a) Characterization of the stress fields – this process designed to help the gaining of insight into the spatial stress distribution is illustrated above.
b) Pitchwise averaging of the 3D stress fields – comparison with the values given by the semi-empirical models
c) Evaluation of the axial decay of the pitchwise average form of the 3D stress fields and comparison with the Bolger's model corresponding decay functions
d) Injection of these 3D stresses into a steady-state simulation run on an identical grid – comparison with the aerodynamic results obtained with the deterministic stress values calculated by the two semi-empirical models

5.5.4.3 Pitchwise averaged stress fields

The final outcome of the semi-empirical models is in the form of an axisymmetrical deterministic stress field which can then be added to the computed aerodynamic field in order to account in some measure for the cyclic stage events induced by the interaction of adjacent blade rows. This axisymmetrical field can also be assembled from the 3D field of an unsteady simulation through a area-weighted pitchwise averaging process and such an operation was performed on the results presented above.

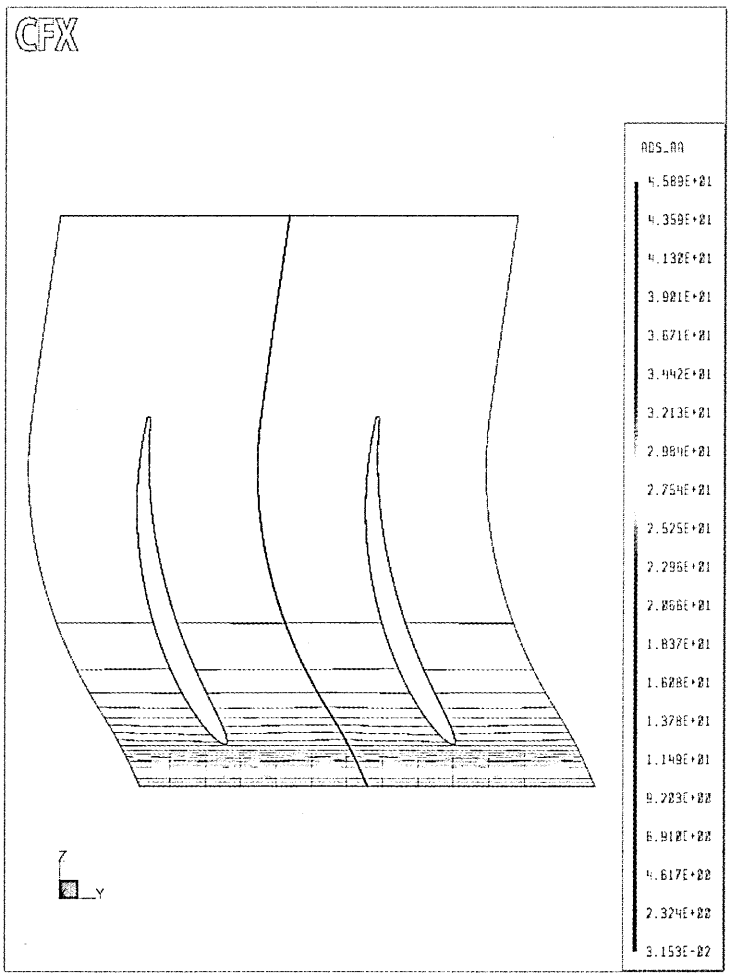

Figure 5-58 HP9 stator axisymmetric distribution of DETS_AA at mid-span and max flow

This work is interested in the radial distribution of deterministic stresses at the vicinity of the interface plane, since this is implicitly the starting point of both models, and additionally is concerned with their rate of axial decay. The axisymmetric version of the blade-to-blade distribution of the $\overline{\rho \tilde{\hat{V}}_z \tilde{\hat{V}}_z}$ deterministic stress field at mid-span shown previously in Figure 5-50 is portrayed above.

This distribution is also appropriately described as a plot of deterministic stress level against axial distance as is done in the chart of Figure 5-59 taken at mid-span. As is self-evident from that chart the intensity of the axial distribution of the axisymmetric $\overline{\rho \tilde{\hat{V}}_z \tilde{\hat{V}}_z}$ deterministic stress field follows an exponential like decline as is postulated in Bolger's model.

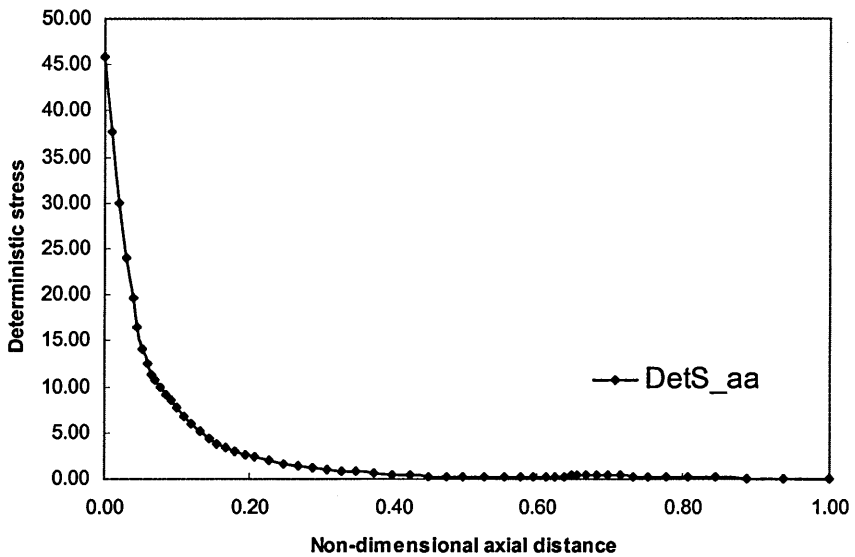

Figure 5-59 Axial decay of DETS_AA at mid-span and max flow

As was seen in Chapter 4, where the theoretical background of the Bolger's formulation was introduced, that particular deterministic model assumes values for the axial decay which have been extracted from a low speed case. Specifically for the $\overline{\rho \tilde{\hat{V}}_z \tilde{\hat{V}}_z}$ stresses the decay function advanced by Bolger is valued at 3.7 irrespective of radial position. The curve fitting of the data of Figure 5-59, which has been done through the least squares fitting capability of the Microcal Origin software, enabled the updating of this value to be

more adjusted to the conditions which apply in the high speed environment of the HP9 compressor. The curve fitting employed a built-in exponential decay function of the form,

$$y = y_0 + A_1 e^{-\frac{x}{t_1}} \tag{5-6}$$

from where the Bolger's model β function is evaluated as $\frac{1}{t_1}$.

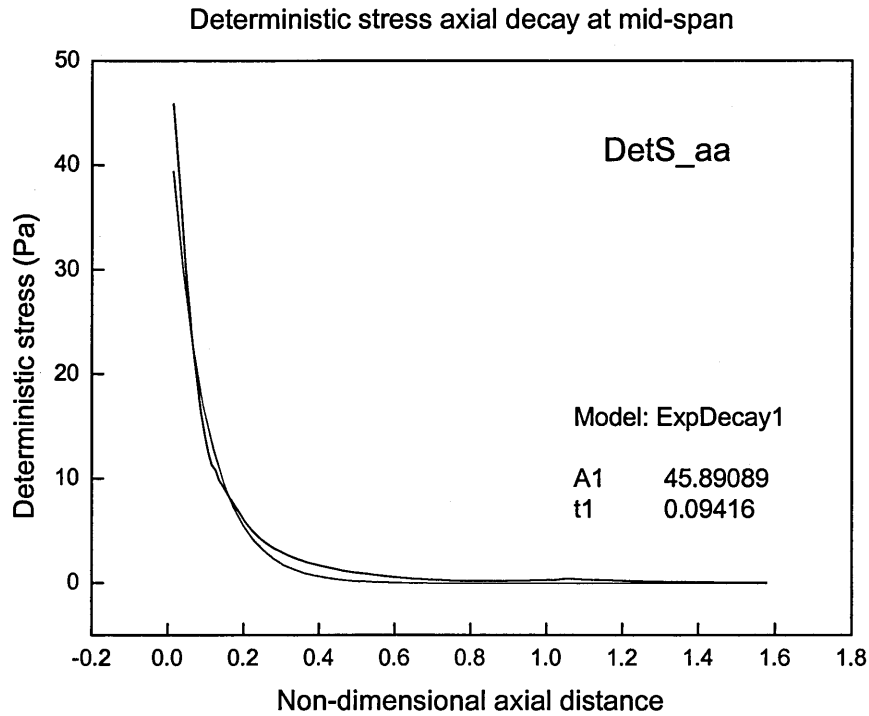

Figure 5-60 Curve fitting plot of axial decay of DETS_AA at mid-span and max flow

In order to produce a value of the β function for each of the deterministic stresses which is broadly representative of their decay throughout the blade span, data was collected at five radial locations, 3, 20, 50, 80 and 97 percent of span, and an area average obtained for the expression of a singular value.

Two provisos need nevertheless to be raised on the subject of the curve fitting programme carried out on that data. Although the majority of the decay traces was fairly well behaved and lent itself to the production of straightforward and unambiguous curve fittings, in some instances this was not achievable such as for the case of the $\overline{\rho \hat{\tilde{V}}_r \hat{\tilde{V}}_\theta}$ term decay taken at 80% span and depicted in Figure 5-61. In cases such as these, the conversion into a single figure was just about possible but where the fitting operation could not be done, in the spirit of the general trends observed elsewhere in the blade span, individual radial locations were ignored and the averaging processed with the remaining points.

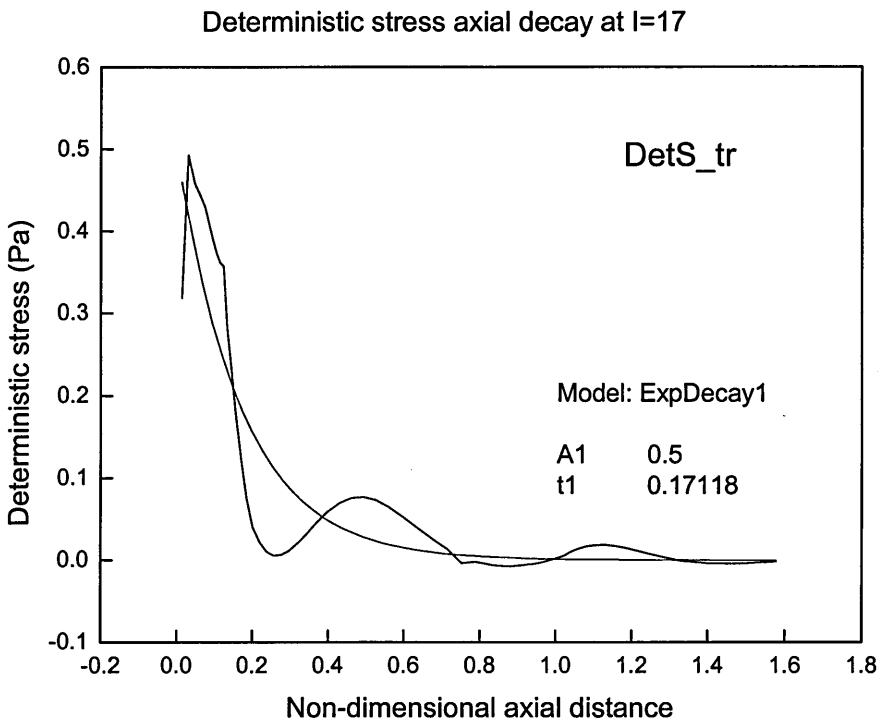

Figure 5-61 Curve fitting plot of axial decay of DETS_TR at mid-span and max flow

The second qualification concerns the behaviour of the deterministic correlations which include energy terms such as $\overline{\rho \hat{\tilde{V}}_r \hat{\tilde{H}}}$ and $\overline{\rho \hat{\tilde{V}}_z \hat{\tilde{H}}}$, where H is the total enthalpy. In general the decay of these terms was not consistent throughout the span and their curve

fitting was somewhat problematic leading to doubts about the quality of the updated decay values.

The HP9 derived β functions are tabulated next together with the original equivalent values obtained from the Bolger model derivation to which the author had access. The values denoted in bold italic type correspond to the cases where the curve fitting of the decay function from which they stem was considered to be particularly unrepresentative and was therefore omitted from the single values calculation process.

Bolger model (original values)								
span %	**Dets_rr**	**Dets_tt**	**Dets_aa**	**Dets_tr**	**Dets_ar**	**Dets_at**	**Dets_rh**	**Dets_ah**
n/a	0.70	4.10	3.70	2.50	3.10	5.00	4.50	2.52
Bolger model (high speed values)								
3	4.09	9.27	10.06	***2.18***	-7.69	14.00	***0.32***	11.76
20	4.63	9.06	10.12	6.64	-7.63	13.78	***-6.67***	8.90
50	4.98	10.15	8.84	3.90	-5.41	13.45	***-5.88***	8.33
70	***-1.41***	11.76	7.17	-4.55	-3.38	12.83	***-2.68***	8.33
97	9.26	8.21	4.75	7.08	9.15	16.56	-4.31	10.00
single value	5.00	10.00	8.50	5.00	7.00	14.00	-4.00	9.00

Table 5-7 Bolger model high speed decay rate function values

It is apparent when comparing the single values of the two versions of the decay functions that the high speed variety is on the whole larger by a factor of about two. In fact when the velocity correlations are considered, only the $\overline{\rho \hat{\tilde{V}}_z \hat{\tilde{V}}_z}$ term escapes this general rule. On the energy correlations front the situation is somewhat less clear with most of the results of the $\overline{\rho \hat{\tilde{V}}_r \hat{\tilde{H}}}$ term being untrustworthy while those of the $\overline{\rho \hat{\tilde{V}}_z \hat{\tilde{H}}}$ term show a more substantial increase.

These updated decay rates have been employed with the Bolger model in the relevant subsequent computations which will be presented in a further section of the present chapter.

5.6 Steady-state simulation II – coarse grid

As well as being employed to provide unsteady data for the calculation of the deterministic stresses, the results of time-accurate computations were used in direct comparisons with steady-state calculations. In order to enable an equitable comparison a number of runs were made with a steady-state variant of the grid which was used in the unsteady simulations.

5.6.1 Grid and solution features

The coarse 'small' steady grid makes use of the rotor and one of the stators used in the unsteady simulation grid set up and the grid sizes are 26x33x62 for the rotor, or 53196 nodes as before and 26x 21x57 or 31122 nodes on the single stator domain.

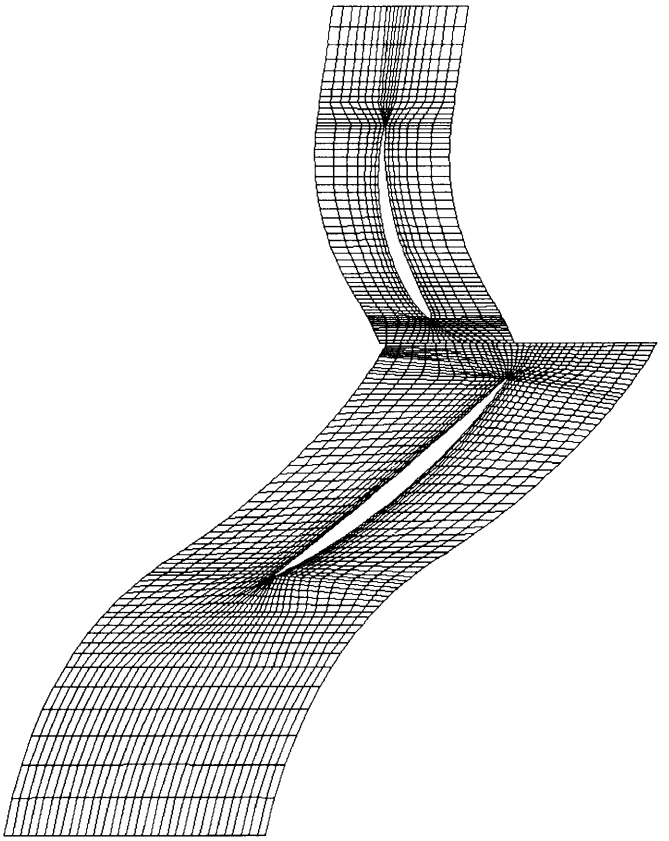

Figure 5-62 Steady-state small grid configuration at mid-span

The boundary conditions replicate exactly those set for the large steady grid runs with a radial profile of total pressure and temperature together with flow direction defining the inlet conditions and an average single static pressure value defining those of the outlet. The information interchange between the two domains is managed via a mixing plane type stage interface as described in 4.4.4 .

5.6.2 HP9 coarse grid baseline results

The two experimental flow conditions already used with the large grid were also run on the coarse grid model. The lowest mass flow that could be achieved by the stepwise lowering of the back pressure was 8.21 Kg/s which is well short of the near-stall operating point whose mass flow is given as 7.23 Kg/s. At the low value the solution was computationally unstable, that is, the convergence was shallow but continuous up to a

low point beyond which the solution diverged all the way up to the eventual crashing of the code, a scenario which is partially depicted in Figure 5-63.

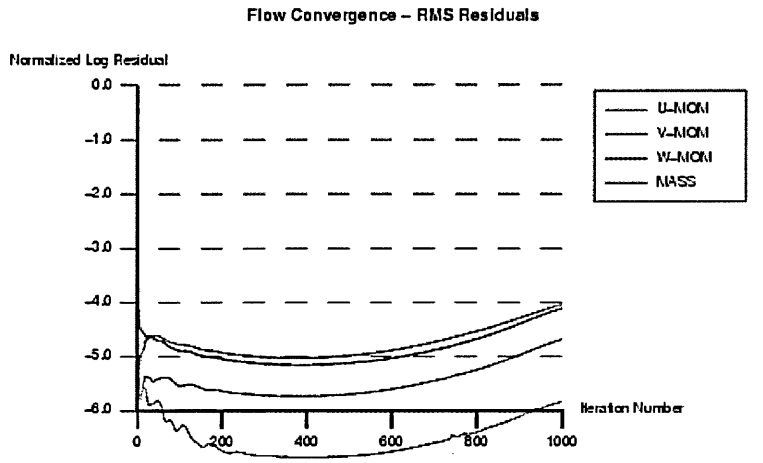

Figure 5-63 Near-stall solution convergence plot

By extracting data around the 380 iterations region of the plot of Figure 5-63 one can obtain results of engineering usefulness even though it is known that the solution is not fully converged.

A measure of the ease of convergence of the max-flow point by contrast is shown in Figure 5-64 where the stiff residual target, 5E-07, is seen to be reached in just about 100 iterations.

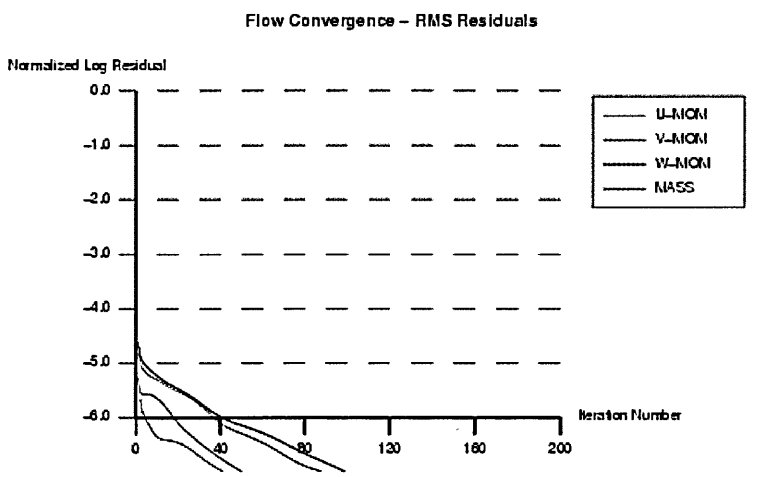

Figure 5-64 Max-flow solution convergence plot

5.6.2.1 Overall performance results

The presentation of the global performance parameters is done in a comparative form in Table 5-8 alongside the results obtained from the large grid simulation and the experimental values. It must be remembered though that the machines simulated in the two grids are not strictly the same since the coarse mesh was derived from the unsteady model which had itself been scaled as described in 5.5.1. This said, as the scaling operation is performed in manner that seeks to reduce its impact on the pre-existent flow field, the comparisons between the steady-state results obtained with the two grids are reasonable and potentially useful.

Performance parameter	Operating point	Large grid	Small grid	Experimental
Pressure ratio	max-flow	1.189	1.190	1.196
	mid-chic	1.251	1.250	1.236
Temperature ratio	max-flow	1.062	1.062	1.061
	mid-chic	1.076	1.077	1.080
Adiabatic efficiency %	max-flow	82.3	82.2	85.7
	mid-chic	86.7	86.0	88.3

Table 5-8 Comparison between the experimental results and steady-state numerical predictions for the HP9 test case

An assessment of the global results acquired with the small grid will reveal the surprising fact that despite its coarse density the small grid nearly is as good, or more to the point in the present case, as bad, as the larger grid in the computation of the overall parameters.

Since what is primarily forfeited in the coarsening process, is the added resolution of the viscous features of the flow associated with the presence of high nodes counts, the main

message of the comparison contained in Table 5-8 seems to be that below a certain grid size the calculation of overall performance is not much affected by some further coarsening. These results also help to confirm Rodrick and Chima's assertion that pressure field calculations are relatively independent of viscous effects and are adequately calculated with relatively simple models, Rodrick and Chima, 1997.

5.6.2.2 Radial distributions

The presentation of the radial distributions is made in the form of comparative plots where the small grid results are denoted by blue squares superimposed on the experimental and large grid values. The radial plots of the max-flow condition, Figure 5-65 to 5-67 and mid-chic point, 5-68 to 5-70, indicate that in parallel with the single value overall performance quantities, there is only a very small variation between the results obtained with the large grid and those which come from the smaller grid model.

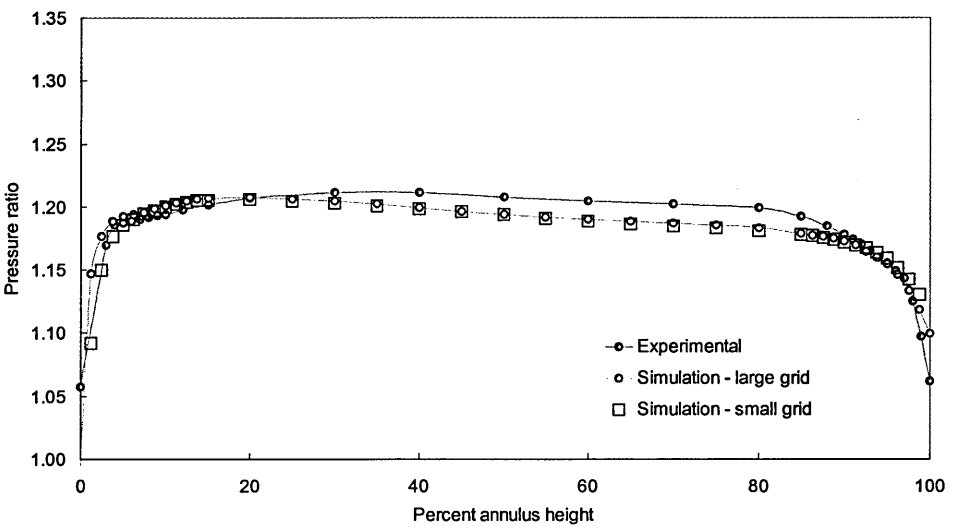

Figure 5-65 Radial variation of total pressure ratio at max-flow - small grid

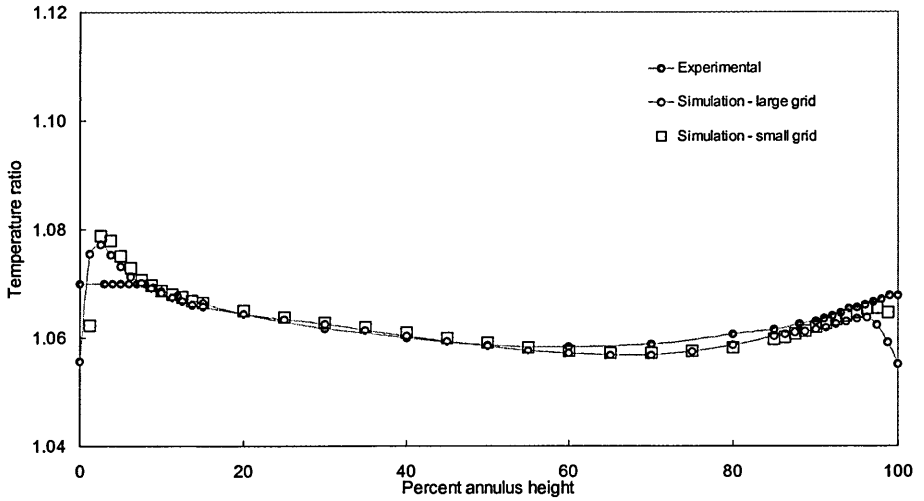

Figure 5-66 Radial variation of total temperature ratio at max-flow - small grid

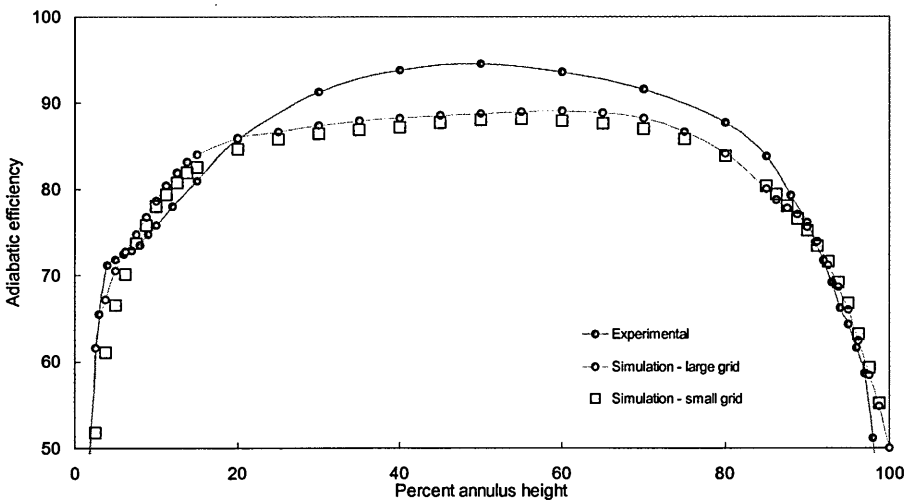

Figure 5-67 Radial variation of adiabatic efficiency at max-flow - small grid

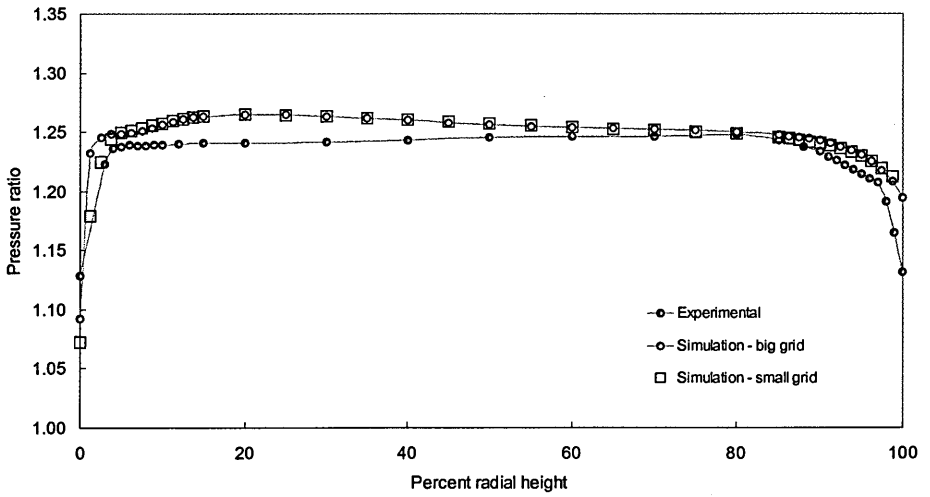

Figure 5-68 Radial variation of total pressure ratio at mid-chic - small grid

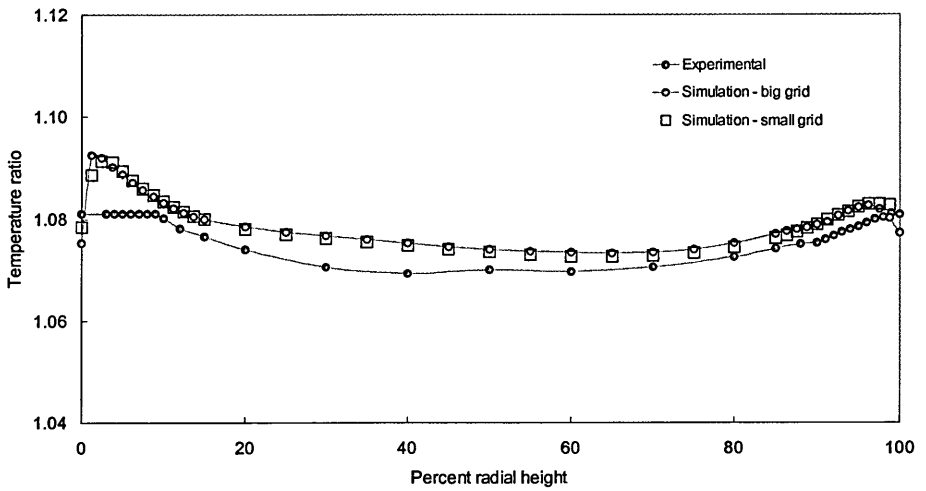

Figure 5-69 Radial variation of total temperature ratio at mid-chic - small grid

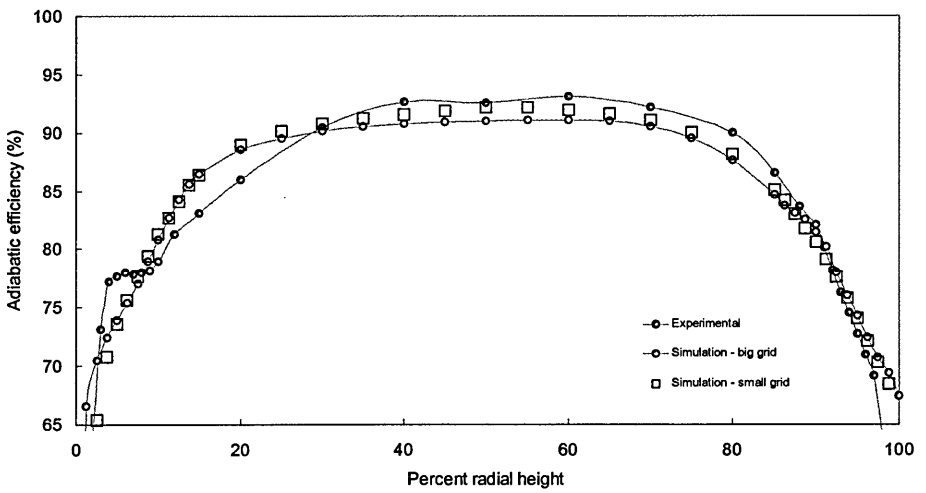

Figure 5-70 Radial variation of adiabatic efficiency at mid-chic - small grid

5.6.2.3 Small versus large grid qualitative comparisons

Apart from the quantitative measures discussed above some qualitative comparisons were also performed between the two sets of results obtained with the two grids. The variation of the radial, tangential and axial velocities at 32 and 67 % of annulus height is shown in Figures 5-71 through 5-76 below.

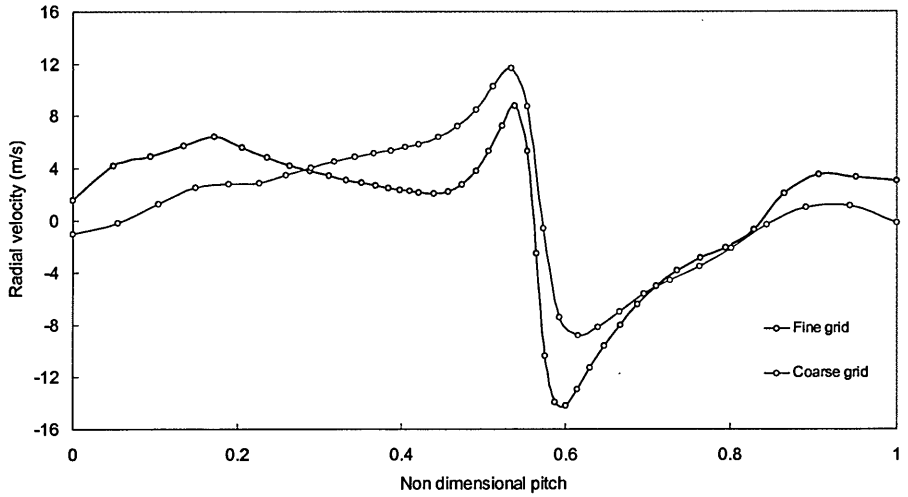

Figure 5-71 Pitchwise variation of radial velocity at 30% span at max-flow

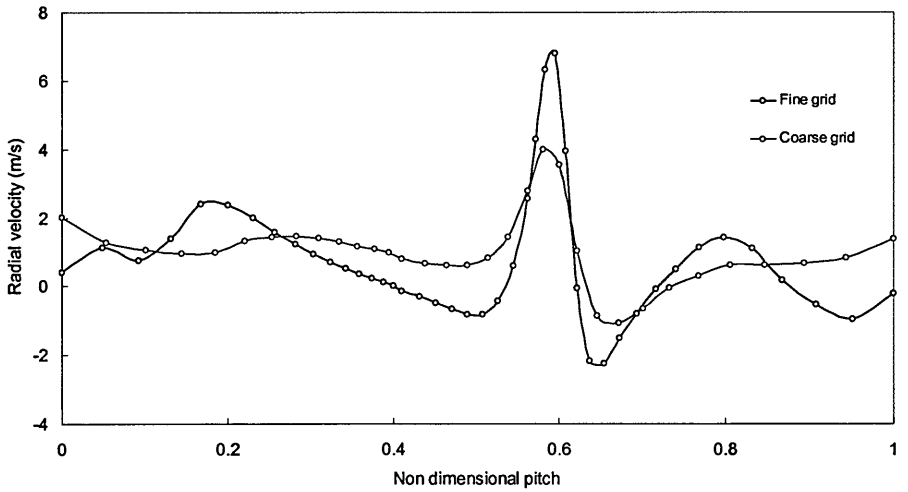

Figure 5-72 Pitchwise variation of radial velocity at 70% span at max-flow

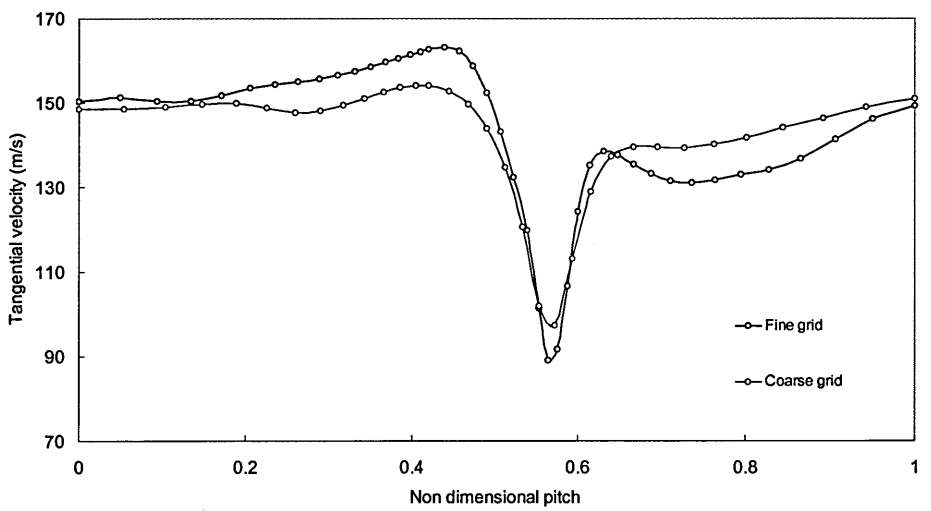

Figure 5-73 Pitchwise variation of tangential velocity at 30% span at max-flow

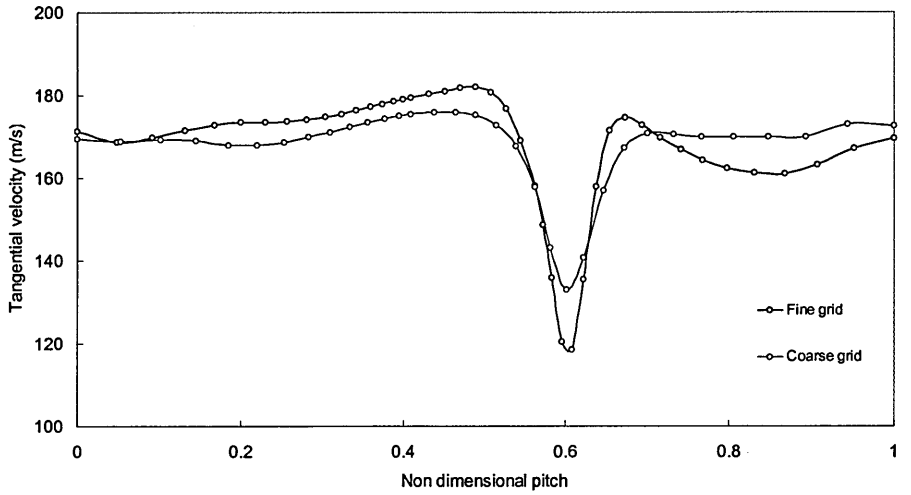

Figure 5-74 Pitchwise variation of tangential velocity at 70% span at max-flow

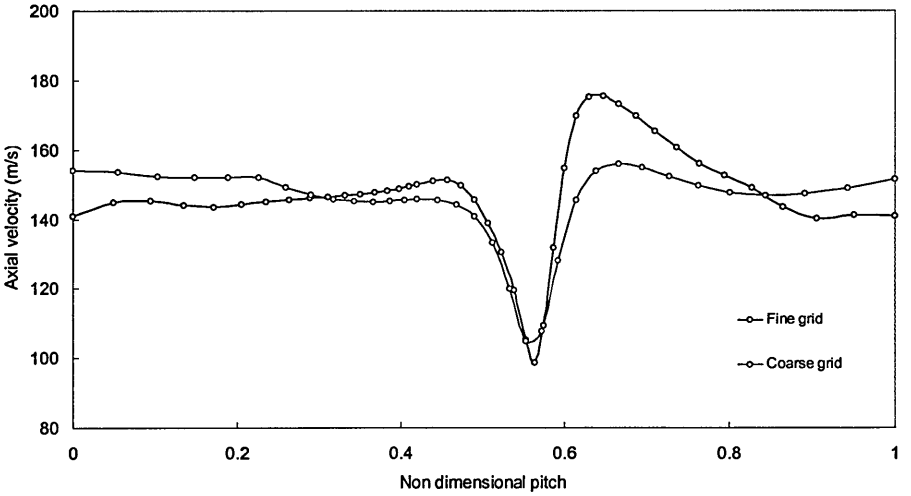

Figure 5-75 Pitchwise variation of axial velocity at 30% span at max-flow

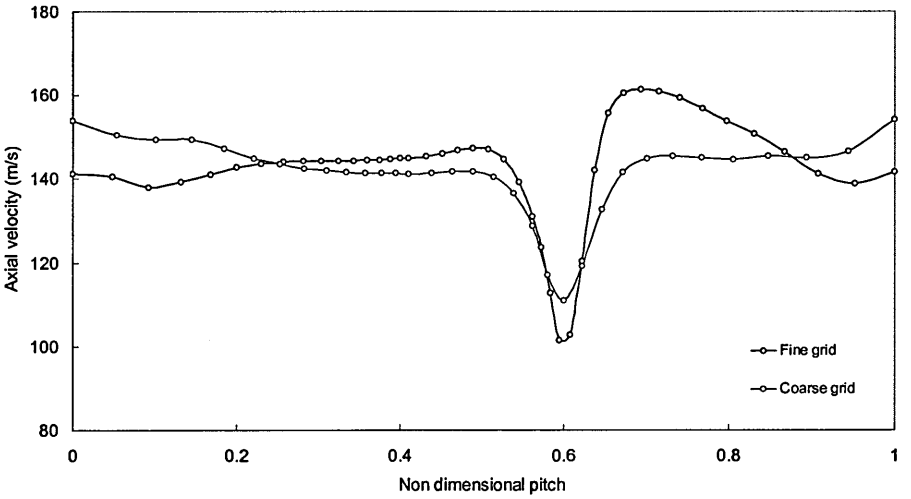

Figure 5-76 Pitchwise variation of axial velocity at 70% span at max-flow

As a rule the wakes predicted by the finer grid are deeper than those originating from the coarse grid calculations. The slightly greater velocity deficits are likely to be caused by the added thickness of the blade profile which is modelled by the finer grid by comparison with the coarse grid blades which were scaled down in pitch and are therefore somewhat thinner. The width of the wakes on the other hand is hardly justifiable on aerodynamic grounds and must be explained by the much sparser nodal density occurring in the blade-to-blade plane.

5.7 Steady-unsteady calculations comparison

The availability of solutions which employ exactly the same grid platform and differ alone in the mode of treatment of the stage coupling interface enables a direct comparison between the results obtained by both methods and an identification of the sources and locations of the differences in the results.

5.7.1 Wake plots

The averaging on the unsteady simulation results was carried out on the three rotor relative velocity components, expressed in a cylindrical coordinate frame, and taken at the rotor outlet domain.

There is a significant variation in the proximity of the radial velocity results which originate from the steady-state simulation to those which are due to the time averaging of the unsteady computations. This discrepancy varies from a quite close agreement such as is encountered near the shroud, Figure 5-77, to a significant disagreement as is the case with the profiles near the hub, Figure 5-78 and this situation is again mirrored by the tangential velocity results obtained at the same locations, Figure 5-80 and 5-81.

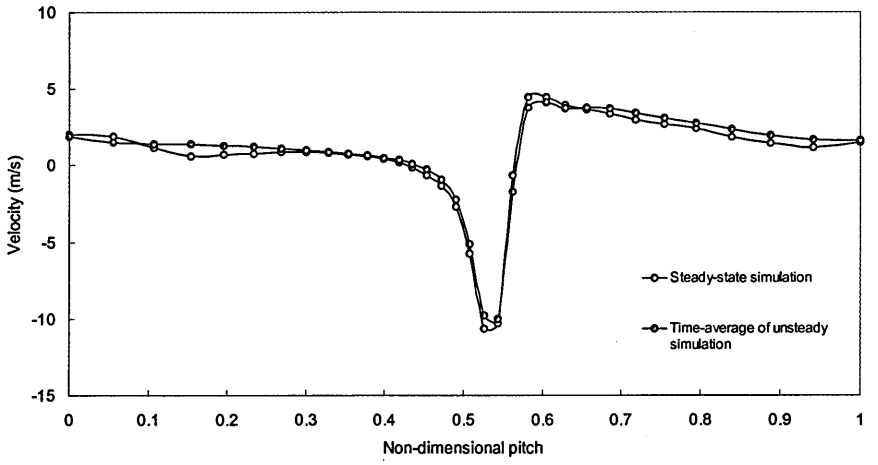

Figure 5-77 Radial velocity pitchwise distribution at 97% radial height – max flow

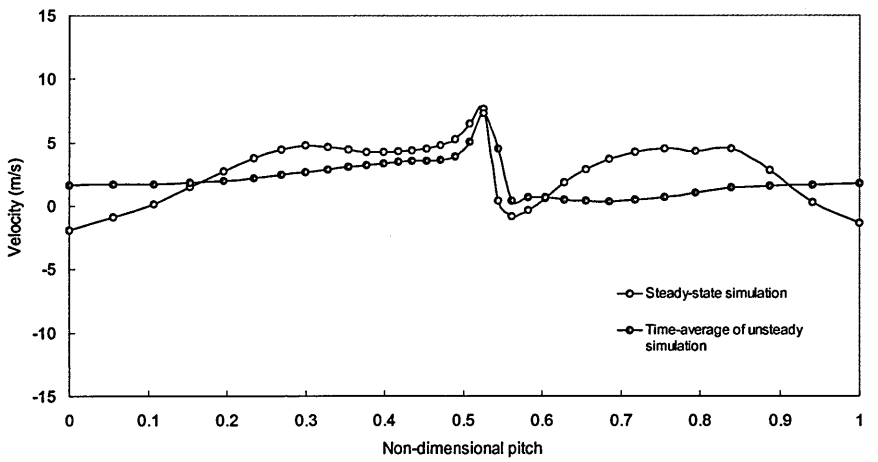

Figure 5-78 Radial velocity pitchwise distribution at 3% radial height – max flow

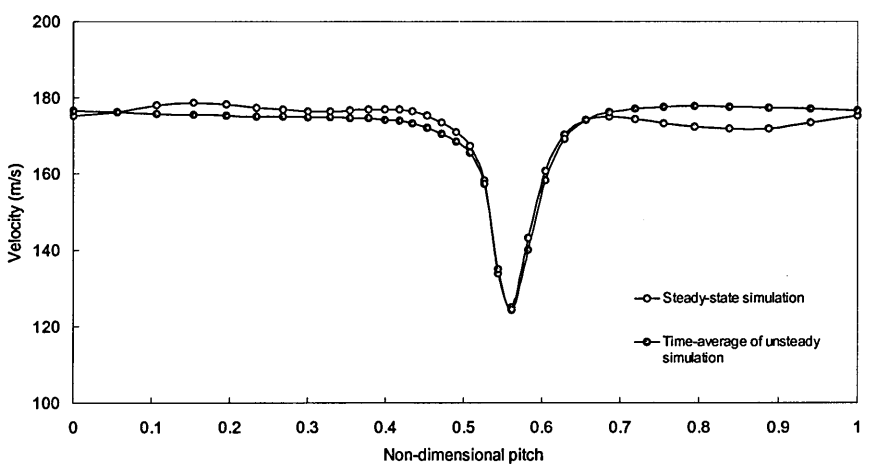

Figure 5-79 Tangential velocity pitchwise distribution at 97% radial height – max flow

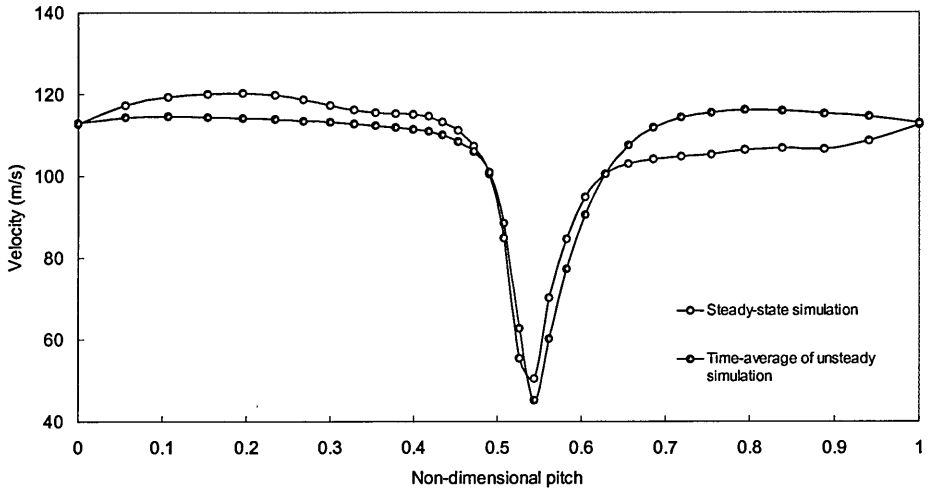

Figure 5-80 Tangential velocity pitchwise distribution at 3% radial height – max flow

The position is somewhat less clear though when the axial velocity is considered, as is seen in Figure 5-81 and Figure 5-82.

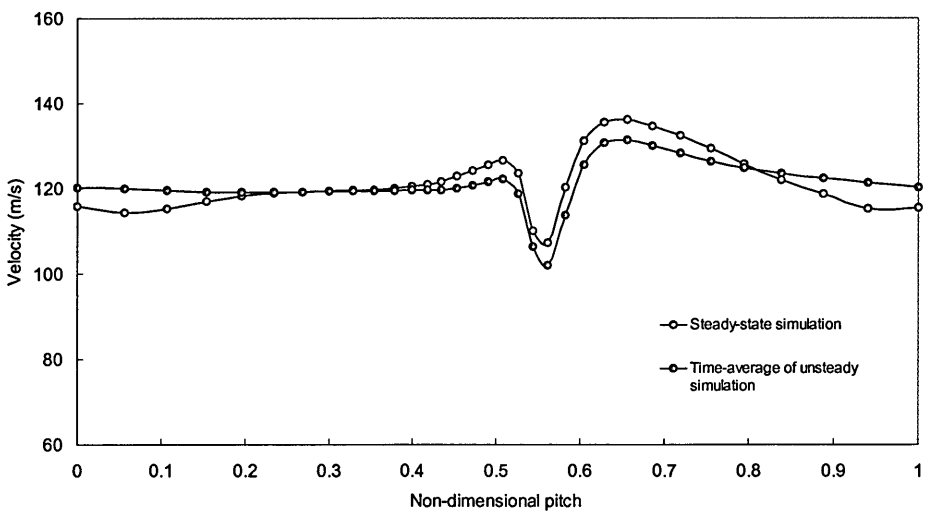

Figure 5-81 Axial velocity pitchwise distribution at 97% radial height – max flow

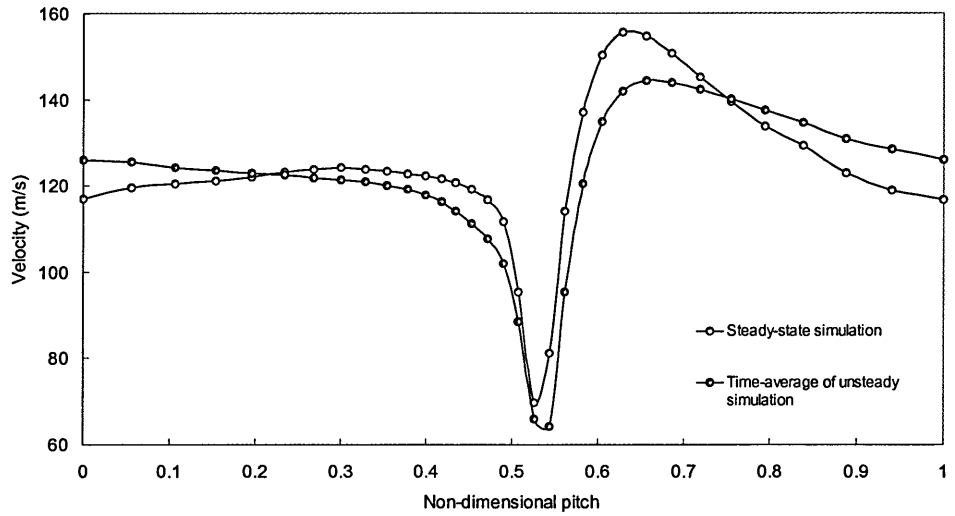

Figure 5-82 Axial velocity pitchwise distribution at 3% radial height – max flow

Seen as a whole these results suggest nevertheless that the variation between the steady-state simulation values and those from the time-average of the unsteady quantities is largest near the hub. A plausible physical explanation for this lies in the fact that whereas in the tip region the rotor wake is fairly thin, near the hub the wake is generally thicker. When subject to the perturbation of a relatively rotating downstream stator blade these wakes are spatially disturbed by different amounts and this is eventually captured by the averaging procedure.

As has been seen previously, the time-average depiction of unsteady stage flows is often associated with a thickness of wakes which is greater than what is calculated in steady-state computations. A clear evidence of this phenomenon is presented by the plots of axial velocity variation across the pitch taken at mid-span, Figure 5-83.

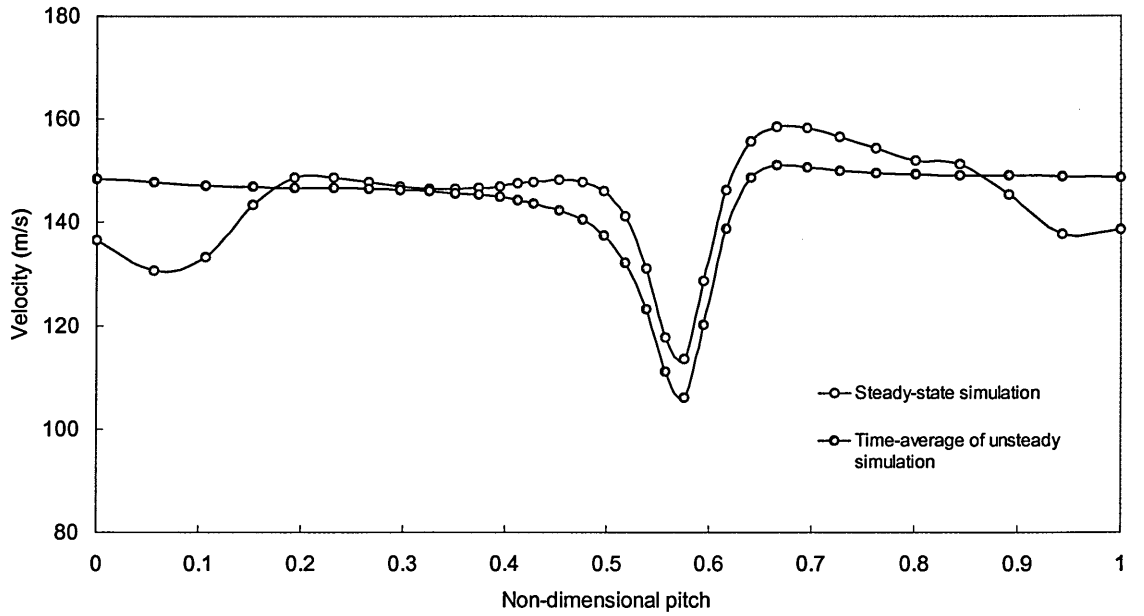

Figure 5-83 Axial velocity pitchwise distribution at 50% radial height – max flow

Another feature of this plot, which is visible also at other radial stations, is the deeper wake prediction yielded by the unsteady computations despite the coincidence in the predictions on the location of the velocity minima.

The added depth of the wake originating from the unsteady simulation is surprising in the light of the fact that it is has been reported that steady-state codes show deeper simulated wakes than those from experimental origin, Dunham and Meauzé, 1998. The explanation advanced by these authors for that discrepancy is that wakes are not only unsteady in pitch but are also unsteady in terms of their velocity deficit due to the periodic vortex shedding. In an experimental set up therefore a laser velocimeter will detect successive velocity minima at different positions and the average wake will be less deep than what is calculated from a steady simulation where no such unsteady action is accounted for.

5.7.2 Contour plots

The evaluation of the differences between the two computation average forms is also usefully performed in a qualitative way through the comparison of a set of contour plots of the main calculated quantities.

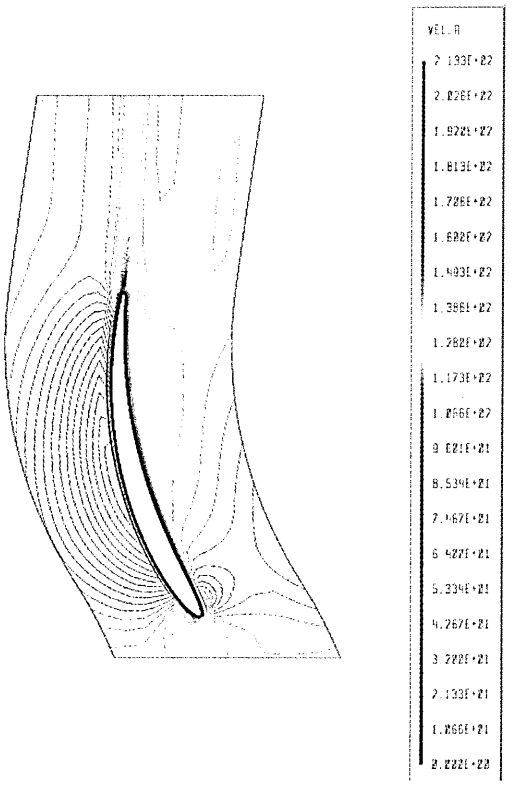

Figure 5-84 Axial velocity at mid-span of stator– steady state simulation

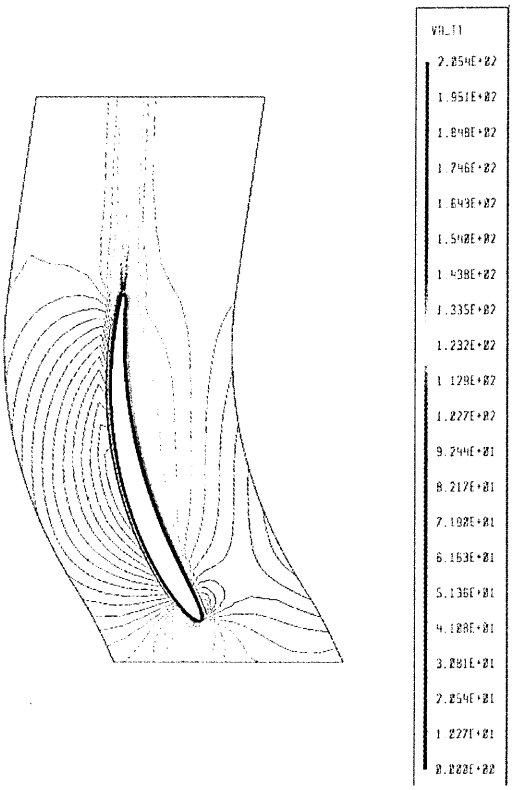

Figure 5-85 Axial velocity at mid-span of stator – time-average of unsteady simulation

The blade-to-blade plots shown above display the axial velocity at mid-span of the stator for the max-flow condition with Figure 5-84 corresponding to steady-state simulation and Figure 5-85 denoting the time-average of the unsteady state simulation. There are few significant differences between the two plots although the plot for the time-average of the unsteady calculation exhibits a slightly wider wake. A surer way to establish the magnitude and locations of the variance between the two distributions nevertheless is to plot the difference calculated at a nodal level, Figure 5-86.

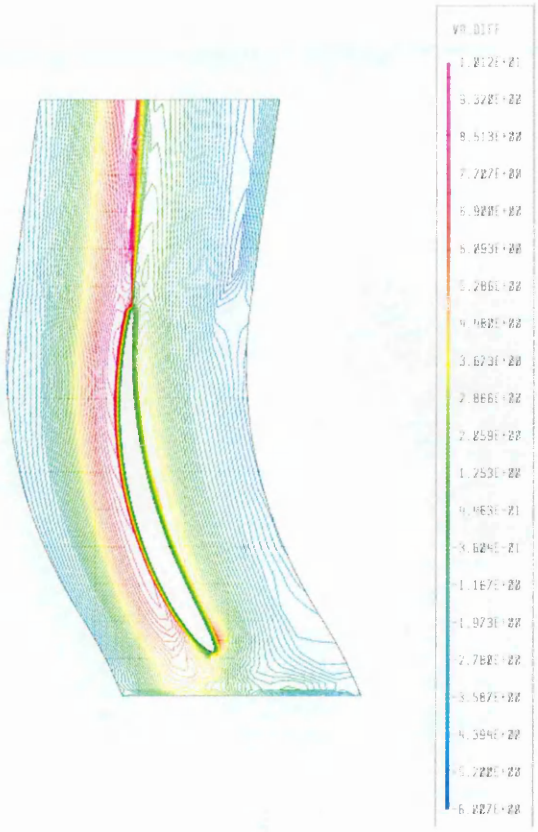

Figure 5-86 Axial velocity difference at mid-span of stator

This plot indicates that for the axial velocity, the dominant variation is predominantly located in the suction side of the blade together with a small region near the blade leading edge. The pattern of the differences is consistent with an unsteady loading regime which acts essentially in vicinity of the suction surface of the blade. The high discrepancy spot located near the leading edge is likely to originate in the variable incidence effects due to the stage interaction. In terms of magnitude the size of the discrepancy is small with typical values representing some 5 or so percent of the freestream values.

The equivalent set of plots for the rotor are Figure 5-87 for the steady-state simulation and Figure 5-88 for the time-average of the unsteady computation.

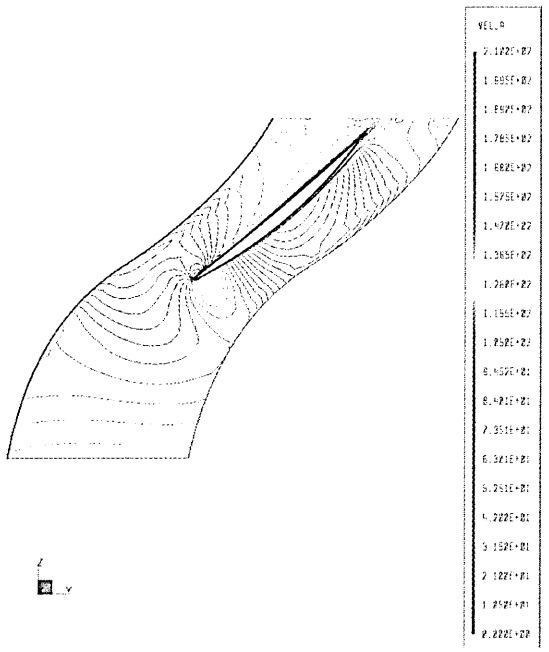

Figure 5-87 Axial velocity at mid-span of rotor – steady state simulation

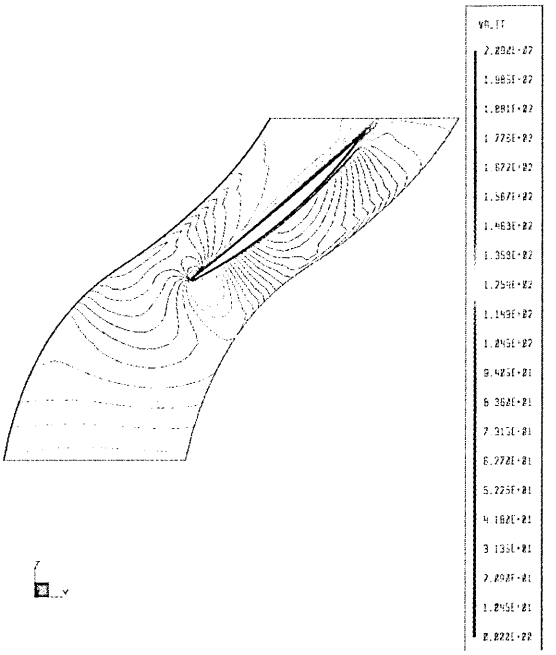

Figure 5-88 Axial velocity at mid-span of stator – time-average of unsteady simulation

The contours in the two plots follow closely the same trends to such an extent as to make identification of disparities between the two particularly difficult and therefore use is made again of the plotting of the nodal differences.

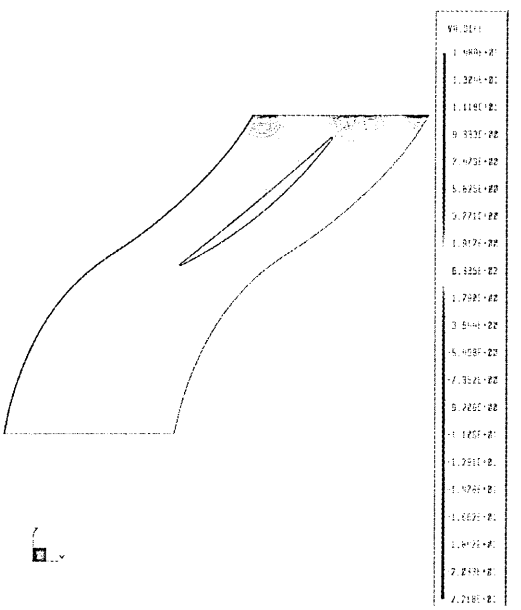

Figure 5-89 Axial velocity difference at mid-span of rotor

The plot of Figure 5-89 confirms that there is in general a quasi absence of variation in axial velocity between the two models. This situation is not altogether unexpected, given that the stage interaction effects are intuitively more likely to affect the tangential velocity component than the axial. The examination of the corresponding plots of the tangential velocity Figure 5-90 and Figure 5-91, nevertheless confirms that both steady formulations are very well matched in the stator domain.

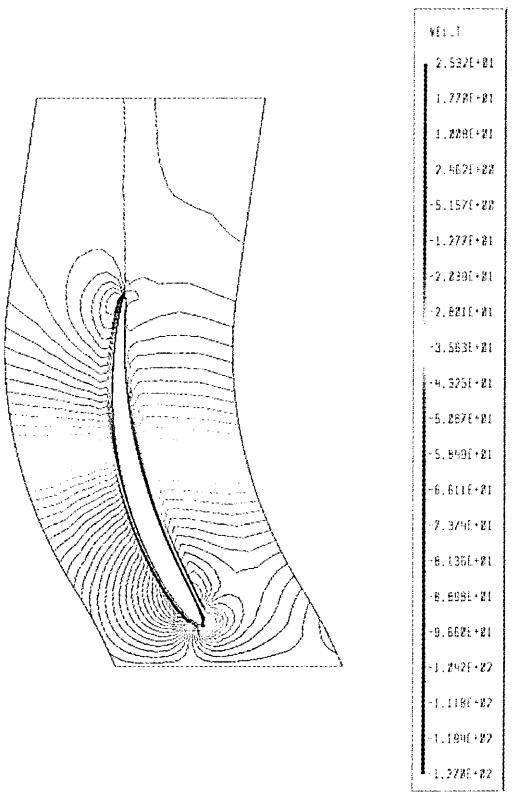

Figure 5-90 Tangential velocity at mid-span of stator – steady state simulation

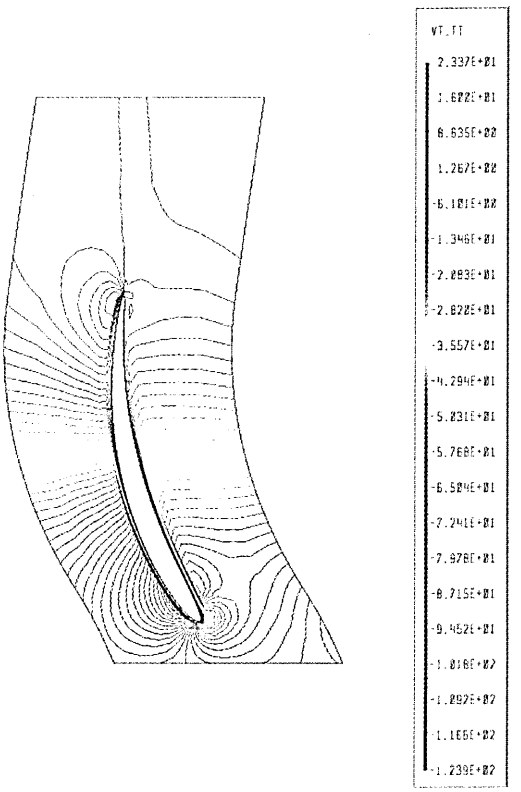

Figure 5-91 Tangential velocity at mid-span of stator – time-average of unsteady simulation

The same situation has been confirmed to exist in the rotor domain where the differences are in the scale of what was seen for the axial velocities. Besides the blade-to-blade plots also passage regions contained in planes perpendicular to the axis of rotation have been examined for evidence of qualitative difference between the two expressions of average flow. The isocontour of axial velocity of the passage downstream of the rotor calculated by steady-state simulation is presented in Figure 5-92 and 5-93 for the time average of the unsteady simulation.

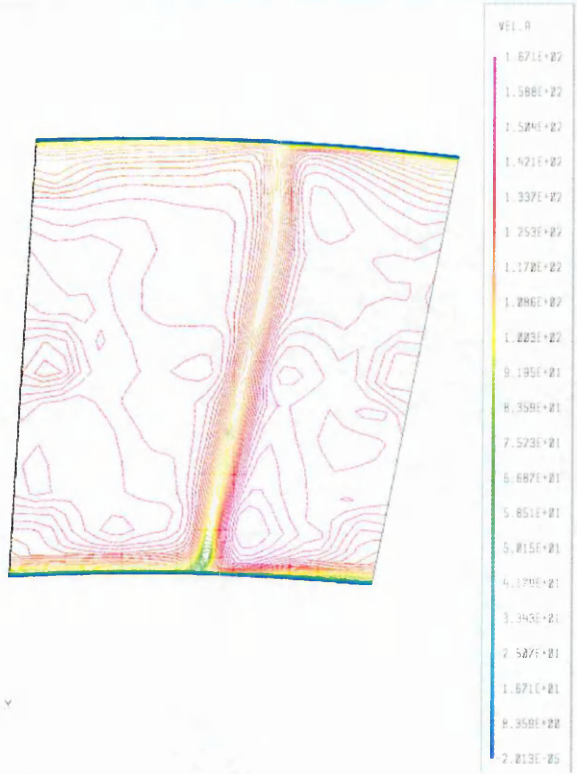

Figure 5-92 Axial velocity downstream of rotor - steady state simulation

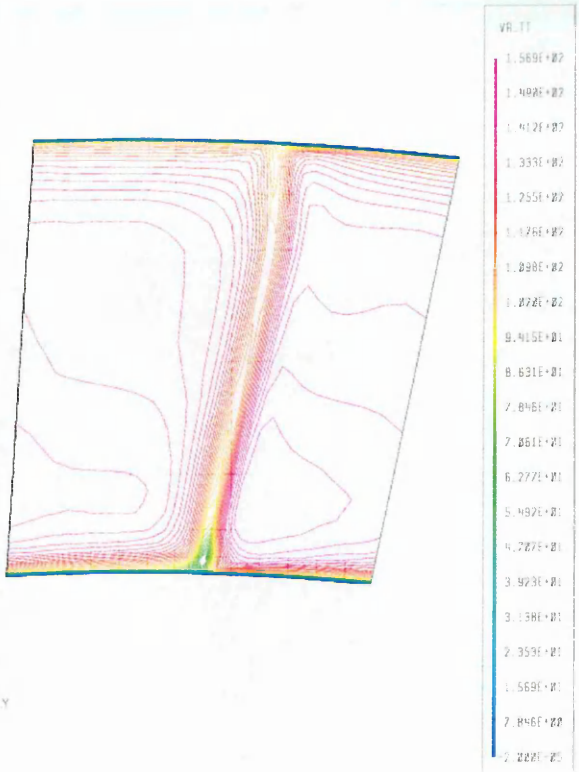

Figure 5-93 Axial velocity downstream of rotor - time-average of unsteady simulation

The passage contours confirm that in a manner similar to the blade-to-blade plots the difference between the rotor wakes of the two methods is slight for this case. There is nevertheless some evidence that in the plot of the time-average of the unsteady simulation the gradients are slightly more spread than in the steady-state computation.

5.8 Results of the application of the semi-empirical models

The two deterministic stress models that have been introduced in Chapter 4 have been applied to the models running on the two grids. For each of these thus three sets of results are available: datum calculation without inclusion of source terms, simulation with added

source terms provided by Bolger's model and idem with source terms calculated through Hall's model.

5.8.1 Large grid models

5.8.1.1 Bolger's model

The starting point of the Bolger's model is the computation at the interface plane of the deterministic stresses from the pitchwise distribution of the components of the correlations, velocities and total energy. This operation requires the calculation of the pitch average of the quantity of interest as is demonstrated graphically in Figure 5-94 on the subject of the tangential velocity.

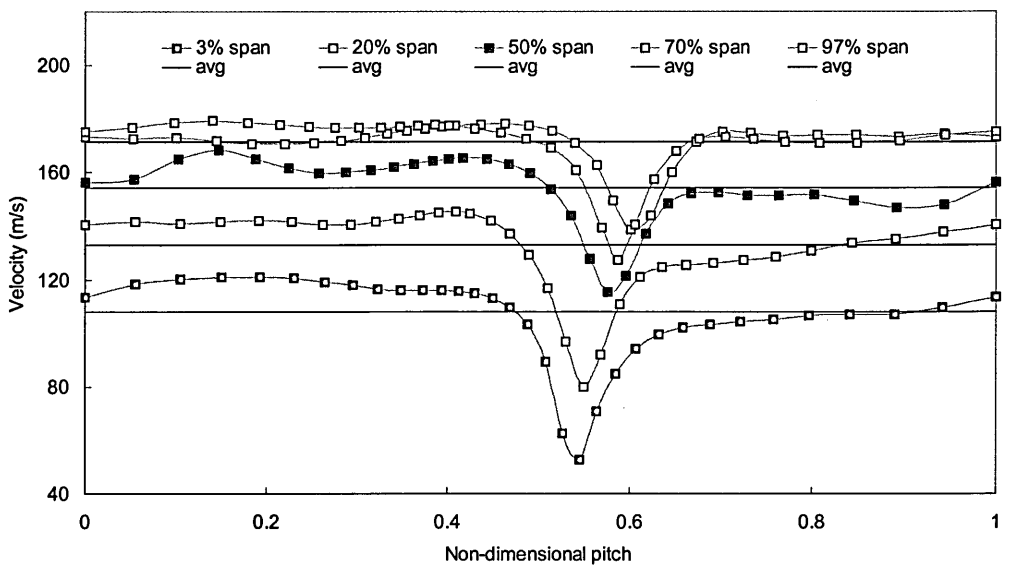

Figure 5-94 HP9 large grid model – tangential velocity at five spanwise locations max-flow

The radial distribution of the interface values of the deterministic stress terms is shown in Figure 5-95 for the velocity-velocity correlations and Figure 5-96 for the velocity-total enthalpy correlations.

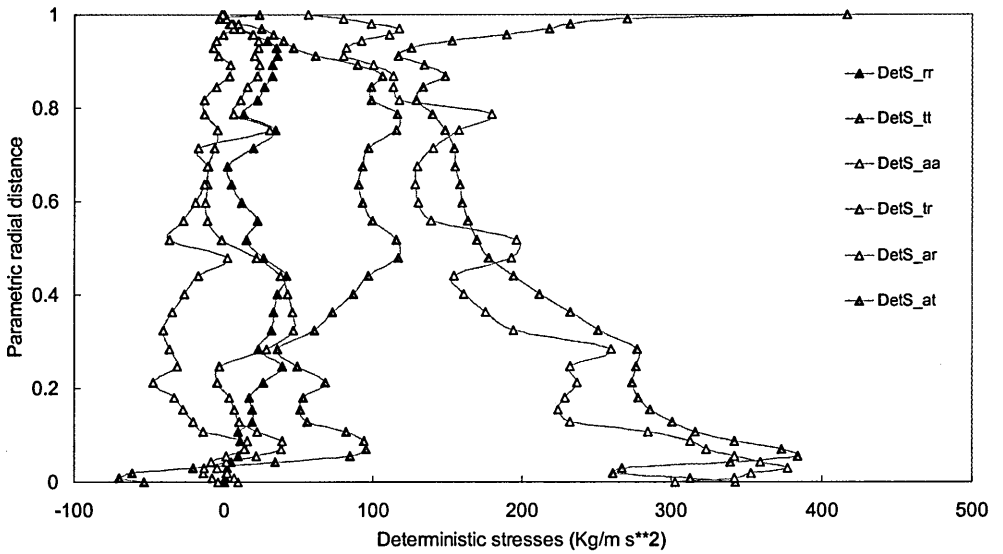

Figure 5-95 Stage interface radial distribution of velocity correlations deterministic stresses at max-flow

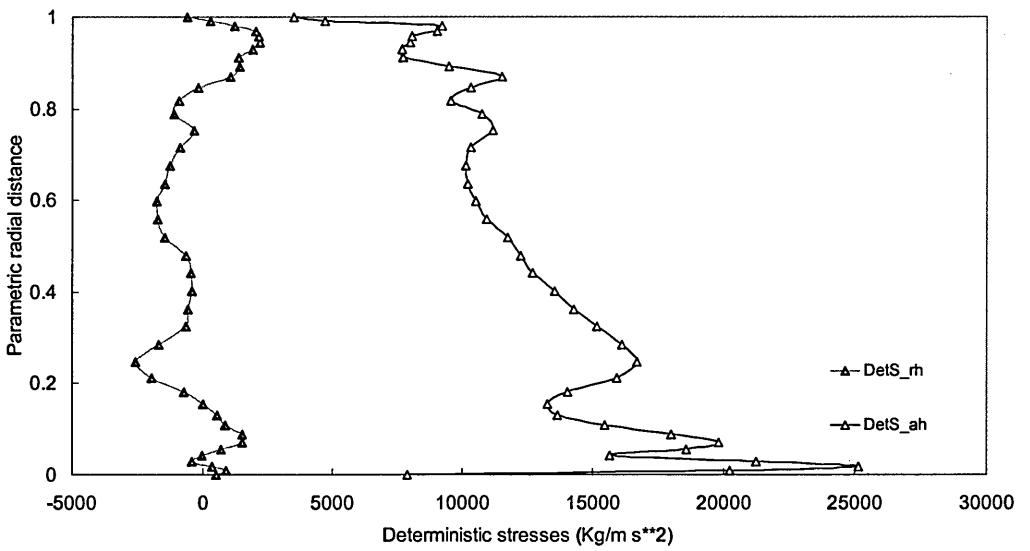

Figure 5-96 Stage interface radial distribution of energy correlations deterministic stresses at max-flow

Once these values are known they are subject to an axial decay which is computed from the high speed versions of the particular decay values of each term as described in

Chapter 4. Finally as each of the TASCflow solution iteration is performed the deterministic stresses are recalculated and supplied to the relevant conservation equation as nodal source terms of the computed variable. The variation of the deterministic stress radial distribution with the operating point is shown in Figure 5-97 for the $\overline{\rho \hat{\tilde{V}}_z \hat{\tilde{V}}_z}$ correlation,

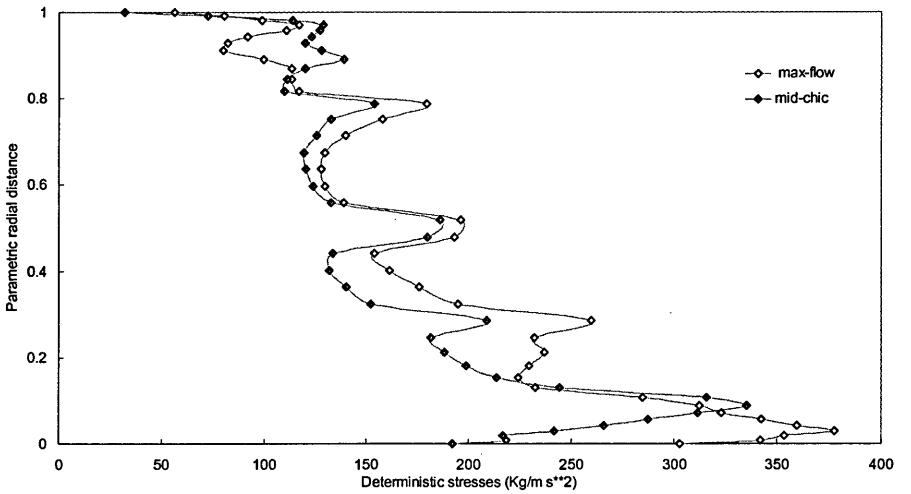

Figure 5-97 Radial distribution of $\overline{\rho \hat{\tilde{V}}_z \hat{\tilde{V}}_z}$ deterministic stress at stage interface

and Figure 5-98 for the $\overline{\rho \hat{\tilde{V}}_z \hat{\tilde{V}}_\theta}$ term.

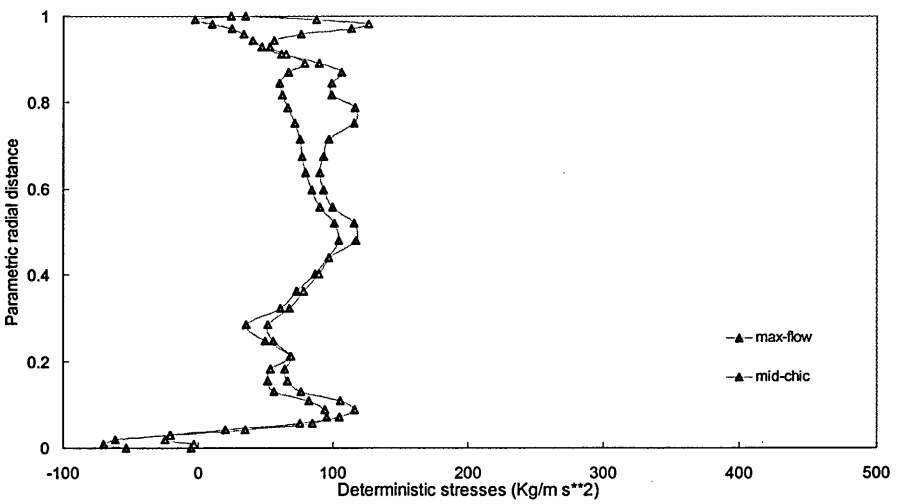

Figure 5-98 Radial distribution of $\overline{\rho \hat{\tilde{V}}_z \hat{\tilde{V}}_\theta}$ deterministic stress at stage interface

As seen from these pictures the variation of the deterministic stresses with the change in conditions between the max-flow and mid-chic points is rather small with the general shape of the distributions remaining essentially unaffected.

The evaluation of the effects of the inclusion of Bolger's model is done through comparisons of tabulated global performance values, radial distributions and qualitative contour plots of the aerodynamic quantities. In Table 5-9 below the parameters from the fine grid datum simulation and Bolger's model are compared for the two higher mass flow operating points.

Performance parameter	Operating point	Datum CFD	Bolger
Pressure ratio	max-flow	1.189	1.189
	mid-chic	1.251	1.253
Temperature ratio	max-flow	1.062	1.061
	mid-chic	1.076	1.076
Adiabatic efficiency %	max-flow	82.3	82.8
	mid-chic	86.7	86.6

Table 5-9 Comparison between HP9 datum and Bolger simulation predictions

The effect of adding deterministic stresses calculated from Bolger's model is shown as a slight decrease in the total temperature ratio and a correspondingly more significant increase in the computed adiabatic efficiency.

In terms of radial distributions the impact of the inclusion of the model is small but perceptible, since the triangles that identify the values obtained with Bolger's model straddle, but are not centred, around the circles corresponding to the CFD datum values, Figure 5-99.

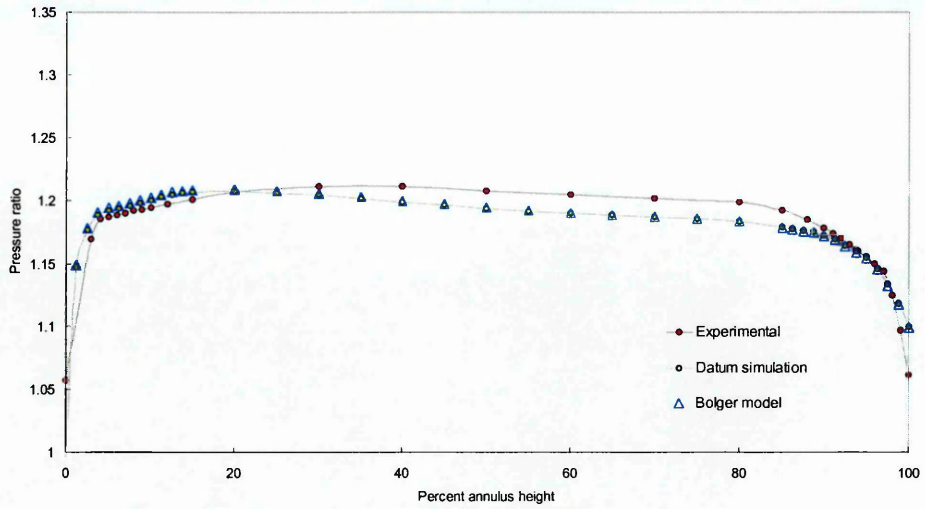

Figure 5-99 Bolger model - radial distribution of total pressure ratio at mid-span

Equally for the contour plots the differences between the datum calculation and that with the model are hardly noticeable

5.8.1.2 Hall's model

This model has at its root the requirement that a stereotypical wake profile be assembled from data obtained from the real wake which is due to the upstream domain blade. The method which has been described in Chapter 4, is graphically illustrated in Figure 5-100 where the similarity wake and the real wake for the axial velocity at mid-span are depicted along with their respective area-weighted pitchwise averages.

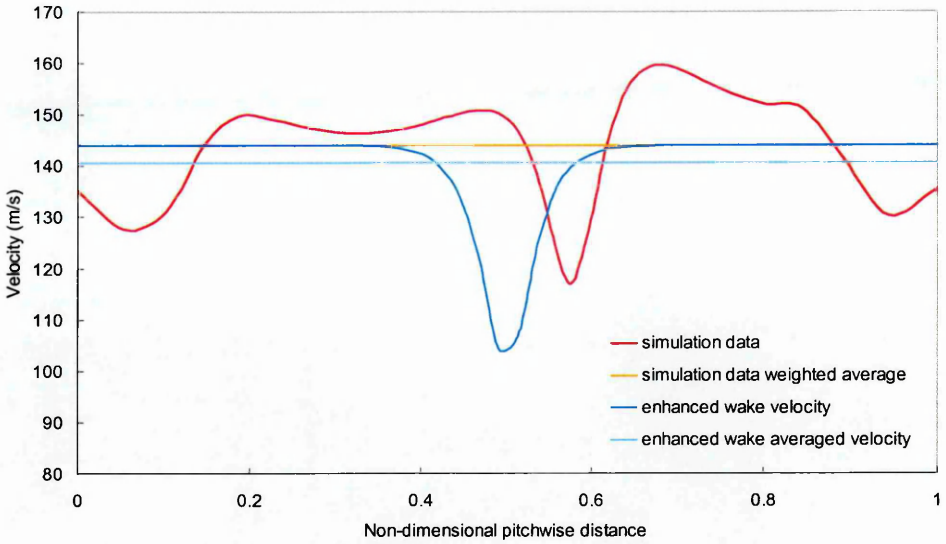

Figure 5-100 Hall's model similarity wake

The decay of the model wakes then proceeds in the manner defined by the enhanced decay correlations presented in Chapter 4 and illustrated in Figure 5-101 below where K denotes the axial grid coordinate index.

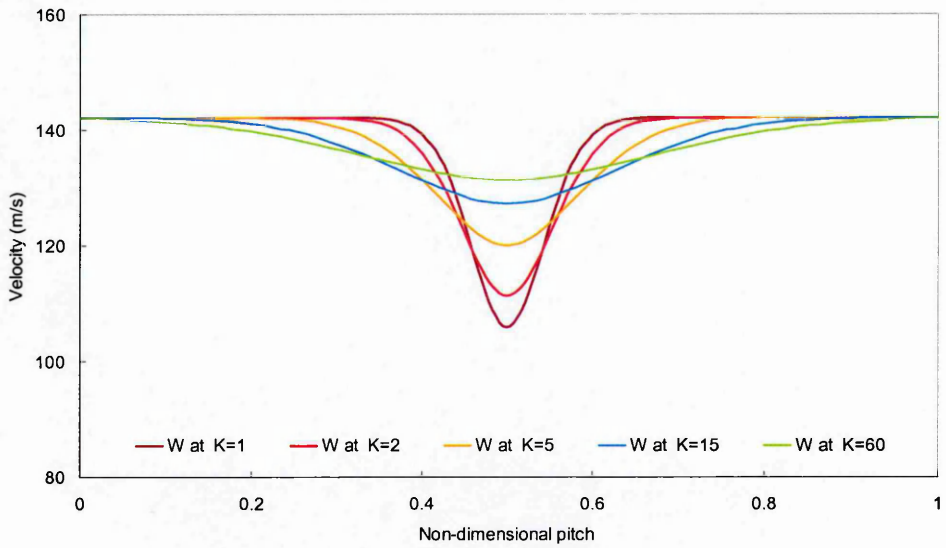

Figure 5-101 Wake decay pitchwise distribution

The effects of the inclusion of Hall's model are also very small for this case as can be seen in the impact of the model in the global parameters shown for comparison in alongside with those of Bolger's model and the equivalent steady-state simulation.

Performance parameter	Operating point	Datum CFD	Bolger	Hall
Pressure ratio	max-flow	1.189	1.189	1.196
	mid-chic	1.251	1.253	1.253
Temperature ratio	max-flow	1.062	1.061	1.063
	mid-chic	1.076	1.076	1.077
Adiabatic efficiency %	max-flow	82.3	82.8	83.4
	mid-chic	86.7	86.7	86.6

Table 5-10 Comparison between HP9 datum, Bolger and Hall simulation predictions – large grid

5.8.1.3 Combined evaluation of the effects of the deterministic stress models

As has been shown above for the different models for the case of the single stage HP9 compressor the effects of the inclusion of either of the deterministic stress models is detectable but small.

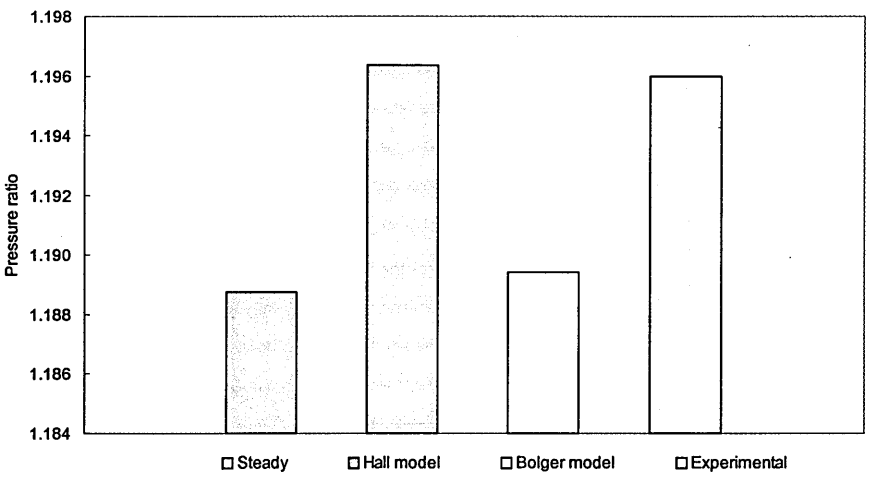

Figure 5-102 Comparative plot of total pressure ratio at max-flow

The plots of Figure 5-102 through to Figure 5-104 express in a graphical manner the variation between the performance results obtained with the models and without, when compared with the values obtained by experimental means at the max-flow condition.

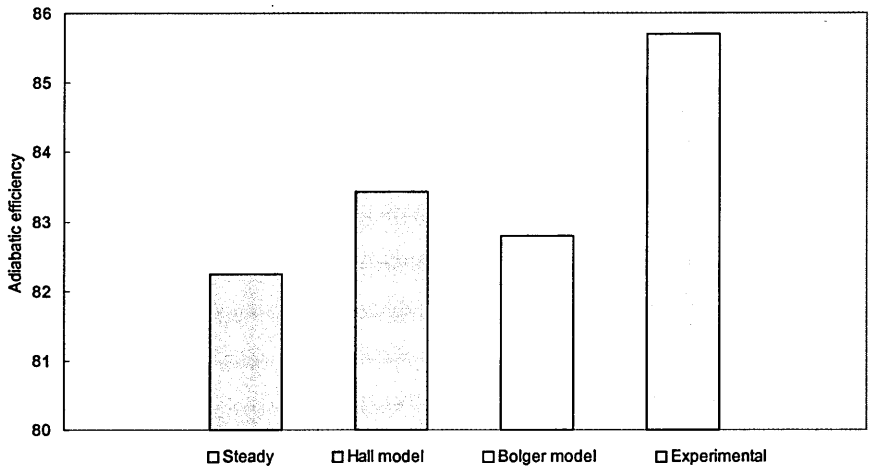

Figure 5-103 Comparative plot of total temperature ratio at max-flow

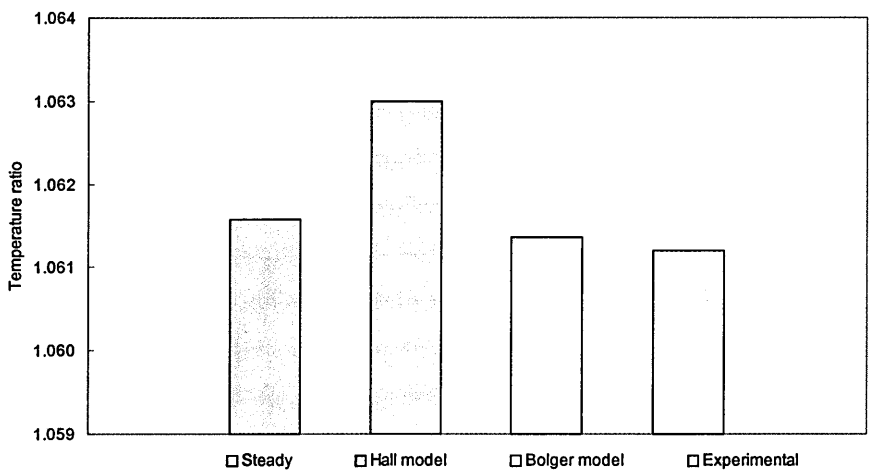

Figure 5-104 Comparative plot of adiabatic efficiency at max-flow

Expressed in these terms and while taking note of the particularly fine scale of the plots which is required to enhance the small existing differences, it can be said that overall the contribution of the addition of the models is to make some contribution to fill the shortfall between the experimental and the standard steady-state results. Of the two

deterministic stress models, Hall's is the one which produces the closest agreement between the two sets of data.

The total pressure ratio calculated from Hall's approach is virtually identical to that reported from experiments but there is an overestimate of the total temperature ratio which is translated then into a modest increase in the calculated value of adiabatic efficiency by reference to the steady-state simulation. Although by different amounts both models yield an increase in the calculated pressure ratio and efficiency.

5.8.2 Coarse grid models

Despite the fact that the object of the semi-empirical models is their inclusion in steady state simulations without recourse to time-accurate runs, the availability of such data enables the comparison, against the experimental data, of results obtained with the standard steady simulation, with both of the deterministic stress models, and with the deterministic stress field obtained from the unsteady computational work. The radial distribution of deterministic stresses obtained directly from the unsteady simulation at max-flow is presented in Figure 5-105.

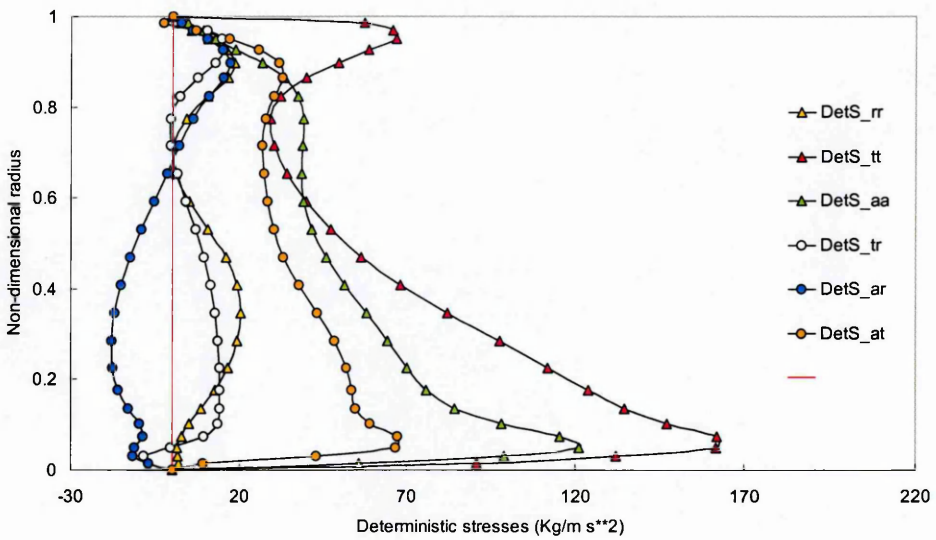

Figure 5-105 Deterministic stress velocity correlations from unsteady simulation at max-flow

The main characteristic of the radial distribution of the deterministic stresses shown above is the smoothness of the contours and the lower values when compared to the equivalent plot shown in Figure 5-95 above a trend which is replicated in the calculations of the models, as seen in Figure 5-106 for the Bolger case.

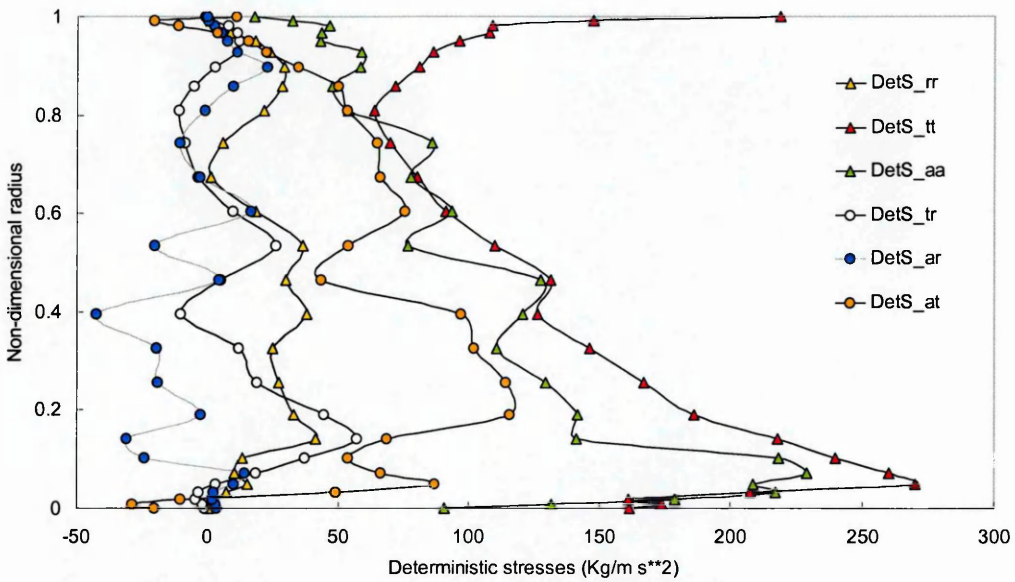

Figure 5-106 Radial distribution of velocity correlations deterministic stresses at max-flow – coarse grid

The computed deterministic stresses in the coarse grid are in general smaller than those of the finer grid, two factors being likely to contribute to this event. Firstly the two configurations of the stator are somewhat different in the two computational models and secondly the wakes which are calculated by the two models are somewhat different as has been seen.

The axial decay of the deterministic stress terms acquired from the two semi-empirical models and directly from the unsteady computations is presented graphically below for the max-flow condition.

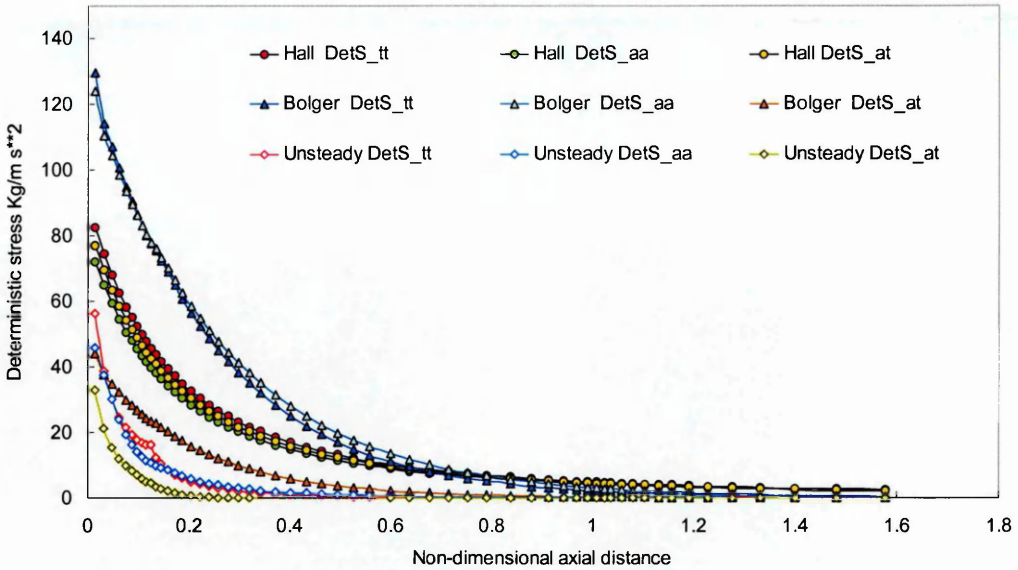

Figure 5-107 Small grid deterministic stresses axial decay

5.8.2.1 Global performance parameters results

The presentation of these results is again made by recourse to bar graphs where alongside the results from the two models, the steady-state results, the average of the unsteady simulation and the steady-state simulations with the unsteady derived deterministic stresses are found.

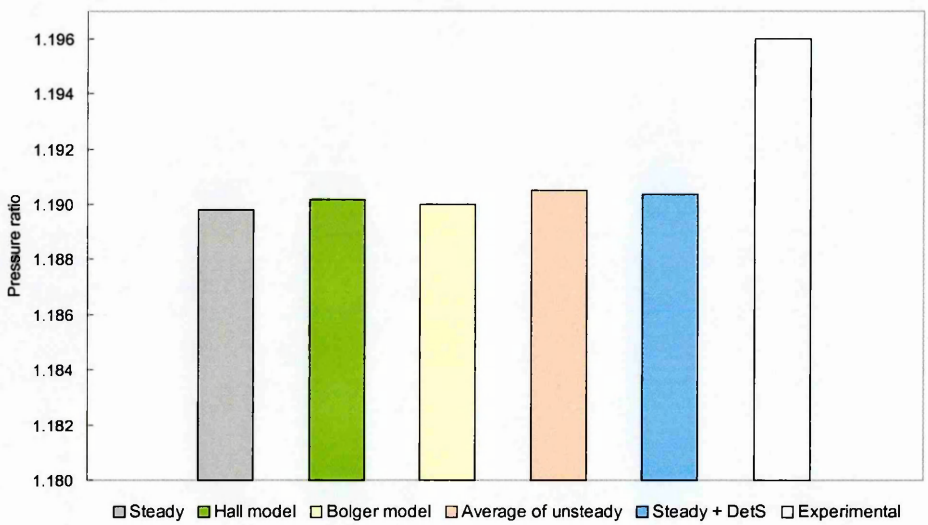

Figure 5-108 Comparison of global values of total pressure ratio at max flow – coarse grid

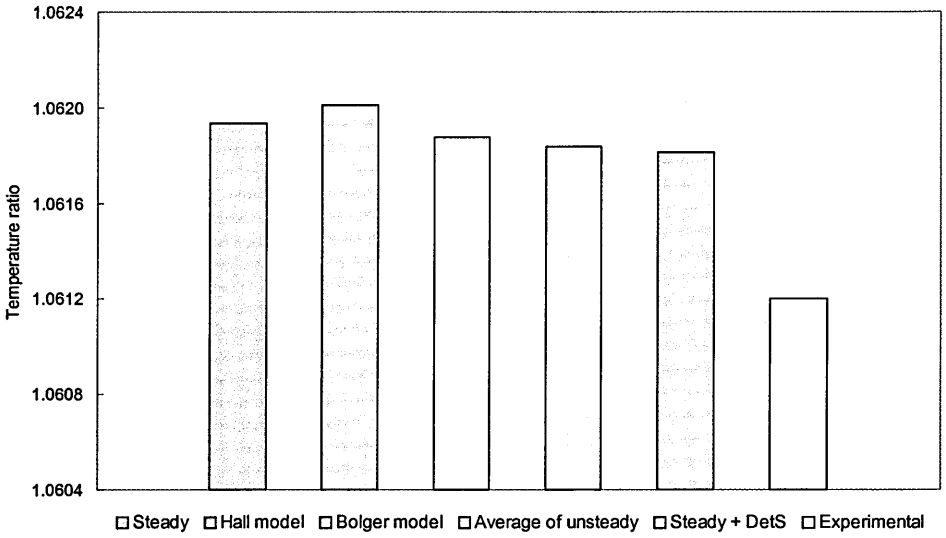

Figure 5-109 Comparison of global values of total temperature ratio at max flow – coarse grid

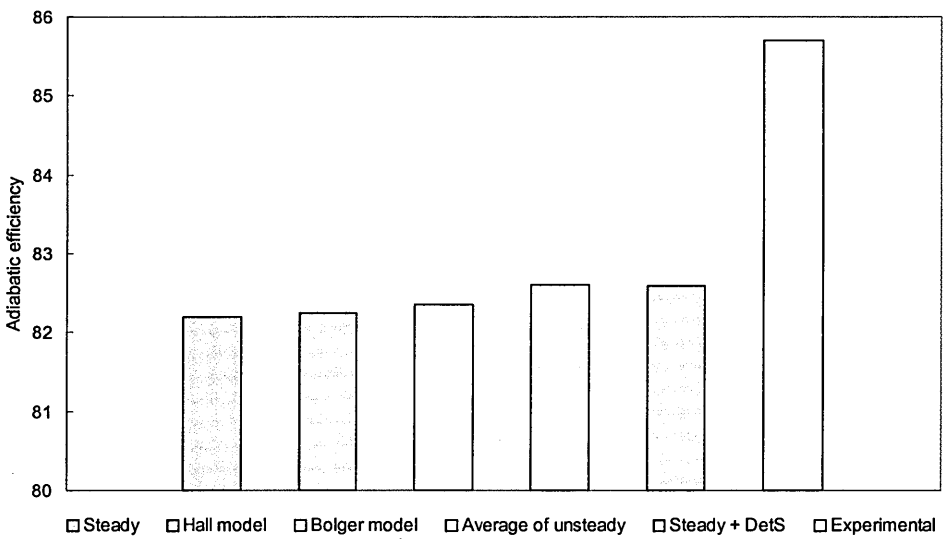

Figure 5-110 Comparison of global values of adiabatic efficiency at max flow – coarse grid

The joint message contained in these graphs is that although the various models do offer a contribution towards closing the gap between the steady-state simulation and the experimental results, this contribution amounts to a nudge at best and does not come near to the push this closing of the gap really requires. Interestingly, but not surprisingly given their underlying principles, it is the averaged form of the unsteady simulation, and its

close relative, the steady-state plus the unsteadily derived deterministic stresses terms, which better replicates the trends of the experimental data.

5.8.2.2 Radial distributions

The radial plots of total pressure ratio and adiabatic efficiency, Figure 5-111 and 5-112 are shown below for completeness.

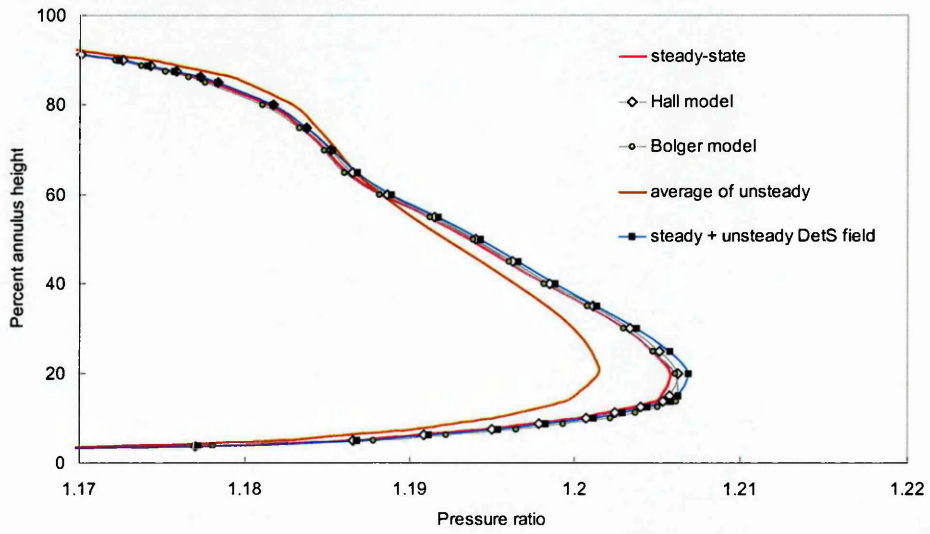

Figure 5-111 Radial distribution of pressure ratio – coarse grid max-flow model comparison

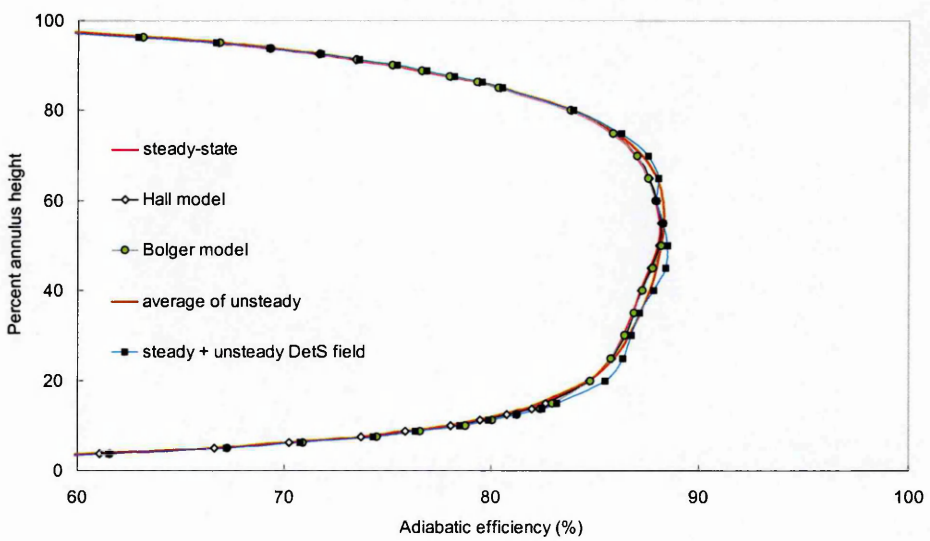

Figure 5-112 Radial distribution of adiabatic efficiency – coarse grid max-flow model comparison

As these plots make clear a strong amplification of the natural scales of the parameter is required in order to expose the variations in the radial values of the flows computed by the various means alluded to above.

5.9 Closure

This chapter described the impact of the application of two semi-empirical deterministic stress models to the Rolls-Royce HP9 high-speed test case while employing two grid sizes. The effects of the deterministic stress models are detectable, but not sufficiently large, to significantly impact on the flow field in the scale required to approximate the basic CFD computation to the experimental data. A single stage configuration is not in any case the intended natural target of these models and therefore, even if the outcome of the application of the method to HP9 does not provide a convincing proof of the utility of the approach, its proper validation requires the employment of a realistic multistage test case and it is this task which is undertaken in the following chapter.

Chapter 6

Computational analysis of the Cranfield High-Speed Research Compressor

6.1 Test case description

6.1.1 Background

The University of Cranfield has operated for many years a Large-Scale Low-Speed Research Compressor facility and results obtained with several of its different builds have been used in experimental studies, for example Smout and Ivey, 1991, Camp and Shin, 1994, and Ivey and Swoboda, 1998, and in the validation of CFD code development, Politis et al, 1993 and Lockwood, 1999, or indeed as a combination of both Lyes and Ginder, 1998.

The Cranfield's LSRC is a four stage parallel annulus machine with a hub-tip ratio of 0.91 and whose typical blade span is about 55mm. The rotational speed of the compressor is about 1000 rpm giving a typical blade tip speed of some 70 m/s and characteristic Reynolds number of 300,000. The first two stages provide suitable entry conditions to the third stage, which is the stage under investigation, while the fourth and last stage supplies the appropriate downstream conditions. The second of the LSRC stator rows can be indexed in relation to the other stators of the machine and in order to enable relative frame measurements to be performed a traverse mechanism,

allowing radial, pitchwise and yaw motion of probes, is attached to the rotating component.

The testing of high speed core compressors, either for the strategic purpose of gaining added knowledge of the flow physics of these machines or for the development of innovative blade shapes, is by all accounts a very costly exercise. It is primarily due to this consideration that whenever possible low speed research compressors are used to undertake some of the more fundamental studies, not only at a fraction of the cost of the running of the machine whose flow physics they model, but also benefiting of the added ease of instrumentation which their large scale affords.

In order to make the blading of low-speed compressors representative of the flow physics of their high-speed brethren, the blades of the low-speed machines are designed to present surface velocity distributions which are similar to those found in high-speed compressors.

Although low-speed compressors are often an appropriate platform to conduct a range of studies which are illustrative of the flow behaviour in high-speed machines, there are also some serious limitations associated with the employment of low-speed machines in this role. In order to achieve similar velocity distributions, low-speed compressor design is characterized by blades which are thicker, and hence have leading edges which are blunter, and are in general more cambered, than the scaled up versions of the equivalent high-speed blades. As a consequence of these design features low speed blades are generally more tolerant of incidence variation and are not prone to passage choking and offer therefore no realistic representation of the stage mismatch which is a feature of the off-design flow behaviour of high-speed compressors.

Furthermore since in a parallel annulus machine the axial velocity is effectively constant, low-speed machines fail to replicate the decay in axial velocity, and hence the de Haller number values, which is observable in high-speed compressors. To compensate for this problem, low speed blade sections are designed to yield distributions of local to trailing edge velocities which are identical to those of high-speed blading and which therefore help to preserve its local diffusion properties.

Other objections to the sole reliance on experimental data acquired in low-speed compressors is that such machines with only a few stages have minimal stage interactions, Baghdadi, 1995 and also that there is no significant temperature rise.

In view of the limitations of the LSRC the Turbomachinery Department of Cranfield University commissioned in the late nineties a preliminary design for a three stages high-speed compressor and embarked on a search of risk sharing partners with whom the raising of this facility could be achieved. These partners were eventually found within an European dimension in the form of the Advanced Compressor Blade or AdComB project.

AdComB is a pan-European project which is sponsored by four industrial partners, MTU and BMW Rolls-Royce both from Germany, ALSTOM Gas Turbines from the UK and Volvo Aero Engines from Sweden. The industrial partners provide the greater part of the development and design work of the project as well as the bulk of the financial support, the balance being made up by a European Commission research fund contribution. The experimental facilities and optimisation research work are contributed by four technical universities which are, besides Cranfield in the UK, Braunschweig, Kassel and the Universität der Bundeswehr in Munich, all from Germany.

The ultimate objective of the project is the attainment of a higher pressure ratio with fewer blade rows thereby implying higher aerodynamic loadings. In order to accommodate the expected blade load rise an innovative 3D rotor and stator blade design will be required. The benefits associated with some of these techniques are reasonably well understood, lean and sweep for example, see Dawes and Denton, 1998, but their full exploitation and integration with other methods such as endwall contouring and profile camber distribution has not been to date completely achieved due to a lack of detailed knowledge of their interaction effects as well as of the potential risks.

Although the rewards of shorter compressors, fewer components and the parallel benefits of weight savings and shorter, less drag inducing engine nacelles, are worth pursuing, such a configuration presents for designers additional challenges given that

the increased blade loading can lead to an insufficient inbuilt surge margin. The development of machines operating under tighter constraints in this sector of the performance curve is therefore intimately linked to a high degree of familiarity with the behaviour of the compressor in off-design flow regimes. While low speed research machines can be usefully used to investigate many aspects of novel blade design, the authoritative experimental development work, particularly of the off-design flow regimes, requires the employment of a compressor whose gas path is more realistically in line with those of operational designs.

Besides the acquisition of expertise in 3D design which directly stems from the core of the project, the availability of detailed high-speed experimental data is extremely valuable to CFD practitioners and code developers. This data enables the validation of the numerical predictions on whose accuracy the further development of 3D design concepts is largely dependent. Although the row-wise consideration of the three-dimensional effects is important and has been the subject of recent reported work, Shang et al, 1993, Weingold et al, 1995 and Sasaki and Breugelmans, 1997, the full exploitation of these features requires a consideration of the whole compressor flow field.

The present work is the numerical complement of the experimental work conducted at Cranfield and is tasked with providing a CFD prediction of the initial datum blading as well as investigating the effects of the addition of deterministic stress terms to the basic simulations in order to offer an added physics description of the machine wide flow field. Some of the simulation data is of direct interest to the experimental workers, supplying for example information on the expected wake widths, which is of direct relevance to the selection of the frequency of the unsteady pressure acquisition system.

6.1.2 Datum design features

The Cranfield HSRC is a three stage machine with IGV and a design pressure ratio of 2.42 and an isentropic efficiency of 88.95% for a mass flow of 10.6 Kg/s at 9300 rpm. The HSRC is intended to replicate the flow conditions which are typical of the

embedded stages of a fairly highly loaded core compressor. The datum blading which is designed to be representative of modern but conventional design techniques is characterized by controlled diffusion blade profiles with continuous curvature leading edges and predicted low deviation angles.

Controlled diffusion blades are the turbomachinery equivalent to supercritical wing aerofoils in that the blade profile is carefully tailored in order to exhibit between the leading and trailing edges a variation of aerodynamic quantities which is thought to be desirable for a particular application. The primary requirements are to have a smooth and continuous acceleration from the leading edge to the point of maximum Mach number on the suction surface followed by the maximum rate of diffusion possible without flow separation, McKenzie, 1997.

By varying the spanwise distribution of properties, the designer can for example prescribe a constant radial distribution of total pressure ratio, this has incidentally been the criterion applied to the design of the HSRC datum rotor blading, while for the stator blade it is the outlet angle which is kept constant. In order to prevent the flow from separating, controlled diffusion blades have a distinctive shape which is characterized by a flattening of the camber line in the latter quarter or so of the blade chord. This geometric feature when associated with the designed-in lack of tendency for separation leads to a predictably small deviation in the order of half to a quarter of that of conventional profiles.

The blades are centroid stacked and have no end-bends and the IGV is not cantilevered. The tip clearance was anticipated in the design phase to be about 1% of the mean blade height.

The HSRC significant aerodynamic parameters at design point are presented below, Table 6-1 in terms of rotor and stator values of blade numbers, absolute inlet angle, flow coefficient, work coefficient, diffusion factor, spacing to chord, aspect ratio, hub-tip ratio, relative Mach number at the rotor tip and the Reynolds number referred to the blade chord .

Parameter	Stage 1	Stage2	Stage 3
Blade No	71 / 91	89 / 107	85 / 116
α_0 (degrees)	15	13	13
Va/U	0.722	0.723	0.736
$\Delta H/U^2$	0.540	0.589	0.452
DF	0.480 / 0.460	0.480 / 0.474	0.465 / 0.468
s/c	0.600 / 0.571	0.550 / 0.585	0.700 / 0.568
AR	1.05 / 1.13	0.91 / 1.00	0.87 / 0.94
h/t	0.85	0.88	0.91
M_{tip}	0.829	0.790	0.742
$Re_c * 10^5$	5.82 / 4.78	6.16 / 5.03	6.04 / 4.91

Table 6-1 Cranfield HSRC aerodynamic design features

The aerodynamic design of the compressor in its original configuration was performed by Dr. Chris Robinson of PCA Engineers, Lincoln, who made use of an inviscid throughflow code to establish the machine axisymmetric flow description. In order to account for losses a Wright and Miller, 1991, correlation was employed, the value for blockage at inlet being set at 3.1% and double that value at the outlet of the machine.

The general dimensions of the initial compressor configuration, as originally supplied by the designer are presented in Figure 6-1 below, with all measurements being expressed in millimetres.

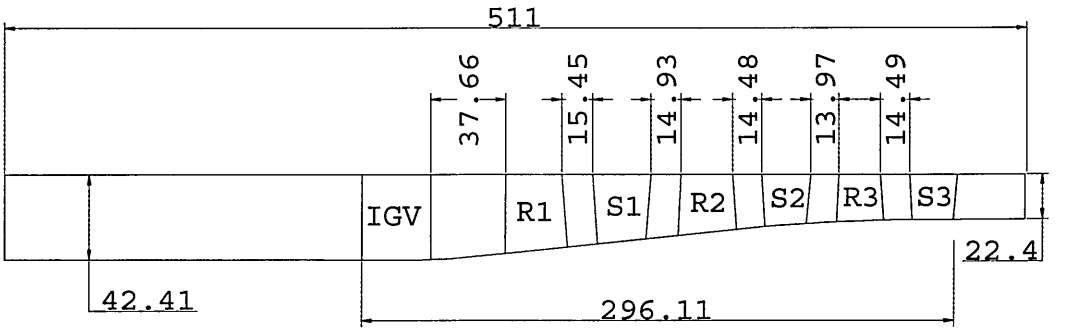

Figure 6-1 HSRC initial design layout

As can be seen from the picture above, the mean axial separation of the adjacent blade rows was set at about 15mm, the IGV excepted, where this distance was significantly greater. This small axial gap follows the contemporaneous trend towards closely spaced blade rows consistent with the goal of limiting the axial dimensions of the compressor.

Seen from the perspective of the wake recovery mechanics a reduced axial gap ought to have a beneficial effect on the compressor aerodynamic performance but this shift however is known to be in conflict with the preservation of the efficiency of a given design as was demonstrated by Gundy-Burlet and Dorney, 1997, in the computational study of a two-and-half stage compressor. For that study the axial gaps between the blade rows were set at 20, 35 and 50% of the average of the axial chord of all blade sections in the compressor. These authors reported that in general lower efficiencies were seen to occur as the axial gap decreased, with the precise magnitude of this decrease being also a function of other design parameters such as the relative clocking between the machine stator rows. This study is also consistent with the findings of Gorrell et al., 1997, who reported a reduction in overall performance with a decrease in axial spacing.

Although useful from an overall gas turbine design perspective, closely spaced blade rows present in addition a considerable challenge to other than non-intrusive experimental methods such that in order to enable the fitting of probes it was deemed necessary to alter the basic configuration of the HSRC so as to increase the inter blade

row axial spacing. This increase is in fact slightly larger than what was strictly required by the experimental apparatus fitted to the initial build but it is also intended to accommodate the anticipated 3D blade designs whose configurations will possibly include sweeping shapes which occupy a greater axial space than those of the datum configuration.

Even so the blade row separation exercise provides a classical illustration of one of the main limitations of conventional testing methods and conversely of the essential attractiveness of the numerical approach with its potential access to data extraction virtually anywhere within the physical domain of the machine.

The updated geometric parameters of the 'experimental' version of the HSRC is shown in Figure 6-2. The significant question raised by the modification of the initial geometry is clearly what is likely to be the impact of the redesign exercise on the aerodynamic behaviour of the machine by comparison with the original design intent.

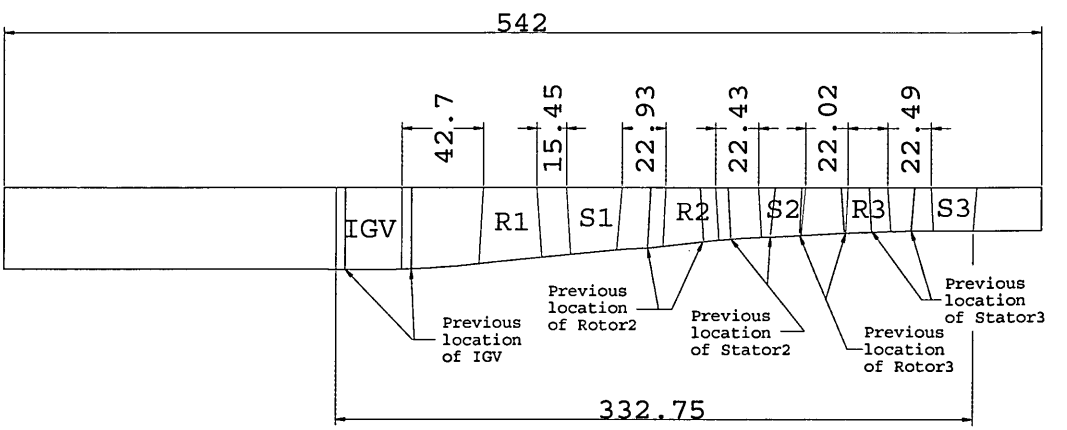

Figure 6-2 HSRC revised axial spacing layout

The axial blade row separation characteristic of the revised geometry is about 22mm except in the IGV-Rotor1 gap where the IGV was displaced upstream by some 5mm and between the first stage components where the Rotor1-Stator1 gap is unchanged as these two rows were the only ones to keep their primitive locations. A three-dimensional perspective of the machine in its final configuration is presented below.

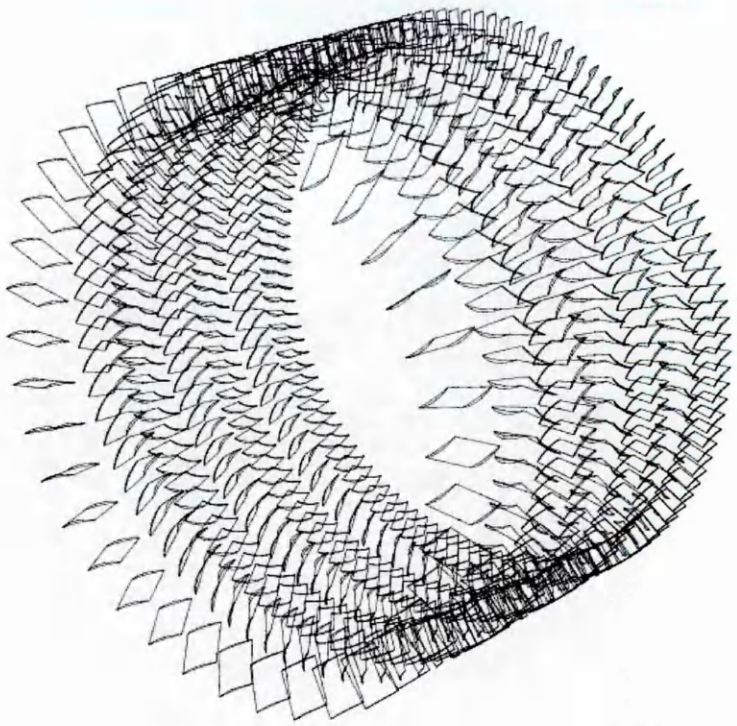

Figure 6-3 Three-dimensional view of the HSRC blading arrangement

The aerodynamic implications of the separation exercise are thought to be minor in terms of the design point conditions, but are likely to have some impact on the surge margin of the compressor.

6.1.2.1 Experimental set-up

The initial experimental programme calls for the evaluation of the global performance parameters, total pressure and temperature ratios and adiabatic efficiency. The HSRC instrumentation schedule for this phase is as follows:

Inlet bellmouth

- 4 'ganged' wall static tappings connected to a Furness micro-manometer pressure indicator – pressure range ± 3 psi
- 4 rakes with 4 total pressure probes each - pressure range ± 3 psi

These instruments supply data for the calculation of mass flow rate and upstream total pressure.

Compressor inlet

- 4 rakes with 3 K-type (exposed) thermocouples each
- 4 rakes with 5 Kiel probes each – pressure range 50 psi

The compressor inlet is, for purposes of performance prediction, considered to be located downstream of the IGV. The function of this component is seen as simply helping to establish the appropriate inlet conditions characteristic of the embedded core compressor the HSRC seeks to replicate, and this is why it is not included in the overall performance calculations.

Compressor outlet

- 4 rakes with 3 K-type (exposed) thermocouples each
- 4 rakes with 5 Kiel probes each – pressure range 50 psi

Unless where specified the pressure transducers are of the 'Druck' piezo-resitive type whose accuracy is given as about ± 0.05% of the readings at the ranges mentioned. The accuracy of the K-type thermocouples is established to be at about ± 1K. The rig is fitted with a torquemeter but for the preliminary evaluation runs the output of this apparatus was considered suspect and thus for the estimation of the isentropic efficiency the results of the temperature sensing devices are used instead.

6.2 Steady-state datum simulation

6.2.1 Initial considerations

If the effects of the axial separation described previously, can be seen as to some degree compromising the basic design, for the CFD analyst the separation exercise offered a welcome relaxation from the known problems, associated with the simulation of closely spaced adjacent blade rows.

When in the latter part of eighties 3D RANS simulations become feasible as a turbomachinery analysis tool, the computation of multistage compressors was performed one blade row at a time. Later on such calculations became practicable in terms of coupled blade rows whereby the solution of the entire machine progressed as before in successive single row increments but where the row of interest was solved together with its downstream neighbour in order to offer some account of the machine environment.

One instance of the use of this technique is presented by the work of Elmendorf et al, 1998, who employed the TASCflow commercial code to compute the flow field of a 15 stage axial compressor. In Elmendorf's approach a 2D streamline curvature method was used to supply the radial profile of static pressure in the exit plane of the computational domain but wherever necessary the pressure level was adjusted to achieve the correct compressor mass flow rate.

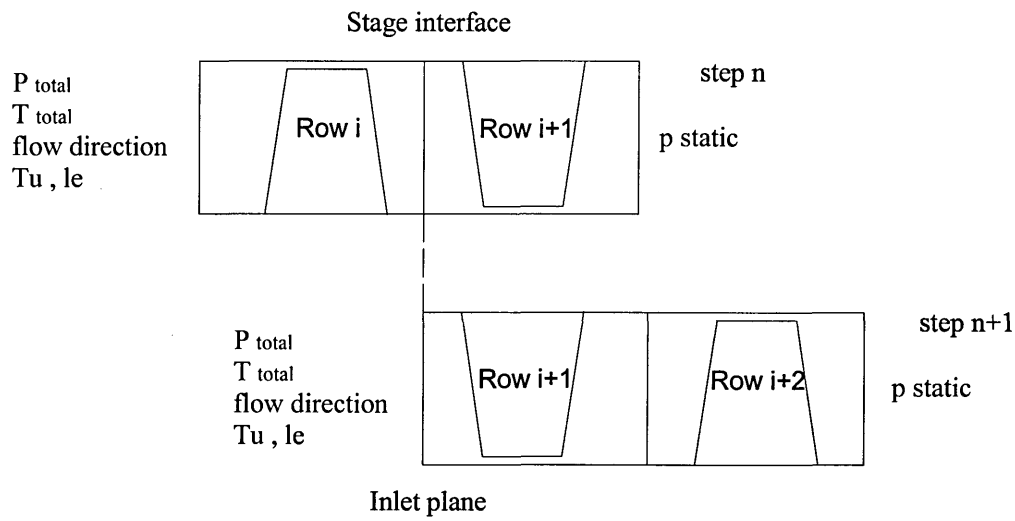

Figure 6-4 Elmendorf multistage solution approach

The Elmendorf technique, schematically described in Figure 6-4, where the stage domain boundary condition variables are denoted in red, ensures that the influence of both the upstream and downstream blade rows is considered. This is, according to the authors, achieved by relying exclusively, for the purposes of data evaluation and

interpretation, on the numerical results of the first blade row of each combination whose boundary conditions are always well defined throughout the computation.

Given that Elmendorf reported very good agreement between the experimental and computed quantities one has to conclude that for any given blade row the main source of information regarding its embedded status is supplied by the upstream rows. Nevertheless the approach employed by Elmendorf is not a stand-alone computation method in that it still depends on a separate machine wide calculation of the static pressure profiles, provided by a throughflow calculation, to supply the required exit boundary condition input to the stepwise solutions.

There is one further complication associated with the procedure employed by Elmendorf and his co-workers which is related to the axial extent of the individual blade row grid domains used in the simulation. Considering again Figure 6-4 it will be seen that for all but the first and last of the machine blade rows, the natural boundaries of the separate domains are located halfway between adjacent blades. For most CFD codes, and that is certainly the case with TASCflow, the closeness of the inflow and outflow boundary conditions to the blades does not offer a sufficient spacing within which to adequately resolve the local variable gradients. This well known problem is rather surprisingly not alluded to in Elmendorf's paper.

It had been an original intention to include in the present work results of an HSRC simulation performed along the lines of the method described by Elmendorf and in fact this author initiated the computation of the first five blade rows according to that scheme. Nevertheless due to convergence difficulties experienced with the stepwise solution of the compressor, this approach was abandoned and therefore the solution of the machine relies exclusively on the simultaneous computation of all the seven blade rows of the machine, Figure 6-5.

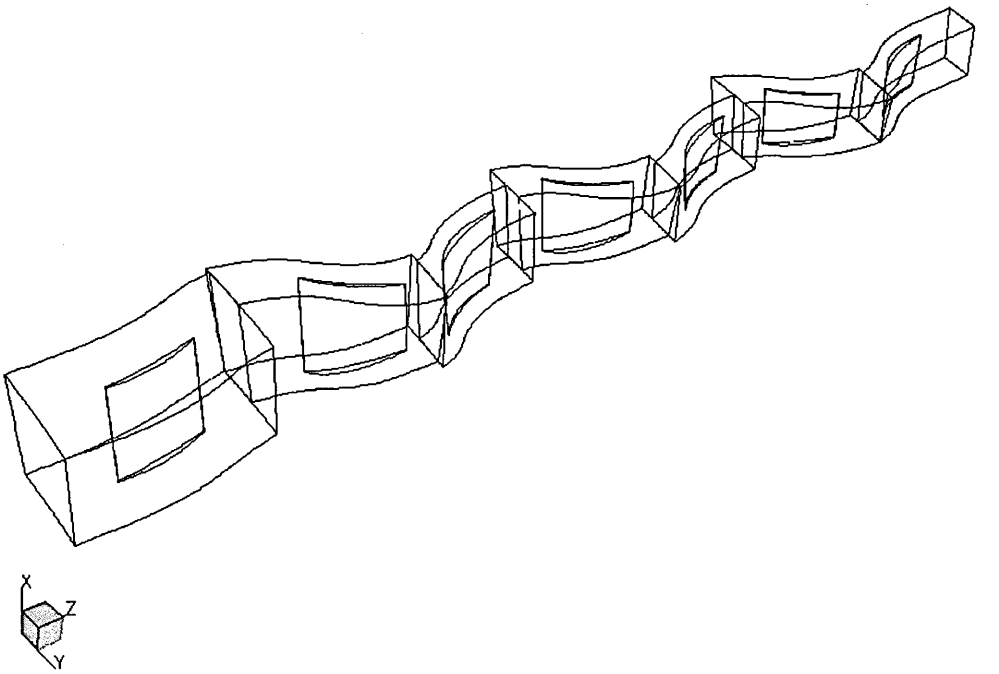

Figure 6-5 HSRC grid domains configuration

6.2.2 Grid assembly and run parameters matters

The geometry of the compressor was supplied in terms of Cartesian coordinate points defining 15 blade profiles and meridional hub and shroud lines, Figure 6-6.

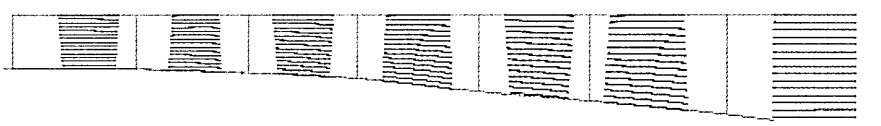

Figure 6-6 Grid generation geometric input data

The grid generation followed the same broad steps outlined for the HP9 case in that the seven blade grids were constructed through the TASCgrid approach described previously and are again single block H type meshes, arranged in an axisymmetric configuration, Figure 6-7.

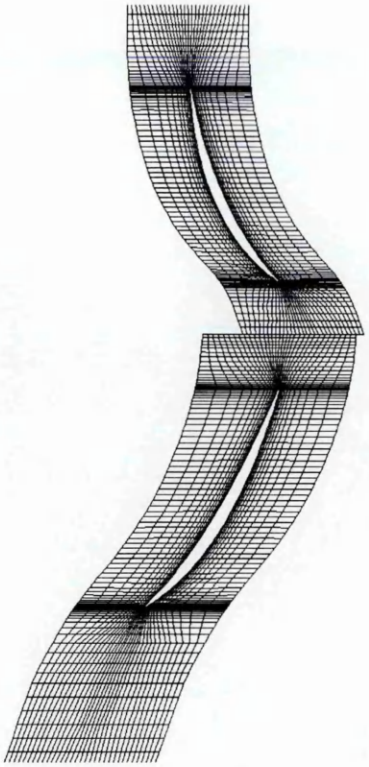

Figure 6-7 HSRC stage1 grid at mid-span

Unlike in HP9 though, the model includes tip clearances in all but the IGV rows with the clearance gap being occupied by some 5 nodes radially. The sizes of the individual blade grids are presented in Table 6-2 below.

Blade row	Dimensions	No nodes
IGV	38 x 53 x 90	181260
R1	42 x 33 x 93	128898
S1	42 x 31 x 90	117180
R2	42 x 33 x 92	127512
S2	42 x 31 x 91	118482
R3	42 x 33 x 92	127512
S3	42 x 33 x 86	119196
Total		920040

Table 6-2 HSRC grid sizes

Although the average size of the different grids is not much greater than about 110,000 nodes and is therefore quite coarse, if the trend identified in the 1998 AGARD comparative study of Rotor 37 by Dunham and Meauzé which has already been alluded to is accepted, the sum total of the whole compressor grid was in general too unwieldy for the resources which were available at the time of the running of the computations.

The greatest obstacle encountered by the author was not so much the length of the runs but more to the point, the frequent absence of available memory to initiate the computation or even to simply post-process its results. The formal memory requirements of the code are given as being about one Kb per node which translates in this case to a basic requirement of around 1Gb of memory for the solution to proceed.

Due to the problems outlined above solutions were only obtained for a limited number of points on the characteristic, all of which corresponding to the 100% running speed line. The inflow boundary conditions, common for all runs, were set as a constant absolute frame total pressure, 101325 Pa, constant absolute frame total temperature, 288 K and an absolute flow direction specified in cylindrical coordinates which was defined as being aligned with the machine axis. The inlet turbulence model boundary values were defined as a 3% turbulence intensity and a 30mm eddy length scale.

The outlet boundary conditions were defined as an average static pressure set over the outlet region, the values of which were varied to obtain the desired mass flows. The initial series of runs was performed with the hub wall of the stator domains set as stationary in the absolute frame. Results were obtained for five points corresponding to the mass flows of 9.67, 10.56, 10,60, 10.63 and 11.01 Kg/s, the back pressures which allowed the machine to pass these mass flow rates being tabulated below.

A latter series of results was obtained with the stator hub wall defined as stationary in the relative frame, these runs including the mass flows of 8.95, 9.82, 10.60, 10.64 and 11.02 Kg/s. Although it is the boundary conditions of the second set of runs which more exactly models the configuration of the real machine, use is also made of the

initial set due to the minor nature of the difference in conditions between the two models.

Mass flow rate (Kg/s)	Static pressure at outlet (Pa)	
	Stationary hub	Rotating hub
8.95	—	225,000
9.67	220,000	—
9.82	—	222,000
10.56	204,105	—
10.60	202,508	204,160
10.63	201,000	—
10.64	—	202,580
11.01	160,000	—
11.02	—	135,000

Table 6-3 HSRC simulation parameters

The 11.02 Kg/s mass flow rate corresponds to the choked condition this being confirmed by the fact that the same flow value was computed when the back pressure was reduced decrementally down to 135,000 Pa.

The graphical expression of Table 6-3 is shown in Figure 6-8 below, where the effect of the selection of the stator hubs as rotating in the absolute frame against the case where they are kept stationary in that frame, can be more easily assessed.

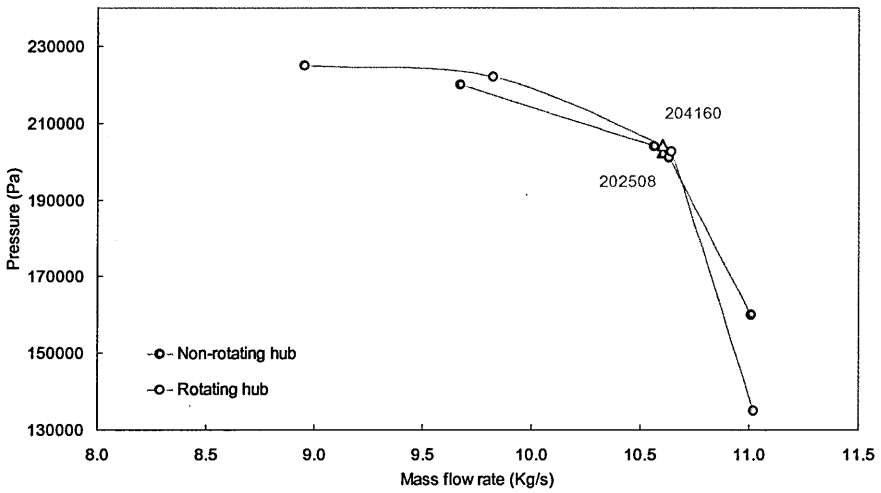

Figure 6-8 Mass flow variation with back pressure for two HSRC models

The discrepancy between the values of back pressure which enable the passing of similar amounts of mass in the two models, can only be exactly evaluated for the design point since it is there alone that the two mass flows are coincident. At this point the difference in the back pressures of the two models is 1652 Pa or 0.8%.

All the steady-state simulations were run on the RMCS Shrivenham Silicon Graphics Origin 2000 16 processor computer as parallel batch jobs. A typical run would take about a week, employing seven active slave processors plus a coordinating master, but due to the sharing of resources with other users of the machine, of the total clock time only about 3.5 days would correspond to actual CPU time. The convergence criterion was, as for the HP9 case, set as an rms residual target of 5.000E-07, this condition being commonly met at about 1300 iterations, with the global domain mass net flow at this point corresponding to around 5×10^{-5} Kg/s.

6.2.2.1 A comment on the computed choked value

Judging by the experience which the author acquired while running the NASA Rotor37 transonic rotor case, the code was likely to present an underestimate of the value of the mass which is passed by the HSRC at choke. The CFD evaluation of Rotor37 was undertaken during the first year of the research project with a view to

both acquiring practical experience of high speed flow simulations and assessing the code's capabilities against a very well documented test case.

The computed value of mass flow for the choked condition of this transonic fan was found to be 20.55 Kg/s against 20.93 Kg/s as recorded experimentally. This discrepancy of some 1.8 % was in the context fairly significant especially when it is known that most of the participants in the AGARD round of simulations of the Rotor 37 case came closer than 1% on the choke flow. In order to isolate the source of this error a fresh look at the whole simulation exercise was undertaken, for as A. Strazisar pointed out in his response to an inquiry on the Rotor37 geometry, "if we don't get the right choke flow we start looking for problems in the code or the geometry".

Having ascertained from this source that the geometric data used for the simulations were indeed correct, an application on the specifics of the simulation was made to B. Hutchinson, who as an entrant on the AGARD WG-26 round of CFD calculations, presented results obtained using the TASCflow code and a grid of similar dimensions, 250K nodes, to that used by the author. Dr. Hutchinson's reply pointed to the sensitivity of this case to the viscous work model used as well as to the appropriate resolution of the blade boundary layers.

In the light of all the information presented above a large number of runs was made with the viscous work parameter enabled together with different combinations of the other high speed model parameters and although a small reduction in the numerical-experimental discrepancy was in time observed, this constituted more of a nudge in the right direction than the shift required to significantly approximate the two values. The highest value for choked flow was obtained with the parameters REYNOLDS_STRESS_WORK_ENERGY and VISCOUS_WORK_ENERGY together with VISCOUS_WORK_MODEL enabled and corresponded to a mass flow of 20.57 Kg/s, the discrepancy having now fallen to 1.7 % of the experimental value.

A further investigation avenue which was also explored arose from the suggestion contained in Calvert,1999, which details the author's analysis of the Rotor37 test case, that "the baseline leading edge shape seems closer to an ellipse than the circle nominally specified". In that work it is pointed out that experiments show that

boundary layer flow around a typical leading edge can be completely changed by small changes in its shape. Calvert suggests that the flow on Rotor37 corresponds to the case with an elliptic leading edge with the flow coming onto the main blade surfaces smoothly and remaining laminar over the front part of the blade surface.

For a k-ε RANS simulation the leading edge shape issue is rather to prevent the spurious growth of the leading edge boundary layer, itself conducive to some increase in the blockage, but more importantly in the case of a transonic compressor, to prevent the excessive growth of the pre-shock layer and hence the scale of the shock-boundary layer interaction and its far greater blockage impact. The circular to elliptic leading edge transformation of Rotor37 is shown in Figure 6-9.

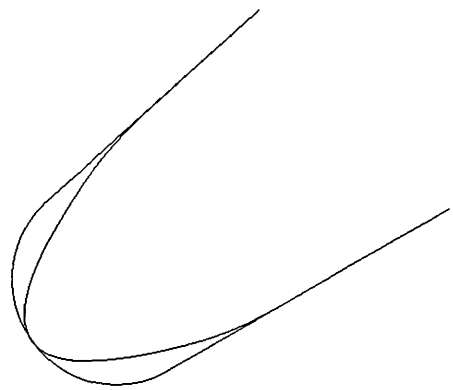

Figure 6-9 Rotor 37 leading edge circular and elliptic shapes

Initial runs conducted with a similar sized grid, 250000 nodes, yielded absolutely no difference in the choke value when compared with the circular leading edge conventional geometry. In order to further explore the potential of the transformed geometry a new grid of about 450,000 nodes was assembled, Figure 6-9, with the blade leading edge having a particularly high node concentration.

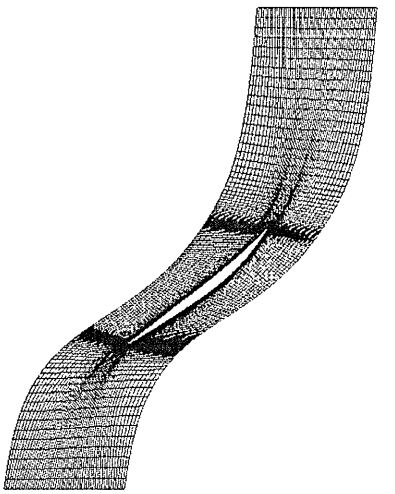

Figure 6-10 Mid-span view of Rotor37 450,000 nodes grid

The good convergence properties exhibited by the solver when using previous grids were forfeited by this mesh enrichment to such an extent that a more robust but somewhat less accurate discretization scheme, Modified Linear Profile Scheme instead of the genuine second order Linear Profile Skew, had to be employed. The significant increase in convergence difficulties finds an explanation in the enhanced capture of flow unsteady features which in turn hinders the steady state resolution of the flow field.

This situation suggests that for a given simulation and a given code there may be an optimum grid size which is consistent with the use of the better advection schemes existent on the code. In the case in point it is suggested that that grid size may be found somewhere between the two grid nodal values employed.

In terms of results, the larger grid choke value shows a very modest increase to 20.6 Kg/s thus reducing the discrepancy to 1.56 %. This value is still a full one percent away from both the experimental uncertainty lower bound value and the stated results of most published CFD simulations of this case.

The experimental value of choke in the HSRC at 9300 rpm was recorded as 11.14

Kg/s against the TASCflow computed value of 11.01 Kg/s for the non-rotating hub model and 11.02 Kg/s for the rotating case, a discrepancy of some 1.2%. A pictorial representation of this condition at the blade-to-blade mid-span region for the non-rotating hub case is shown in Figure 6-11 and Figure 6-12 for the case where the stator hubs rotate. These plots make readily apparent the location of the shockwave in Stator 3 and it is also interesting to notice the presence of the high velocity spots in the pressure sides of the blades which can be attributed to the occurrence of a large negative incidence.

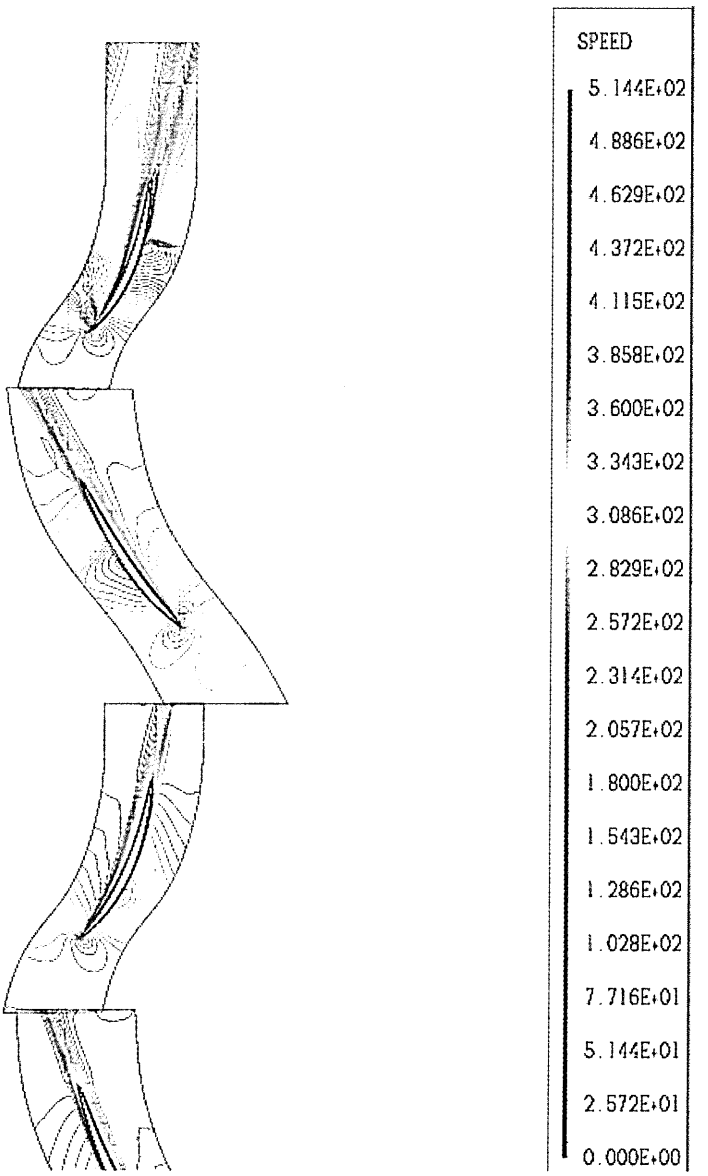

Figure 6-11 HSRC shockwave location at choke flow

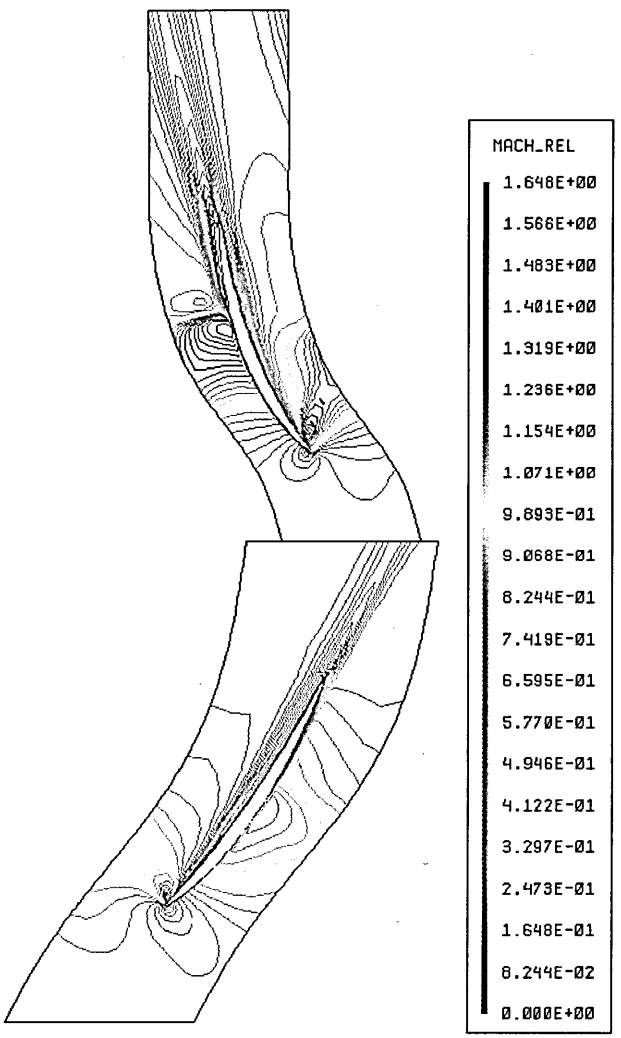

Figure 6-12 HSRC shockwave location at choke – detail plot

The results on the other end of the characteristic, corresponding to the mass flow of 8.95 Kg/s, are assumed to be representative of the onset of compressor stall rather than that of developed surge. The support for this assertion arises from the analysis of the convergence plot of that particular run, Figure 6-13.

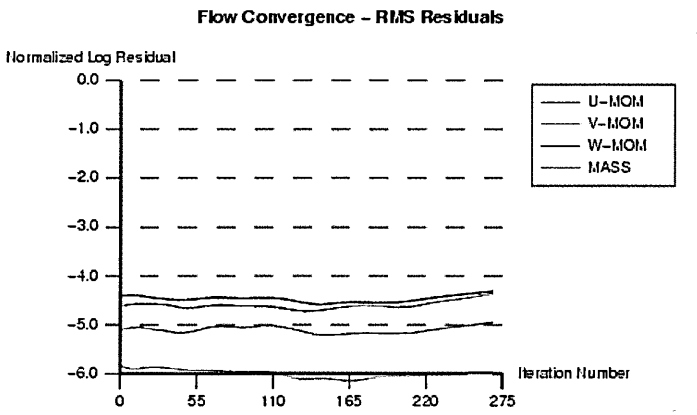

Figure 6-13 Residual convergence plot of HSRC 8.95 Kg/s point

The general implication of this plot, is that the code has ceased to fully converge at the computed point, due to the appearance of instabilities in the flow which are likely to be associated with high blade-relative flow incidences. The variation amplitude of the incidence at the leading edge of Rotor 2 at mid-span, is shown below, as a comparison between the choke and near-surge flow conditions.

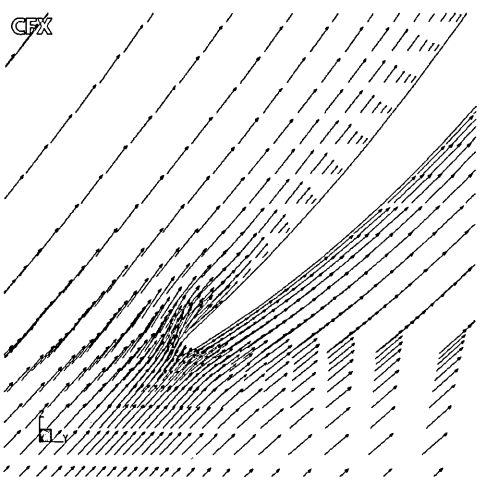

Figure 6-14 Flow incidence at Rotor 2 mid-span at choke point

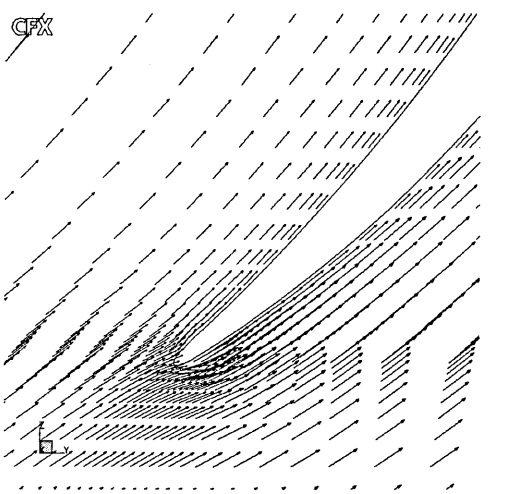

Figure 6-15 Flow incidence at Rotor 2 mid-span at near surge

The mass which is computed for the near surge point is in fact not well matched between the inlet and outlet planes of the compressor, the value at the former corresponding to 9.028 Kg/s while at the latter that quantity is 8.951 Kg/s. For this

reason the lowest calculated mass flow which is reliable enough for purposes of comparison is the higher 9.82 Kg/s point.

6.2.3 HSRC steady-state baseline results

Given the large time span occupied by the different steps of the commissioning of the HSRC, throughout nearly all of the duration of the project there was no experimental data against which the computational results could be validated. Given the absence of this data the only existing measure of the performance of the compressor was that which was given as part of the design submission in the form of the results of an SC90 throughflow code applied to the 10.6 Kg/s design mass flow point.

Very late in the project however the author had access to a preliminary set of global performance results consisting exclusively of integrated values. The results presented hereby are therefore only validated experimentally for the overall performance values, but comparisons are possible for these performance figures as well as radial distributions against the throughflow simulation for design point. The qualitative plots, contour and vector distributions, are presented ahead of any other results against which to contrast these.

6.2.3.1 Overall performance results

The preliminary experimental global performance parameter results for the HSRC datum build is presented below in the form of maps of total pressure ratio, Figure 6-16, and temperature based isentropic efficiency, Figure 6-17.

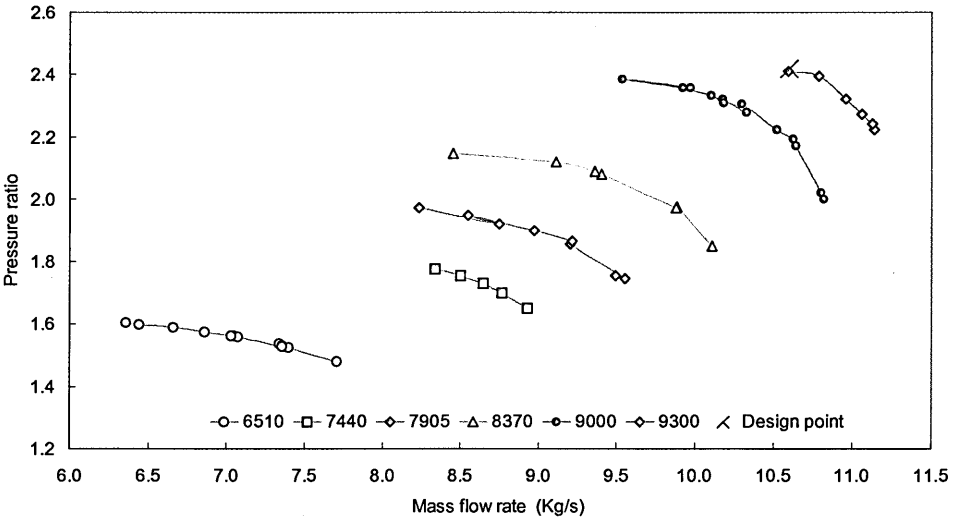

Figure 6-16 HSRC datum build total pressure ratio map (experimental)

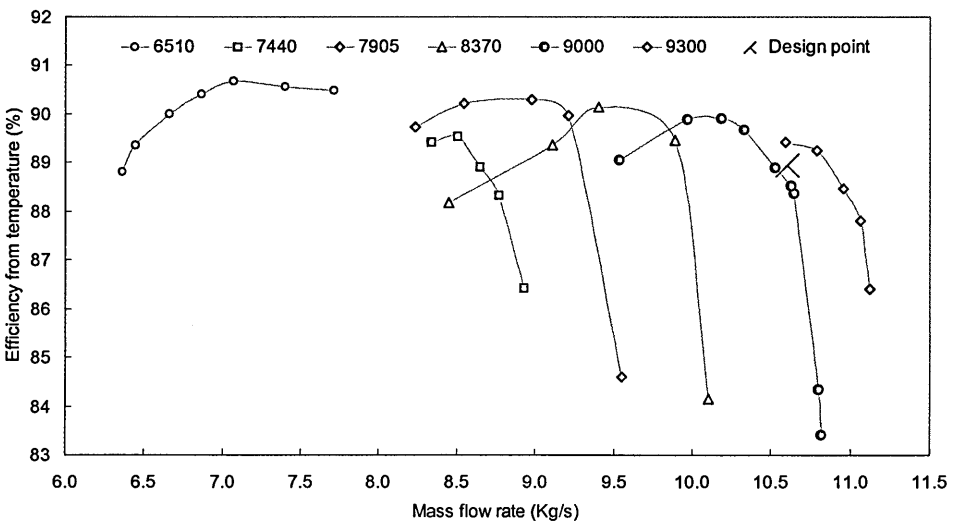

Figure 6-17 HSRC datum build adiabatic efficiency map (experimental)

The comparative tabulation of the computed results, obtained with both models, and the experimental data is presented below, Table 6-4.

Mass flow (Kg/s)	Pressure ratio			Adiabatic efficiency (%)		
	Hub stat	**Hub rot**	**Expmtl**	**Hub stat**	**Hub rot**	**Expmtl**
9.67	2.39	—	—	85.68	—	—
9.82	—	2.41	—	—	86.94	—
10.56	2.29	—	—	85.81	—	—
10.59	—	—	2.41	—	—	89.42
10.60	2.28	2.29	—	85.64	86.49	—
10.63	2.26	—	—	85.44	—	—
10.64	—	2.28	—	—	86.27	—
10.79	—	—	2.39	—	—	89.24
10.96	—	—	2.32	—	—	88.46
11.01	1.95	—	—	75.37	—	—
11.06	—	—	2.27	—	—	87.80
11.12	—	—	2.24	—	—	86.41
11.14	—	—	2.22	—	—	86.92

Table 6-4 Total pressure ratio and adiabatic efficiency from CFD models and experiments

The results of Table 6-4 are shown in a graphical mode below.

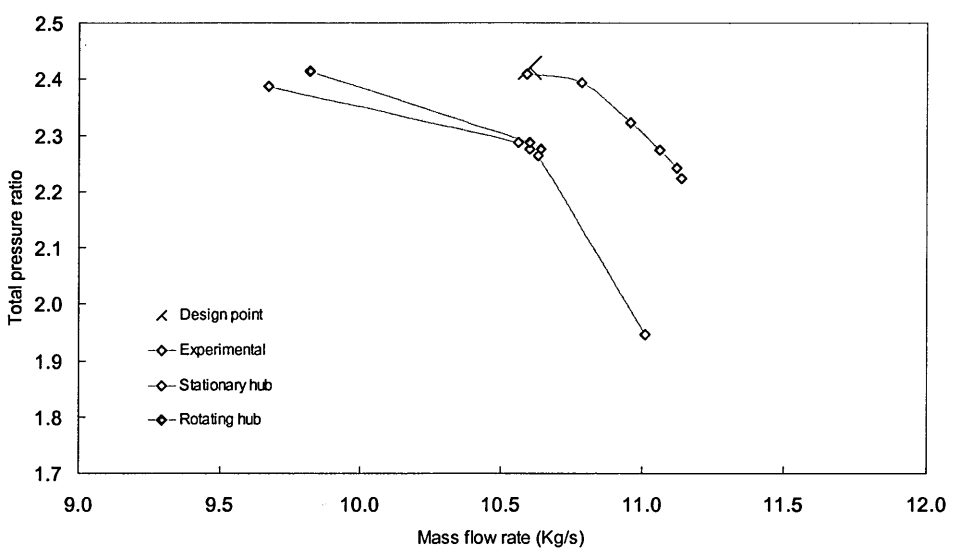

Figure 6-18 Comparison of total temperature ratios from CFD models and experiments

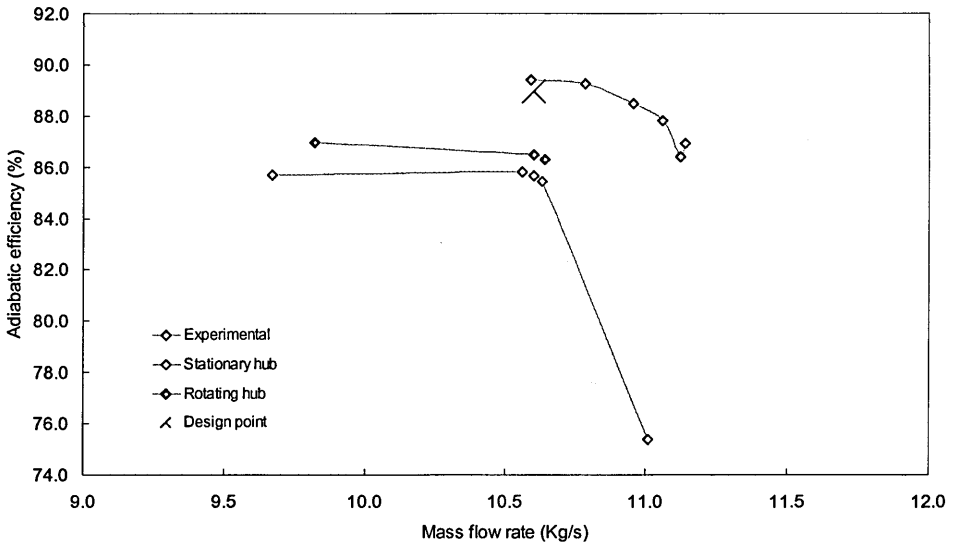

Figure 6-19 Comparison of adiabatic efficiencies from CFD models and experiments

Before engaging in an assessment of these global results, which apply to the entire machine, we will consider the incremental development of these same quantities throughout the compressor. These calculations are based on the simple stacking of blade rows with the S1 point of the ordinate of the plots corresponding to the calculation of the first stage, R2 to the calculation of the first stage plus rotor 2 and so forth.

The simulation results employed are those of the definitive model boundary condition formulation corresponding to the case with the rotating stator hub sections. The total pressure ratios for the 10.64, 10.60 and 9.82 Kg/s are shown as Figure 6-20, Figure 6-21 and Figure 6-22 together with the results of the throughflow simulation for the design point.

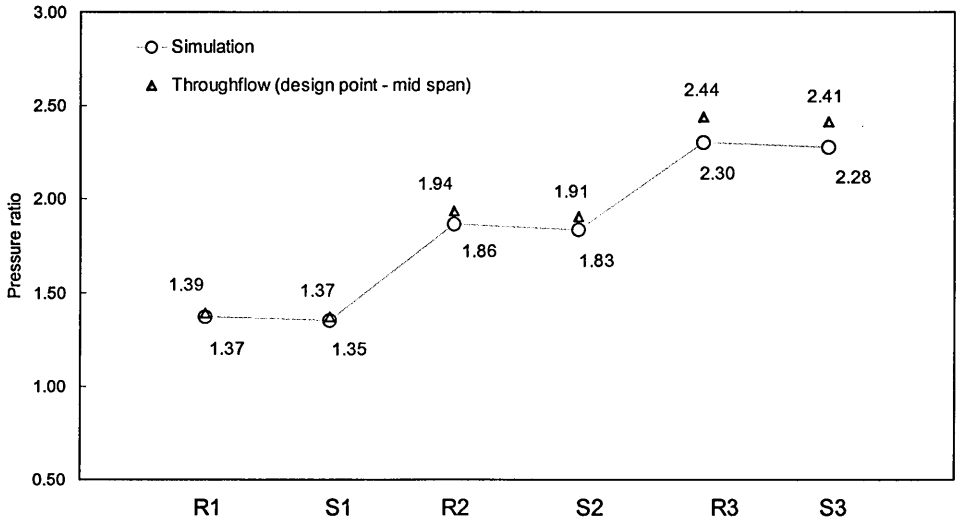

Figure 6-20 Incremental total pressure ratio for 10.64 Kg/s mass flow rate

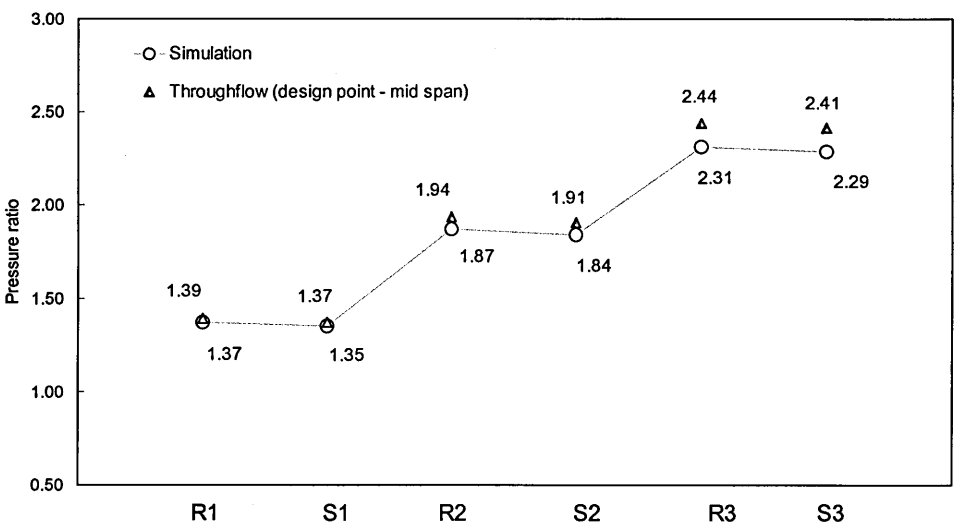

Figure 6-21 Incremental total pressure ratio for 10.60 Kg/s mass flow rate

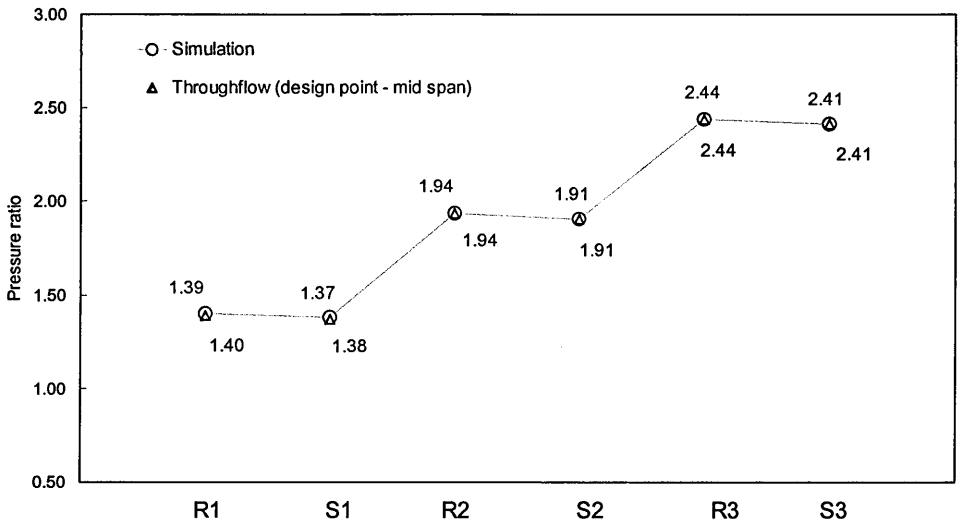

Figure 6-22 Incremental total pressure ratio for 9.82 Kg/s mass flow rate

The equivalent plots for the total temperature ratio, presented here for completeness are shown as Figures 6-23 through to 6-25.

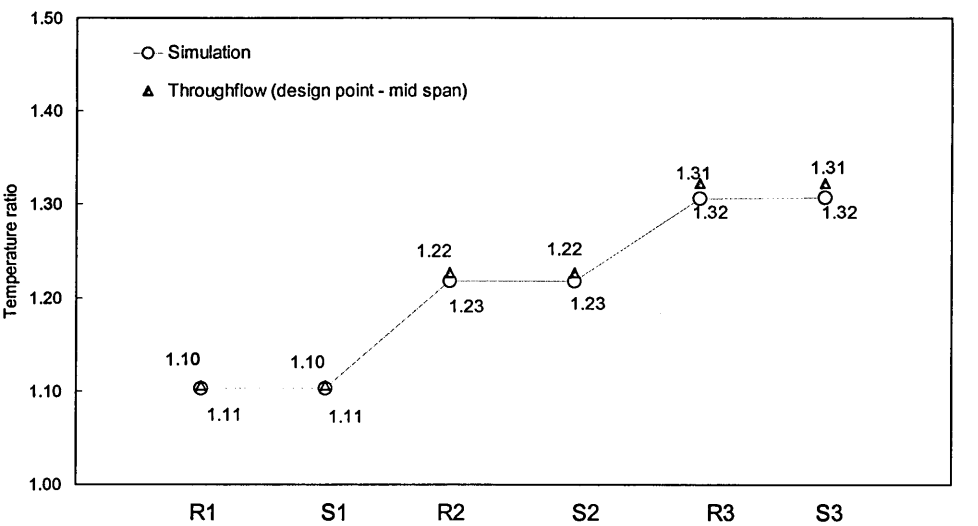

Figure 6-23 Incremental total temperature ratio for 10.64 Kg/s mass flow rate

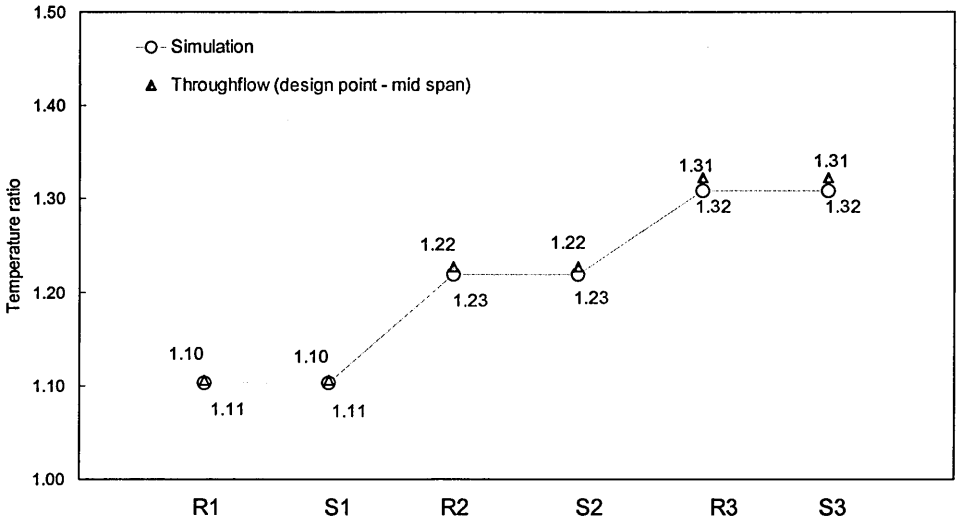

Figure 6-24 Incremental total temperature ratio for 10.60 Kg/s mass flow rate

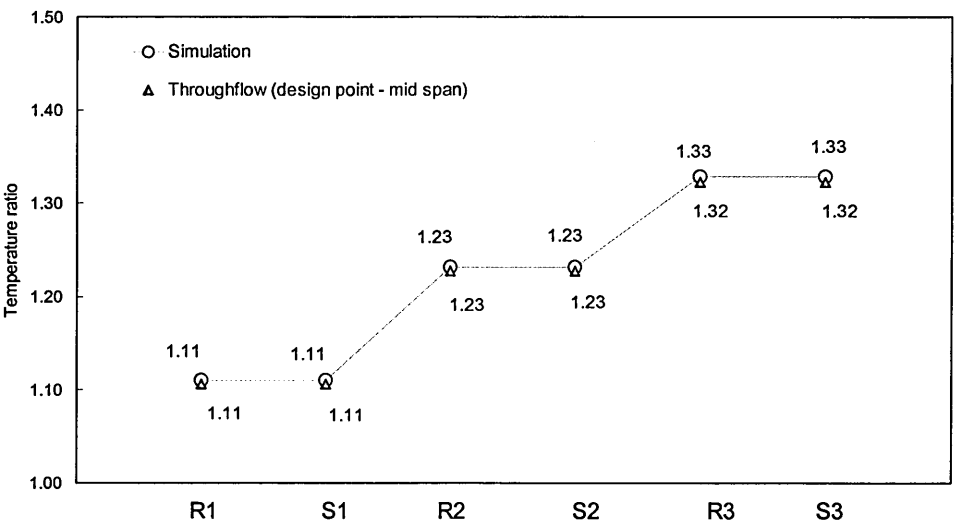

Figure 6-25 Incremental total temperature ratio for 9.82 Kg/s mass flow rate

Lastly the computed results of the adiabatic efficiencies are shown in Figure 6-26 through to Figure 6-28.

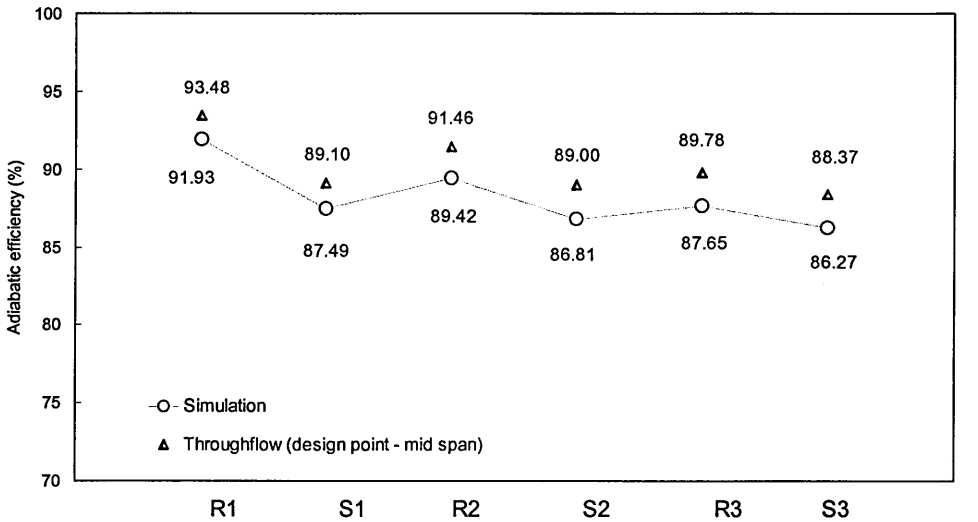

Figure 6-26 Incremental adiabatic efficiency for 10.64 Kg/s mass flow rate

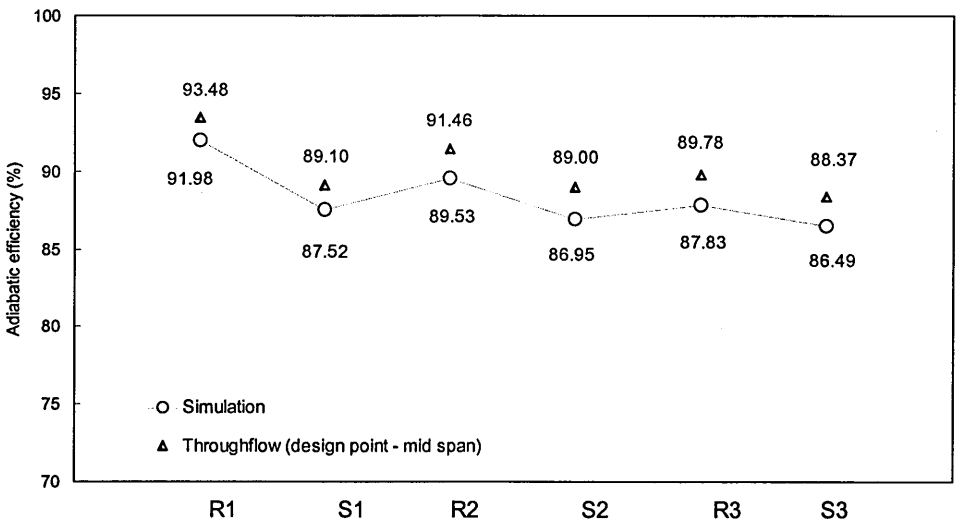

Figure 6-27 Incremental adiabatic efficiency for 10.60 Kg/s mass flow rate

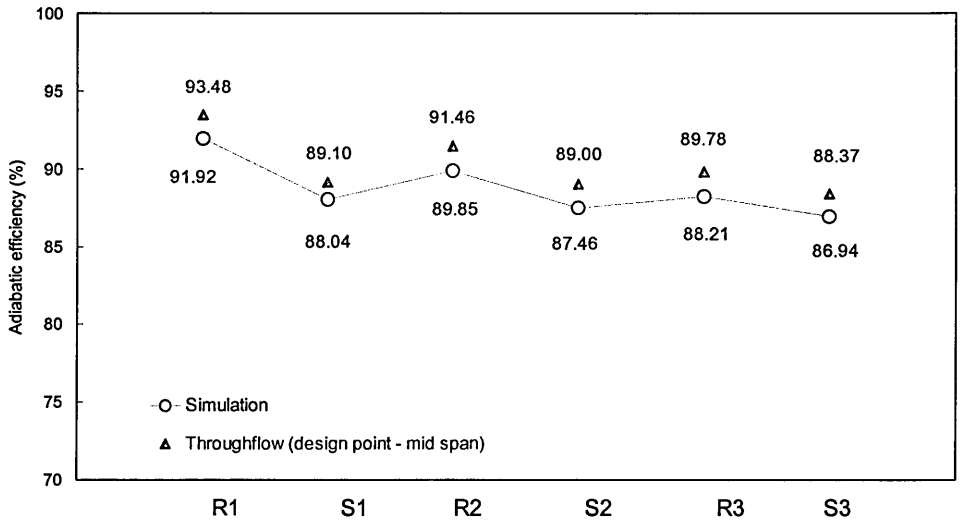

Figure 6-28 Incremental adiabatic efficiency for 9.82Kg/s mass flow rate

It is felt, for the purposes of the present comparison, that given the multistage substratum of the throughflow code design, its greater reliance on experimentally derived empirical inputs and the very extensive validation that these codes have attracted, the values computed by the throughflow method offer in the circumstances the best estimate of the integrated performance quantities.

In the high mass flow plots of total pressure ratio, Figures 6-16 and 6-17, it is noticeable how the good agreement between the two codes in the early rows of the compressor steadily degenerates as the computations progress downstream. This situation nevertheless is not arrested but is in fact slightly reversed in the computation of the 9.82 Kg/s point where the overlap of the two solutions is remarkably close.

With reference to this set of graphs it is possible to extract two conclusions:

a) the computation of the total pressure losses throughout the compressor is nearly the same when done by TASCflow for the 9.82 point as was calculated by the SC90 throughflow code for the design 10.60 point.

b) the introduction of sizeable disparities between the results of both codes tends to occur in the calculation of the rotors.

It is known that the conservation scheme which is applied to the mixing plane in TASCflow ensures the conservation of the mass, momentum and energy fluxes, but is not conservative of the total and static pressures.

The introduction of errors in a multistage computation through the action of the mixing-planes in the TASCflow code has been demonstrated by Lockwood, 1999, where the author compared experimental data from the Cranfield LSRC with the simulation of a one-and-half stage section of that four stages compressor. Lockwood's conclusion was that the accuracy of the multi-row simulation, in terms of the calculated whirl angles, and hence of the different velocities, as well as in terms of the computed static pressures, was seen to decrease as one progressed downstream of the compressor.

The situation in terms of the prediction of the temperature rise follows the same trends displayed by the pressure with a slight underprediction at the two higher mass points, Figure 6-23 and 6-20, followed in this case by a small overprediction of the temperature in the lower mass point, Figure 6-25. The work input, when seen as a single value, is consistent with the throughflow calculation for the three cases.

The variation of the computed efficiencies follows a more complex pattern which is more clearly grasped through the plotting of the variations of the individual points with respect to the throughflow design point, Figure 6-29. The calculation of the efficiency through Rotor 1 yields very similar values for all the flow conditions but increases steadily thereafter and in general by different amounts according to the flow condition. The largest increase occurs in Stage 2, predominantly in Rotor 2 and in the last stage there is actually a slight decrease.

Figure 6-29 helps to establish the fact that although all the simulated conditions correspond to an overestimate of the losses, having as reference the SC90 throughflow solution, the least overestimate corresponds to the 9.82 Kg/s regime.

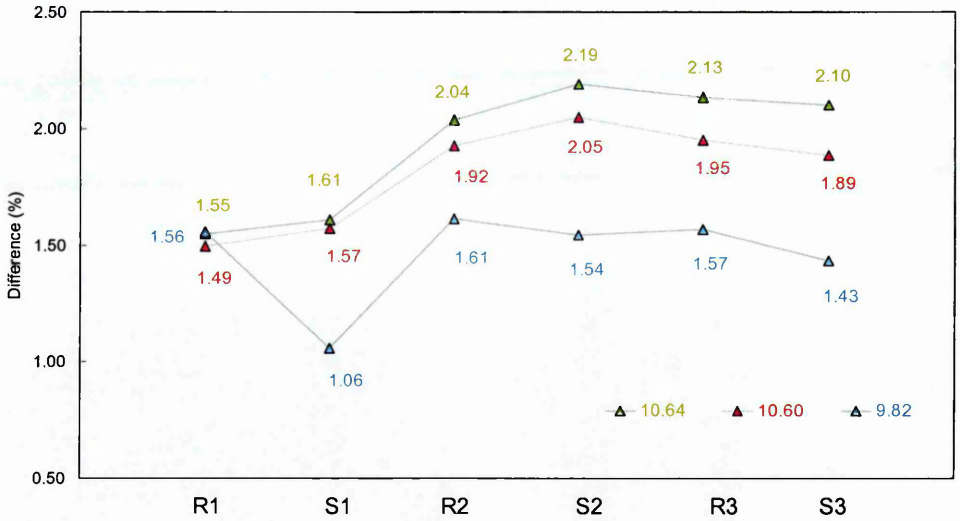

Figure 6-29 Percentual variation of adiabatic efficiency from design point throughflow calculations

6.2.3.2 Radial distributions I – velocity profiles

The plots of radial distributions include axial velocities for the three flow conditions taken at the outlets of the computational domains, Figure 6-30 to 6-32. The velocities of these plots are area-weighted pitchwise averaged.

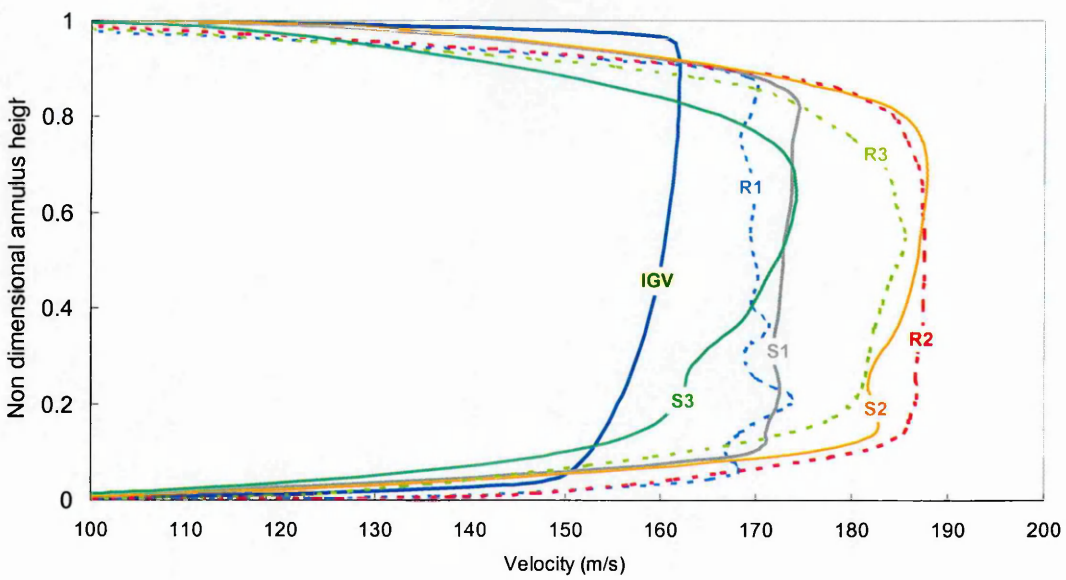

Figure 6-30 Radial distribution of axial velocity at 10.64 Kg/s

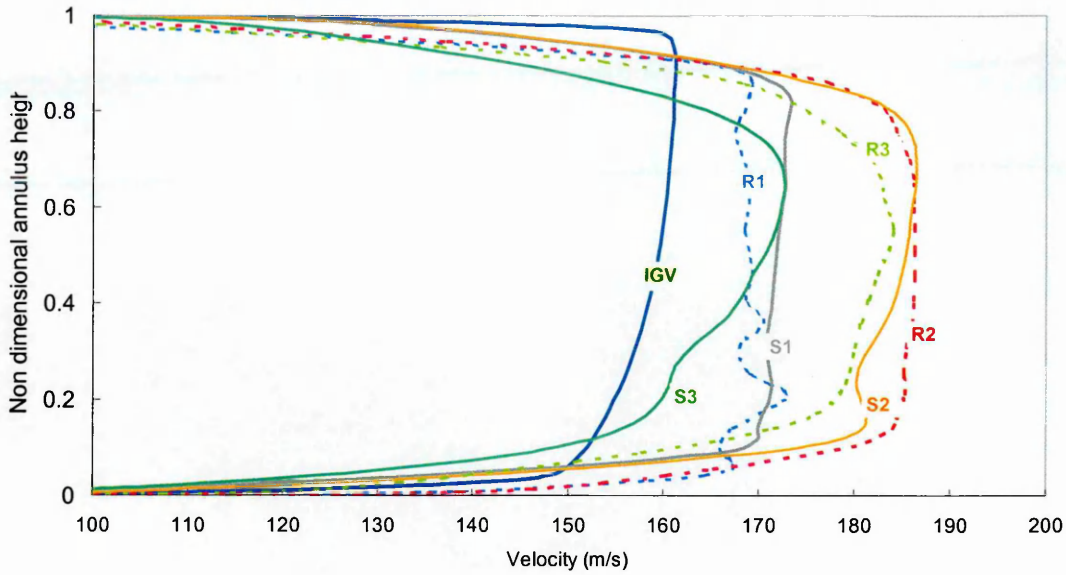

Figure 6-31 Radial distribution of axial velocity at 10.60 Kg/s

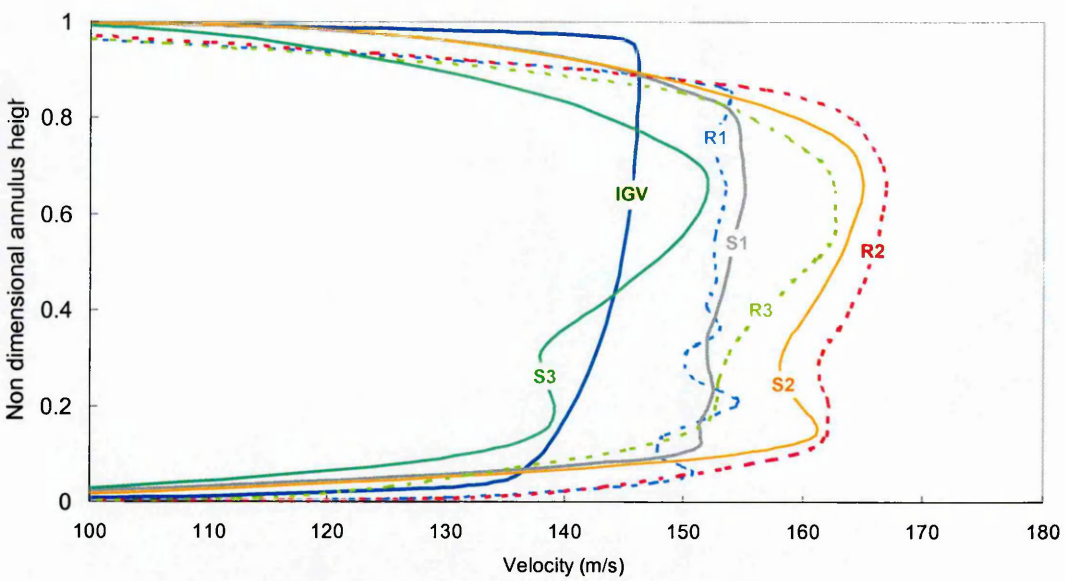

Figure 6-32 Radial distribution of axial velocity at 9.82 Kg/s

The machine-wide radial distributions of axial velocity shown above illustrate the growth of the endwall boundary layers from a very minor fraction of the annular height, visible in the IGV outlet profile, to the substantial dimension which is associated with the Stator 3 outlet plane.

In the hub region there seems to be a clear demarcation between the endwall flow region, denoted by the sharp turning of the profile upwards, but in the casing region this boundary is generally well defined as one progresses downstream. This progressive blurring of the endwall flow boundaries suggests the initiation of a situation such as is described by Gallimore and Cumpsty, 1986, who found that there was no clear edge to the viscous region on the annulus walls inside a multistage compressor and that the mixing and the variation in stagnation pressure extended right across the annulus, Cumpsty, 1989.

It is appropriate however to acknowledge that other investigators, namely Wisler, Bauer and Okiishi, 1987, reported the presence, in a very efficient four stage compressor, of a clear boundary between the annulus boundary layer flows and a freestream core despite the occurrence of strong cross-annular mixing effects.

The radial distributions of axial velocity for the seven blade rows at the three flow conditions plotted against the values calculated by the throughflow code are presented below in Figure 6-33 through to Figure 6-39.

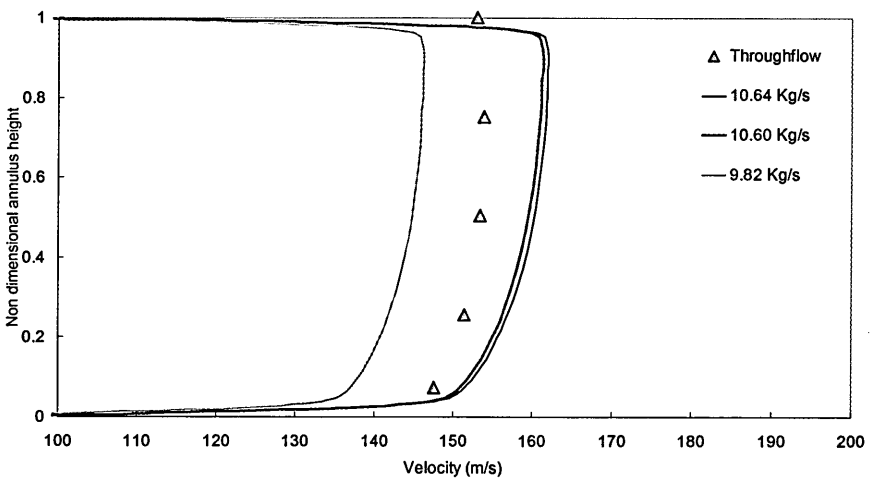

Figure 6-33 IGV radial distribution of axial velocity

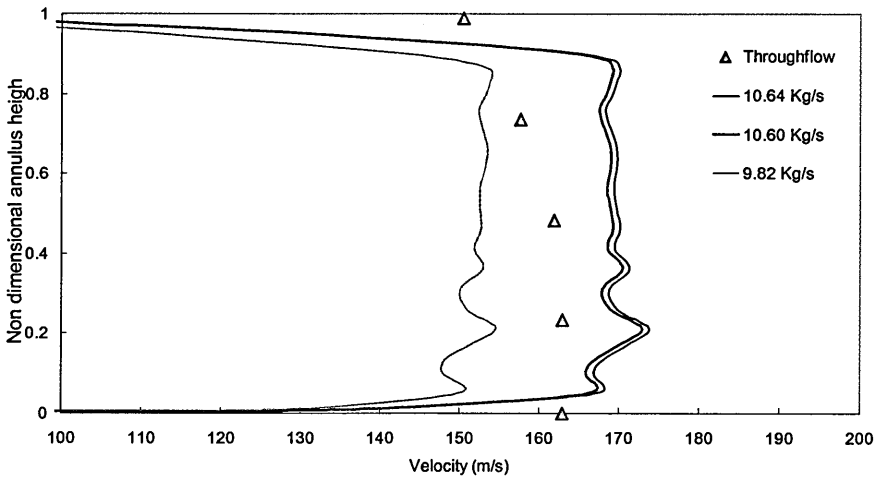

Figure 6-34 Rotor1 radial distribution of axial velocity

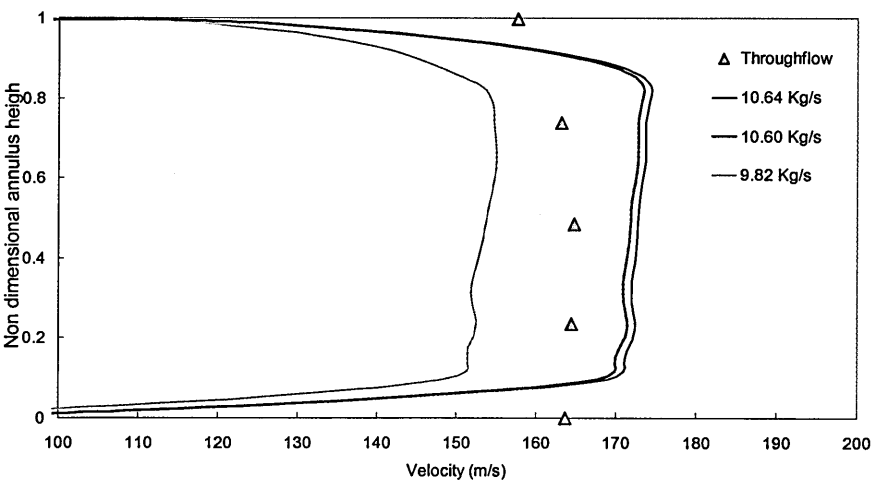

Figure 6-35 Stator1 radial distribution of axial velocity

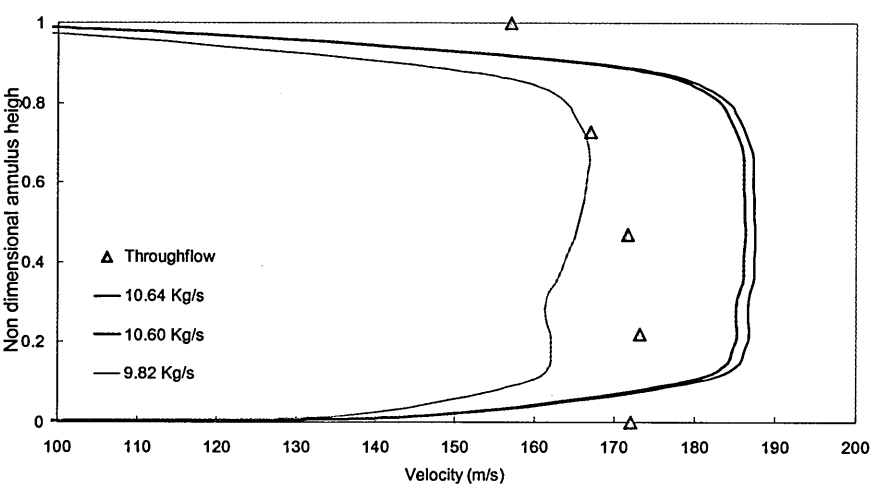

Figure 6-36 Rotor 2 radial distribution of axial velocity

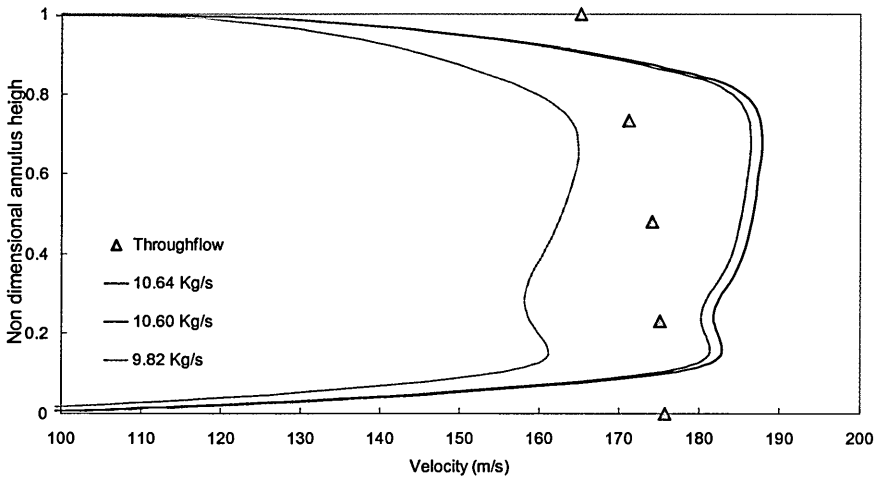

Figure 6-37 Stator 2 radial distribution of axial velocity

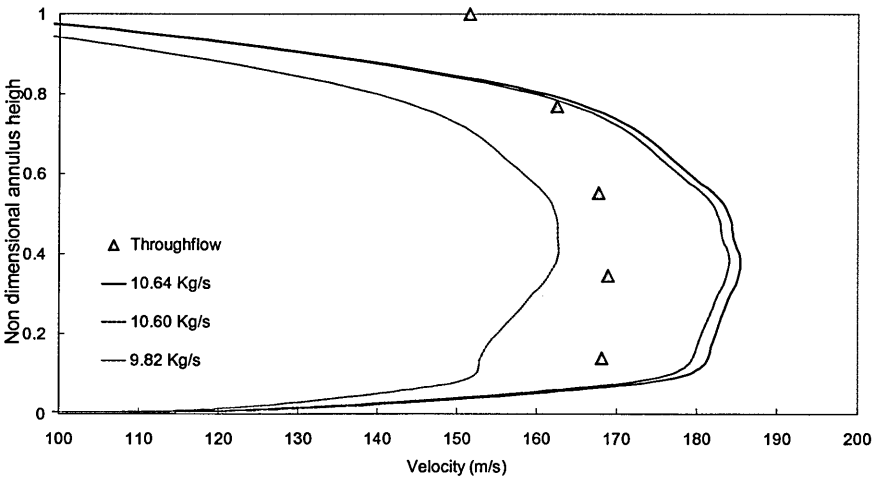

Figure 6-38 Rotor 3 radial distribution of axial velocity

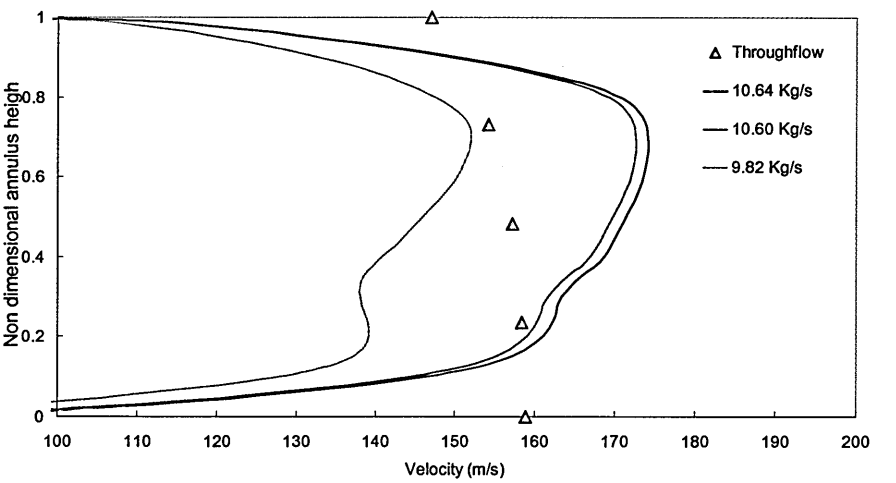

Figure 6-39 Stator 3 radial distribution of axial velocity

The agreement between the axial velocities computed by the SC90 code and TASCflow is at best tenuous, particularly in terms of the radial trends where in fact a more apt description would be non-existent or even opposite, but this said the computed values from the two sources are never further apart than a few percent points.

The radial distributions of absolute total pressure is presented next and again use is made of the throughflow design point results for comparative purposes.

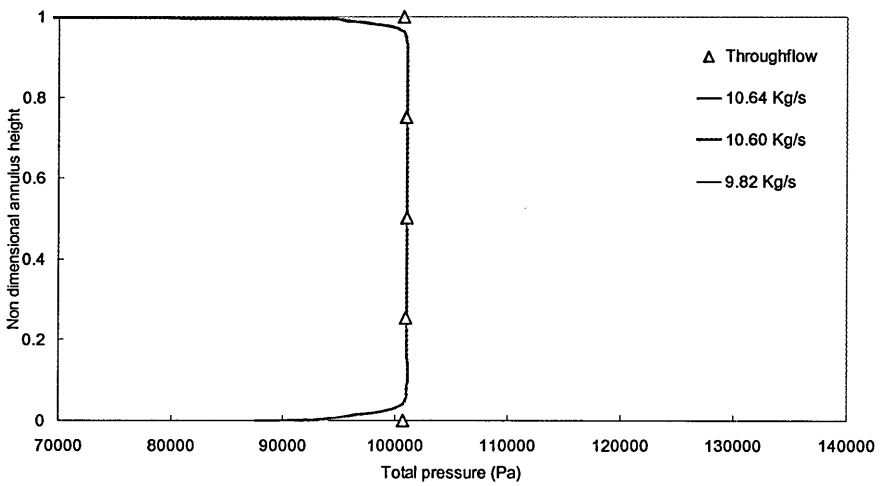

Figure 6-40 Radial distribution of absolute total pressure at outlet of IGV

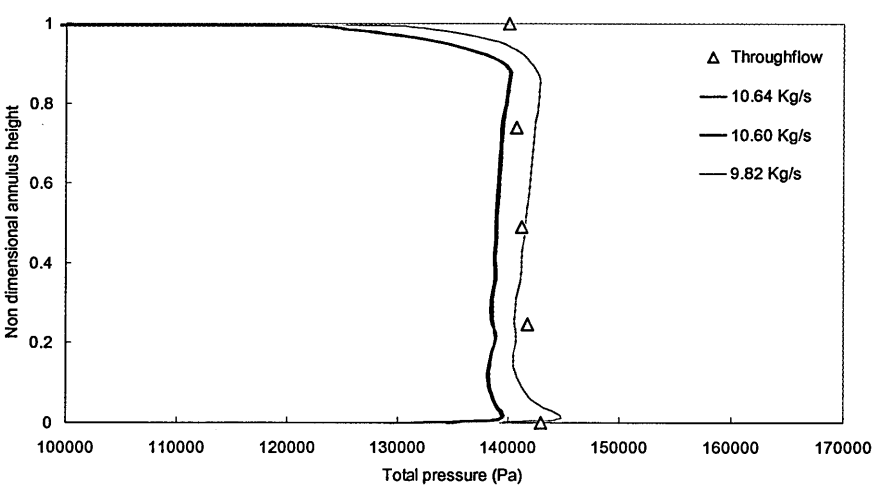

Figure 6-41 Radial distribution of absolute total pressure at outlet of Rotor 1

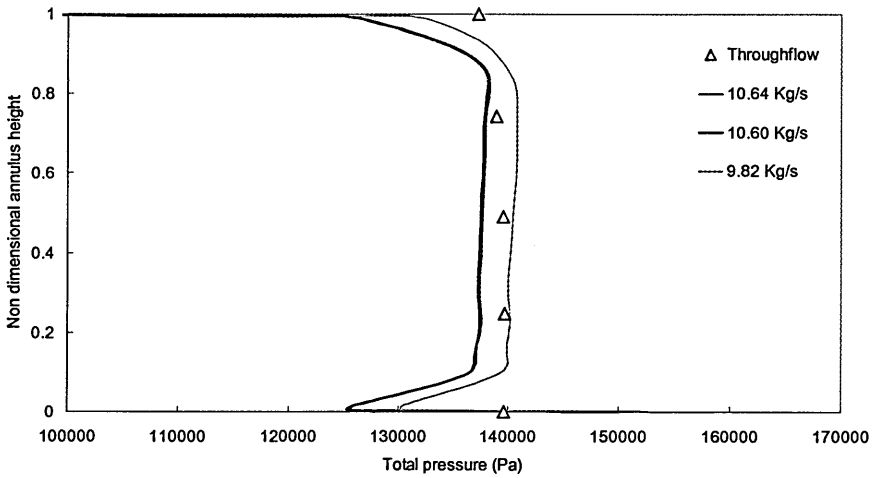

Figure 6-42 Radial distribution of absolute total pressure at outlet of Stator 1

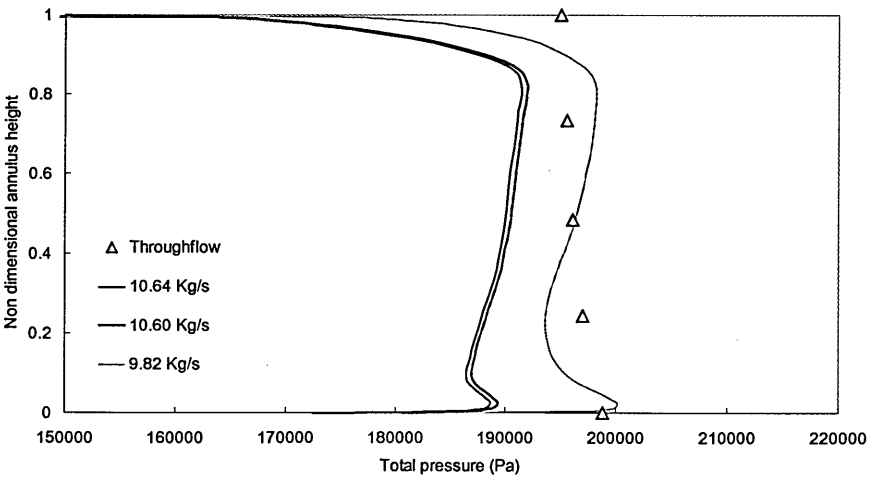

Figure 6-43 Radial distribution of absolute total pressure at outlet of Rotor 2

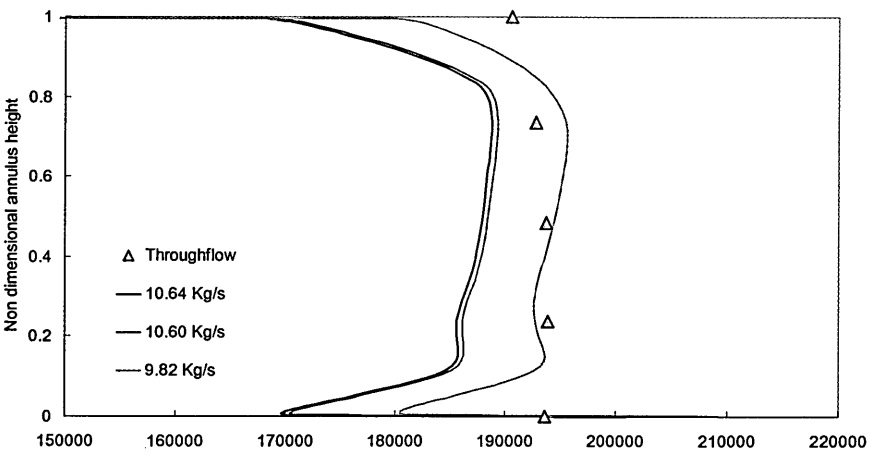

Figure 6-44 Radial distribution of absolute total pressure at outlet of Stator 2

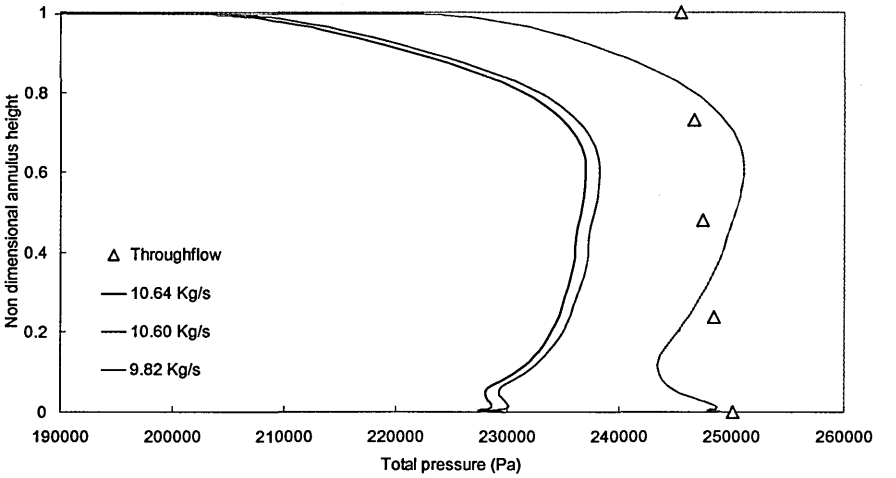

Figure 6-45 Radial distribution of absolute total pressure at outlet of Rotor 3

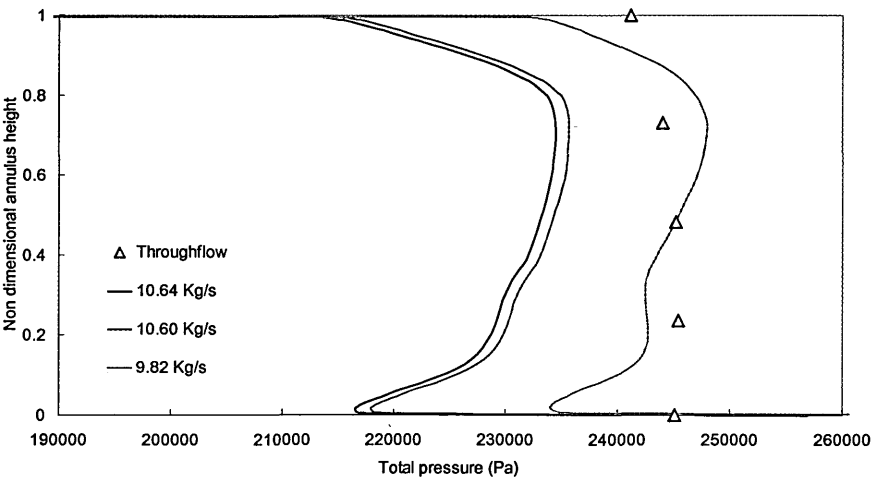

Figure 6-46 Radial distribution of absolute total pressure at outlet of Stator 3

The development of the radial profiles of absolute total pressure within the compressor, Figure 6-40 to Figure 6-46, gives credence to the contention of Gallimore and Cumpsty regarding the absence of a clearly defined boundary between the endwall and freestream flows. The levels total of pressure which are predicted by the throughflow code are systematically better approximated by the 9.82 Kg/s point even though no proper agreement in terms of the shapes of the distributions is ever achieved.

6.2.3.3 Radial distributions II – flow angles

The radial distributions of flow angles for the three regimes, 10.64, 10.60 and 9.82 Kg/s together with the throughflow code results as calculated for the design point are presented in Figure 6-47 through to Figure 6-53.

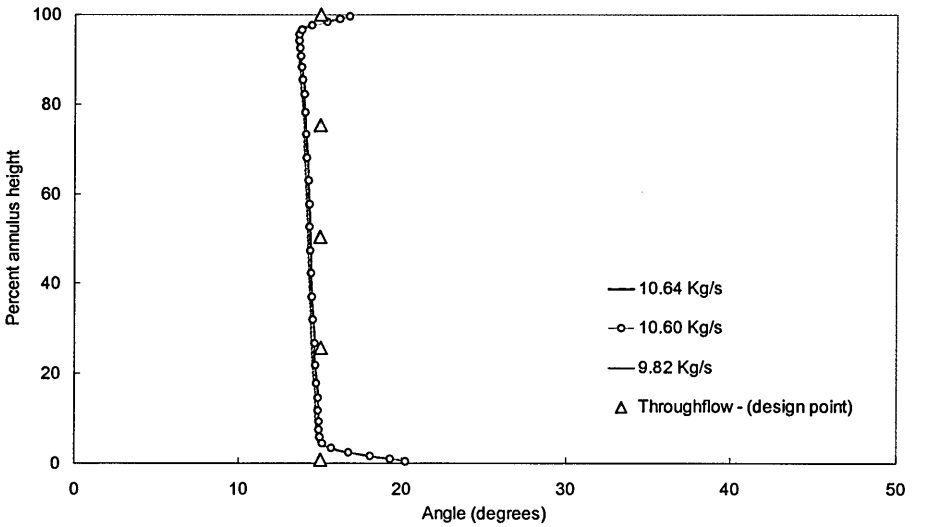

Figure 6-47 Absolute flow angle at outlet of IGV

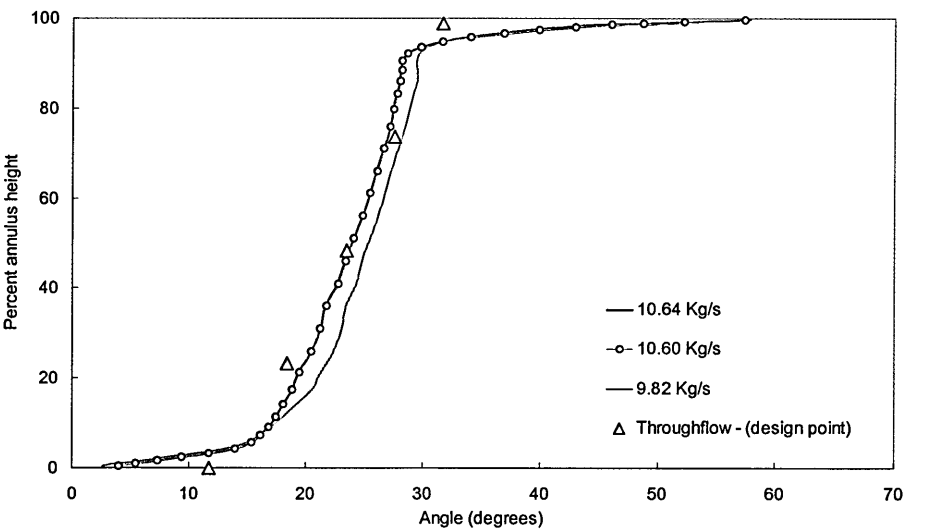

Figure 6-48 Relative flow angle at outlet of Rotor 1

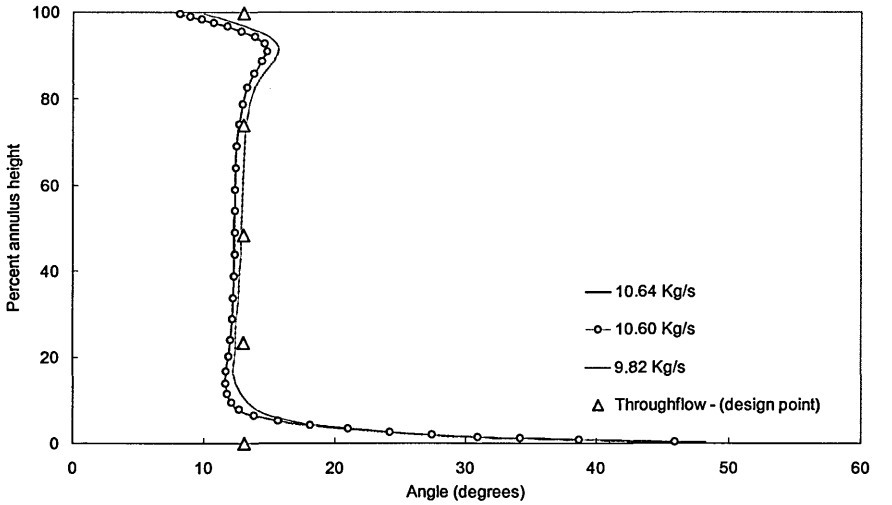

Figure 6-49 Absolute flow angle at outlet of Stator 1

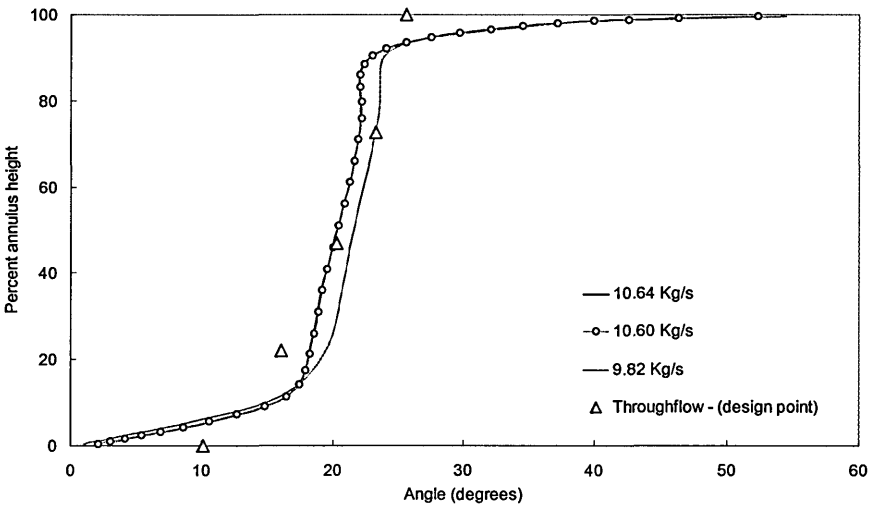

Figure 6-50 Relative flow angle at outlet of Rotor 2

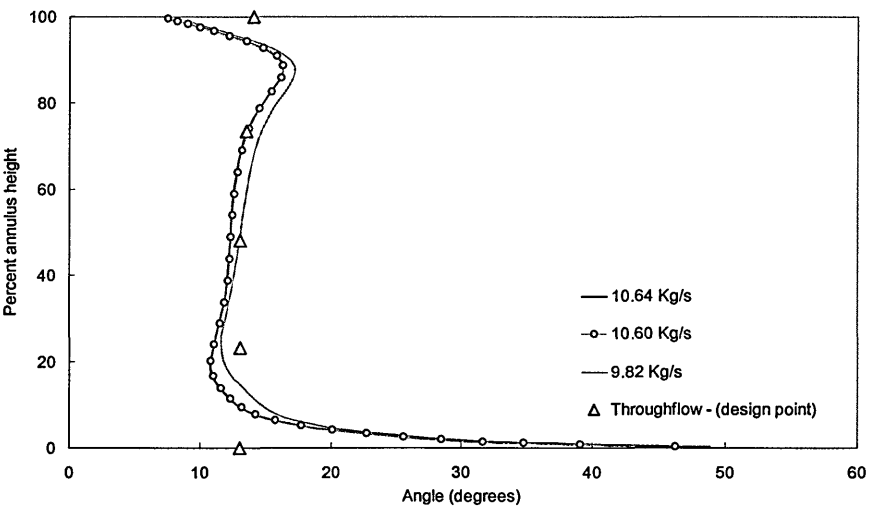

Figure 6-51 Absolute flow angle at outlet of Stator 2

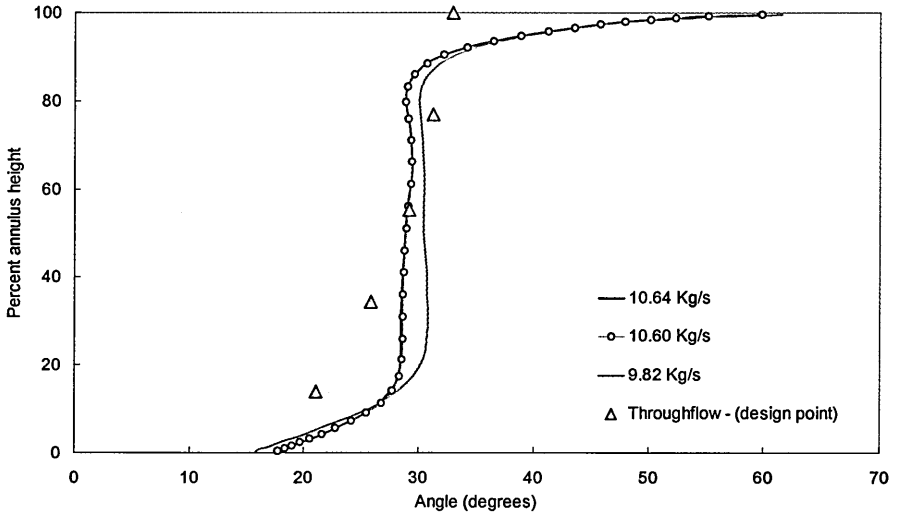

Figure 6-52 Relative flow angle at outlet of Rotor 3

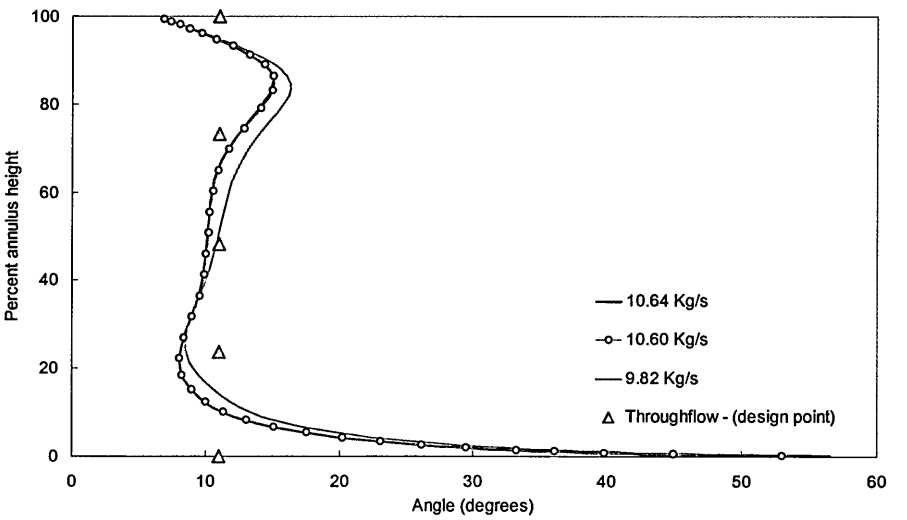

Figure 6-53 Absolute flow angle at outlet of Stator 3

There is consistent agreement in the trends of the central regions presented by all results in the first two stages but towards the end of the compressor the level of concurrence between the TASCflow and throughflow data is much less satisfactory. Naturally the throughflow code misses the contribution of the wall effects towards the spanwise angle variation and as these events become more pronounced as one travels downstream in the machine, the disparity between the predictions is inevitably seen to grow.

Except for the case of the IGV, Figure 6-47, all blades produce a certain amount of over and under-turning which can be seen as departures from the idealized radial

angular distribution prescribed by the designer. These deviations from the expected flow directions translate, for the downstream blade row, into a disparity from the forecasted incidence likely to lead to larger local losses than is desirable.

It is to assist in controlling the endwall flow path and limit the local drifting of the blade outlet flow angles, and its associated loss potential, that current design practice favours the incorporation of blade 'end bends'. In effect the end bends do not directly realign the blade departing flow but act instead through the promotion of local secondary flows which act dynamically to contain the direction of the flow in a more favourable direction.

6.2.3.4 Contour plots – blade-to-blade

The presentation of the blade-to-blade contour plots, Figure 6-54 to Figure 6-77, is restricted to two flow points, 9.82 Kg/s and 10.64 Kg/s and three spanwise locations, near hub, mid-span and near shroud, the plotted quantity being the relative Mach number. In all of the plots which are located in the vicinity of blade tips, near shroud for rotors and near hub for stators, there is evidence of flow entrainment due to the neighbourhood of clearance flows. In these locations there is no evidence of actual cross-over but rather of the presence of a tangential component of variable intensity which acts on the core flow structure, as seen in the mid-span plots, in order to generate the jet-like configuration seen in these plots, ie Figures 6-58, -59, -60, etc.

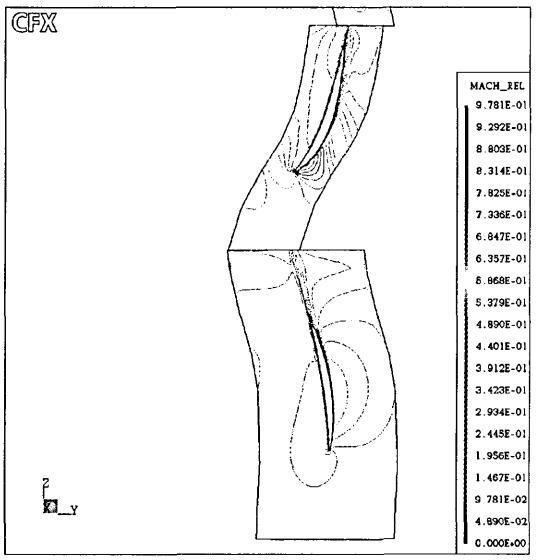

Figure 6-54 IGV and Rotor1 relative Mach number at 9.82 Kg/s – near hub

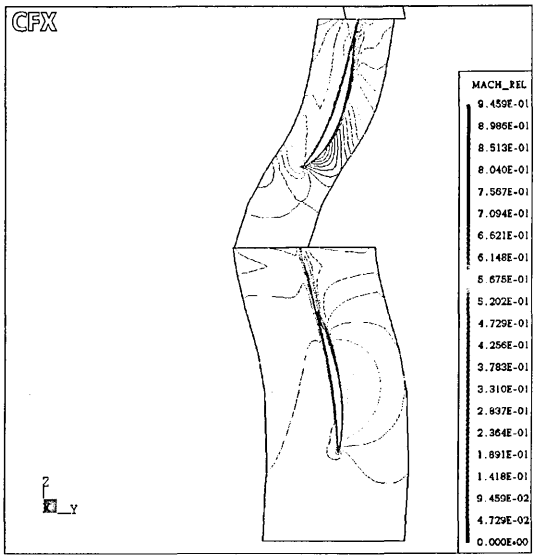

Figure 6-55 IGV and Rotor1 relative Mach number at 10.64 Kg/s – near hub

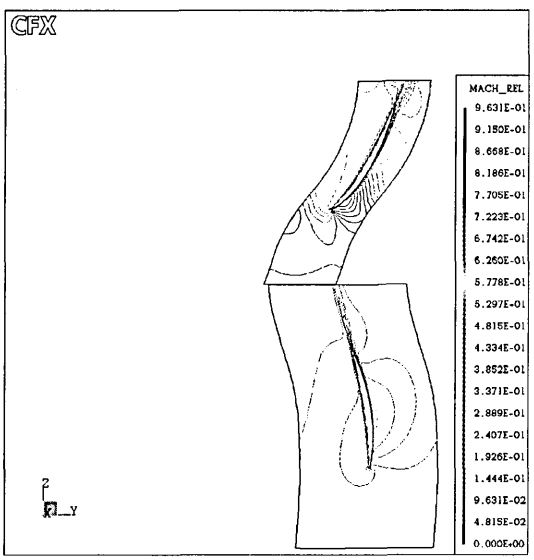

Figure 6-56 IGV and Rotor1 relative Mach number at 9.82 Kg/s – mid-span

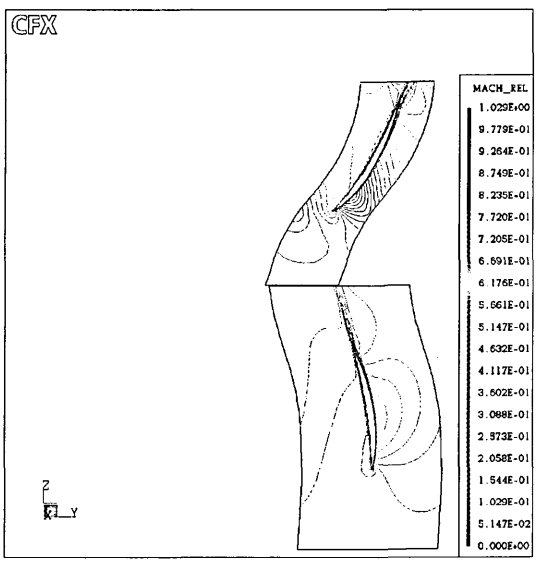

Figure 6-57 IGV and Rotor1 relative Mach number at 10.64 Kg/s – mid-span

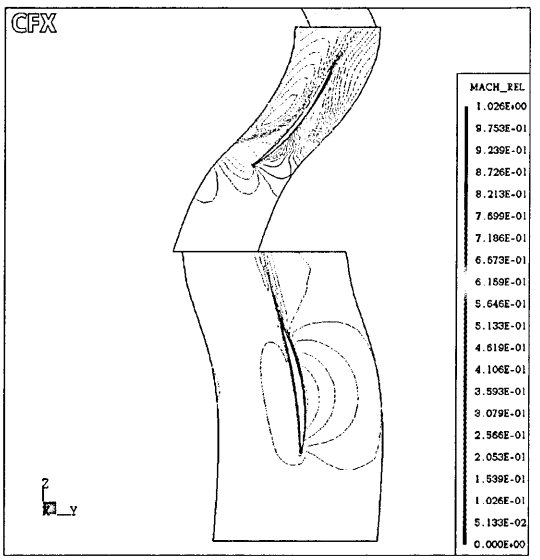

Figure 6-58 IGV and Rotor 1 relative Mach number at 9.82 Kg/s – near shroud

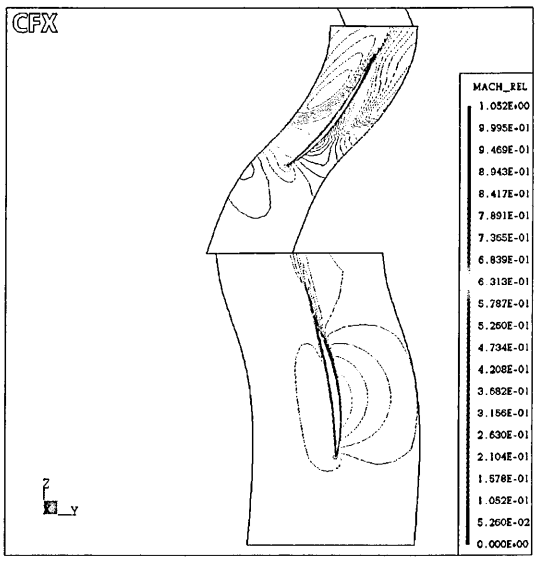

Figure 6-59 IGV and Rotor 1 relative Mach number at 10.64 Kg/s – near shroud

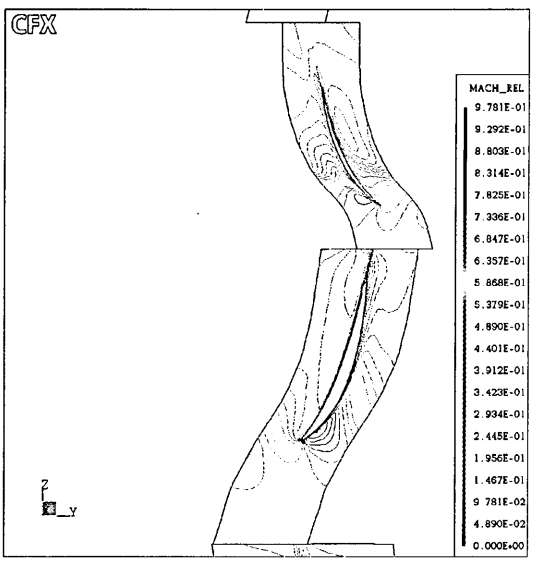

Figure 6-60 Rotor1 and Stator 1 relative Mach number at 9.82 Kg/s – near hub

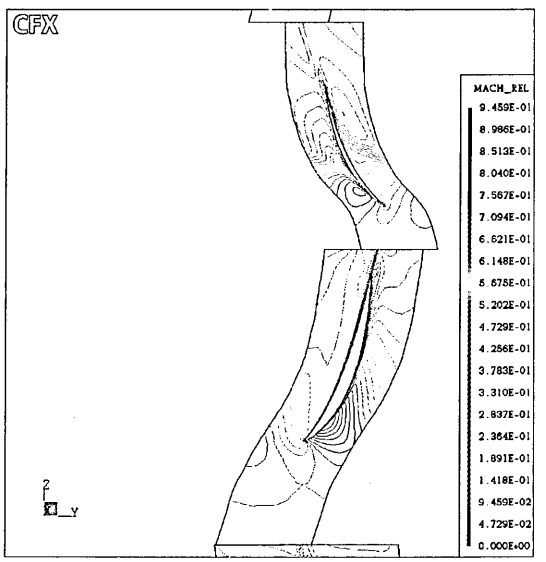

Figure 6-61 Rotor1 and Stator 1 relative Mach number at 10.64 Kg/s – near hub

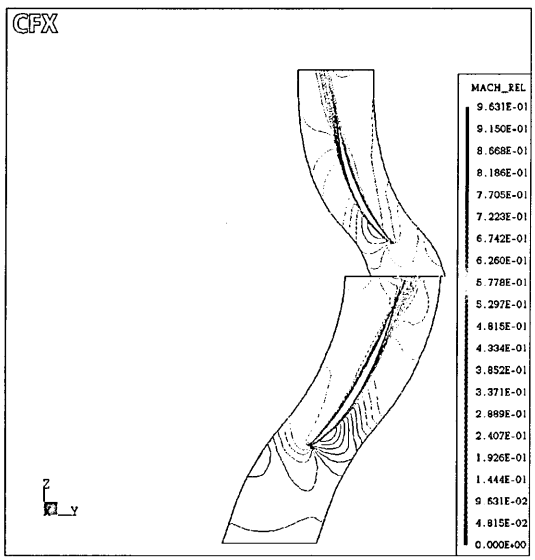

Figure 6-62 Rotor1 and Stator 1 relative Mach number at 9.82 Kg/s – mid-span

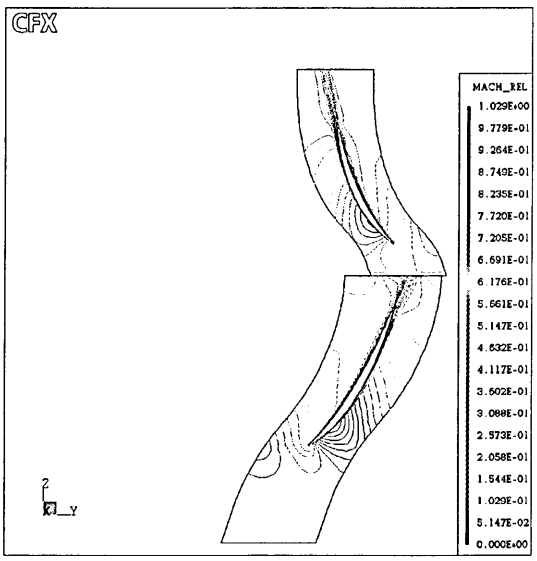

Figure 6-63 Rotor1 and Stator 1 relative Mach number at 10.64 Kg/s – mid-span

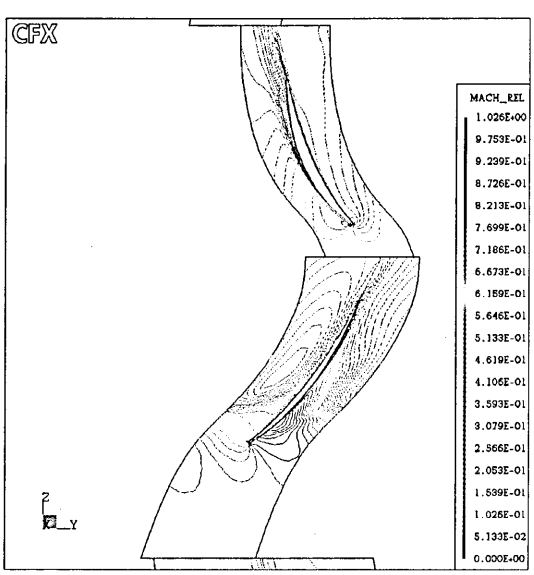

Figure 6-64 Rotor1 and Stator 1 relative Mach number at 9.82 Kg/s – near shroud

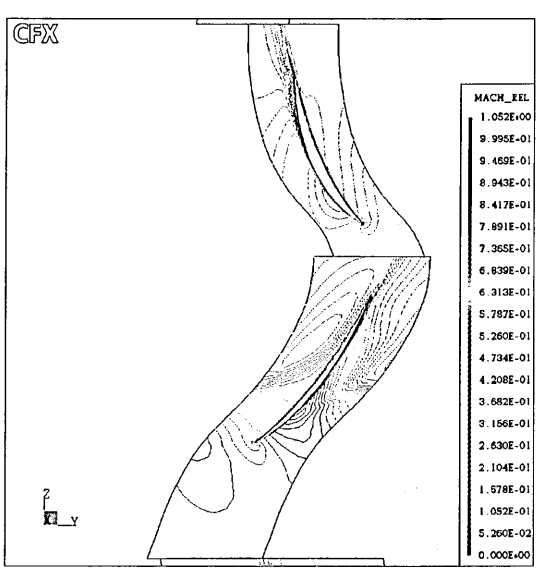

Figure 6-65 Rotor1 and Stator 1 relative Mach number at 10.64 Kg/s – near shroud

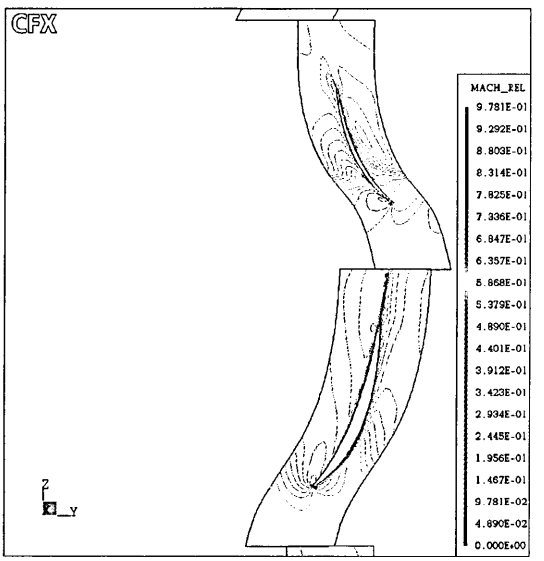

Figure 6-66 Rotor2 and Stator 2 relative Mach number at 9.82 Kg/s – near hub

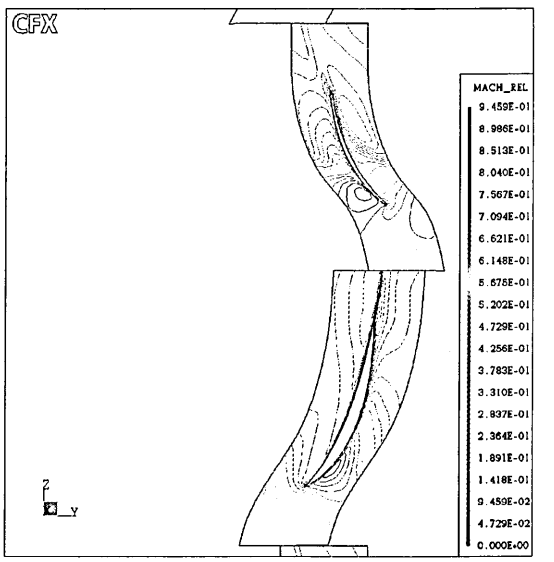

Figure 6-67 Rotor2 and Stator 2 relative Mach number at 10.64 Kg/s – near hub

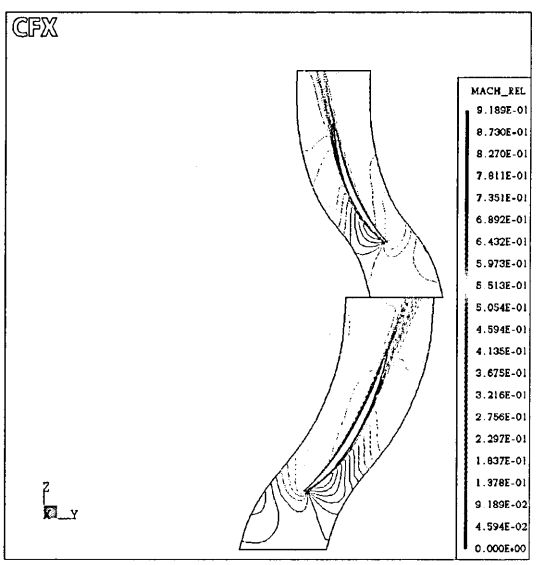

Figure 6-68 Rotor2 and Stator 2 relative Mach number at 9.82 Kg/s – mid-span

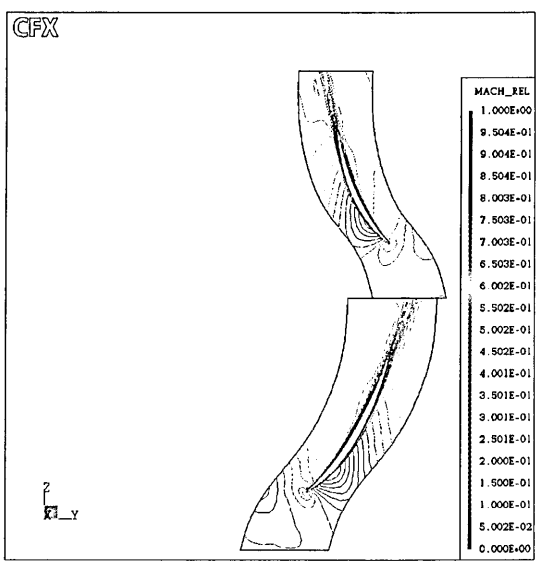

Figure 6-69 Rotor2 and Stator 2 relative Mach number at 10.64 Kg/s – mid-span

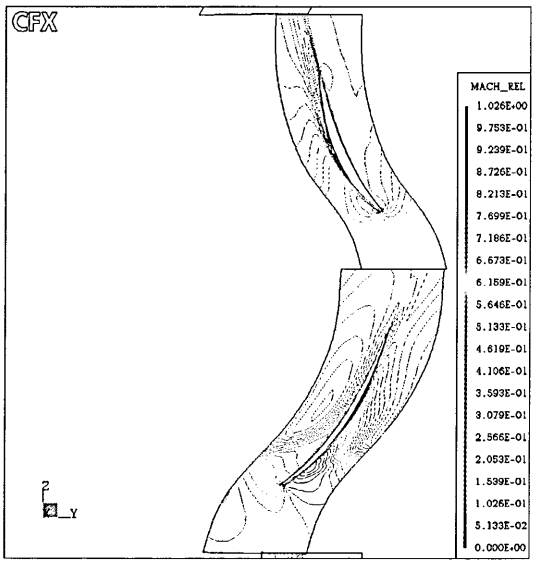

Figure 6-70 Rotor2 and Stator 2 relative Mach number at 9.82 Kg/s – near shroud

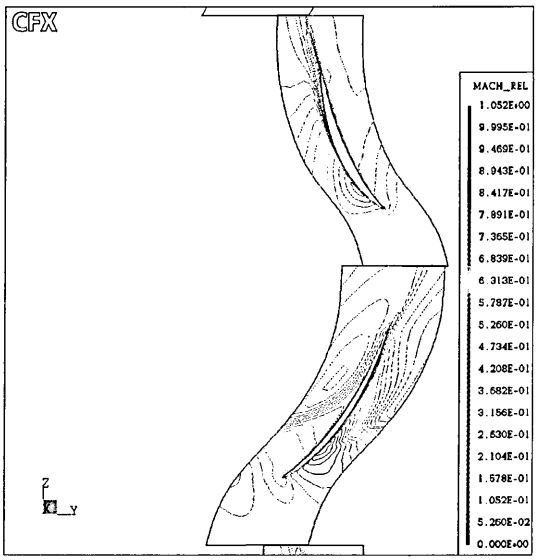

Figure 6-71 Rotor2 and Stator 2 relative Mach number at 10.64 Kg/s – near shroud

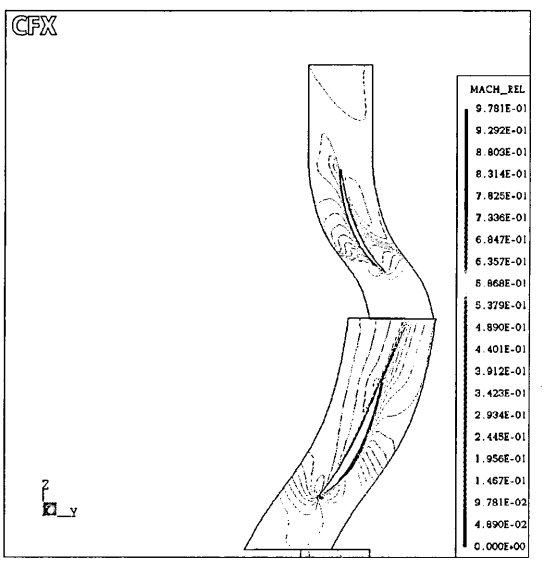

Figure 6-72 Rotor3 and Stator 3 relative Mach number at 9.82 Kg/s – near hub

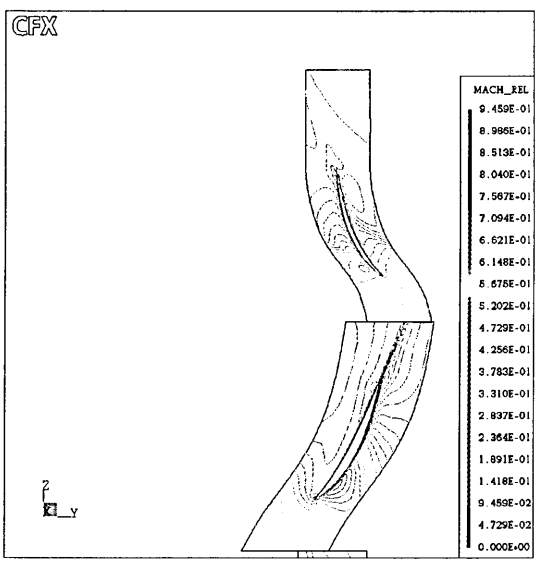

Figure 6-73 Rotor3 and Stator 3 relative Mach number at 10.64 Kg/s – near hub

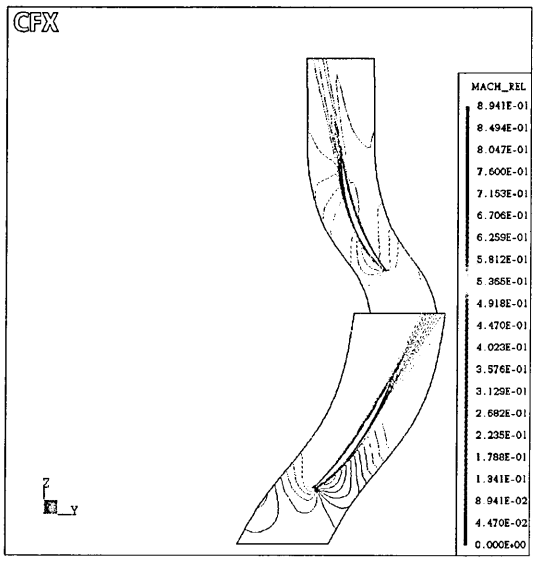

Figure 6-74 Rotor3 and Stator 3 relative Mach number at 9.82 Kg/s – mid-span

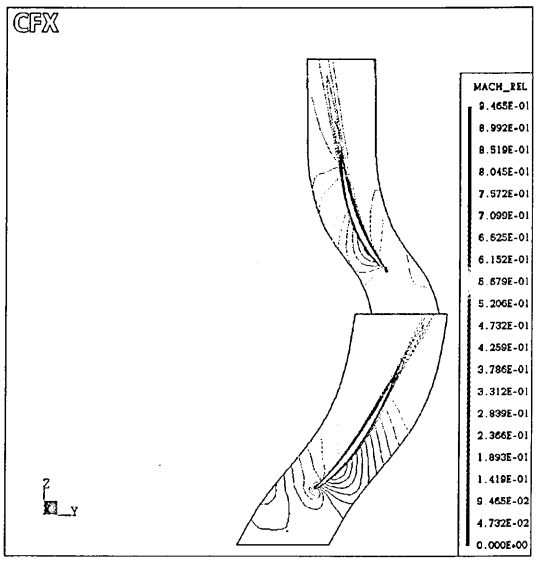

Figure 6-75 Rotor3 and Stator 3 relative Mach number at 10.64 Kg/s – mid-span

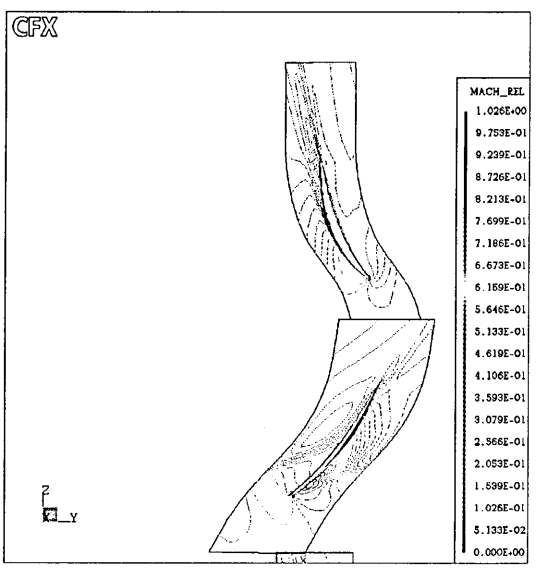

Figure 6-76 Rotor3 and Stator 3 relative Mach number at 9.82 Kg/s – near shroud

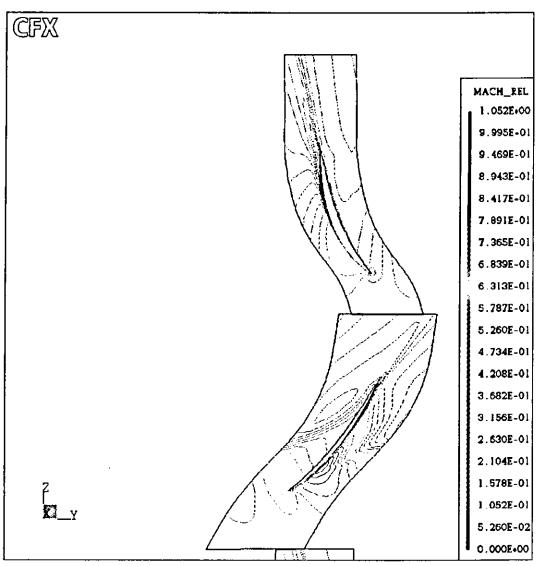

Figure 6-77 Rotor3 and Stator 3 relative Mach number at 10.64 Kg/s – near shroud

Interestingly enough these flows are seen to lose coherence and intensity towards the outlet of the compressor, presumably due to the loss of influence of the axial velocity component associated with the growth of the endwall boundary layers, which has been identified in the radial profiles of the axial velocity component, Figure 6-33 through to Figure 6-39. In the sections of blade trailing edges which are located in these regions, a large amount of deviation is readily apparent, leading to the presentation to the downstream row of a large inlet incidence and an attending pressure side early boundary layer separation

In the mid-span areas it is noteworthy how despite the small difference in the mass flows of the two points, the flow patterns, particularly the wake widths, are substantially different. All plots are associated with a local scale whereby the values correspond to the range present in the actual plot. It is interesting to note the occurrence of patches of high Mach values, occasionally to include in fact transonic values, distributed throughout the whole machine and including the hub region.

6.2.3.5 Contour plots – passage positions

The passage contour plots, Figure 6-78 to Figure 6-91, refer to the upstream displaced side of the six stage interfaces. Again although the two points covered by the plots are positioned fairly close within the compressor characteristic, this difference is sufficient to highlight the emergence of clear trends, besides of course providing an illustration of the computed flow physics near the design point and thereabouts.

In general the higher mass isocontours plots are characterized by a sharper image, indicative of the presence of more intense speed gradients, the figures 6-86 and 6-87 providing a conclusive example in point.

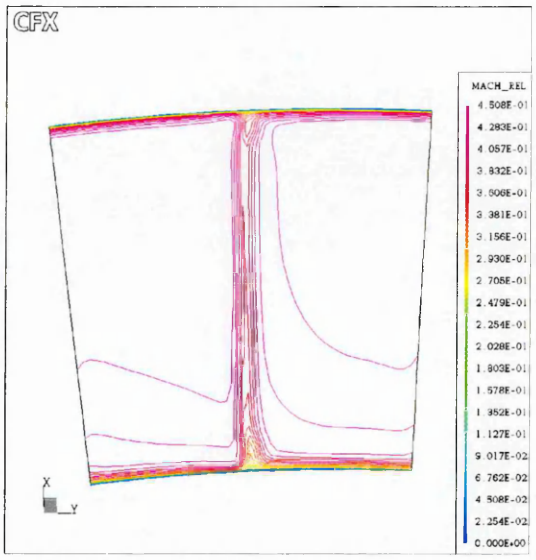

Figure 6-78 IGV outlet absolute Mach number at 9.82 Kg/s

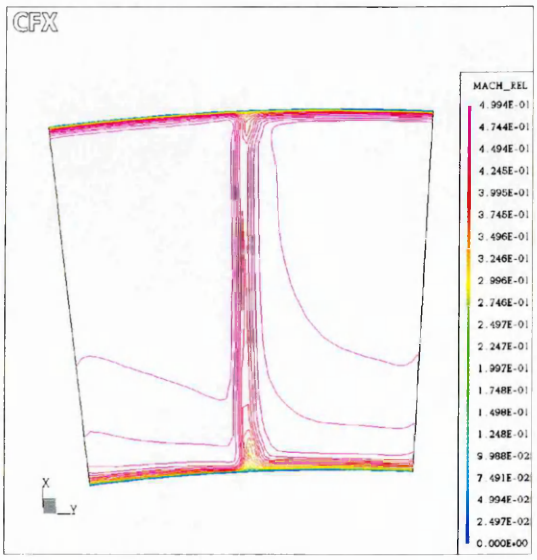

Figure 6-79 IGV outlet absolute Mach number at 10.64 Kg/s

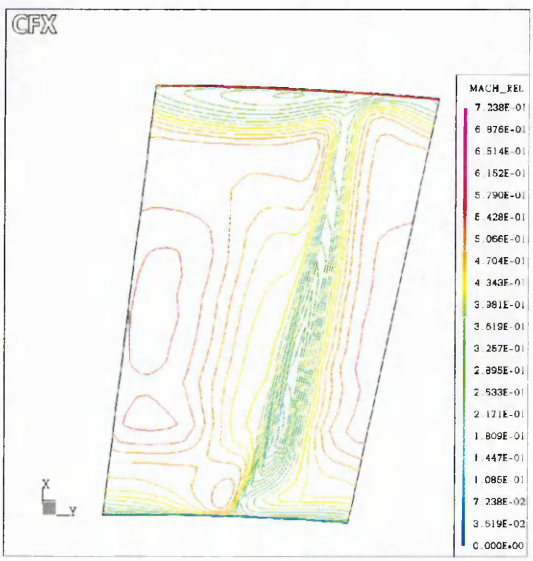

Figure 6-80 Rotor 1 outlet relative Mach number at 9.82 Kg/s

Figure 6-81 Rotor 1 outlet relative Mach number at 10.64 Kg/s

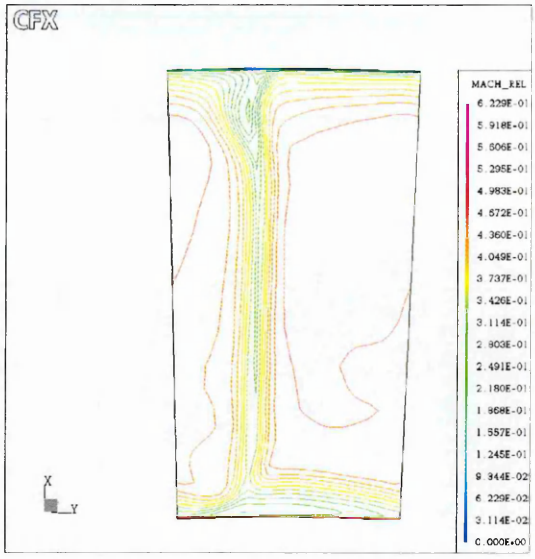

Figure 6-82 Stator 1 outlet absolute Mach number at 9.82 Kg/s

Figure 6-83 Stator 1 outlet absolute Mach number at 10.64 Kg/s

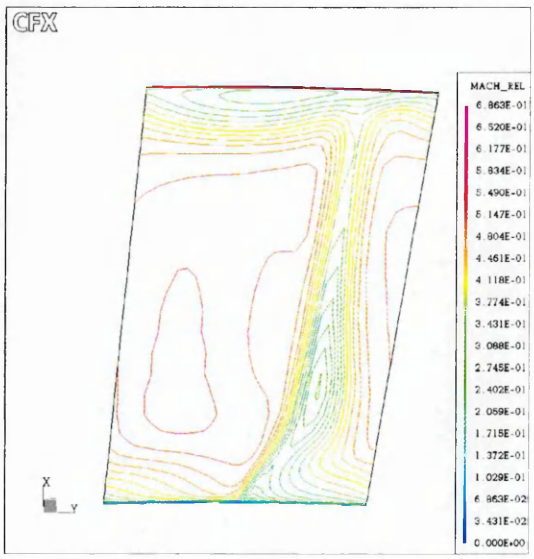

Figure 6-84 Rotor 2 outlet relative Mach number at 9.82 Kg/s

Figure 6-85 Rotor 2 outlet relative Mach number at 10.64 Kg/s

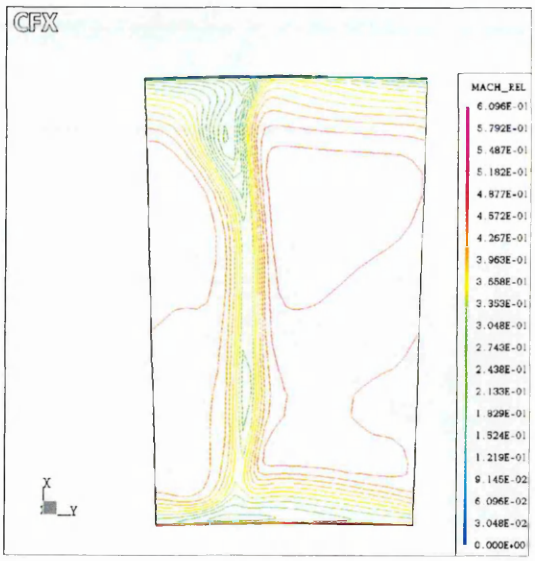

Figure 6-86 Stator 2 outlet absolute Mach number at 9.82 Kg/s

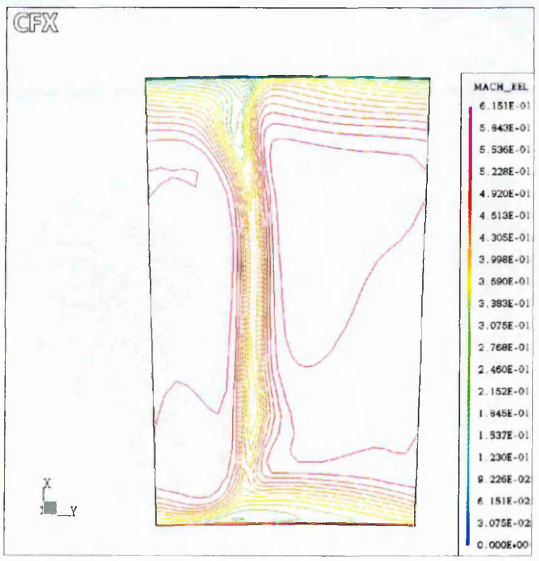

Figure 6-87 Stator 2 outlet absolute Mach number at 10.64 Kg/s

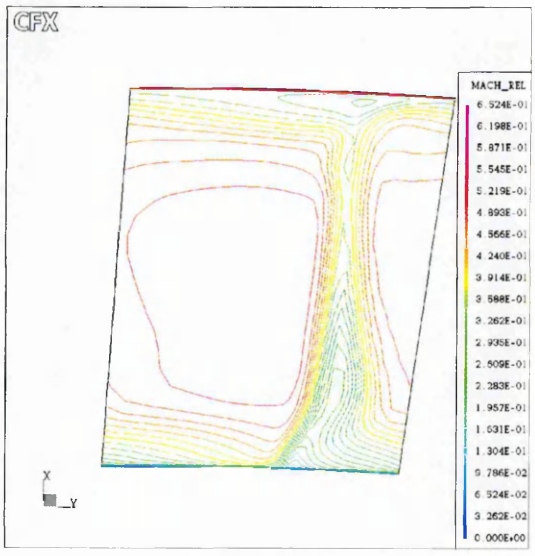

Figure 6-88 Rotor 3 outlet relative Mach number at 9.82 Kg/s

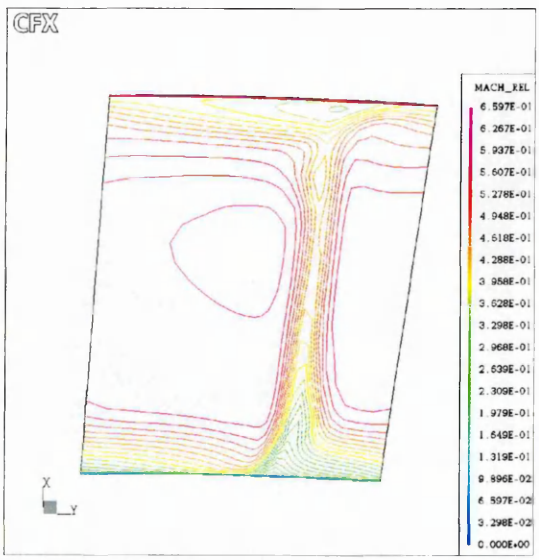

Figure 6-89 Rotor 3 outlet relative Mach number at 10.64 Kg/s

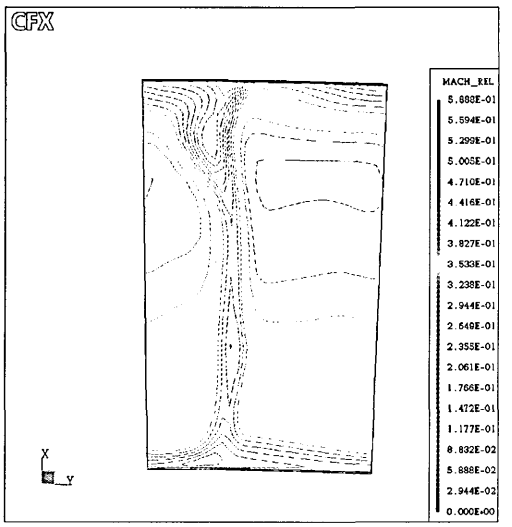

Figure 6-90 Stator 3 outlet relative Mach number at 9.82 Kg/s

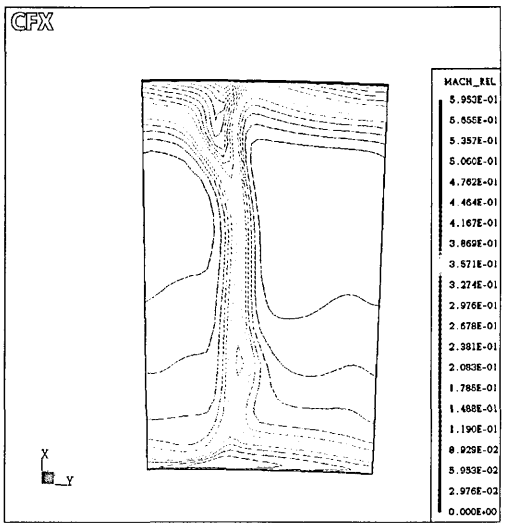

Figure 6-91 Stator 3 outlet relative Mach number at 10.64 Kg/s

Besides the differences pointed above, the plots of the lower mass point show a considerable widening of the wakes downstream of the rotors, that same effect being much less clear in the stator domains. The regions where the disparity between the two flow regimes is more readily apparent are the wake structures associated with the roots of the blades, predominantly the lower middle spans of the rotors.

In stage one, Figure 6-80 to 6-83, the fall in mass flow seems to affect the rotor flow pattern minimally and has a slightly more noticeable impact in the stator through a deepening of the speed deficit near the stator root. This behaviour reinforces the suggestion that the more notable changes observed elsewhere are to a considerable degree due to cumulative effects of upstream derived events.

The change in stage two is far more marked with a sizeable expansion of the wake base area of Rotor 2, Figure 6-84 and 6-85 and a corresponding growth in the stator hub. This trend is further accentuated in the third stage where the enlargement of the wake is extensive both in width as well as spanwise. This evolution process in the axial direction is illustrated by recourse to three planes, A through C, whose location in Rotor 3 is shown in Figure 6-92 to Figure 6-94.

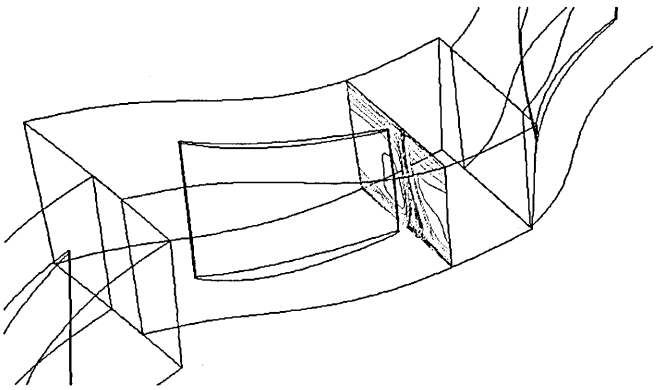

Figure 6-92 Location of Plane **A** downstream of Rotor 3 blade

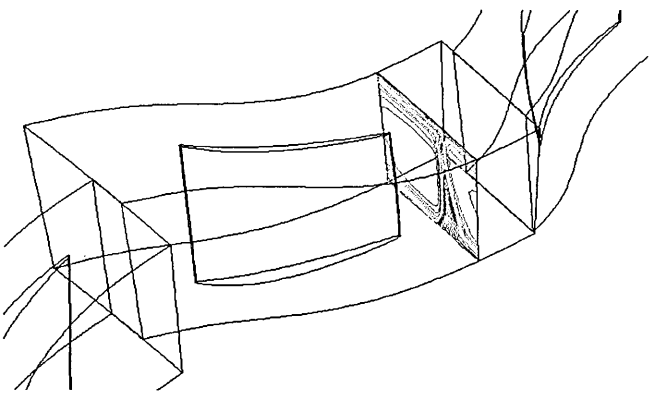

Figure 6-93 Location of Plane **B** downstream of Rotor 3 blade

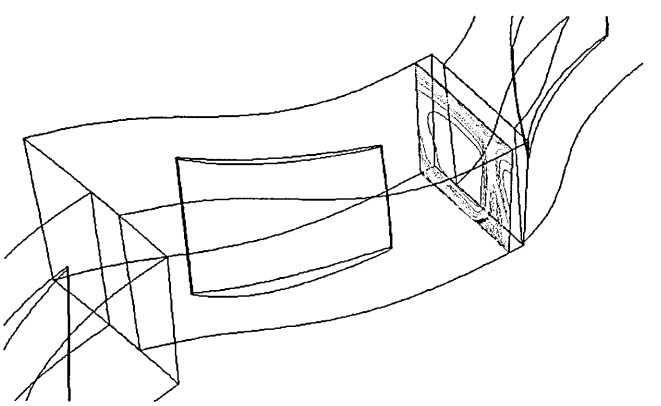

Figure 6-94 Location of Plane **C** downstream of Rotor 3 blade

Figure 6-95 Rotor 3 relative Mach number at 9.82 Kg/s – Plane A

Figure 6-96 Rotor 3 relative Mach number at 10.64 Kg/s – Plane A

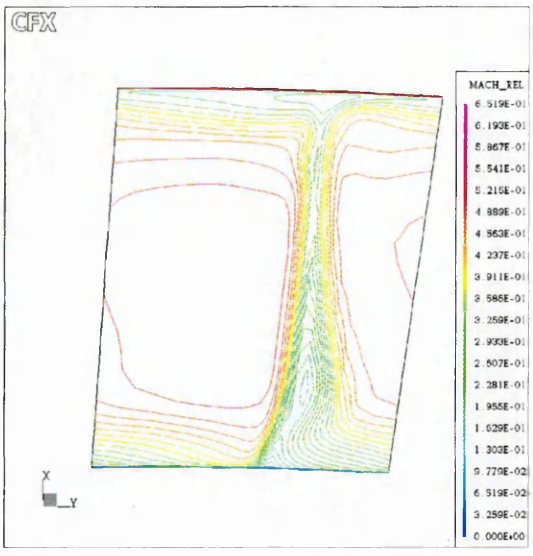

Figure 6-97 Rotor 3 relative Mach number at 9.82 Kg/s – Plane B

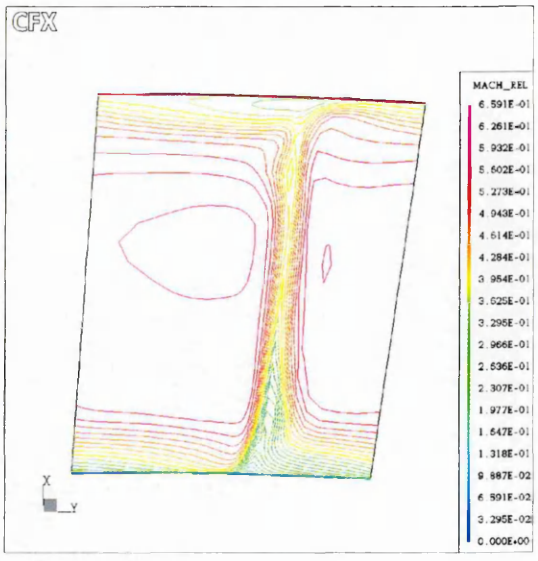

Figure 6-98 Rotor 3 relative Mach number at 10.64 Kg/s – Plane B

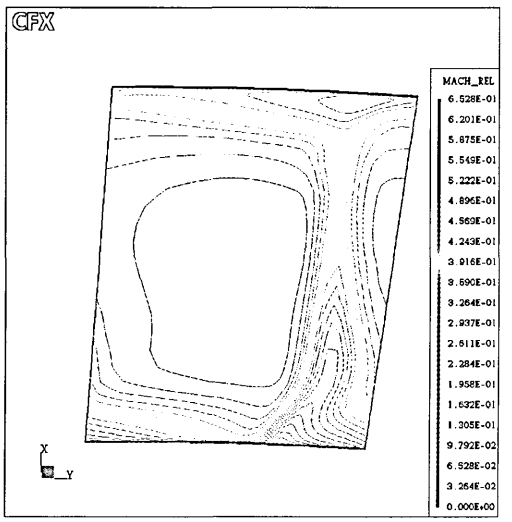

Figure 6-99 Rotor 3 relative Mach number at 9.82 Kg/s – Plane C

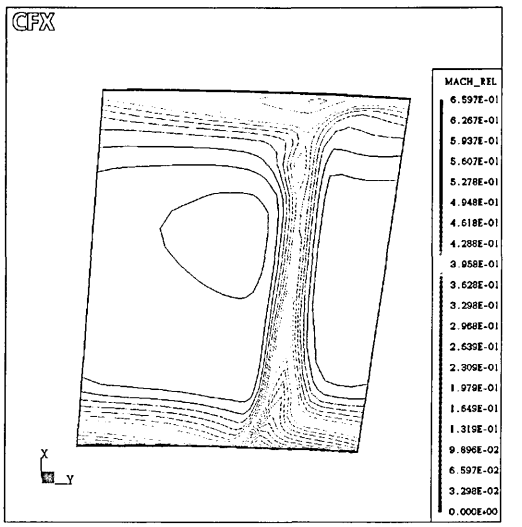

Figure 6-100 Rotor 3 relative Mach number at 10.64 Kg/s – Plane C

The significance of these plots lies in the clarity with which they reveal the wake decay behaviour taking place within a small distance from the wake trailing edge. Directing our attention to the high mass flow plots, Figures 6-96 to 6-100, it will be apparent the substantial variation occurring in about half a blade chord. The plot of Figure 6-96 is dominated by a crisp narrow wake whose velocity deficit is well defined. In the equivalent plot of Plane B, Figure 6-98, the dimensions of the wake remain substantially unaltered but the deficit is seen to 'fill out' with the green colouring being replaced by yellow, indicative of a higher velocity, over the majority of the span. Finally in Figure 6-100 the mixing process is seen to be more effective with the smearing of the sharpest gradients particularly near the endwalls.

In the lower mass case the process is broadly similar but there are also some visible differences. Given that the initial state was much less intense, there are very few high speed red isocontours in the wake region, the decay is much briefer such that by Figure 6-99 the plot shows only a distant likeness to the original pattern. This is particularly striking when considering the very sharp quasi-vertical trace associated with the pressure side velocity profile, Figure 6-95, of which virtually nothing remains at Plane C.

6.3 Source code assembly approach

6.3.1 General comments

As was noted in 4.2.4 the code follows for assembly of the global solution matrices a minimization routine which will operate on the individual grid blocks according to the transformation matrices contained in the relevant section of BCF, the boundary conditions file. The HSRC transformation schedule is presented below with the comment that the first of the grids, corresponding in the HSRC to the IGV is denoted by default in the code as MAIN.

```
 1 MAIN
38     0     1     0     0
53     0     0     1     0
90     0     0     0     1
 2 R1
42    34     0    -1     0
33    96    -1     0     0
93    94     0     0    -1
 3 S1
42    32     0    -1     0
31   306    -1     0     0
90    91     0     0    -1
 4 R2
42    34     0    -1     0
33   180    -1     0     0
92    93     0     0    -1
 5 S2
42    32     0    -1     0
31   264    -1     0     0
91    92     0     0    -1
 6 R3
42    34     0    -1     0
33   138    -1     0     0
92    93     0     0    -1
 7 S3
42    34     0    -1     0
33   222    -1     0     0
86    87     0     0    -1
```

The visualization of the transformations operated in the pre-processing phase of the solution is a crucial step of the development of a source code approach, particularly when the calculations require that the evaluation of individual nodal values be performed by reference to those of its neighbours. The graphical HSRC solution matrix assembly scheme is shown in Figure 6-101 where the blue numbers denote global coordinate values and those in red refer to the local coordinates of the individual blade domains. It will be recalled from Table 6-2 that all grid domains, with the exception of that of the IGV, contain 42 nodes in the spanwise direction and that the typical node count in the pitchwise direction is 33 nodes.

It thus follows from the transformation schedule shown above that except for the IGV all grids were the subject of rotations as is shown by the disposition of the local IJK coordinate axii which are visible in Figure 6-3. Some elements of the code matrix minimisation algorithm, the knowledge of which can be beneficial as an added criterion in the selection of grid sizes in multistage simulations, are obvious from the analysis of the disposition of the individual domains within the global matrix.

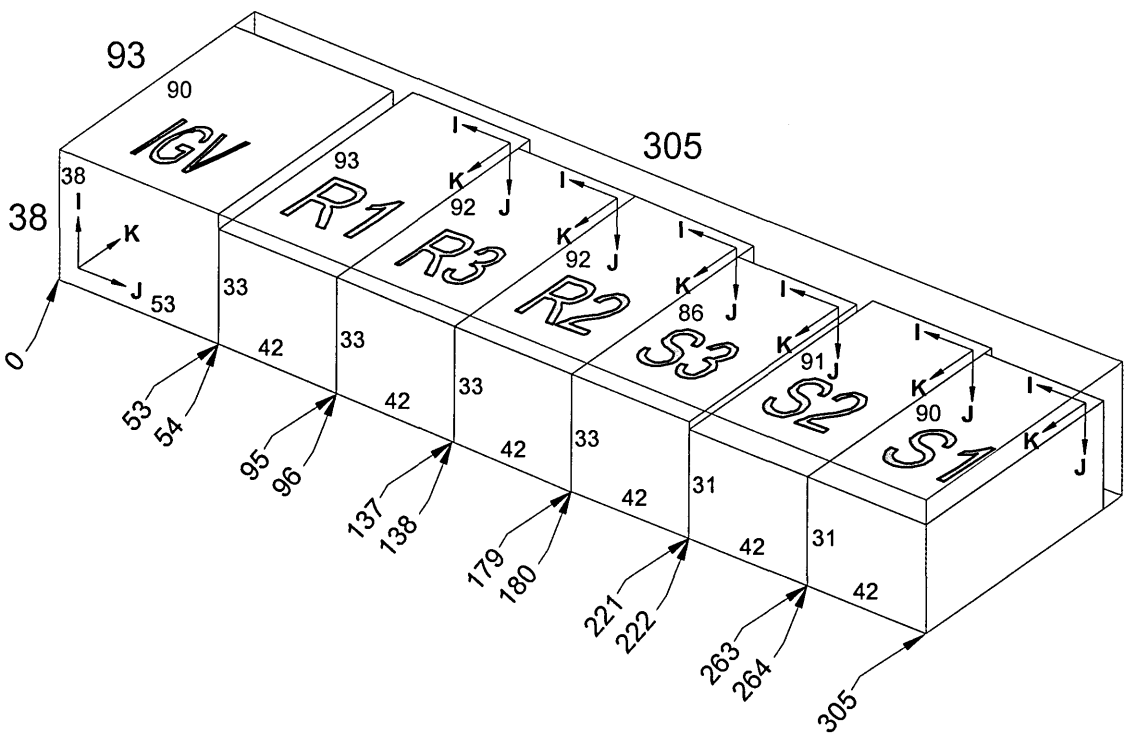

Figure 6-101 HSRC solution matrix assembly scheme

The code retains the datum grid initial coordinates and will transform the other grids in order to as far as possible obtain new configurations that replicate the spatial arrangement of the 'MAIN' grid. Specifically the pitchwise node count 33 seems to have been the candidate to match the datum 'I' value since it is the only figure that is smaller than the 38 count of that coordinate. Given this step the selection of 42, in preference to the higher 90 counts, as the value chosen to be associated with the datum 'J' coordinate is understandable but the requirement for the inversion of the local 'K' directions is much less obvious.

As a matter of fact the minimisation routine, even when limited to the sideways placement of grids domains, does not seem to accomplish the most efficient use of resources. Whereas the global matrix as assembled contains 38x93x305 or 1,077,870 entries, this value would have been 964,782 or 42x93x247, a saving of more than 110,000 entries had the initial disposition of the grids been retained and these just assembled side-by-side into a global matrix.

6.3.2 Bolger model

6.3.2.1 Source code formulation

The construction of the source code, which is similar to the version employed in the HP9 case, is presented below in a schematic form. The first of the flow charts details the algorithmic structure of the code as applied to the complete compressor while the second chart presents the deterministic stress routine which is called by the main portion of the code.

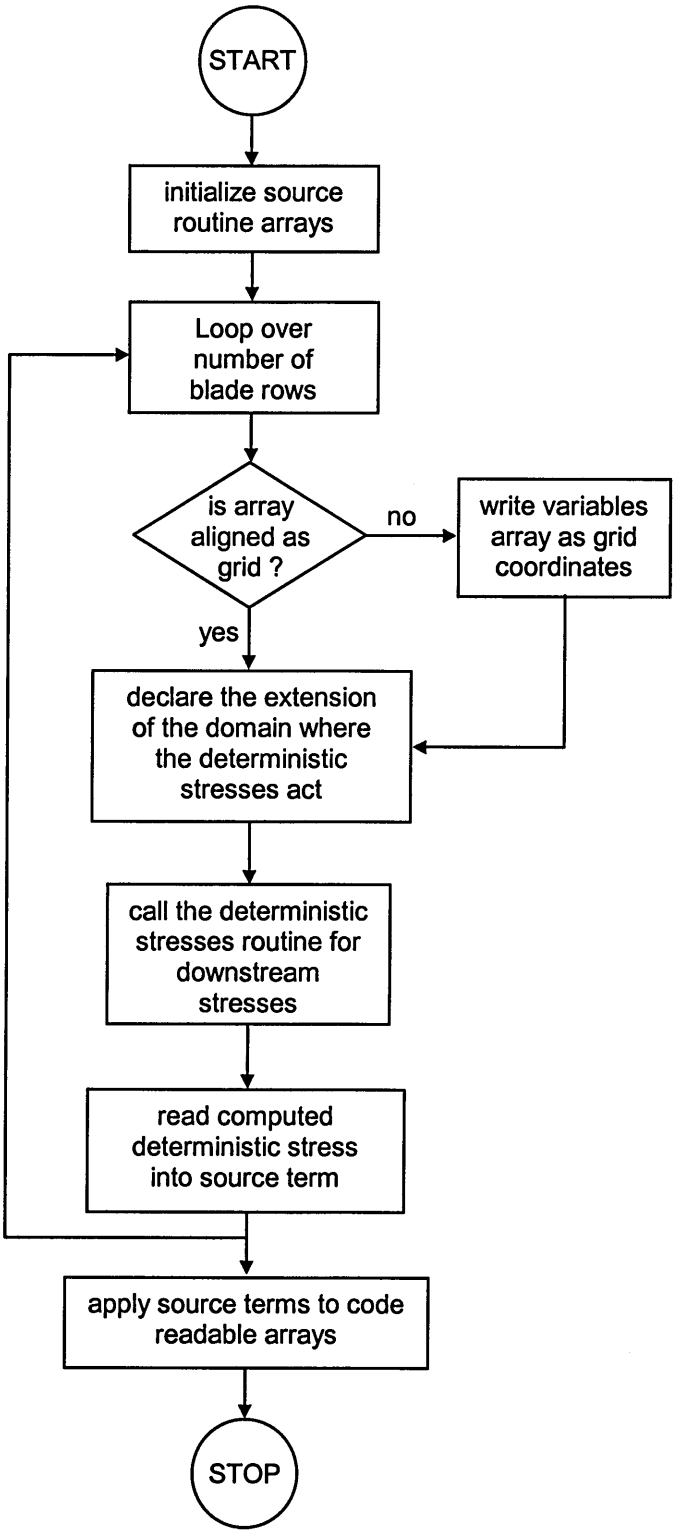
START
initialize source routine arrays
Loop over number of blade rows
is array aligned as grid ?
no
write variables array as grid coordinates
yes
declare the extension of the domain where the deterministic stresses act
call the deterministic stresses routine for downstream stresses
read computed deterministic stress into source term
apply source terms to code readable arrays
STOP

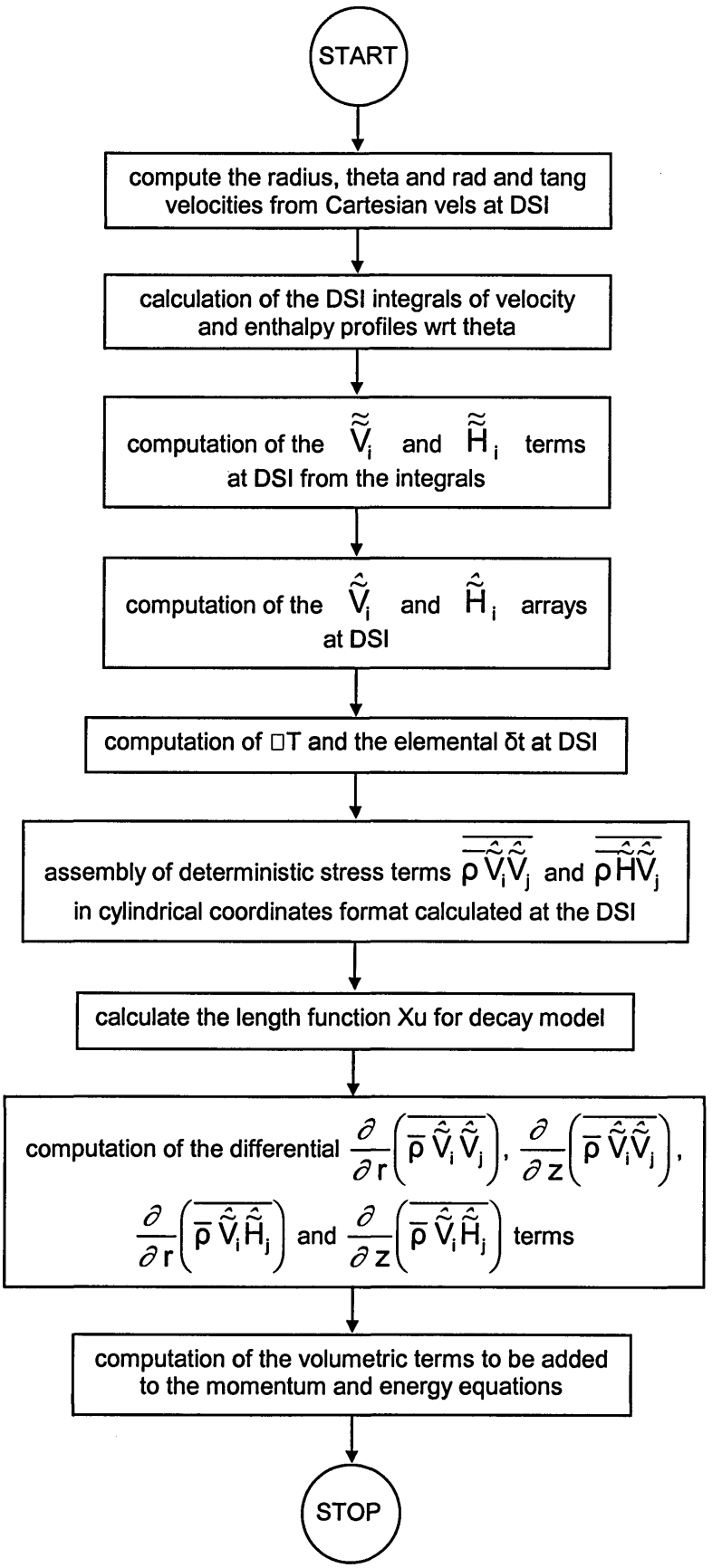
START
compute the radius, theta and rad and tang velocities from Cartesian vels at DSI
calculation of the DSI integrals of velocity and enthalpy profiles wrt theta
computation of the $\tilde{\tilde{V}}_i$ and $\tilde{\tilde{H}}_i$ terms at DSI from the integrals
computation of the $\hat{\tilde{V}}_i$ and $\hat{\tilde{H}}_i$ arrays at DSI
computation of □T and the elemental δt at DSI
assembly of deterministic stress terms $\overline{\bar{\rho}\hat{\tilde{V}}_i\hat{\tilde{V}}_j}$ and $\overline{\bar{\rho}\hat{\tilde{H}}\hat{\tilde{V}}_j}$ in cylindrical coordinates format calculated at the DSI
calculate the length function Xu for decay model
computation of the differential $\frac{\partial}{\partial r}\left(\overline{\bar{\rho}\hat{\tilde{V}}_i\hat{\tilde{V}}_j}\right)$, $\frac{\partial}{\partial z}\left(\overline{\bar{\rho}\hat{\tilde{V}}_i\hat{\tilde{V}}_j}\right)$, $\frac{\partial}{\partial r}\left(\overline{\bar{\rho}\hat{\tilde{V}}_i\hat{\tilde{H}}_j}\right)$ and $\frac{\partial}{\partial z}\left(\overline{\bar{\rho}\hat{\tilde{V}}_i\hat{\tilde{H}}_j}\right)$ terms
computation of the volumetric terms to be added to the momentum and energy equations
STOP

6.3.2.2 Wakes characterization

The wakes profiles at the displaced sides of the interfaces, or DSI, contain the information which is employed in the assembly of the deterministic stresses at that axial station. The pitchwise distributions of the relative components of the velocity vector and total enthalpy for the two mass flows of 10.64 and 9.82 Kg/s were taken at three radial annular heights wit the red line in these plots indicating the value of the pitchwise weighted-average of the applicable quantity.

Although a broad analysis of the wake profiles is strictly more appropriate within the context of a general description of the aerodynamics of the machine, a discussion of this topic is included in this section given the dependency of the deterministic stresses models on the features of the wakes.

IGV – The wake profiles are analogous for the two flow conditions and the major distinctions occur primarily between endwall and core flows. The magnitudes of all the velocities are comparatively quite similar for the two mass points. There is evidence of secondary flows at mid-span, Figure 6-102, as well as in the endwalls where the directions have opposite senses, Figure 6-103 and 6-104.

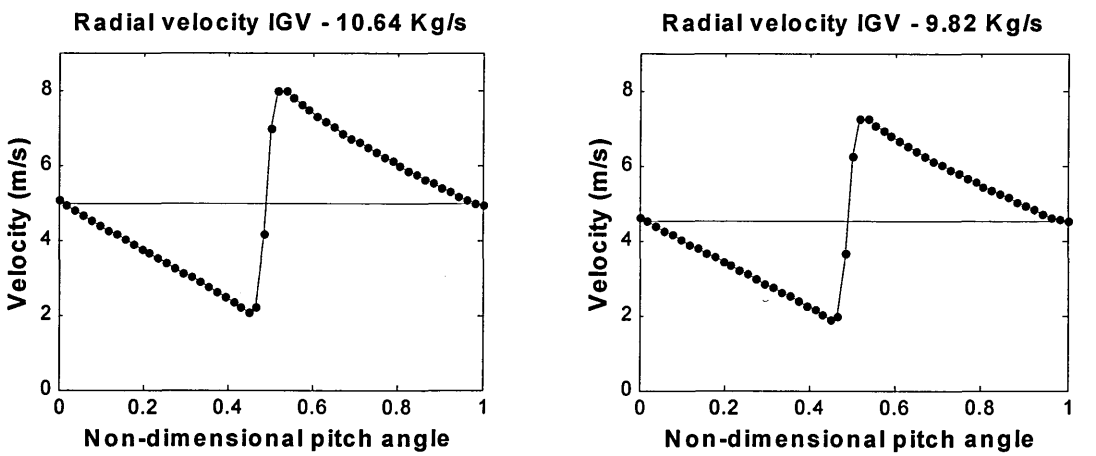

Figure 6-102 Radial velocity pitchwise distribution at the IGV/Rotor1 DSI – mid span

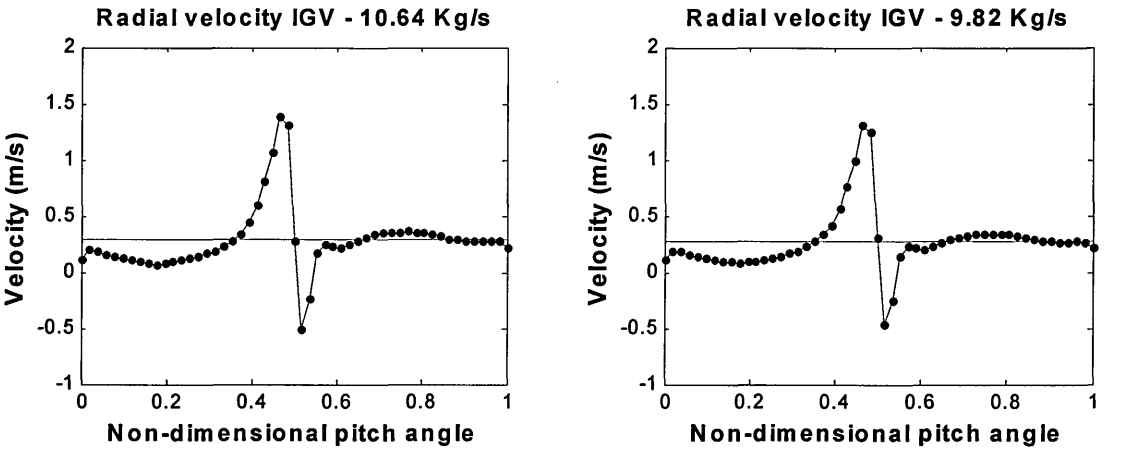

Figure 6-103 Radial velocity pitchwise distribution at the IGV-Rotor1 DSI – near shroud

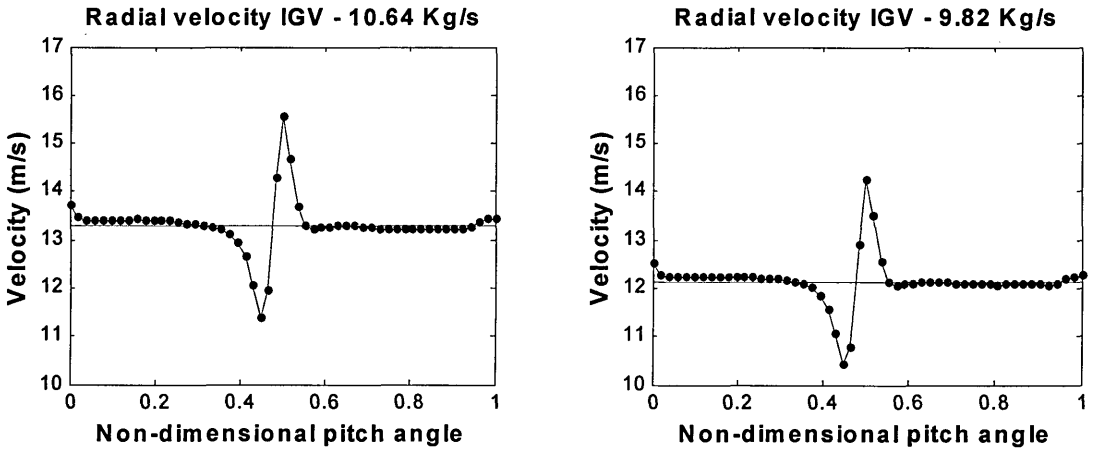

Figure 6-104 Radial velocity pitchwise distribution at the IGV/Rotor1 DSI - near hub

Stage 1 – Other than the existing similarities between the two flow conditions it is difficult to identify in the rotor wakes any pattern which can be said to be common between the same types of velocities at the three spanwise locations. In fact only the axial velocity profile for the mid-span can be said to conform to the idealized wake format of a nearly symmetrical deficit from a main flow core. Near the hub there is hardly any difference between the two flow patterns whereas near the shroud the variation takes primarily the form of a broadening of the separate wakes rather than a reduction in the

local minima. In the stator the wakes are characterized by clear dips and extensive regions of mainstream flow. The radial velocity near the shroud is unique in showing a strong dissimilarity with the variation of the mass flow, Figure 6-105.

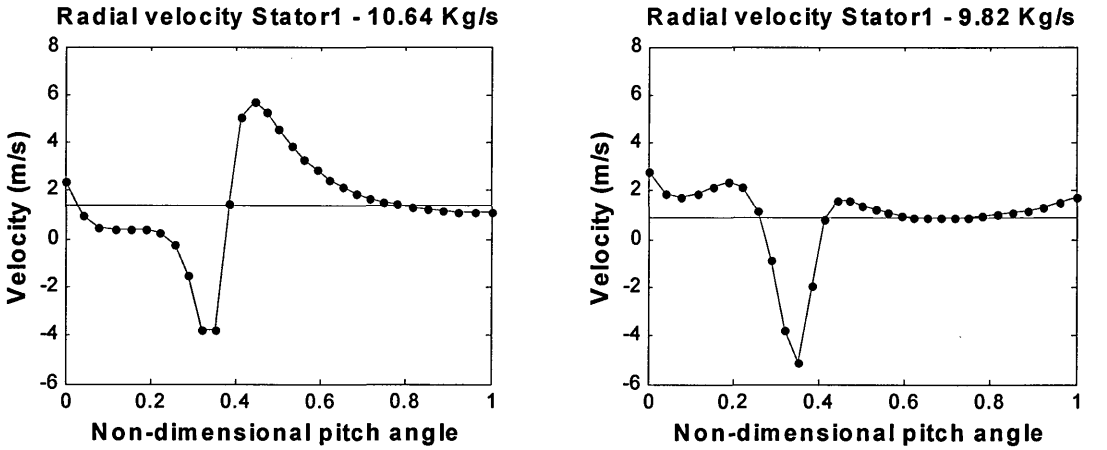

Figure 6-105 Radial velocity pitchwise distribution at the Stator1/Rotor2 DSI – near shroud

Stage 2 – In Rotor 2 the variation between the two mass flows, other than a small change in the magnitude the velocities, is confined to the near shroud region where in general the 9.82 Kg/s wakes show greater mixing effects by way of a considerably larger width as seen in the picture below..

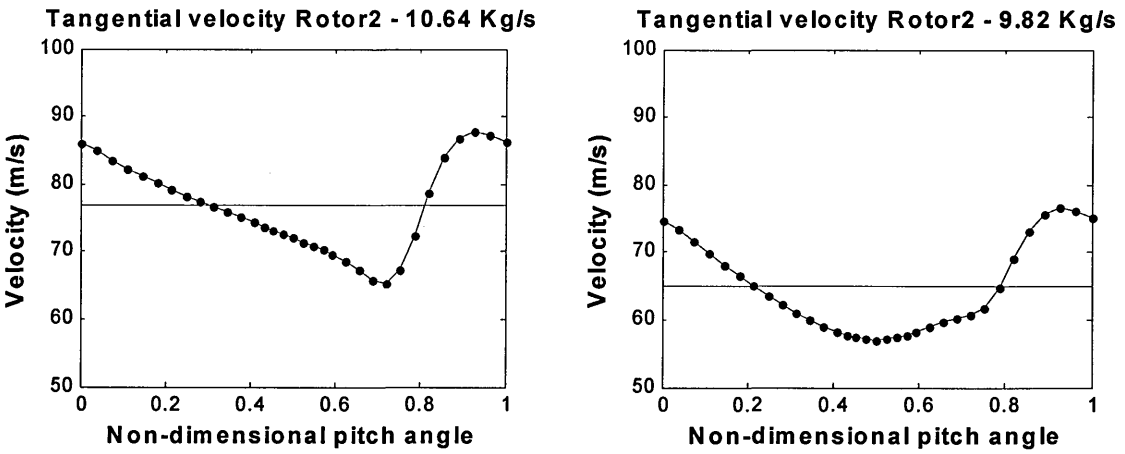

Figure 6-106 Tangential velocity pitchwise distribution at the Rotor2/Stator2 DSI – near shroud

In the near hub the wake configuration suggests the presence of a vortical structure possibly emanating from the corner region and which seems essentially unaffected by the change in flow regime, Figures 6-107 and 6-108.

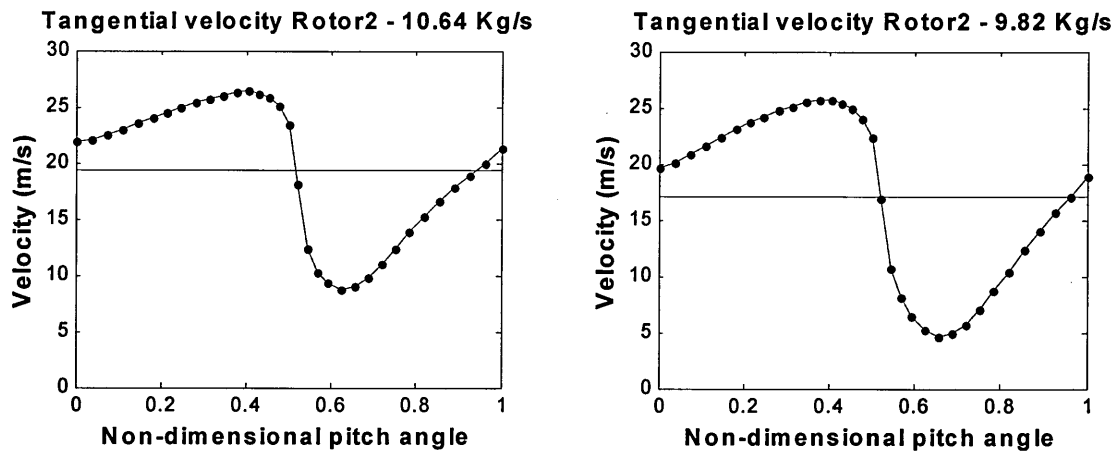

Figure 6-107 Tangential velocity pitchwise distribution at the Rotor2/Stator2 DSI – near hub

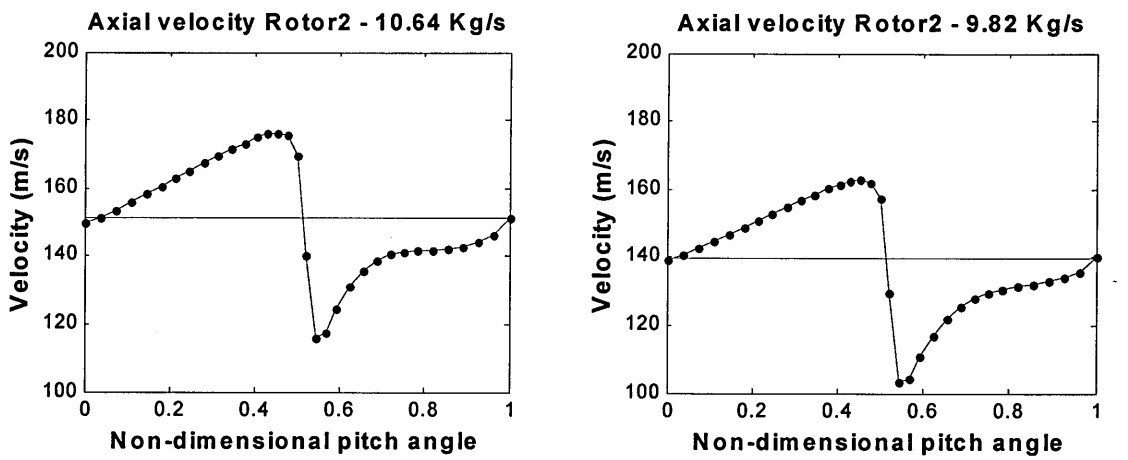

Figure 6-108 Axial velocity pitchwise distribution at the Rotor2/Stator2 DSI – near hub

This pattern is further encountered in Stator 2 again in the blade root region and presumably due to the same mechanism.

Stage 3 – In general wake patterns of Rotor3 are those where the greater impact of the change in mass passing is more clearly shown as in Figure 6-109. It is significant to note the great similarity of the wake profiles in the near shroud region as well as the mild gradients of these wakes. It is thought that these features are due to the significant growth of the wall boundary layers placing the data collection region within the wall viscous influence.

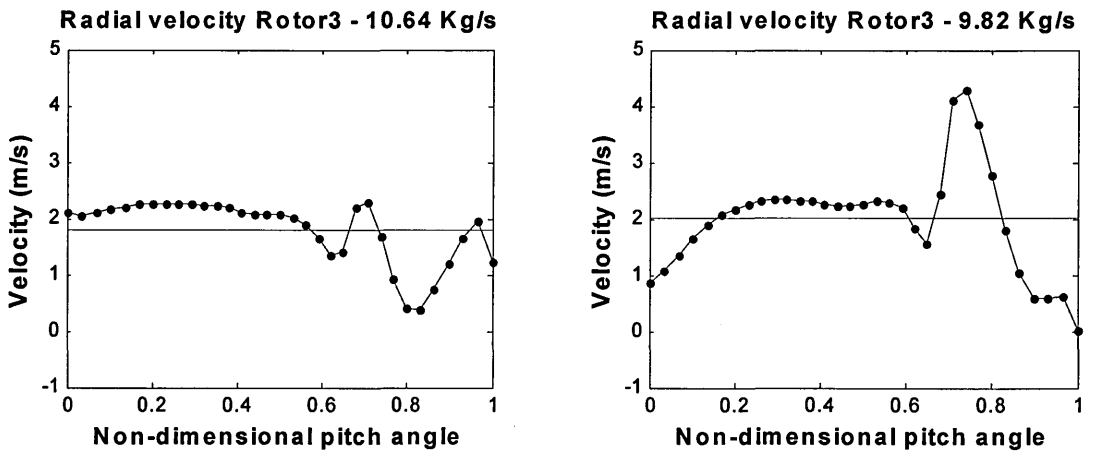

Figure 6-109 Radial velocity pitchwise distribution at the Rotor3/Stator3 DSI – near hub

The effects of the application of Bolger's model to the HSRC case are dealt with together with the results due to Hall's model in section 6.4.

6.3.3 Hall's model

Unlike in Bolger's model the successful application of the Hall model is dependent on the successful modelling of a 'real' wake and these therefore need to be amenable to such a process by, if at all possible, conforming to the stereotype upon which the model in based and which is loosely that of a Gaussian distribution. Where the wakes severely fail to conform to this desired configuration, as has been abundantly demonstrated above, the model as was applied to the HP9 case is liable to break down by yielding estimates that are inconsistent with the physics of the problem. In view of this situation, which is in the view of the author due to the untypical separation occurring on the HSRC, leading to the emergence in the stage interface region of decaying wakes of quasi-arbitrary

configurations, an expedient to make the code still usable under the circumstances was required.

The approach adopted herein is an hybrid form of both semi-empirical methods whereby the decay rates obtained from the apparent wake concept, calculated through the Hall methodology, are matched to Bolger's deterministic stresses interface plane calculation method. This approach comes across as relieving some of the implicit limitations present in the original formulations of both models, namely the requirement to conduct an expensive and time consuming simulation as demanded by Bolger's model, in order to determine the β decay functions, or the reliance on a problematic wake description scheme as is done in the Hall method.

Specifically the approach employed in the current work consists in interactively adjusting the wake definition parameters enclosed in the Hall decay correlations,

$$\frac{\delta}{S} = \frac{1.63632\left(\frac{s}{c}\right)C_D^{\frac{1}{8}} - 0.01944}{2.5\left(\frac{s}{c}\right)C_D^{\frac{1}{8}} + 1.0} \tag{6-1}$$

and

$$\left(\frac{W_{DC}}{W_0}\right)\left(\frac{1}{C_D^{\frac{1}{4}}}\right) = \frac{1.17543\left(\frac{s}{c}\right) + 1.28626}{21.0\left(\frac{s}{c}\right) + 1.0}. \tag{6-2}$$

As for the Bolger model the results are presented in a comparative manner in part 6-4 of the current Chapter.

6.4 Effects of the application of empirical models

6.4.1 Introduction

Although simulations of the two representative points, 9.82 and 10.64 Kg/s cases were run, difficulties associated with access to equipment with the required memory capacity have only enabled the post-processing of the two models on the lower mass point. An added complication when solving the whole compressor model with source term codes is that, if the code is dependent for the calculation of nodal values, on locations other than that of the node of interest, the local executable cannot be run on parallel solution mode.

This constitutes a grievous limitation on the practicability of the whole enterprise since the workspace required by the compound solver, basic plus source term local executable, amounted in the present case to about 1.5Gb. In practice this amount of RAM space is commonly only available in multiprocessor machines which make use of a shared memory architecture and although the University had for a time such a machine on loan, the period was not long enough to fully investigate the capabilities of the method.

Both models showed a slight increase in the mass passed by the compressor for the same values of average static back pressure, 220,000 Pa, as employed in the datum simulation as is shown in Table 6-5.

Model	Datum	Bolger	Hall
Mass flow	9.92	10.05	10.06
Percent variation	n/a	+ 2.32	+ 2.42

Table 6-5 HSRC mass flow variation with model selection

This increase in the mass flow, given the fact that the pressure and rotational speed were kept steady, can only come from a reduction in blockage which is precisely at the core of the argument advanced in favour of the employment of deterministic stress models which was developed by Dawes and Denton, 1998, and is presented in 4.3.2.

The case put forward by these two authors is that static pressure is seen to present a step across mixing-plane type formulations and that this step is connected to the introduction by the averaging process of degree of false blockage together with a variation in the direction of the flow.

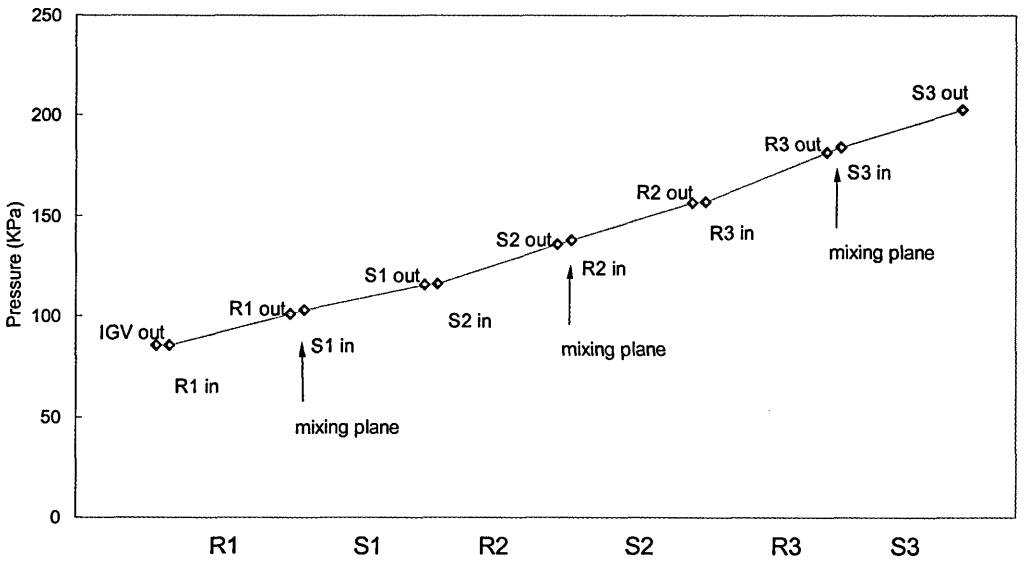

Figure 6-110 Axial variation of area-averaged static pressure at 10.64 Kg/s mass flow

In the plot of Figure 6-110, which presents a graphical illustration of the occurrence of this phenomenon on the HSRC 10.64 Kg/s simulation, it is noticeable how the gradient of the static pressure rise is broadly maintained, and actually exceeded in the rotors, across the mixing-planes zero length. The numerical proportions of this jump are shown in Table 6-6 below. The analysis of the data on this table raises two major comments:

- The pressure jumps in the rotors are some two and a half to three times those of the stators seemingly due to the greater flow direction nonuniformity present in the first of these components.
- Since the pressure jumps are independent of the local pressure and this continuously rises through successive blade rows, the relative importance of the step in the value

reduces in the axial direction.

Inlet P_{static}	Rotor1	Stator1	Rotor2	Stator2	Rotor3	Stator3
Upstream (Pa)	85,745	100,864	115,492	135,638	156,260	183,910
Downstream (Pa)	85,711	102,940	116,229	137,951	157,090	202,584
Jump (Pa)	-35	2075	736	2313	830	2097

Table 6-6 HSRC static pressure jump at mixing-planes – 10.64 Kg/s

The effects of the enforcement of an averaging process at the stage interfaces is also noticeable in the redistribution of the flow angles across the mixing planes, Figure 6-111 to Figure 6-115.

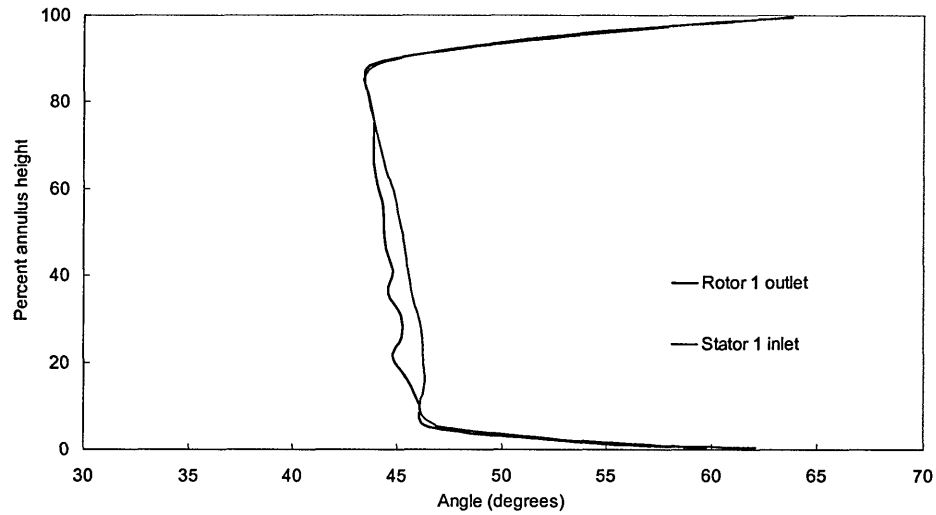

Figure 6-111 Radial distribution of absolute flow angle at the Rotor1/Stator1 interface plane – 10.64 Kg/s

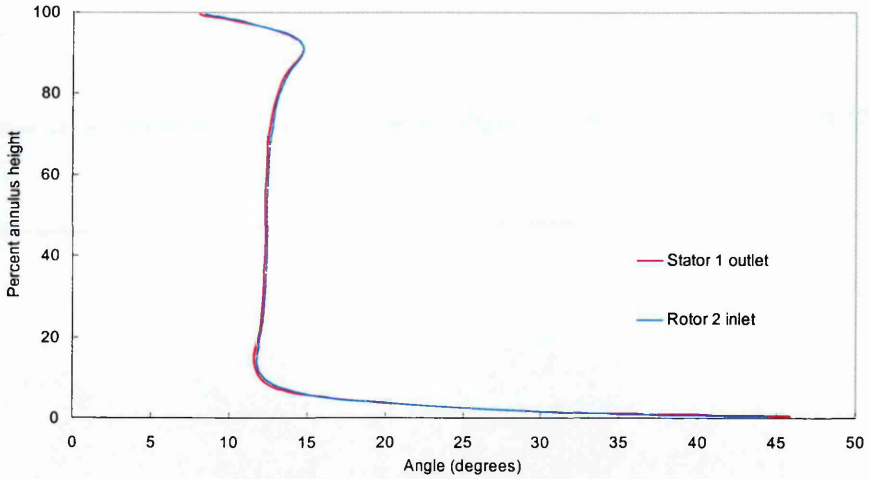

Figure 6-112 Radial distribution of absolute flow angle at the Stator1/Rotor2 interface plane – 10.64 Kg/s

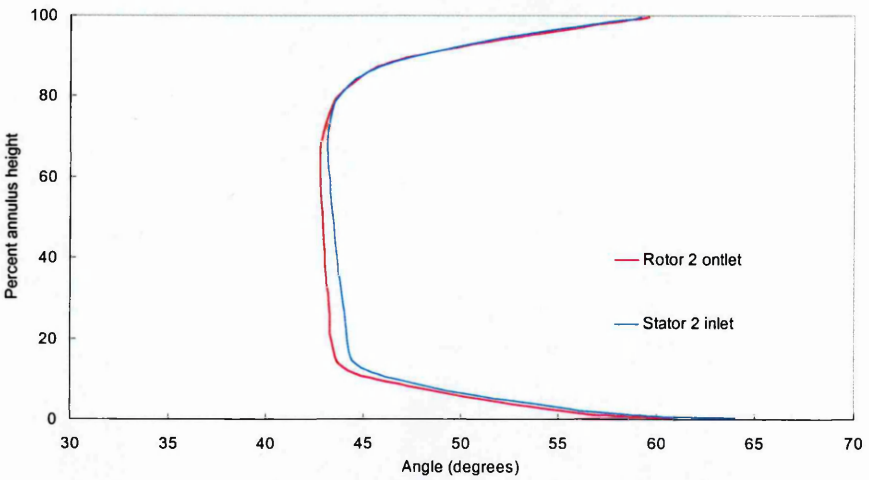

Figure 6-113 Radial distribution of absolute flow angle at the Rotor2/Stator2 interface plane – 10.64 Kg/s

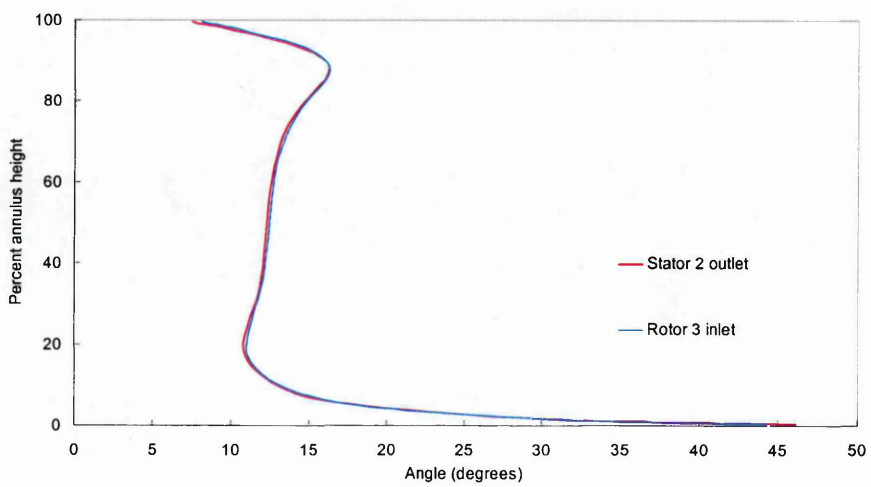

Figure 6-114 Radial distribution of absolute flow angle at the Stator2/Rotor3 interface plane – 10.64 Kg/s

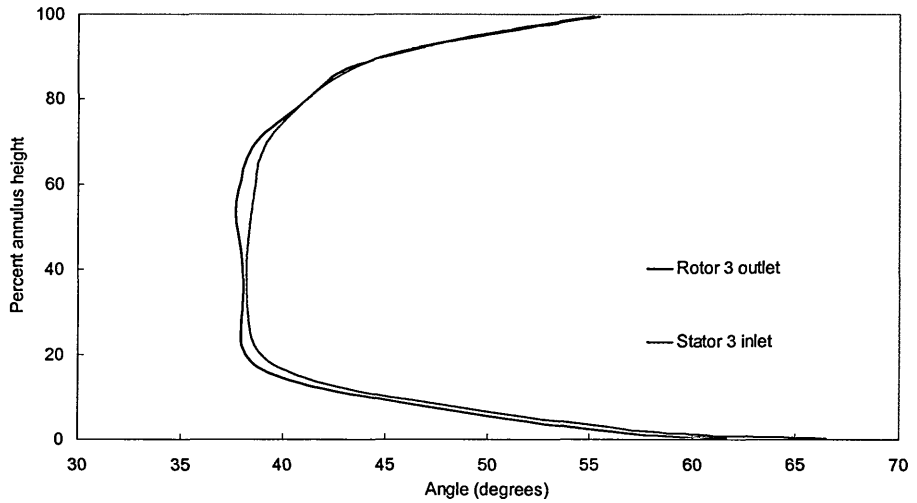

Figure 6-115 Radial distribution of absolute flow angle at the Stator2/Rotor3 interface plane – 10.64 Kg/s

The radial distributions of the pitchwise area-averaged absolute flow angles at the mixing planes follow the pattern already established for the static pressure whereby while both rotors and stators exhibit differences across the planes, it is at the former that these are largest. The magnitude of the angular discrepancies although small, about 1.5 to 3 degrees for rotors and 0.3 to 1.2 degrees for stators is, in percentage terms, larger than that of the corresponding pressure step.

6.4.2 Global performance parameters

The assessment of the effects of the integration of the deterministic stress model source code with the basic solver is done, as will be recalled, on the basis of a common back pressure value but slight mass flows. This point needs to be borne in mind when evaluating the results of the two semi-empirical models given that some of the variation in the results can in effect be due to the slightly altered aerodynamic conditions which apply at the different masses.

The comparison of the global performance parameters is done as for the datum simulations by considering the incremental development of the relevant quantities throughout the compressor. The trend established in the datum simulations between the

9.82 and 10.60 Kg/s points was that to a decrease in the mass flow corresponded an increase in the pressure ratio and therefore the increase in mass brought about by the application of the models ought to have been accompanied by a small decrease in total pressure ratio. In fact the change which is observed with the deterministic stress models is of a small increase which therefore cannot be attributed to the effects of the mass variation from the 9.82 Kg/s point but rather to the effects of the models themselves. Furthermore the rise of the pressure ratio for the new points of 10.05 and 10.06 Kg/s, introduced by the action of the models, is consistent with the predictable trend of that section of the characteristic line, by placing the computed pressure ratios above that of the intended design point, Figure 6-116.

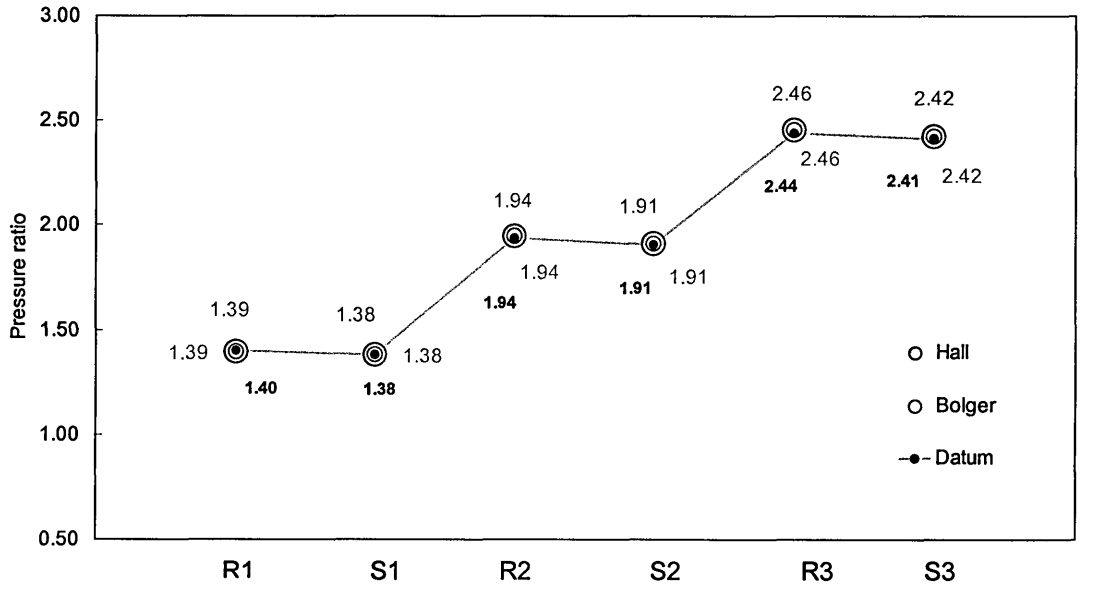

Figure 6-116 Incremental total pressure ratio - deterministic stress models vs datum simulation

The substance of this argument can also be extended to the total temperature ratio calculations, Figure 6-117. Given the closeness of the global results computed from the different sources, these are superimposed in the relevant charts, the degree of concentricity of the marks indicating the level of agreement of the individual points.

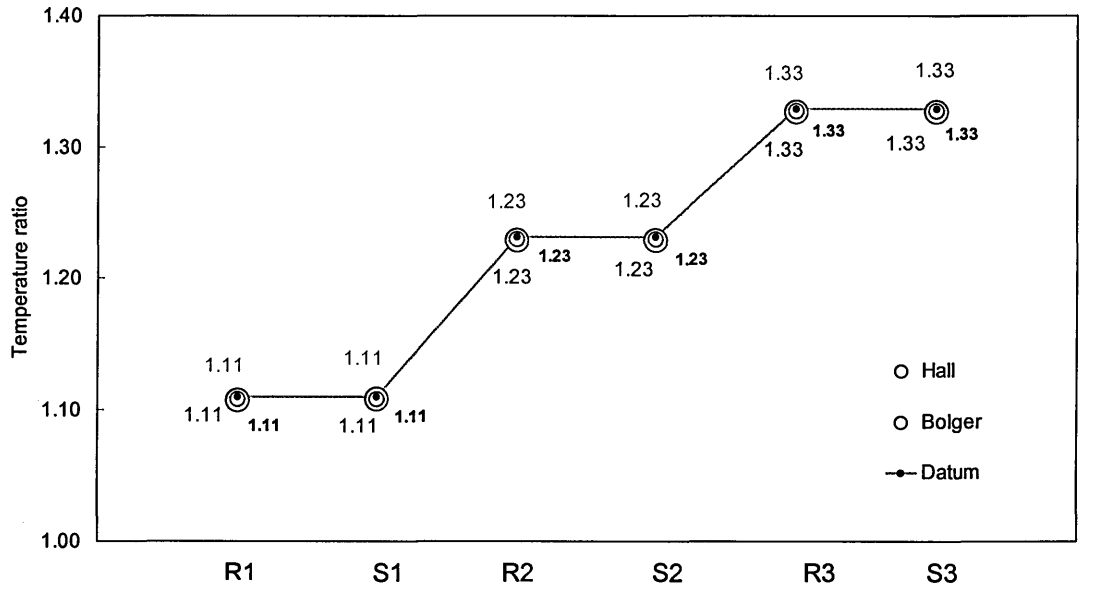

Figure 6-117 Incremental total temperature ratio - deterministic stress models vs datum simulation

The compounded effects of these small but positive changes on the computation of the adiabatic efficiency, is described in Figure 6-118 where it can be seen that the inclusion of the semi-empirical models, contributes some 1 to1.2 percent points to the efficiency value estimated through the basic CFD model.

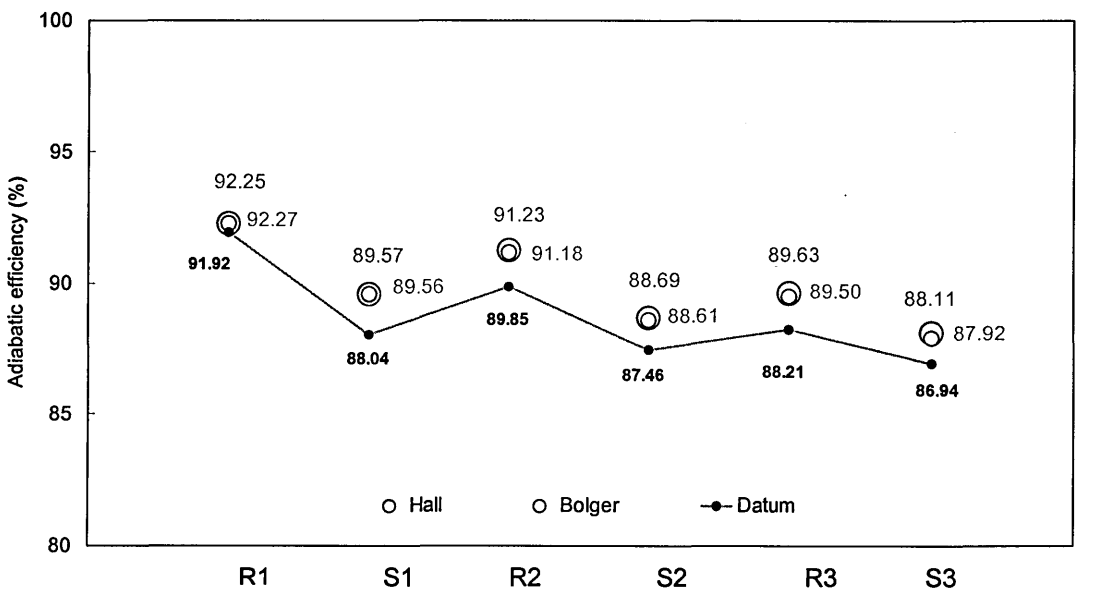

Figure 6-118 Incremental adiabatic efficiency - deterministic stress models vs datum simulation

This increase in the calculated efficiency values is by itself not sufficient to plug the sizeable gap observed previously, about 2.7% at design point, but offers nonetheless a sizeable, around 44 %, reduction in the magnitude of that discrepancy.

6.4.3 Radial distributions

The radial distributions of axial velocity taken upstream of the outlet planes of the whole compressor, the IGV excepted, are presented in Figure 6-119 through to 6-124.

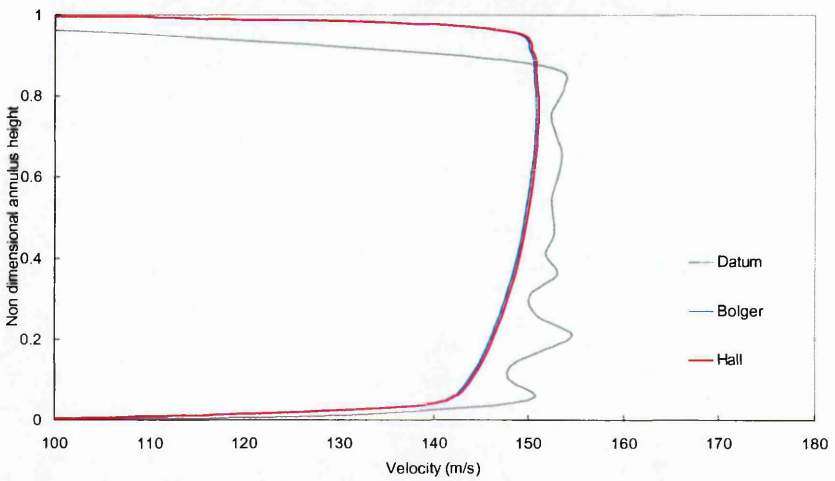

Figure 6-119 Radial distribution of axial velocity at Rotor1/Stator1 interface – deterministic stress models vs datum simulation

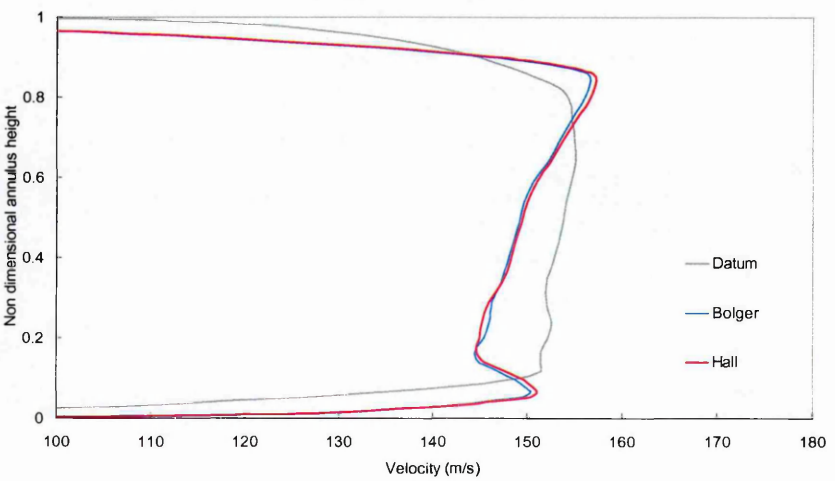

Figure 6-120 Radial distribution of axial velocity at Stator1/Rotor2 interface – deterministic stress models vs datum simulation

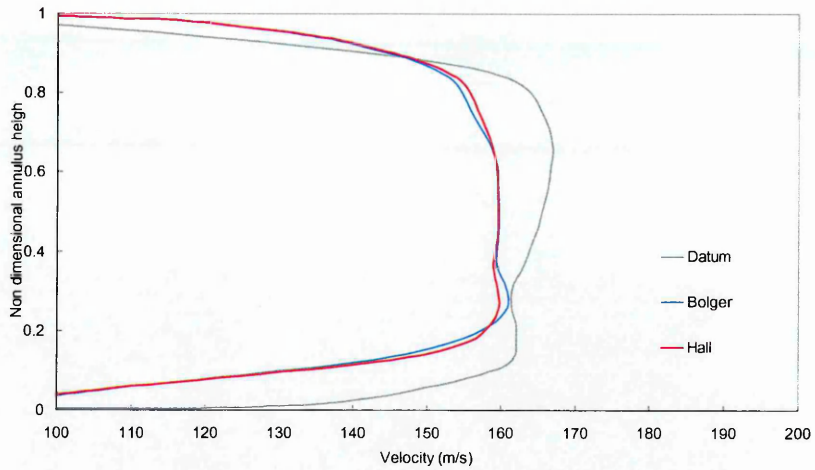

Figure 6-121 Radial distribution of axial velocity at Rotor2/Stator2 interface – deterministic stress models vs datum simulation

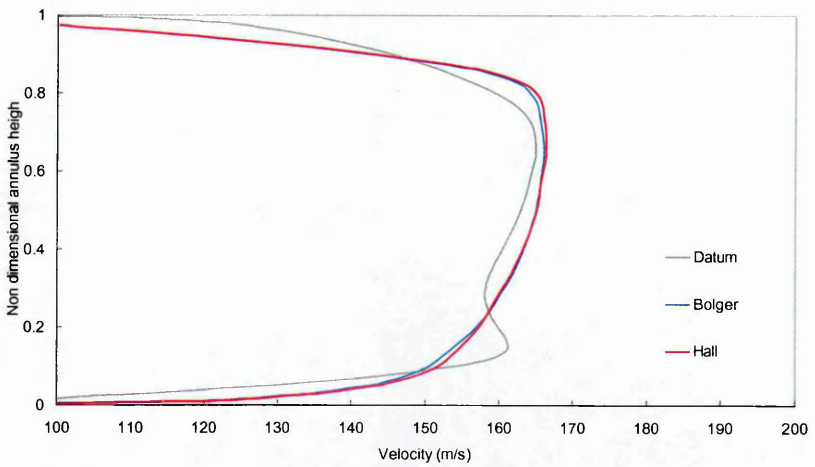

Figure 6-122 Radial distribution of axial velocity at Stator2/Rotor3 interface – deterministic stress models vs datum simulation

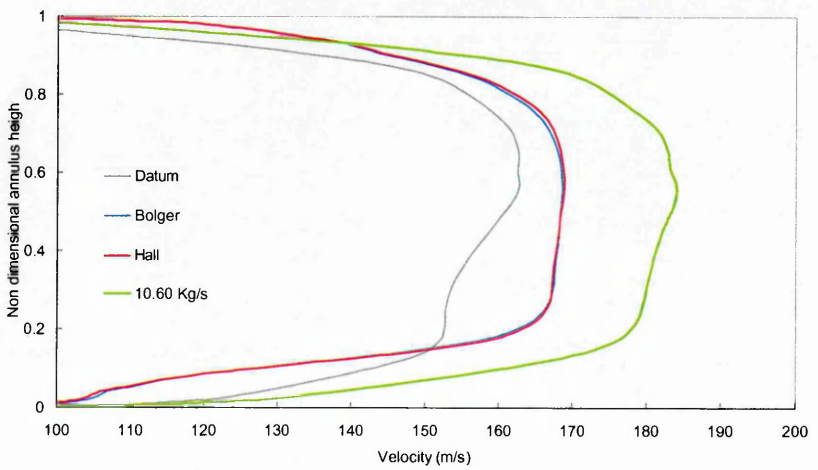

Figure 6-123 Radial distribution of axial velocity at Rotor3/Stator3 interface – deterministic stress models vs datum simulation

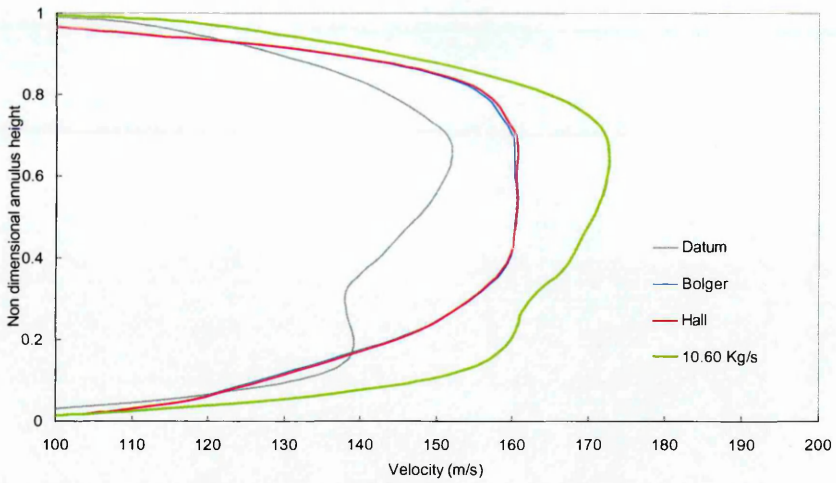

Figure 6-124 Radial distribution of axial velocity at Stator3 outlet plane – deterministic stress models vs datum simulation

The effects of the semi-empirical models on the overall magnitude of the axial speed is in general limited, the third stage excepted, and in some cases such as at the exit plane of Stator2, rather small, Figure 6-122. In terms of the radial profiles however the scene is altogether different as there the impact of the incorporation of the code is rather conspicuous and has a major effect on the rearranging of the velocity distributions and the attending endwall blockage extent.

It is not immediately apparent from the analysis of these plots the precise extent of the endwall blockage, an examination of the Stator 3 outlet plane plot, Figure 6-124, suggesting an increase in the net blocked area but this we have seen disproved by the mass flow increase associated with the two cases. Armed with this note of caution it is possible to say that the deterministic stress models are seen to change the blockage patterns, with the near casing profiles showing a more gradual increase while near the hub there is a variation from rotor to stators.

Overall there is also evidence of an enhanced mixing action leading to a greater radial uniformity in the values of the core flows. In both Figures 6-124 and 6-125 the results of the 10.60Kg/s point have been included so as to give a feeling for the consequence of the mass variation and therefore assist in the evaluation of the changes which are specifically attributable the action of the models.

6.4.4 Qualitative plots

The presentation of the blade-to-blade contour plots of the simulations which include the two models is restricted to the mid-span region.

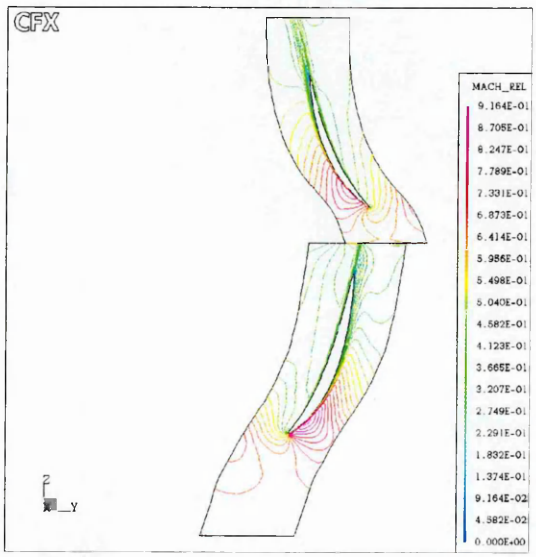

Figure 6-125 Stage 1 relative Mach number at mid-span – Bolger model

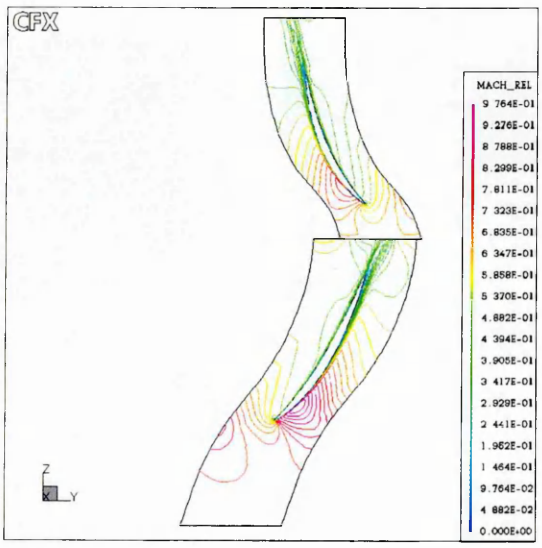

Figure 6-126 Stage 1 relative Mach number at mid-span – Hall model

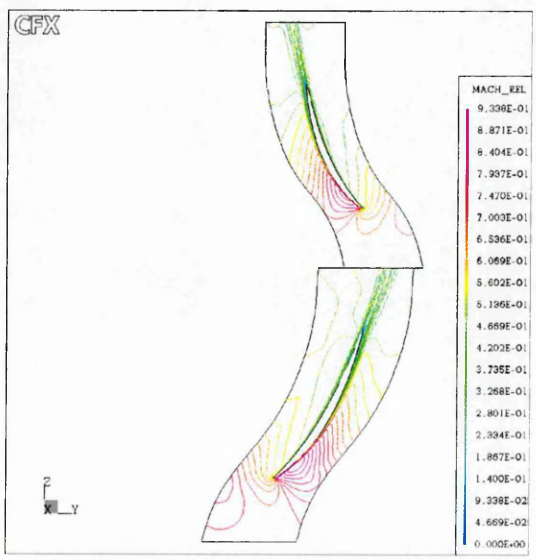

Figure 6-127 Stage 2 relative Mach number at mid-span – Bolger model

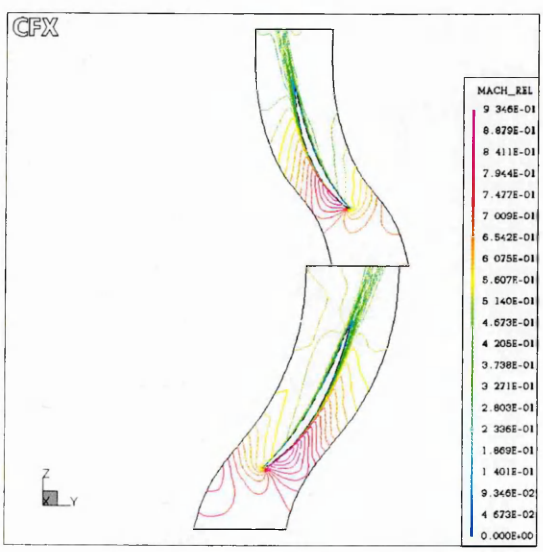

Figure 6-128 Stage 2 relative Mach number at mid-span – Hall model

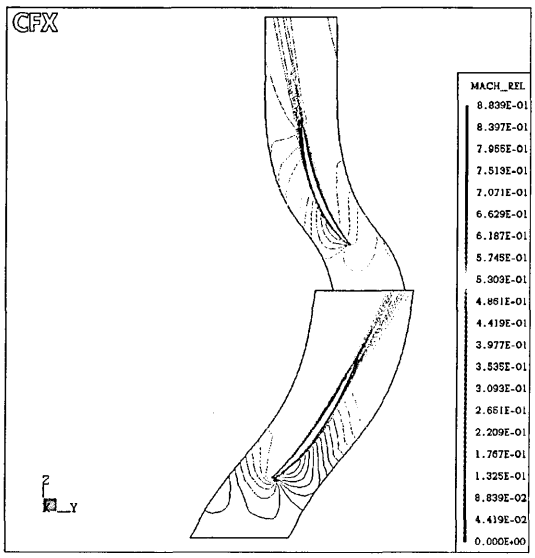

Figure 6-129 Stage 3 relative Mach number at mid-span – Bolger model

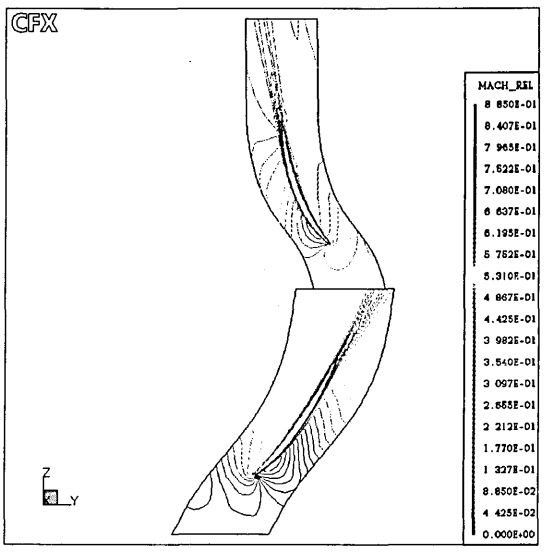

Figure 6-130 Stage 3 relative Mach number at mid-span – Hall model

The plots originating from both models, Figure 6-125 to 6-130, are in general very similar and a comparison between these and the blade-to-blade distributions of the datum simulation, taken to be for this purpose the 9.82 Kg/s point, allows the raising of the following comments:

- The blade wakes are generally slender than those of the datum model
- The blade boundary layers are less developed than those of the datum model

The validity of the comparison is however to some extent compromised by the disparity in mass flow conditions of the model runs and that of the datum and again only a certain amount of these differences can be attributed to the action of the models. The presentation of the passage contour plots at the outlet of the blade domains is made below in Figure 6-131 through to Figure 6-142.

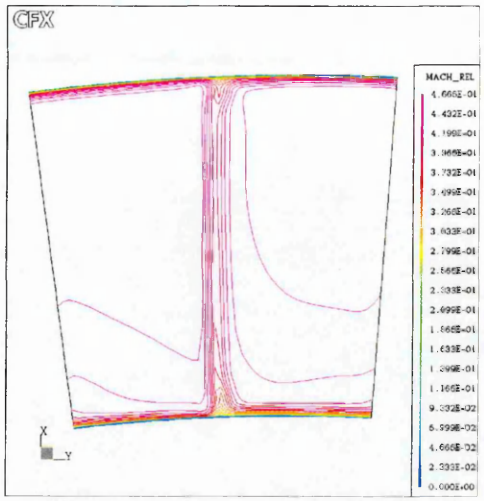

Figure 6-131 IGV outlet relative Mach number- Bolger model

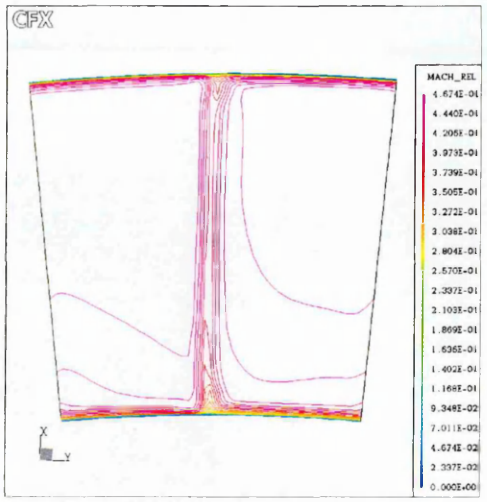

Figure 6-132 IGV outlet relative Mach number- Hall model

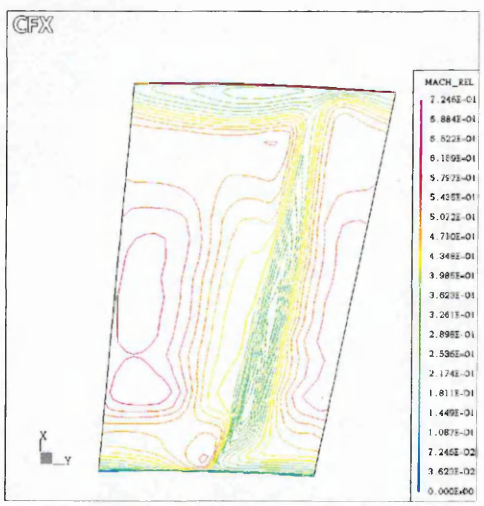

Figure 6-133 Rotor 1 outlet relative Mach number- Bolger model

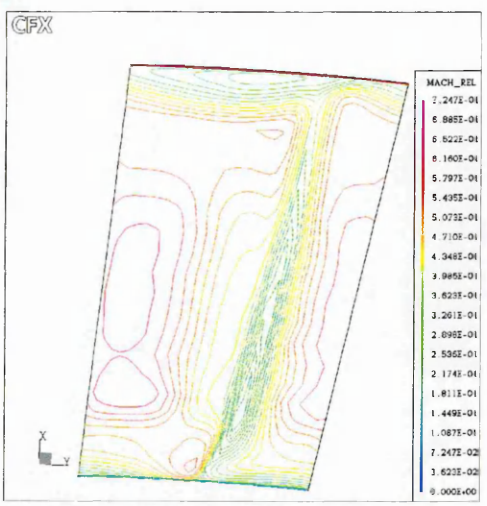

Figure 6-134 Rotor 1 outlet relative Mach number- Hall model

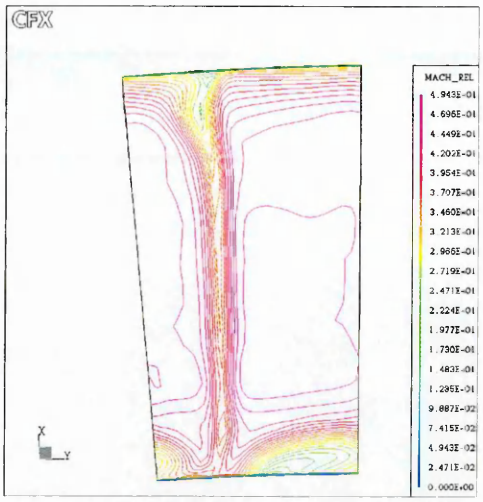

Figure 6-135 Stator 1 outlet relative Mach number- Bolger model

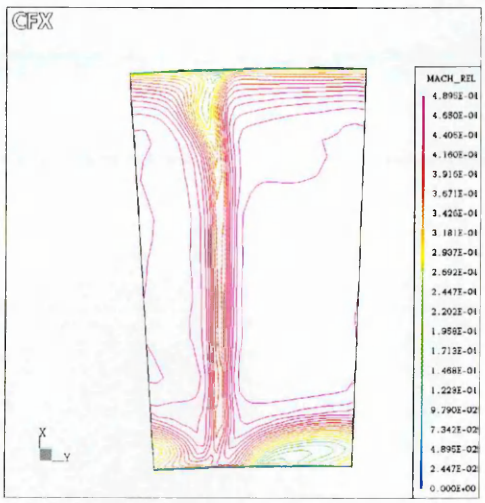

Figure 6-136 Stator 1 outlet relative Mach number- Hall model

Figure 6-137 Rotor 2 outlet relative Mach number- Bolger model

Figure 6-138 Rotor 2 outlet relative Mach number- Hall model

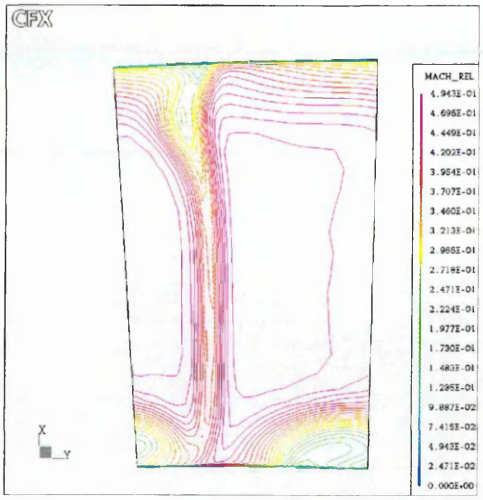

Figure 6-139 Stator 2 outlet relative Mach number- Bolger model

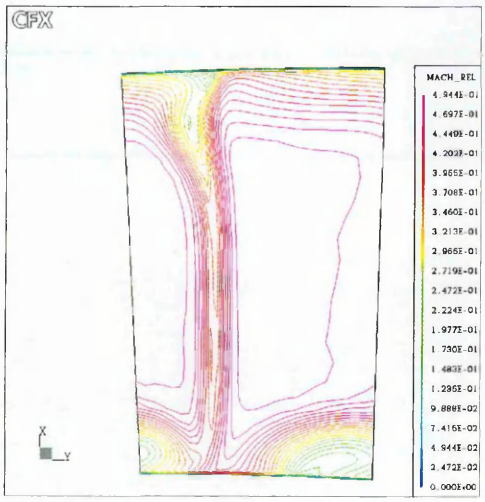

Figure 6-140 Stator 2 outlet relative Mach number- Hall model

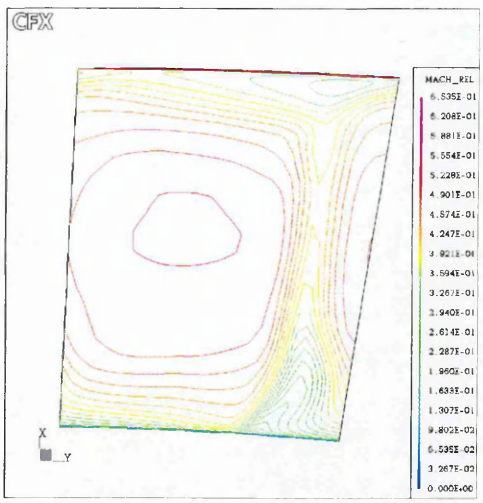

Figure 6-141 Rotor 3 outlet relative Mach number- Bolger model

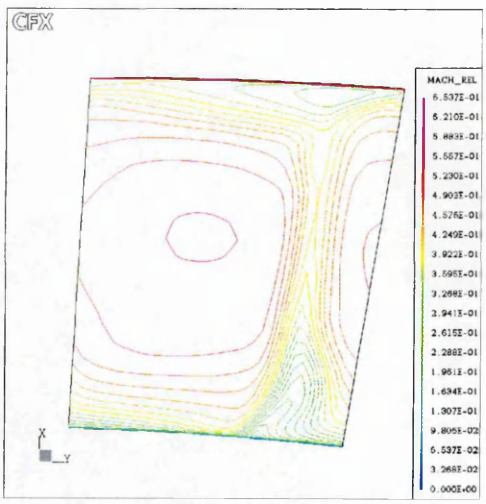

Figure 6-142 Rotor 3 outlet relative Mach number- Hall model

6.5 Closure

This chapter detailed the application of Bolger's and Hall's deterministic stress models to the Cranfield High Speed Research Compressor case. The computational requirements of the inclusion of these models within the TASCflow code are substantial both in terms of solution running space and duration of the run. These problems arise from the inability of the code to employ a parallel solution procedure when coupled to a source term routine which computes values in locations other than the node itself.

The axial separation of the compressor blades, possibly coupled to the wake properties characteristic of the profiles employed, was seen to produce wakes which show a significant non-uniformity at the interface planes. This feature of the case made the application of the conventional formulation of Hall's model impracticable but by combining the deterministic stresses interface calculation method of Bolger with Hall's decay rates, a robust hybrid method was assembled and successfully applied.

The effects on the HSRC case of the application of the models show for the moment a greater impact than that which was previously identified with the HP9 single stage but a fuller appraisal must await more extensive experimental validation in order to establish the exact potential of the models. In terms of integrated overall performance values, where initial experimental data is available, the inclusion of source terms derived from the models offers one third to a half reduction in the discrepancy between these experimental values and the quantities numerically calculated through the basic code approach. However the redistribution of radial properties observed raises some fundamental questions which will require answering as the experimental data becomes available.

Chapter 7

Conclusions and further work suggestions

7.1 Introduction

This Chapter is divided into two distinct but complementary parts, the noting of the conclusions of the project and the suggestion of some ideas which might be exploited through further work.

The generality of the present work is somewhat compromised by the grid sizes employed in the two test cases. It is manifest that none of the results can be seen as grid independent and in some cases such as the unsteady simulations there is evidence that the coarseness of the grid has a marked effect on the quality of the computations.

Nevertheless it is the belief of the author that most of the conclusions are likely to lend themselves to refinement rather than fundamental revision and therefore, although the work is to some extent compromised by the computational limitations of the models its contribution is notwithstanding of practical use.

7.2 Conclusions

The work on the HSRC is presented ahead of any experimental data other than the basic performance data and even this is still subject to a certain degree of uncertainty due to the fact that its was acquired during the early commissioning period of rig. In the absence of experimentally originating data, validation was performed in a limited form against a well established throughflow code and in general good agreement has established wherever the codes offer compatible predictive capabilities, i.e. core flow main trends rather than endwall flow details etc.

The impact of the employment of the deterministic semi-empirical models has been seen to be moderately advantageous but against this benefit, the inordinate cost of its application, mostly due to the inability of running on a parallel mode, has to be carefully outweighed. It is in all probability more cost-effective to run larger mesh cases in a parallel mode than to accept the constraints of a serial solution in single processor for such a marginal gain in solution accuracy.

The axisymmetric grid constraint is furthermore within the TASCflow environment a key restriction to the expedient assembly of meshes, done for example through the Turbogrid mesh generator, besides which it raises problems in terms of cell skew and the attending issues of local accuracy and solution convergence properties.

The evaluation of effectiveness of the semi-empirical deterministic stress models is inseparable from a thorough understanding of the precise averaging process carried out within the code mixing plane formulation. Although for users of TASCflow this information is fairly limited, the fact that the mixing-plane formulation of the code allows for the presence of pitchwise gradients on both sides of the stage interface surface, marks it as an evolved variety of this approach and therefore one which carries a less stringent modelling penalty when compared with simple circumferential averaging.

The general limitations of the mixing plane model are well known, the lack of physical realism of the averaging process with its attending degree of uniformity of pitchwise distributions, to say nothing of the presentation to the downstream row of steady boundary conditions representing a process which is eminently unsteady. Nevertheless the particular treatment of the variables at the interface plane, ranging from simple averaging of flow properties to the formulations which allow circumferential variation of the fluxes on both sides of that plane while enforcing conservation of fluxes, the method employed in the TASCflow code, is known to have an impact on the accuracy of multistage simulations.

It therefore follows that when an author offers a comparison between the results obtained with a mixing plane formulation and with the addition of deterministic stress models, a crucial question must be answered, what is the formulation of the mixing plane used. It is worth at this juncture to return to Dawes and Denton, 1998 where the authors reflect on the fact that it is not clear how much improvement can been obtained by the use a deterministic stress model over a modern mixing plane approach.

The addition of simplistic models to the baseline simulations was shown to add no more than a small contribution to the lost physics of the unsteady stage effects and these, as is demonstrated in the HP9 case though the results of the time-accurate simulations, do not by themselves fill the gap between the computational and experimental results. Even where, as was done with the Rolls-Royce test case, the tri-dimensional deterministic stress field was appended to the baseline steady-state simulation, the addition of these terms could only approximate the results of the average of the time-accurate computations and those of its steady-state equivalent.

The fundamental limitations of simulations which adopt the mixing-plane numerical approach are therefore far more likely to relate to the problems associated with the description of the turbulent phenomena, and in particular its impact on the loss balance sheet of the particular blade row, with the limited means of the models employed for that purpose.

7.3 Further work suggestions

The time span of the research work coupled to subsequent writing-up saw the introduction of a number of improvements in the TASCflow code namely the unsteady formulation, the extension of the solution to a parallel architecture and latterly the addition of an LES capability. The fruitful exploitation of these combined features calls for large computational resources well in excess of what has been previously available in the university. This situation is nevertheless about to be significantly modified with the involvement of Cranfield and Cambridge universities in the partnership of a very large, several hundred processor computer located in the second of these institutions.

This expansion of the resources will enable the revisiting of some of the cases run for the present work while enabling the acquisition of a potentially changed outlook on the cases specifically in terms of the capture of unsteady flow features, and their measurable effects in terms of performance effects.

Specifically it is proposed that employing the HP9 geometry the following work be conducted:

- Extension of the unsteady investigation to more realistic mesh densites in order to re-evaluate the steady-state/average-of-the-unsteady level of agreement while departing from a platform of grid-independence or nearly so. It is not altogether inconceivable that the results of such an investigation might offer a different perspective on the level of agreement established in the present work given its manifest and acknowledged limitations.

Making use of the HSRC case:

- Simulation of a computational equivalent of the Poensgen and Gallus experimental work described in Chapter 4 and depicted below as Figure 7-1.

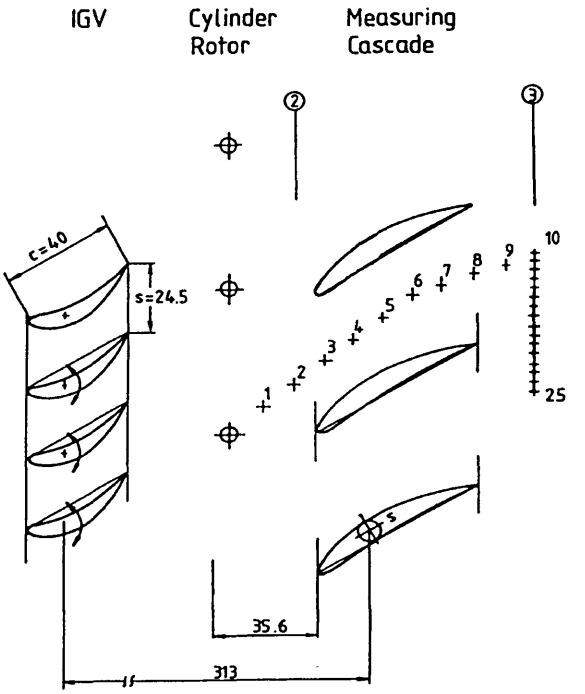

Figure 7-1 Poensgen and Gallus, 1990, wake decay investigation method

This study could be conducted over several stage combinations, Rotor1- Stator1-Rotor2, Stator1-Rotor2-Stator2, etc. The use of a practical configuration, employing actual blades geometries rather than cylinders as done in Poensgen's work can supply valuable information on the occurrence, or otherwise, of Hall's 'apparent wake' over different blade row combinations. A broadening of this research might possibly include the effects of 3-D blading on the features of the 'apparent wake'. This work could be complemented with a similar investigation employing for example the LSRC on order to contrast the high and low speed cases.

- A common critique of multistage simulations is that whatever errors are introduced by individual mixing planes these tend to accumulate in downstream rows leading to a progressive degeneration of the quality of the solution as one progresses trough the machine. Seen from this perspective it would be desirable to secure the best possible evaluation of the interface quantities of the different stages through the successive time-accurate analysis of those planes.

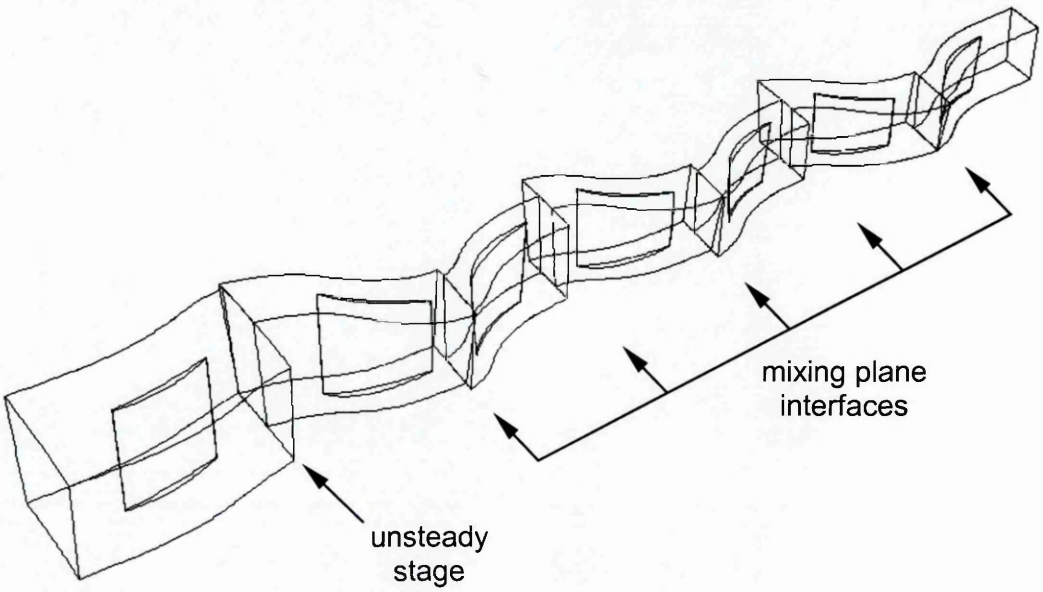

Figure 7-2 Proposed HSRC investigation scheme

The arrangement of Figure 7-2 is representative of the initial step of one such simulation. For the following step the unsteady stage would move downstream and a mixing plane formulation be made to replace the vacated location. A useful amount of information could be acquired through this method on the particular interaction effects of the separate blade rows within their embedded context, produce steady averages at the interfaces for comparison with the steady-state calculation and as the final goal simultaneously inject the appropriate steady average values at all the interface locations though the source term interface. This exercise has the capability to offer an assessment of the cumulative errors as well as an improved flow description of the compressor particularly if coupled to LES.

Equally the successive unsteady simulation of all stages enables the acquisition of information on the variation of the deterministic stress fields as one progresses downstream in the machine.

As a complement of the work outlined above the two following points are also proposed:

- Experimental acquisition of unsteady data, possibly using hot-wire and/or laser anemometry, leading to the assembly of deterministic stress plots of the compressor's inter blade row planes in order to enable validation of numerical models.

- Exploration of the principle that for research compressors, unsteady CFD simulation needs can be, whenever possible and consistent with accepted design practice, accommodated through the provision of minimum common integer pitch ratios for blade counts .

References

Adamczyk, J. (1985). Model Equation for Simulating Flows in Multistage Turbomachinery. ASME Paper 85-GT-226.

Adamczyk, J. (1992). Unsteady Aerodynamic Interaction Effects on Turbomachinery Blade Life and Performance. AIAA Paper 92-0149.

Adamczyk, J., Mulac, R. And Celestina, M. (1986). A Model for Closing the Inviscid Form of the Average-Passage Equation System. ASME Paper 86-GT-227. ASME *Journal of Turbomachinery*, Vol.108, No. 2, 180-186.

Adamczyk, J., Celestina, M., Beach, T. And Barnett, M. (1989). Simulation of Three-Dimensional Viscous Flow Within a Multistage Turbine. ASME Paper 89-GT-152. ASME *Journal of Turbomachinery*, Vol. 112, No. 3, 370-376.

Adamczyk, J. (1996). Wake Mixing in Axial Flow Compressors. ASME Paper 96-GT-29.

Adamczyk, J., Celestina, M. and Chen, J. (1994). Wake-Induced Unsteady Flows: Their Impact on Rotor Performance and Wake Rectification.
ASME Paper 94-GT-219.

Addison, J. and Hodson, H. (1992). Modeling of Unsteady Transitional Boundary Layers. ASME Paper 91-GT-282.

Adkins, G. G. and Smith, L. H. (1982). Spanwise Mixing in Axial-Flow Turbomachines. ASME *Journal of Engineering for Power*, No 104, 97-110

Arnone, A. and Bienvenuti, E. (1994). Three-Dimensional Navier-Stokes Analysis of a Two-Stage Gas Turbine. ASME Paper 94-GT-88

Arnone, A., Carnevale, E. and Marconcini, M. (1997). Grid Dependency Study for the Nasa Rotor 37 Compressor Blade. ASME Paper 97-GT-384.

Arnone, A. and Pacciani, R. (1995). Rotor-Stator Interaction Analysis Using the Navier-Stokes Equations and a Multigrid Method. ASME Paper 95-GT-177.

Baghdadi, S. (1995). Modelling Tip Clearance Effects in Multi-Stage Axial Compressors. ASME Paper 95-GT-291.

Barankiewicz, W. and Hathaway, M. (1997). Effects of Stator Indexing on Performance in a Low Speed Multistage Axial Compressor. ASME Paper 97-GT-496

Baldwin, B. S. and Barth, T. J. (1991). A One-Equation Turbulence Transport Model for High Reynolds Number Wall-Bounded Flows. AIAA Paper 91-0610.

Baldwin, B. S. and Lomax, H. (1978). Thin-Layer Approximation and Algebraic Model for Separated Turbulent Flows. AIAA Paper 78-257.

Biesinger, T., Savill, A. and Coupland, J.(1998). Refined k-ε Turbulence Model Q3D-Predictions in Compressor Cascades at Design and Off-Design. ASME Paper 98-GT-322.

Birch, S. F. (1995). One Equation Models Revisited. AIAA Paper 92-2903.

Blaha, C., Hennecke, D., Fritsch, G., Hoeger, M. and Beversdorff, M. (1997). Laser-2-Focus Measurements in a Transonic Compressor Blisk-Rotor and Comparison with 3D Numerical Simulations. ISABE Paper 97-7069. *Proceedings of the Thirteenth International Symposium on Air Breathing Engines*, 7-12 September 1997, Chattanooga, Tennessee,USA, 484-493.

Bolger, J. and Horlock, J. (1995). Predictions of the Flow in Repeating Stages of Axial Compressors Using Navier-Stokes Solvers. ASME Paper 95-GT-199.

Broichhausen, K. (1994). Aero Design of Turbomachinery Components – CFD in Complex Systems. published in *Turbomachinery Design Using CFD*. AGARD LS-195.

Busby, J., Sondak, D., Staubach, B. and Davis, R. (1999). Deterministic Stress Modeling of Hot Gas Segregation in a Turbine. ASME Paper 99-GT-76.

Camp, T. R. and Shin, H.-W. (1994). Turbulence Intensity and Length Scale Measurements in Multistage Compressors. ASME Paper 94-GT-4.

Chen, S.and Prueger, G. (1993). Multistage Turbomachinery Flow Solutions Using Three-Dimensional Implicit Euler Method. AIAA Paper 93-2382.

Chima, R. (1998). Calculation of Multistage Turbomachinery Using Steady Characteristic Boundary Conditions. AIAA Paper 98-0968.

Choi, D., Sabnis, J. S. and Barber, T. J. (1994). Application of an RNG k-ε Model to Compressible Turbulent Shear Layers . AIAA Paper 94-0188.

Coakley, T. J. (1983). Turbulence Modeling Methods for the Compressible Navier-Stokes Equations. AIAA Paper 83-1693.

Copenhaver, W., Hah, C. and Puterbaugh, S. (1992). Three-Dimensional Flow Phenomena in a Transonic, High-Throughflow, Axial-Flow Compressor Stage. ASME Paper 92-GT-169. ASME *Journal of Turbomachinery*, Vol. 115, No. 2, 240-248.

Cumpsty, N. A. (1989). *Compressor Aerodynamics*. Longman, London.

Cumpsty, N., Dong, Y. and Li, Y. (1995). Compressor Blade Boundary Layers in the Presence of Wakes. ASME Paper 95-GT-443.

Davis, R. L., Shang, T., Buteau, J. and Ni, R.-H. Prediction of 3D Unsteady Flow in Multistage Turbomachinery Using an Implicit Dual Time-Step Approach. AIAA Paper 96-2565.

Dawes, W. N. (1990). Toward Improved Throughflow Capability: The Use of Three-Dimensional Viscous Flow Solvers in a Multi-Stage Environment. ASME Paper 90-GT-18. ASME *Journal of Turbomachinery*, Vol. 114, No. 1, 8-17.

Dawes, W. N. (1991). Multi-Blade Row Navier-Stokes Simulations of Fan-Bypass Configurations. ASME Paper 91-GT-148.

Dawes, W. N. (1995). Unsteady Flow and Loss Production in Centrifugal and Axial Compressor Stages. published in *Aerodynamic Losses in Turbomachines*. AGARD CP-571.

Dawes, W. and Denton, J. (1998). CFD for Turbomachinery Design. Proceedings of the seminar *The Successful Exploitation of CFD in Turbomachinery Design*, IMechE, 19 March 1998, London, Paper 1.

Denton, J. (1985). The Calculation of Fully Three-Dimensional Flow Through Any Type of Turbomachine Blade Row. Paper 9, AGARD LS-140.

Denton, J. (1990). The Calculation of Three-Dimensional Viscous Flow Through Multi-Stage Turbomachines. ASME Paper 90-GT-19. ASME *Journal of Turbomachinery*, Vol. 114, No. 1, 18-26.

Deregel, P. And Tan, C. (1996). Impact of Rotor Wakes on Steady-State Axial Compressor Performance. ASME Paper 96-GT-253.

Dimmock, N. A. (1963). *A Compressor Routine Test Code*. HMSO, London.

Dorney, D. J. and Mosebach, A. (1996). A Parametric Study of the Effects of Unsteady Wake Passing on the Flow Field in a Compressor Cascade. AIAA Paper 96-2567.

Dorney, D. and Sharma, O. (1996). Evaluation of Flow Field Approximations for Transonic Compressor Stages. ASME Paper 96-GT-371.

Dorney, D., Sharma, O. and Gundy-Burlet, K. (1998). Physics of Airfoil Clocking in a High Speed Axial Compressor. ASME Paper 98-GT-82.

Dorney, D. J. and Schwab, J. R. (1995). Unsteady Numerical Simulations of Radial Temperature Profile Redistribution in a Single-Stage Turbine. ASME Paper 95-GT-178.

Dring, R. and Spear, D. (1990). The Effects of Wake Mixing on Compressor Aerodynamics. ASME Paper 90-GT-132. ASME *Journal of Turbomachinery*, Vol. 113, No. 4 , 600-607.

Dring, R., VanSeters, R. and Zacharias, R. (1993). A Three-Dimensional Navier-Stokes Calculation Applied to an Axial Compressor Rotor and Stator. ASME Paper 93-GT-113.

Dunham, J. and Meauzé, G. (1998). An AGARD Working Group Study of 3D Navier-Stokes Codes Applied to Single Turbomachinery Blade Rows. ASME Paper 98-GT-50.

Eckardt, D. (1986). Advanced Experimental Techniques for Turbomachinery Development. published in *Advanced Experimental Techniques in Turbomachinery*, editor David Japikse, Concepts ETI, Norwich, VM, USA.

Elmendorf, W., Mildner, F., Röper, R., Krüger, U.and Kluck, M. (1998). Three-Dimensional Analysis of a Multistage Compressor Flow Field. ASME Paper 98-GT-249.

Erdos, J. I., Alzner, E. and McNally, W. (1977). Numerical Solution of Periodic Transonic Flow Through a Fan Stage. AIAA *Journal*, Vol. 15, No. 11, 1559-1568.

Escudier, M. P. and Spalding, D. B. (1966). A Note on the Turbulent Uniform-Property Hydrodynamic Boundary Layer on a Smooth Impermeable Wall Comparisons of Theory with Experiment. ARC/CP-875, HMSO, London

Eulitz, F. and Engel, K. (1997). Numerical Investigation of Wake Interaction in a Low Pressure Turbine. AIAA Paper 97-3027.

Eulitz, F., Engel, K. and Pokorny, S. (1995). Numerical Investigation of Inviscid and Viscous Interaction in a Transonic Compressor. published in *Aerodynamic Losses in Turbomachines*. AGARD CP-571.

Fleeger, D and Seyb, N. (1975). On the Measurement of the Fluctuating Total and Static Pressures in Turbomachines Including the Determination of Correct Time-Weighted Pressures. published in *Modern Methods of Testing Rotating Components of Turbomachines (Instrumentation)*. AGARD AG-207

Fritsch, G. and Giles, M. (1993). An Asymptotic Analysis of Mixing Loss. ASME Paper 93-GT-345. ASME *Journal of Turbomachinery*, Vol. 117, No. 3, 367-374.

Gallimore, S. J. (1998). Axial Flow Compressor Design. Proceedings of the seminar *The Successful Exploitation of CFD in Turbomachinery Design*, IMechE, 19 March 1998, London, Paper 5.

Gallimore, S. and Cumpsty, N. (1986). Spanwise Mixing in Multistage Axial Flow Compressors: Part I - Experimental Investigation. ASME Paper 86-GT-20.

Gallus, H. and Hoenen, H. (1986). Experimental Investigations of Airfoil- And Endwall Boundary Layers in a Subsonic Compressor Stage. ASME Paper 86-GT-143.

Galpin, P. F. and Raithby, G. D. (1986). Numerical Solution of Problems in Incompressible Fluid Flow: Treatment of the Temperature-Velocity Coupling. *Journal of Numerical Heat Transfer*, Vol. 10, pp. 105-129.

Gerolymos, G. A.and Hanisch, C. (1999). Interaction Effects Between Blade Rows in Turbomachines. IMechE *Proceedings*, Vol. 213, Part A, pp 243-261.

Gerolymos, G. A., Vinteler, D., Haugeard, R., Tsanga, G. and Vallet, I. (1996). On the Computation of Unsteady Turbomachinery Flows Part2 – Rotor/Stator Interaction using Euler Equations. published in *Aerodynamic Losses in Turbomachines*. AGARD CP-571.

Giles, M. B. (1988). Stator/Rotor Interaction in a Transonic Turbine. AIAA Paper 88-3093. AIAA *Journal of Propulsion and Power*, Vol. 6, No. 5, 621-627.

Giles, M. B. (1988). UNSFLO: A Numerical Method for Unsteady Inviscid Flow in Turbomachinery. Massachusetts Institute of Technology GTL Report 195.

Giles, M. B. (1990). Non-refecting Boundary Conditions for Euler Equation Calculations, AIAA *Journal*, Vol. 28, No. 12, 2025-2058.

Giles, M. B. (1992). An Aproach for Multistage Calculations Incorporating Unsteadiness. ASME Paper 92-GT-282.

Giles, M. B. (1998). Some Thoughts on Exploiting CFD for Turbomachinery Design. Proceedings of the seminar *The Successful Exploitation of CFD in Turbomachinery Design*, IMechE, 19 March 1998, London, Paper 2.

Gorrell, S., Copenhaver, W. and Chriss, R. (1997). Effects of Upstream Wakes on the Performance of a Transonic Compressor Stage. ISABE Paper 97-7070. *Proceedings of the Thirteenth International Symposium on Air Breathing Engines*, 7-12 September 1997, Chattanooga, Tennessee,USA, 494-501.

Goto, A. (1991). Three-Dimensional Flow and Mixing in an Axial Flow Compressor with Different Rotor Tip Clearances. ASME Paper 91-GT-89.

Goulas, A. and Stapountzis, H. (1997). Study of the Interaction Between a Boundary Layer and a Moving Wake on the Pressure side of a Blade. ISABE Paper 97-7185. *Proceedings of the Thirteenth International Symposium on Air Breathing Engines*, 7-12 September 1997, Chattanooga, Tennessee,USA, 1369-1377.

Goyal, R. and Dawes, W. (1992). A Comparison of the Measured and Predicted Flow Field in a Modern Fan-Bypass Configuration. ASME Paper 92-GT-298. ASME *Journal of Turbomachinery*, Vol. 115, No. 2, 273-282.

Gundy-Burlet, K. and Dorney, D. (1997). Investigation of Airfoil Clocking and Inter-Blade-Row Gaps in Axial Compressors. AIAA Paper 97-3008.

Hah, C., Puterbaugh, S. L. and Copenhaver, W. W. (1997). Unsteady Aerodynamic Flow Phenomena in a Transonic Compressor Stage. AIAA Paper 93-1868. *Journal of Propulsion and Power*, Vol. 13, No. 3, 329-333.

Haig, L. B. (1960). A Design Procedure for Thermocouple Probes. ASE Paper I58C. presented at the *SAE National Aeronautic Meeting*, 5-8 April 1960, New York.

Hall, E. (1997a). Aerodynamic Modelling of Multistage Compressor Flowfields - Part 1: Analysis of Rotor/Stator/Rotor Aerodynamic Interaction. ASME Paper 97-GT-344.

Hall, E. (1997b). Aerodynamic Modelling of Multistage Compressor Flowfields - Part 2: Modelling Deterministic Stresses. ASME Paper 97-GT-345.

Hall, E. J. and Delaney, R. A. (1995). Investigation of Advanced Counterrotation Blade Configuration Concepts for High Speed Turboprop Systems: Task VII – ADPAC User's Manual. NASA CR 195472.

Halstead, D., Wisler, D.,Okiishi, T., Walker, G., Hodson, H. and Shin, H-W. (1995a). Boundary Layer Development in Axial Compressors and Turbines Part 1 of 4: Composite Picture. ASME Paper 95-GT-461.

Halstead, D., Wisler, D.,Okiishi, T., Walker, G., Hodson, H. and Shin, H-W. (1995b). Boundary Layer Development in Axial Compressors and Turbines Part 2 of 4: Compressors. ASME Paper 95-GT-462.

Halstead, D., Wisler, D.,Okiishi, T., Walker, G., Hodson, H. and Shin, H-W. (1995c). Boundary Layer Development in Axial Compressors and Turbines Part 4 of 4: Computations and Analyses. ASME Paper 95-GT-464.

Heidrick, T. R. (1986). Pressure and Velocity Measurements. published in *Advanced Experimental Techniques in Turbomachinery*, editor David Japikse, Concepts ETI, Norwich, VM, USA.

Heneka, A. and Bubeck, H. (1939). Measuring Errors of Pneumatic Multi-Hole-Probes. ITSM – Universität Stuttgart, BRD.

Ho, Y.-H. and Lakshminarayana, B. (1993). Computation of Unsteady Viscous Flow Through Turbomachinery Blade Row Due to Uostream Rotor Wakes. ASME Paper 93-GT-321.

Huber, F. and Ni, R. (1989). Application of a Multi-Stage 3-D Euler Solver to the Design of Turbines for Advanced Propulsion Systems. AIAA Paper 89-2578.

Ivey, P. C. and Swoboda, M. (1998). Leakage effects in the rotor tip-clearance region of a multistage axial compressor, Part I: Innovative measurements. ASME Paper 98-GT-591.

Izsak, M. and Chiang, H-W. (1993). Turbine and Compressor Wake Modeling for Blade Forced Response. ASME Paper 93-GT-236.

Jameson, A. (1991). Time Dependent Calculations Using Multigrid with Applications to Unsteady Flows Past Airfoils and Wings. AIAA Paper 91-1596.

Japikse, D. (1986). Solving 100 Turbomachinery Fluid Dynamic Test Problems. published in *Advanced Experimental Techniques in Turbomachinery*, editor David Japikse, Concepts ETI, Norwich, VM, USA.

Jennions, I. and Adamczyk, J. (1995). Evaluation of the Interaction Losses in a Transonic Turbine HP Rotor / LP Vane Configuration. ASME Paper 95-GT-299.

Jones, W. P. and Launder, B. E. (1973). The Calculation of Low Reynolds Number Phenomena with a Two-Equation Model of Turbulence. ASME *Journal of Heat and Mass Transfer*, Vol. 16, 1119.

Jorgenson, P. C. and Chima, R. (1988). An explicit Runge-Kutta Method for Unsteady Rotor-Stator Interaction. AIAA Paper 88-GT-0049.

Kerrbrock, J.and Mikolajczak, A. (1970). Intra-Stator Transport of Rotor Wakes and its Effect on Compressor Performance. ASME Paper 70-GT-39.

Kirtley, K. (1991). An Algebraic RNG-Based Turbulence Model for Three-Dimensional Turbomachinery Flows. AIAA Paper 91-0172.

Krain, H. (1989). A Study on Centrifugal Impellor and Diffuser Flow. ASME Paper 81-GT-9.

Kwon, O and Ames, F. E. (1995). Advanced k–epsilon Modeling of Heat Transfer. NASA CR-4679, Lewis Research Center, USA.

Lacor, C. (1999). Solving the Reynolds Averaged Navier-Stokes Equations. *Industrial Computational Fluid Dynamics* lecture series, Von Karman Institute for Fluid Dynamics, Brussels.

Lakshminarayana, B. and Davino, R. (1979). Mean Velocity and Decay Characteristics of the Guidevane and Stator Blade Wake of an Axial Flow Compressor. ASME Paper 79-GT-9.

Lee, Y., Hah, C. and Loellbach, J. (1994). Flow Analyses in a Single-Stage Propulsion Pump. ASME Paper 94-GT-139. ASME *Journal of Turbomachinery*, Vol. 118, No. 2, 240-249.

LeJambre, C., Zacharias, R., Biederman, B., Gleixner, A. and Yetka, C. (1995). Development and Application of a multistage Navier-Stokes Flow Solver Part II: Application to a High Pressure Compressor Design. ASME Paper 95-GT-343.

Leonard, B. P. (1979). A Stable and Accurate Convective Modeling Procedure Based on Quadratic Upstream Interpolation. *Computational Methods Applied to Mechanical Engineering.*, vol. 19, 59-98.

Lesage, F. and Raw, M. J. (1992). Computational Fluid Dynamic Applications of a Navier-Stokes Code in External Ballistics. AIAA Paper 92-0637.

Lyes, P. A. (1999). *Low-Speed Axial Compressor Design and Evaluation:High Speed Representation and Endwall Flow Control Studies.* Cranfield University PhD Thesis.

Lyes, P. A. and Ginder, R. B. (1998). Low-Speed Compressor Tests for Code Validation and for Simulating High-Speed Designs.

Leylek, J. and Wisler, D. (1990). Mixing in Axial-Flow Compressors: Conclusions Drawn From Three-Dimensional Navier-Stokes Analyses and Experiments. ASME Paper 90-GT-352. ASME *Journal of Turbomachinery*, Vol. 113, 161-179.

Liamis, N., Bacha, J. L. and Burgaud, F. (1995). Numerical Simulations of Stator-Rotor Interactions on Compressor Blade Rows. published in *Aerodynamic Losses in Turbomachines.* AGARD CP-571.

Liu, B, Moore, J. G. and Moore, J. (1998). Total Unsteadiness Analysis for an Axial-Flow Compressor Rotor. AIAA Paper 98-0967.

Lockwood, C. (1999). *Comparison of average-passage equation closures through simulation of single & multi-row axial compressors; the limitations of using a commercial CFD code.* Cranfield University PhD Thesis.

Majjigi, R. K. and Gliebe, P. R. (1984). Development of a Rotor Wake/V0rtex Model. NASA CR 174849.

Mathieu, J. and Scott, J. (2000). *An Introduction to Turbulent Flow.* Cambridge University Press, Cambridge.

Menter, F. R. (1993). Zonal Two Equation k-ω Turbulence Models for Aerodynamic Flows. AIAA Paper 93-2906.

Michelassi, V., Martelli, F., Dénos, R., Arts, T. and Sieverding, C. H. (1998). Unsteady Heat Transfer in Stator-Rotor Interaction bt Two Equation Turbulence Model. ASME Paper 98-GT-243

Miller, C. and Podbody, G. (1990). Euler Analysis Comparison With LDV Data for an Advanced Counter-Rotation Propfan at Cruise. AIAA Paper 90-0438.

Mohammadi, B and Pironneau, O.. (1994). *Analysis of the k-Epsilon Turbulence Model.* Wiley, Chichester.

Mulac, R. and Adamczyk, J. (1991). The Numerical Simulation of a High-Speed Axial Flow Compressor. ASME Paper 91-GT-272. ASME *Journal of Turbomachinery*, Vol. 114, No. 3, 517-527.

Mulac, R., Celestina, M., Adamczyk, J., Misegades, K. and Dawson, J. (1987). The Utilization of Parallel Processing in Solving the Inviscid Form of the Average-Passage Equation System for Multistage Turbomachinery. AIAA Paper 87-1108.

Mulac, R., Schneider, J. and Adamczyk, J. (1989). Average-Passage Simulation of Counter-Rotating Propfan Propulsion Systems as Applied to Cruise Missiles. AIAA Paper 89-2943.

Ni, R. and Bogoian, J. (1989). Prediction of 3-D Multi-Stage Turbine Flow Field Using a Multiple-Grid Euler Solver. AIAA Paper 89-0203.

Ning, F. and Xu, L. (2001). Numerical Investigation of Transonic Compressor Rotor Flow Using an Implicit 3D Flow Solver with One-Equation Spalart-Allmaras Turbulence Model. ASME Paper 2001-GT-0359.

Niestroj, O. and Came, P. (1998). Three-Dimensional Flow Predictions in Axial-Flow Turbine Cascades. ASME Paper 98-GT-325.

Patel, V. C., Rodi, W. and Scheuerer, G. (1984). Turbulence Models for Near-Wall and Low Reynolds Number Flows: A Review. AIAA *Journal*, Vol. 23, No. 9, 1308-1319.

Philbrick, D. A. and Topol, D. A. (1993). Fan Noise Prediction System Development: Wake Model Improvements and Code Evaluations. NASA Contract NAS325952, Task 3 Informal Report.

Poensgen, C. and Gallus, H. (1990). Three-Dimensional Wake Decay Inside of a Compressor Cascade and Its Influence on the Downstream Unsteady Flow Field. ASME Paper 90-GT-21.

Politis, E., Giannakoglou, K. and Papailiou, K. (1997). Axial Compressor Stage Analysis Through a Multi-Block 3-D Navier-Stokes Solution Method. ASME Paper 97-GT-93.

Prato, J. and Lakshminarayana, B. (1993). Investigation of Compressor Rotor Wake Structure at Peak Pressure Rise Coefficient and Effects of Loading. ASME Paper 92-GT-32. ASME *Journal of Turbomachinery*, Vol. 115, No. 3, 487-500.

Rai, M. M. (1987). Unsteady Three-Dimensional Navier-Stokes Simulations of Turbine Rotor Stator Interactions. AIAA Paper 87-2058.

Raithby, G. D. (1976). Skew Upstream Differencing Schemes for Problems Involving Fluid Flow. *Computational Methods Applied to Mechanical Engineering.*, vol. 9, 153-164.

Ravindranath, A. and Lakshminarayana, B. (1980) Three Dimensional Mean Flow and Turbulence Characteristics of the Near Wake of a Compressor Rotor Blade. NASA CR-159518.

Raw, M. (1996). Robustness of Coupled Algebraic Multigrid for the Navier-Stokes Equations. AIAA Paper 96-0297.

Reynolds, B. and Lakshminarayana, B. (1979) Characteristics of Lightly Loaded Fan Rotor Blade Wakes. NASA CR-3188.

Rhie, C., Gleixner, A., Spear, D., Fischberg, C. and Zacharias, R. (1995). Development and Application of a Multistage Navier-Stokes Solver. Part I: Multistage Modeling Using Bodyforces and Deterministic Stresses. ASME Paper 95-GT-342.

Robinson, C. J. (1991). *End-Wall Flows and Blading Design for Axial Flow Compressors*. Cranfield Institute of Technology PhD Thesis, page 115.

Rodi, W. (1980). Turbulence Models and their Aplication in Hydraulics. International Association for Hydraulic Research, *state of the art paper* , Delft.

Rubesin, M. W. (1977). Numerical Turbulence Modelling. published in *Computational Fluid Dynamics*. AGARD LS-86.

Schmidt, D. and Okiishi, T. (1977). Multistage Axial-Flow Turbomachine Wake Production, Transport, and Interaction. AIAA Paper 77-202. AIAA *Journal*, Vol. 15, No. 8, 1138-1145.

Shaw, C. T. (1992). *Using Computational Fluid Dynamics*. Prentice Hall, Hemel Hempstead.

Shepherd, I. C. (1979). A Four Hole Pressure Probe for Fluid Flow Measurements in Three Dimensions. ASME *Journal of Fluid Engineering*, Vol. 103, 590-594.

Shikano, Y. (1993). Numerical Analysis of the Flow Field Through a Turbine Stage with Bucket Tip Clearance. Jpn. Soc. Mech. Eng. *Transactions*, Vol. 59, No. 563, 2202-2208. (Japanese original). JSME *International Journal* - Series B, Vol. 38, No.4, 593-599. (English translation).

Shima, E. and Egami, K. (1994). Navier-Stokes Computation of a High-Lift System Using Spalart-Allmaras Turbulence Model. AIAA Paper 94-0162.

Singh, U. and Smith, G. (1998). A Comparison of Measured and Predicted Unsteadiness in a Transonic Fan. ASME Paper 98-GT-274.

Sitaram, N. and Lakshminarayana, B. (1983). End-wall Flow Characteristics and overall Performance of an Axial Flow Compressor Stage. NASA CR-3671.

Sleiman, M., Robichaud, M., Peeters, M., Tam, A., Habashi, W. and Fortin, M. (1996). Turbomachinery Multistage Simulation by a Finite Adaptive Approach. ASME Paper 96-GT-418.

Smout, P. and Cook, S. (1991). The Dependence of Thermocouple Probe Calibration on Stagnation Density Changes. AIAA Paper 96-GT-146.

Smout, P. D. and Ivey, P. C.. (1991). Investigation of Wedge Probe Wall Proximity Effects: Part 1 – Experimental Study. ASME Paper 91-2276. ASME *Journal of Engineering for Gas Turbines and Power*, Vol. 119, No 3, 598-611.

Solomon, W. and Walker, G. (1995). Observations of Wake-Induced Transition on an Axial Compressor Blade. ASME Paper 95-GT-381.

Spalart, P. R. (2000). Trends in Turbulence Treatment. AIAA Paper 2000-2306.

Storer, J. and Cumpsty, N. (1993). An Approximate Analysis and Prediction Method for Tip Clearance Loss in Axial Compressors. ASME Paper 93-GT-140.

Stow, P. (2000). Engineering Simulation – An Emerging Reality. Presentation to the seminar *CFD in Turbomachinery Design*, 2000, Cranfield.

Suryavamshi, N. and Lakshminarayana, B. (1991a). Numerical Prediction of Wakes in Cascades and Compressor Rotors Including the Effects of Mixing: Part I - Cascade Wakes Including the Effects of Incidence and Free-Stream Turbulence. ASME Paper 91-GT-225. ASME *Journal of Turbomachinery*, Vol. 114, 607-616.

Suryavamshi, N. and Lakshminarayana, B. (1991b). Numerical Prediction of Wakes in Cascades and Compressor Rotors Including the Effects of Mixing: Part II - Rotor Passage Flow and Wakes Including the Effects of Spanwise Mixing. ASME Paper 91-GT-222.

Tannehill, J. C., Anderson, D. A. and Pletcher, R. H. (1997). *Computational Fluid Mechanics and Heat Transfer*. Taylor & Francis, Washington, DC, USA.

TASCflow *Theory Documentation*, Advanced Scientific Computing Ltd., Waterloo, Ontario, Canada, 1995.

Test Cases for Computation of Internal Flows in Aero Engine Components, AGARD AR 275, 1990. – Report by Ginder, R. B. and Harris, D.

Thomas, M. E., Shimp, N. R., Raw, M. J., Galpin, P. F. and Raithby, G. D. (1989). The Development of an Efficient Turbomachinery CFD Analysis Procedure. AIAA Paper 89-2394.

Turner, M. G. (1986). Multistage Turbine Simulations with Vortex-Blade Interactions. ASME *Journal of Turbomachinery*, Vol. 118, 643-653.

Tweedt, D., Hathaway, M. and Okiishi, T. (1985). Multistage Compressor Stator/Rotor Interaction. AIAA Paper 85-0009. AIAA *Journal of Propulsion and Power*, Vol. 1, No. 6, 449-455.

Valkov, T. and Tan, C. (1998a). Effect of Upstream Rotor Vortical Disturbances on the Time-Average Performance of Axial Compressor Stators: Part 1 - Framework of Technical Approach and Wake-Stator Blade Interaction. ASME Paper 98-GT-312.

Valkov, T. and Tan, C. (1998b). Effect of Upstream Rotor Vortical Disturbances on the Time-Average Performance of Axial Compressor Stators: Part 2 - Rotor Tip Vortex-Stator Blade Interactions. ASME Paper 98-GT-313.

Van Doormaal, J. P. and Raithby, G. D. (1984). Enhancements of the Simple Method for Predicting Incompressible Fluid Flows. Journal of Numerical Heat Transfer, Vol 7, pp 147-163.

VanZante, D., Adamczyk, J., Strazisar, A. and Okiishi, T. (1997). Wake Recovery Performance Benefit in a High-Speed Axial Compressor. ASME Paper 97-GT-535.

Walker, G. and Oliver, A. (1972). The Effect of Interaction Between Wakes From Blade Rows in an Axial Flow Compressor on the Noise Generated by Blade Interaction. ASME Paper 72-GT-15.

Walker, G., Hughes, J. and Solomon, W. (1998). Periodic Transition on an Axial Compressor Stator - Incidence and Clocking Effects. Part I - Experimental Data. ASME Paper 98-GT-363.

Walraevens, R. E., Gallus, H. E., Jung, A. R., Mayer, J. F. and Stetter, H. (1998). Experimental and Computational Study of the Unsteady Flow in a 1.5 Stage Axial Turbine with Emphasis on the Secondary Flow in the Second Stator. ASME Paper 98-GT-254.

Wennerstrom, A. (1990). A Review of Predictive Efforts for Transport Phenomena in Axial Flow Compressors. ASME *Journal of Turbomachinery*, Vol. 113, 175-179.

Weyer, H. (1975). On the Measurement of the Fluctuating Total and Static Pressures in Turbomachines Including the Determination of Correct Time-Weighted Pressures. published in *Modern Methods of Testing Rotating Components of Turbomachines (Instrumentation)*. AGARD AG-207

Wilcox, D. C. (1984). A Complete Model of Turbulence Revisited. AIAA Paper 84-176.

Wilcox, D. C. (1993). A Two-Equation Turbulence Model for Wall-Bounded and Free-Shear Flows. AIAA Paper 93-2905.

Wilcox, D. C. and Rubesin, M. W. (1980). Progress in Turbulence Modelling for Complex Flow Fields Including Effects of Compressibility. NASA TP 1517.

Wilde, G. L. (1994). A New Approach to the Design of the Large Turbofan Power Plant. Proc IMechE, Vol 209.

Wisler, D., Bauer, R. and Okiishi, T. (1987). Secondary Flow, Turbulent Diffusion and Mixing in Axial-Flow Compressors. ASME Paper 87-GT-16.

Wright, P. I. And Miller, D. C. (1991). An Improved Compressor Performance Prediction Model Proceedings of the European Conference *Turbomachinery – Latest Developments in a Changing Scene*, IMechE, 19-20 March 1991, London, Paper C423-028.

Yakhot, V. and Orszag, S. A. (1986). Renormalization Group Analysis of Turbulence I Basic Theory. *Journal of Scientific Computing*, Vol. 1, No. 1.

Yang, R.-J. and Lin, S.-J. (1994). Numerical Solutions of Two-Dimensional Multistage Rotor/Stator Unsteady Flow Interactions. *Journal of Propulsion and Power*, Vol. 10, No. 6, 876-883.

Yao, J., Ji, S., Liu, F. and Jennions, I. (1998). Computation of Steady Flow in a Turbomachinery Stage by a Third-Order Accurate Scheme. AIAA Paper 98-0920.